Titre: Title:	Integrated Microphotonic-MEMS Inertial Sensors
Auteur: Author:	Kazem Zandi
Date:	2013
Type:	Mémoire ou thèse / Dissertation or Thesis
Référence: Citation:	Zandi, K. (2013). Integrated Microphotonic-MEMS Inertial Sensors [Thèse de doctorat, École Polytechnique de Montréal]. PolyPublie. https://publications.polymtl.ca/1113/

UNIVERSITÉ DE MONTRÉAL

INTEGRATED MICROPHOTONIC-MEMS INERTIAL SENSORS

KAZEM ZANDI

DÉPARTEMENT DE GÉNIE PHYSIQUE

ÉCOLE POLYTECHNIQUE DE MONTRÉAL

THÈSE PRÉSENTÉE EN VUE DE L'OBTENTION

DU DIPLÔME DE PHILOSOPHIAE DOCTOR

(GÉNIE PHYSIQUE)

AVRIL 2013

UNIVERSITÉ DE MONTRÉAL

ÉCOLE POLYTECHNIQUE DE MONTRÉAL

Cette thèse intitulée:

INTEGRATED MICROPHOTONIC-MEMS INERTIAL SENSORS

présentée par: ZANDI Kazem

en vue de l'obtention du diplôme de : Philosophiae Doctor

a été dûment acceptée par le jury d'examen constitué de :

Mme SANTATO Clara, Ph. D., présidente

M. PETER Yves-Alain, Dr. Sc., membre et directeur de recherche

M. MARTEL Sylvain, Ph. D., membre

M. FRÉCHETTE Luc, Ph. D., membre

DEDICATION

To my mom and my unconditionally devoted sister Massoumeh

ACKNOWLEDGEMENTS

First of all, I would like to express my gratitude to my research director Yves-Alain Peter for helping me in carrying out my research works. I would like to also thank the members of MPBC Inc. for their collaboration on this work, especially Dr. Roman V. Kruzelecky for his helpful suggestions. I gratefully acknowledge the constructive suggestions of Linh Ngo-Phong from the Canadian Space Agency as well as the financial assistance of the Canadian Space Agency for this work. I am grateful to Dr. Pierre Pottier for his friendly and generous assistance. We had many fruitful discussions especially on the integration of FP with optical waveguides. I also thank Ahmad Hayat for his help in mechanical characterization of FP devices. Many special thanks to Alireza Hajosseini Mesgar for his help in electrical testing of the MEMS comb drive actuator. I am also grateful to him for sharing his experiences and knowledge in times of need. I would like to express my most sincere appreciation to my friend Dr. Alireza Hassani for his assistance in many aspects. He has always been available when I needed help, whether academic or otherwise. I also wish to give my thanks to Philippe Vasseur, Christophe Clément, and Marie-Hélène Bernier for their constructive support in cleanroom. I have learned a lot from them during my Ph. D studies. Also thanks to all other people that have been omitted from the above list, those who have provided aid, support and discussions. Finally, I would like to thank my family for their constant mental support and love. I definitely would not have gotten this far without their love and support.

RÉSUMÉ

Au cours de la dernière décennie, le développement du contrôle d'attitude de petits satellites a évolué vers une stabilisation complète à trois axes et un contrôle précis alors que leur application augmente dans les télécommunications et les missions de connaissance de l'espace. Pour les systèmes spatiaux, les principaux facteurs sont la puissance, la masse et la fiabilité dans l'environnement spatial. Ceci est associé à une nécessité croissante de systèmes de navigation inertielle compacts et de faible puissance. Les systèmes de navigation actuels d'engins spatiaux consistent en différents capteurs et processeurs qui ne sont pas optimisés pour fonctionner ensemble. Cela est coûteux et peut exiger une réduction considérable de la masse et des ressources en puissance disponibles sur un petit engin spatial. Par conséquent, les composants doivent être optimisés par rapport à leur taille, design et procédé de fabrication.

L'objectif de cette thèse est de concevoir, simuler, fabriquer et caractériser des accéléromètres et des capteurs de vitesse de rotation (gyroscopes) planaires miniatures à haute sensibilité et faible coût à base de microsystèmes électromécaniques (MEMS) à bande interdite photonique (PBG) sur un substrat silicium-sur-isolant (SOI) afin d'intégrer un réseau à deux axes de ces capteurs sur une même plate-forme SOI. L'utilisation de dispositifs optiques à guide d’ondes intégrés avec des MEMS sur SOI pour les systèmes de capteurs multicanaux/multifonctions permet l'utilisation de capteurs multiples pour étendre la gamme de mesure et la précision. Cela fournit une redondance essentielle qui rend possible une fiabilité à long terme dans l'environnement spatial, réduisant ainsi la possibilité de défaillance du système. Un navigateur sur puce représente également la capacité à accommoder divers capteurs d'attitude et inertiels sur la même puce afin d'éliminer le besoin de nombreux capteurs séparés. Le produit final présente une réduction de plusieurs ordres de grandeur de la masse et de la taille du système. En outre, la redondance améliore la performance nette et la précision des systèmes de mesure de navigation.

Deux classes d'accéléromètres/gyroscopes optiques sont examinées dans cette thèse pour application dans la navigation de petits satellites, l'une fondée sur un filtre accordable Fabry-Perot (FP), où le capteur est actionné par l'accélération appliquée fournissant un décalage de la longueur d'onde d'opération qui varie linéairement avec l'accélération appliquée, et l'autre fondée sur un atténuateur optique variable (VOA), où le capteur est actionné par l'accélération appliquée fournissant pour les petits déplacements un changement linéaire de l'intensité relative du signal

avec l'accélération appliquée. Dans le cas de capteurs à base de FP, la microcavité FP se compose de deux réflecteurs de Bragg distribués (DBR) dont un miroir DBR est attaché à la masse sismique du système. À la suite d'une accélération/rotation, le déplacement relatif du miroir mobile par rapport au miroir fixe change la longueur de la cavité et modifie la résonance FP. Dans le cas de capteurs à base de VOA, un procédé de modulation d'obturation est utilisé pour moduler l'intensité de la lumière couplée à un guide d'onde multimode en silicium. Un miroir DBR qui est attaché à la masse sismique du système du capteur est positionné dans l'espace entre deux guides d'onde multimodes d'entrée et de sortie. Le déplacement du miroir de Bragg en présence d'accélération/rotation module l'intensité du signal optique transmis entre les guides d'onde d'entrée et de sortie. La sensibilité du capteur est inversément proportionnelle à la largeur des guides d'onde à la jonction du VOA et est inversément proportionnelle à la fréquence de résonance du système.

La principale différence entre les capteurs à base de FP et de VOA présentés ici est que le filtre FP permet une détection optique très sensible du déplacement à une échelle nanométrique, mais nécessite des sources et détecteurs optiques plus complexes, alors que les capteurs à base de VOA n'exigent pas des sources à haute qualité spectrale et la détection est beaucoup plus simple étant donné que l'intensité de la lumière est mesurée à la sortie plutôt que la longueur d'onde. Cependant, pour obtenir un capteur de haute sensibilité, des déplacements au niveau du micromètre sont nécessaires.

Pour les gyroscopes, le capteur utilise un oscillateur à peigne électrostatique de type MEMS pour faire osciller la masse sismique du MEMS le long de l'axe des *x* à des fréquences de l'ordre de 500 à 1000 Hz. Une rotation appliquée dans l'axe des *z* provoque le déplacement linéaire de la masse sismique et l'actionneur de détection du VOA / miroir FP mobile, le long de l'axe des *y* perpendiculaire, proportionnel à la vitesse de rotation. Ce déplacement est modulé alternativement par les oscillations selon l'axe des *x*, modulant l'actionneur du VOA / l'espacement FP et le signal optique / la longueur d'onde transmise résultante. L'oscillateur électrostatique du MEMS nécessite environ 100 V en courant alternatif pour exciter les oscillations, tel que validé expérimentalement. Cela déplace la masse sismique périodiquement de l'ordre de +/- 3 µm. Ce déplacement n'est pas suffisant pour fournir une modulation élevée du signal optique transmis dans le cas où un VOA est utilisé. Un mécanisme de micro-levier conforme est donc appliqué pour amplifier le déplacement du dispositif de détection à VOA.

Dans le cas du capteur à base de FP, une structure conforme n'est pas nécessaire étant donné que même un déplacement de l'ordre du nanomètre peut déplacer de manière significative le pic de transmission du FP. En raison de la conception symétrique de tous les capteurs inertiels présentés ici, ils ont le potentiel d'être conçus comme des capteurs à deux axes.

Des tranches de SOI de différentes épaisseurs sont utilisées en fonction de la performance requise du dispositif et des besoins d'optimisation des procédés. Les étapes de fabrication (procédés de photolithographie et de gravure ionique réactive profonde [DRIE]) ont dû être optimisées à chaque fois que l'épaisseur de SOI a été changée. Pour les tranches de SOI plus épaisses, des résines plus épaisses sont nécessaires comme masque pour le procédé DRIE. L'utilisation de résines épaisses rend la fabrication plus difficile car elle limite la résolution de la photolithographie. Pour chaque épaisseur, les tranchées gravées ont dû être contrôlées par rapport à deux phénomènes bien connus dans le procédé DRIE, à savoir le "scalloping" et le "notching". En particulier, il est très important de minimiser le scalloping sur les parois de silicium, car il génère des pertes optiques par diffusion pour les guides d'onde. Au début de ce travail, du SOI de 30 µm d'épaisseur a été utilisé pour fabriquer les dispositifs. La méthode de couplage bout à bout a été utilisée pour coupler la lumière des fibres optiques aux guides d'onde canaux en silicium. Étant donné que la sensibilité et la résolution du capteur sont proportionnelles à la masse sismique du système, le fait d'utiliser des plaquettes de SOI plus épaisses augmente la masse sismique du capteur pouvant être atteinte, améliorant par conséquent la performance des capteurs. Cela permet également d'intégrer des fibres optiques à la puce et en plus de minimiser les problèmes de désalignement et les instabilités de signal. En outre, cela réduit la sensibilité interaxiale du capteur (en raison d'une raideur interaxiale plus grande). Par conséquent, dans la $2^{ème}$ phase du projet, du SOI d'épaisseur 47 µm a été choisi pour intégrer passivement des fibres optiques de 80 µm à la puce en utilisant des fentes en U. La masse sismique pouvant être atteinte a été étendue par l'ajout de la masse de la plaquette de Si sous-jacente à la masse sismique du capteur sur la couche du dispositif. Cette approche (que nous appelons “Vertically Extended Mass” (VEM)) peut fournir la plus forte sensibilité d'accélération possible jusqu'à moins de 10 µg. Comme il n'y a pas de substrat sous-jacent, l'approche VEM assure également la plus basse friction possible. Toutefois, la fabrication nécessite deux étapes distinctes de DRIE, et le rendement de fabrication qui en résulte est faible, ce qui nécessite une optimisation additionnelle

de procédé. Pour finir, des tranches de SOI de 75 µm d'épaisseur ont été utilisées pour permettre l'interfaçage des guides d'onde en silicium avec les fibres optiques télécom standards de 125 µm.

Contrairement au cas du SOI de 47 µm, pour les cas de SOI de 30 µm et 75 µm, tous les composants du capteur ont été fabriqués en une seule étape de DRIE. Dans le cas du SOI de 47 µm, une plaquette de double SOI a été également utilisée pour guider la lumière uniquement à l'intérieur de la couche supérieure du dispositif, ce qui permet d'avoir des guides d'onde plus minces et ainsi de diminuer la perte optique par diffusion provenant de la rugosité des parois latérales générée pendant le procédé DRIE. Également, avec cette configuration, le phénomène de notching des guides d'onde est évité. Deux types de guides d'onde, à savoir des guides d'onde "rib" et "strip" (canal), sont utilisés pour guider la lumière des fibres optiques au capteur, et vice versa. Pour créer un guide d'onde rib, une autre étape de fabrication est nécessaire sur le dessus du dispositif. Cela nécessite une bonne couverture de résine sur la région de topographie. À cette fin, une nouvelle méthode appelée tension de surface dynamique (DST) a été utilisée dans ce projet.

Des essais mécaniques ont été effectués après chaque libération de dispositif et avant la caractérisation optique en utilisant un montage à sonde afin de s'assurer que le dispositif est complètement libéré.

Les réponses statiques des accéléromètres ont été mesurées en l’exposant à la gravité. L'accéléromètre à base de FP fabriqué sur du SOI de 30 µm a démontré une sensibilité de 2,5 nm/g et une résolution de 4 mg. La performance du capteur a été améliorée en abaissant la fréquence propre du capteur (en utilisant une plus grande masse sismique et des ressorts plus souples), conduisant à une sensibilité de 90 nm/g et 111 µg de résolution pour le capteur. La réponse du capteur est linéaire et sa performance a le potentiel d'atteindre la résolution du µg. L'accéléromètre VEM à base de VOA fabriqué sur du double SOI de 47 µm a démontré avoir une sensibilité de 1.5±0.3 dB/g et une réponse linéaire sur 0,7 g d'accélération appliquée. La sensibilité a été améliorée par un facteur de 2.5±0.3 en réduisant autant la fréquence de résonance que les largeurs des guides d'onde à la jonction du VOA lorsqu’une tranche de SOI de 75 µm d’épaisseur était utilisée comme substrat.

ABSTRACT

Over the last decade, the development of small satellites attitude control has moved towards full three axis stabilization and precise control as their application increases in telecom and space knowledge missions. For space-based systems, the major drivers are power, mass and reliability in the space environment. This is associated with an increasing necessity for compact, low-power inertial navigation systems. Current spacecraft navigation systems consist of various sensors and processors that are not optimized to operate together. This is costly and can require a considerable reduction of the mass and power resources available on a small spacecraft. Therefore the components need to be optimized relative to their size, design, and fabrication process.

The objective of this thesis is to design, simulate, fabricate and characterize high sensitive low cost in-plane photonic-band-gap (PBG)-micro electromechanical systems (MEMS)-based miniature accelerometers and rotational rate sensors (gyroscopes) on a silicon-on-insulator (SOI) substrate in order to enable the integration of an array of two-axis of these sensors on a single SOI platform. Use of guided-wave optical devices integrated with MEMS on SOI for multichannel/multifunction sensor systems allows the use of multiple sensors to extend the measurement range and accuracy. This provides essential redundancy which makes long-term reliability in the space environment possible therefore reducing the possibility of system failure. The navigator microchip also represents the ability of accommodating diverse attitude and inertial sensors on the same microchip to eliminate the need of many separate sensors. The end product exhibits orders of magnitude reduction in system mass and size. Furthermore, redundancy improves the net performance and precision of the navigation measurement systems.

Two classes of optical accelerometers/gyroscopes are considered in this thesis for application in smallsats navigation, one based on tunable Fabry-Perot (FP) filter, where the sensor is actuated by the applied acceleration providing a shift in the operating wavelength that varies linearly with the applied acceleration and the other one based on variable optical attenuator (VOA), where the sensor is actuated by the applied acceleration providing a linear change for small displacements around the waveguide propagation axis in the relative signal intensity with the applied acceleration. In the case of FP-based sensors, the FP microcavity consists of two distributed Bragg reflectors (DBR) in which one DBR mirror is attached to the proof mass of the system. As

a consequence of acceleration/rotation, the relative displacement of the movable mirror with respect to the fixed mirror changes the cavity length and modifies the FP resonance. In the case of VOA-based sensors, a shutter modulation method is used to modulate the coupled light intensity to a multimode strip silicon waveguide. A DBR mirror that is attached to the system proof mass of the sensor is positioned in the gap between two input and output multimode waveguides. The displacement of the Bragg mirror in the presence of acceleration/rotation modulates the intensity of the transmitted optical signal between the input and the output strip waveguides. The sensor sensitivity is inversely proportional to both waveguides widths at the VOA junction and system resonant frequency.

The main differences between FP-based and VOA-based sensors presented here is that the FP filter enables a highly sensitive optical detection of displacement at a nanometer scale but requires more complex optical sources and detectors, whereas VOA-based sensors do not require high spectral quality sources and the detection is much simpler since the intensity of light is measured at the output instead of the wavelength. However to obtain a high sensitive sensor, displacements at the level of micrometer are required.

For gyroscopes, the sensor uses a MEMS electrostatic comb-drive with interdigital fingers to oscillate the MEMS proof mass along the x-axis at rates of about 500 to 1000 Hz. An applied rotation in the z-axis causes the proof mass and the VOA sensing actuator/FP movable mirror to be linearly displaced along the perpendicular y-axis, proportional to the rotation rate. This displacement is ac modulated by the x-axis oscillations, modulating the VOA actuator/FP gap and the resultant transmitted optical signal/wavelength. The MEMS electrostatic oscillator requires about 100 V ac to deflect the proof mass periodically by about +/- 3 microns, as validated experimentally. This displacement is not enough to provide high modulation on the transmitted optical signal in the case where VOA is used. Therefore a compliant microleverage mechanism is introduced to amplify the displacement of the VOA sensing device. A two stage micro-lever mechanism is proposed, providing 7 x displacement amplification. In the instance of the FP-based sensor, a compliant structure is not required since even nano-displacement can significantly shift the transmission peak of the FP.

Due to the symmetrical design of all inertial sensors presented here, they have the potential to be designed as two-axis sensors.

SOI wafers with different thicknesses are used depending on required device performance and process optimization needs. The fabrication steps (photolithography and deep reactive ion etching (DRIE) processes) had to be optimized every time the SOI thickness was changed. For thicker SOI wafers, thicker resists are required as a mask for the DRIE process. Using thick resists make the fabrication more challenging since it limits the photolithography resolution. For each thickness the etched trenches had to be checked for two well-known phenomena in DRIE process namely, scalloping and notching. In particular, it is very important to minimize the scalloping on the silicon walls since they generate scattering optical losses for the waveguides. At the beginning of this work 30 μm thick SOI wafer was used to fabricate the devices. Butt coupling method was used to couple light from optical fibers to the silicon strip waveguides. Since the sensor sensitivity and resolution are both proportional to the system proof mass, using thicker SOI wafers increases the attainable sensor proof mass, consequently improving the sensors performance. This also allows integrating optical fibers to the chip and moreover minimizing the misalignment issues and signal instabilities. Moreover, it reduces the cross-axis sensitivity of the sensor (due to the greater cross-axis stiffness). Therefore in the 2nd phase of the project 47 μm thick SOI wafer was chosen to passively integrate 80 μm optical fibers to the chip using U-grooves. The attainable proof mass was extended further vertically by adding the mass of the underlying Si wafer to the sensor proof mass on the device layer. This method is named as "Vertically Extended Mass" (VEM) approach. This approach can provide the highest achievable acceleration sensitivity to below 10 μg. As there is no underlying substrate, the VEM approach also provides the lowest achievable stiction. However, the fabrication requires two separate DRIE steps and the resulting fabrication yield is low, requiring additional process optimization. Finally 75 μm thick SOI wafers were used to enable interfacing the silicon waveguides to the standard 125 μm telecom optical fibers.

Unlike the case of 47 μm SOI, for the cases of 30 μm and 75 μm SOI, all sensor components were fabricated in one single DRIE step. In the case of 47 μm SOI, a double SOI wafer was also used to guide light only inside the top device layer providing thinner waveguides and therefore lowering scattering optical loss from the side-walls roughness generated during DRIE process. Also with this configuration the notching phenomenon at the bottom of the waveguides is avoided. Two types of waveguides, namely rib and strip waveguides are used to guide the light from optical fibers to the sensor and vice versa. To create a rib waveguide another fabrication

step is required on top of the device. This requires good resist coverage on the topography region. For that purpose a new method called dynamic surface tension (DST) was developed in this project. Mechanical testing was performed after each device releasing and prior to optical characterization by using a probe station setup to ensure that the device is completely released.

The static responses of the accelerometers were measured by exposing them to gravity. The FP-based accelerometer fabricated on 30 μm SOI wafer demonstrated 2.5 nm/g sensitivity and 4mg resolution. The sensor performance was improved by lowering the sensor natural frequency (using bigger proof mass and softer springs) leading to 90 nm/g sensitivity and 111μg resolution for the sensor. The sensor response is linear and its performance has the potential to reach μg resolution. The VEM VOA-based accelerometer fabricated on 47 μm double SOI demonstrated 1.5±0.3 dB/g sensitivity and a linear response over 0.7 g applied acceleration. The sensitivity was improved by a factor of 2.5±0.3 by reducing both, the resonance frequency and the width of the waveguides at the VOA junction where 75 μm single SOI wafer was used as the substrate.

SUMMARY

Although optical inertial sensors with high performance have been previously reported, none of them is integrated with optical waveguides for in-plane detection purposes. In this work, fully integrated high performance optical MEMS inertial sensors are presented for the first time. All the optical and MEMS components have been integrated on a single silicon-on-insulator (SOI) chip. In-plane optical accelerometers and gyroscopes with two different working principal were successfully fabricated on SOI wafers with different device layer thicknesses. Optical accelerometers were also successfully characterized. These inertial sensors have been designed for micro-satellites navigation purposes where a high performance, compact and low power microchip is required. The most important characteristic of these sensors aside being integrated is their immunity to electromagnetic interferences, making them suitable for space applications. Two different designs with different working principle integrated with optical waveguides are presented. First one is a micro electromechanical systems Fabry-Perot (MEMS FP) based sensor. It is actuated by an applied acceleration to provide a shift in the FP resonance wavelength. Device shows a linear response over its free spectral range with demonstrated 90 nm/g sensitivity and 111μg resolution at 450 Hz. Device has the potential to reach μg resolution if larger mass and softer spring is used. The second one is a MEMS variable optical attenuator (VOA)-based sensor. A Bragg mirror that is attached to the sensor proof mass is positioned in the middle of the gap of two optical waveguides: input and output waveguides. When the device is actuated by the applied acceleration, the intensity of the transmitted light from the input waveguide to the output waveguide is modulated by the displacement of the Bragg mirror. Sensor shows a linear response over 0.6 g applied acceleration and 3.4±0.4 dB/g sensitivity. Its performance can be improved by reducing the width of the waveguides at the VOA junction and/or using larger mass and softer springs. The gyroscopes mechanical response was also tested using an integrated MEMS electrostatic comb-drive with interdigital fingers. Device was actuated at 10 Hz frequency for an applied voltage of 100 V leading to 3 μm in-plane displacement. Integration of an array of two-axis of accelerometers and gyroscopes on a single SOI substrate using optical waveguides is possible in future, representing a light, multifunction, low power, high performance, low cost, robust and reliable microchip navigator.

TABLE OF CONTENTS

LIST OF TABLES

LIST OF FIGURES

LIST OF ABBREVIATIONS

$\vec{E}$	Electric field
$\vec{H}$	Magnetic field
n	Refractive index
k	Wave vector
r	Reflection coefficient
t	Transmission coefficient
R	Reflectance
T	Transmittance
λ	wavelength
x	Gap of Fabry-Perot
m	Order of Fabry-Perot
h	Order of Bragg mirror
F	Finesse
$\delta\lambda_R$	Full width at half maximum
b	Damping factor
M	Mass
k	Spring constant
ω	Angular frequency
Δx	Displacement
μ	Medium viscosity
ξ	Damping ratio
a	Accelaration
w_0	Gaussian beam waist size

z_R	Rayleigh range
P	Optical power
L	Optical loss
Ω	Angular rotation
Q	Quality factor
E	Young's modulus
l	Beam length
n_f	Number of fingers of a comb drive
V	Applied voltage
ε_0	Vacuum permittivity

INDICES

1	Medium 1
2	Medium 2
c	Coriolis (Force)
D	Driving (Frequency)
eff	Effective
H	High refractive index
i	Medium i
L	Low refractive index
n	natural (Frequency)
p	Mode p
q	Mode q
R	Reflectance
t	Medium t

ABBREVIATIONS

VEM	Vertical Extended Mass
AFM	Atomic force microscopy
DBR	Distributed Bragg reflectors
DRIE	Deep reactive ion etching
DST	Dynamic surface tension
EMI	Electromagnetic interference
FOG	Fiber optical gyroscope
FP	Fabry-Perot
FPI	Fabry-Perot interferometer
FSR	Free spectral range
FWHM	Full width at half maximum
MEMS	Microelectro-mechanical systems
micro-PIC	Microphotonic integrated circuits
NA	Numerical aperture
OSA	Optical spectrum analyzer
PBG	Photonic-band-gap
RLG	Ring laser gyroscope
SEM	scanning electron microscopy
SMF	Single mode fiber
SOI	Silicon on insulator
VOA	Variable optical attenuator
WHU	Wafer handling unit

LIST OF APPENDICES

CHAPTER 1 INTRODUCTION

Microphotonics is a new technology using miniaturized photonic elements with wafer-level integrated systems which sense, emit, and transmit light and other forms of energy with photon as quantum unit. Microphotonics technology is comprised of a variety of new devices, materials, processes, namely Photonic Integrated Circuits (PICs), Micro Opto Electromechanical Systems (MOEMS), Photonic-Band-Gap structures (PBGs), smart materials, and quantum photonic system.

Microphotonic integrated circuits (micro-PICs) are the integration of two or more photonic devices on a single substrate alike microelectronic chips. Nevertheless, instead of guiding electricity, a micro-PIC transmits light beams. The main difficulty that microphotonics should solve is system integration. Integrating different optical components on a unique substrate, will contribute in reducing the amount of external fiber optic interconnections, consequently decreasing the overall system mass and size, and contributing the optimization of the system reliability as well as its cost efficiency. Many fields use microphotonics technology for their operations, namely: space, medicine, telecommunications, security and military. The application of microphotonics technology in space has to recognize the specific needs of the space industry, the space operational field as well as the technical feasibility. Based on the systems needs for space, the components need to be optimized relative to their size, design, and fabrication process. Over the last decade, the development of small satellites attitude control has moved towards full three axis stabilization and precise control as their application increases in telecom and space knowledge missions. This results in an increasing need for compact, low-power inertial navigation systems. An inertial navigation system (INS) is a combination of motion sensors (accelerometers) and rotation sensors (gyroscopes). The navigation is accomplished by integrating the output of the sensors to continuously calculate the position, orientation, and velocity (direction and speed of movement) of the satellite. Accelerometers measure linear acceleration with respect to an inertial frame and gyroscopes (angular rate sensors) measure angular rotation rates with respect to an inertial space. Essentially, an INS contains three accelerometer and three gyroscopes as an arbitrary motion in space requires six degree of freedom. Satellite navigation system can take advantage of implementing micro-PIC and micro-electro-mechanical systems (MEMS) technologies. The integration of PBGs with MEMS

(PBG/MEMS) and guided-wave optics on a single platform present new feasibilities for miniature space systems that have a significant effect on system performance, size, weight, data integrity, power consumption and lowering the cost of space-based systems [1]. Table 1-1 summarizes the requirements of accelerometers being used in the current microsats based on their missions.

Table 1-1: Requirements of accelerometers that are used in current microsats

Parameter	Requirement	Mission/ Microsat.	Sensor Requirement
Position Accuracy	+/-300 m over 45 min. Measurement time per orbit	Nadir Earth Observation	< +/- 0.010 mg
Cross-axis sensitivity			1% is current performance for best MEMS capacitance sensors
Typical acceleration levels for satellite in orbit	1 to 50 mg		100 mg full scale should cover most in-orbit acceleration (except the launching)
Launch vibration levels	<11 g rms typically	Proba 2	About 20 g peak
Frequency range of operation	1-10Hz for navigation control of typical spacecraft		10 Hz sensor measurement rate
Operating temperatures	-40 ^{o}C to +60 ^{o}C	Proba-2	-40 ^{o}C to +60 ^{o}C

There are mainly two technologies being considered as platforms, namely Silicon-On-Insulator (SOI) and Indium-Gallium-Arsenide-Phosphide (InGaAsP). The principal differences between the two platforms are higher costs and less experimented fabrication technologies for the III-V compound semiconductors. Currently, the SOI platform is widely being used because of its compatibility with high-speed CMOS integrated electronics making the fabrication process easier. Also the size of the integrated optical structures is smaller due to the high index contrast between silicon and air. Consequently, in most cases, the SOI would constitute the preferred choice of substrate for integrating the microphotonics technologies for diverse space applications.

Accelerometers have many applications depending on their resolution, range, and bandwidth. The earliest large scale application is in automotive industry, where they are used in the air bag system. In micro scale, they have much broader applications such as in: *consumer products* such as camcorders to stabilize the image, three-dimensional mousses, laptop and tablet computers, mobile phones and remote controllers, games, toys, etc; *biomedicine* such as activity monitoring; *industry* such as robotics, vibration monitoring in machines, and shock monitoring for goods transportation; *geology* such as scientific research of earthquakes; *military* such as accurate guidance in missiles and other ordnance, aircrafts; *space* such as inertial navigation applications. In the latter case, very high resolution in the order of micro-gravity is required. This type of accelerometers manufacturing is very challenging due to their high required performance. They are also used in geophysical and oil-field applications. Today maybe the largest market for the motion sensors application is in smart phones such as i-phones (allowing the device to know when it is tilted on its side) and location based services (GPSs). Indeed, accelerometers in recent years have become the world's hottest electronic products making them the top selling MEMS devices. Especially when they are combined with short range radio sniffers like Wifi, they provide a marvelous navigation for the users.

There are four main kinds of accelerometers, piezoresistive accelerometers, piezoelectric accelerometers, capacitive accelerometers, and optical accelerometers. In a piezoresistive accelerometer, piezoresistors are placed on suspension beams. As the support frame moves due to the external acceleration, the suspension beams bend resulting in a change of the resistivity of their embedded piezoresistors. In a piezoelectric accelerometer, when a piezoelectric material is stressed, an electrical charge signal is generated as a function of acceleration. On the other hand, in capacitive accelerometers, capacitance between the sensor proof mass and a fixed conductive electrode changes as a function of acceleration. Capacitive accelerometers provide several benefits compared to piezoelectric/piezoresistive accelerometers namely, high sensitivity, good noise performance, and low temperature sensitivity [2]. The method of acceleration detection in capacitive and piezoelectric/ piezoresistive accelerometers is based on electrical detection and therefore they are not immune to electromagnetic interferences (EMI). Unlike them, optical accelerometers are based on optical detection hence they are immune to EMI. These types of accelerometers will be addressed in the next section (1.1).

MEMS capacitance accelerometers are currently used in the navigation systems of spacecraft. Figure 1-1 shows two types of MEMS capacitance accelerometers; Analog Devices MEMS capacitance accelerometer and coplanar MEMS capacitance accelerometer. Analog Devices MEMS sensors are based on surface micromachining techniques and therefore offer the opportunity to integrate the sensor and interface circuitry on a single chip. In these devices, the deflection of the structure due to an input acceleration is measured using a differential capacitor. For example ADXL210A (Figure 1-1 (a)) is a polysilicon surface-micromachined dual-axis accelerometer built on top of a silicon wafer. Since surface micromachined accelerometers have small proof mass they suffer from high mechanical noise (mechanical noise is inversely proportional to proof mass) and low resolution. Coplanar MEMS capacitance accelerometer is a z-axis accelerometer (Figure 1-1 (b)) consisting of an underlying fixed electrode and a suspended electrode that can tilt in response to the applied acceleration.

Zhang et al. [3] have developed a single-chip CMOS-MEMS capacitance accelerometer with microgravity sensitivity. The sensor is fabricated on a SOI wafer and integrated with CMOS interface circuit. In order to get a high sensitivity the handle layer of the wafer is used to build the proof mass while the springs are defined on the device layer (Figure 1-2). Sensor has the ability to measure accelerations in µg range.

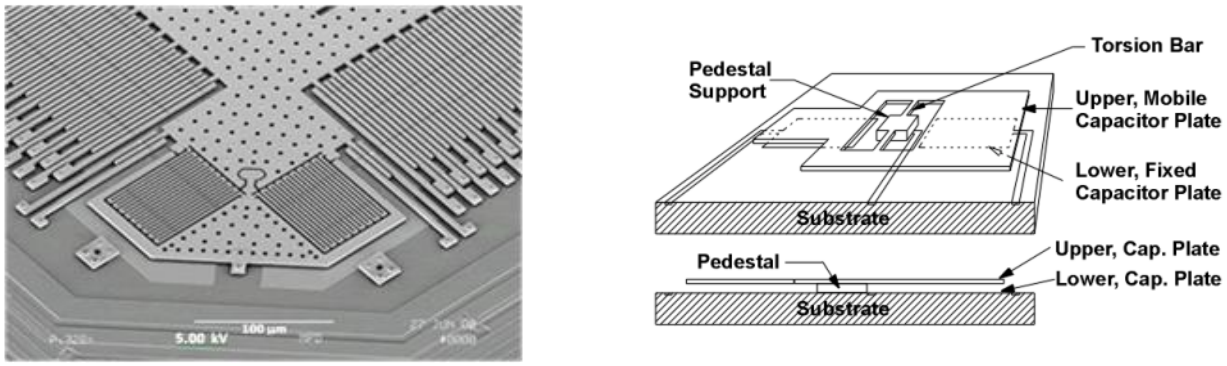

(a) (b)

Figure 1-1: (a) Analog devices MEMS capacitance dual-axis accelerometer ADXL210A, (b) Coplanar MEMS capacitance accelerometer, Silicon Design SD2012-10 [2].

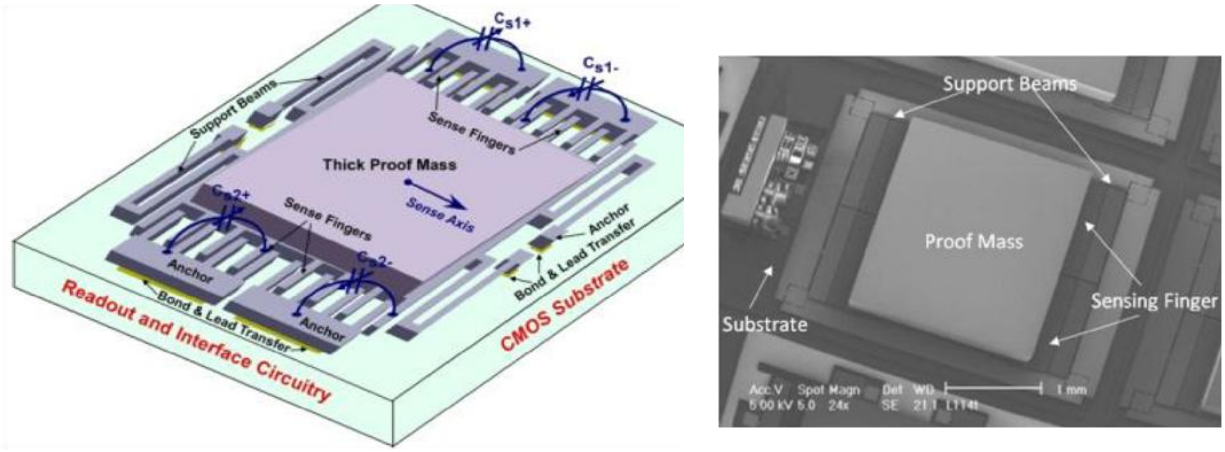

(a) (b)

Figure 1-2: Single-chip CMOS-MEMS capacitance accelerometer with microgravity sensitivity: (a) schematic illustration of the sensing element, (b) SEM view of the fabricated device [3].

Regarding the gyroscopes, there are essentially three types of gyroscopes that are extensively employed today for inertial navigation and rotation rate sensing. The selection of the type of gyroscope for any particular application depends on the performance and cost requirements and also the fabrication complexity. Firstly, there are capacitive MEMS gyroscopes which are light, easy to fabricate and have a relatively high performance however they are not immune to EMI and usually sensitive to the mechanical vibration and acceleration. MEMS silicon-gyroscopes have no exact life-limiting features due to their low power consumption, resulting in a long life of more than 15 years for space applications [5]. Figure 1-3 (a) shows a principal operation of a gyro MEMS-based. A suspended mass is excited in one dimension (x in this figure) and the out-of-plane (z direction) vibration is induced by the rotation due to the Coriolis force leading to the capacitance change between the suspended mass and the substrate. The amount of this capacitance change is then electrically sensed and converted to a rotation rate. Device can also be driven into vibration in both the *x* and *y*-directions, and the angular rate is measured by detecting the phase variation in the lateral vibration signal [6]. Figure 1-3 (b) shows a gyroscope developed by H. Yang based on this concept.

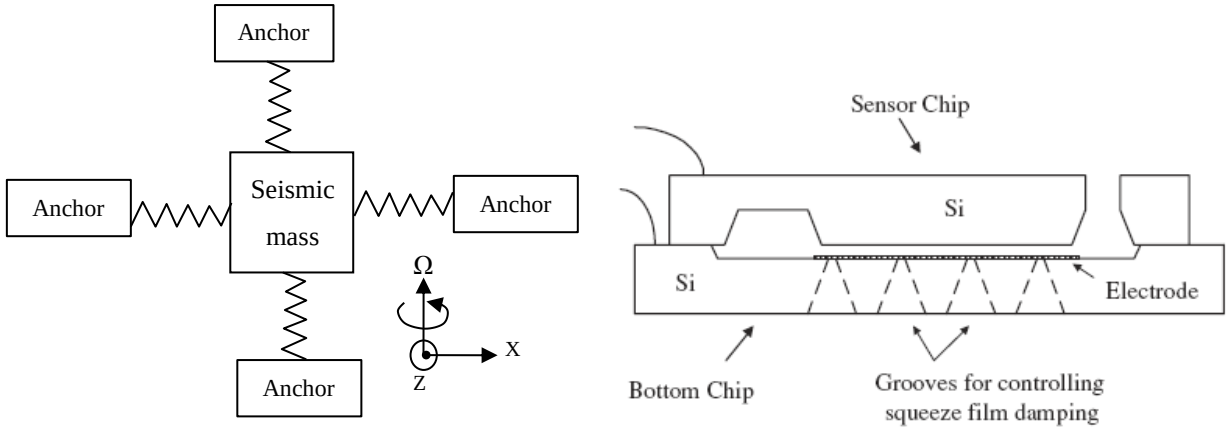

(a) (b)

Figure 1-3: (a) Working principal of a MEMS-based gyroscope, (b) Schematic view of the gyroscope reported by H. Yang [6].

Secondly and thirdly, ring laser gyroscope (RLG) and fiber optical gyroscope (FOG) whose working function are based on the Sagnac effect. The Sagnac effect states that, when two beams of light propagate in the opposite directions along a common path in a rotating frame of reference, these beams experience a phase difference which is proportional to the rotational rate. RLG and FOG gyroscopes provide very high dynamic range and sensitivity. They are also accurate, robust, and immune to mechanical vibrations but they are very difficult to manufacture and expensive. In addition, RLGs are heavy and not appropriate for smallsats applications. A RLG weigh typically is 20 pounds.

Among all, optical accelerometers and gyroscopes offer advantages in comparison to electrical-detection -based sensors because of their:

• Immunity to electromagnetic interference (EMI)
• Insensitivity to charging that can occur in the space environment
• Simple MEMS micromechanical structures
• High dynamic signal measurement range
• Resistance to aggressive environments
• Electrical and fire safety
• Small, lightweight sensing elements allowing arrays of sensors on an SOI microchip

These characteristics make them a good candidate to be used for the space navigation system.

1.1 History (State-of the-art)

To our knowledge, the first optical accelerometer using optical fiber and micromachined structures was reported in 1984 [8], [9]. Subsequently, a large range of fiber optic and waveguide-based micromachined accelerometers were reported. Most of them are based on Variable Optical Attenuator (VOA) [10], [11], [12], [13], [14], interferometric [15], optical diffraction detection [16], [17], [18] , Anti Resonant Reflecting Optical Waveguides (ARROW) [19], [20] or wavelength dependent [26], [27], [28], [37] methods. Although some of them are very sensitive [14], [16], [17], [37], none of them is designed simultaneously for in-plane detection and compactness, consequently they cannot be integrated with other optical functions. Some of the most recent optical-MEMS-based optical accelerometers will be discussed briefly here. Fiber Bragg grating (FBG) acceleration sensors have also been reported by several groups [40], [41], [42]. Although in some cases FBG can reach a relatively high sensitivity (77 pm/g) [40], the optical fibers need manual positioning and cannot be integrated with other optical structures on a planar chip.

Figure 1-4 shows an optical accelerometer based on Anti Resonant Reflecting Optical Waveguides (ARROW) developed by J. A. Plaza, et al.[20]. A waveguide, which is the sensing part of the device, is attached to the seismic mass of the accelerometer and is aligned with two other waveguides on the silicon frames. When there is an offset of the mass due to the acceleration, the transmitted light intensity at the output is modulated, and an intensity loss is generated, which is used to measure the acceleration. The device sensitivity is different for different directions (2.3 dB/g for negative and 1.7 dB/g for positive acceleration). The acceleration resolution is not reported. This device is designed for out-of-plane detection.

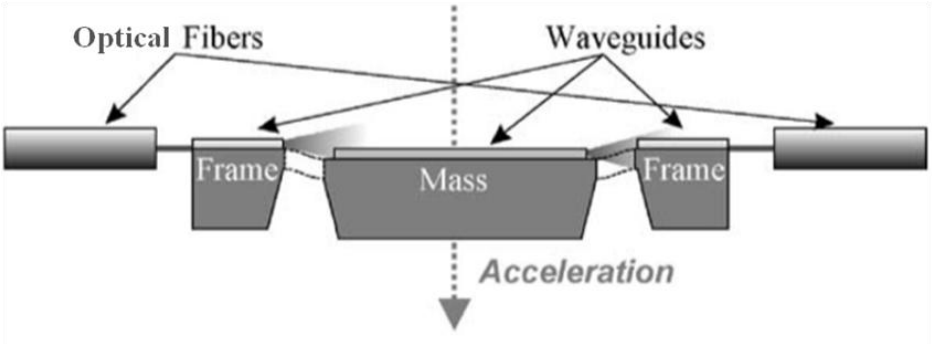

Figure 1-4: ARROW-based optical accelerometer operational principle [20].

Figure 1-5 shows another approach presented by A. Perez and A. M. Shkel [37]. This device is based on Fabry-Perot (FP) interferometer and consists of two deep reactive ion etched silicon substrates that are assembled to create a FP optical cavity. These two silicon substrates act as the FP mirrors and are coated with quarter wavelength multilayer reflector of silicon dioxide, amorphous silicon and silicon nitride to increase the mirror reflectivity.

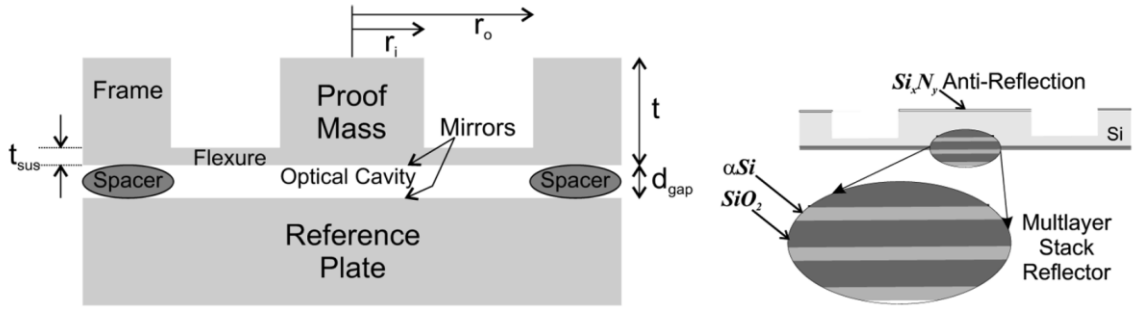

Figure 1-5: FP-based optical accelerometer working principle reported by [37].

One of the mirrors is composed of proof mass and flexure beams created by deep reactive ion etching (DRIE). The device has high sensitivity and resolution (1V/g and 30 µg respectively) but it is bulky (as it is composed of two different silicon wafer bonded by spacers), not integrated on a single chip, and has been designed for out-of-plane vibration detection purposes.

In 1998, a fiber optic based accelerometer (Figure 1-6) using a FP as the sensing element was presented by Schröpfer [26].

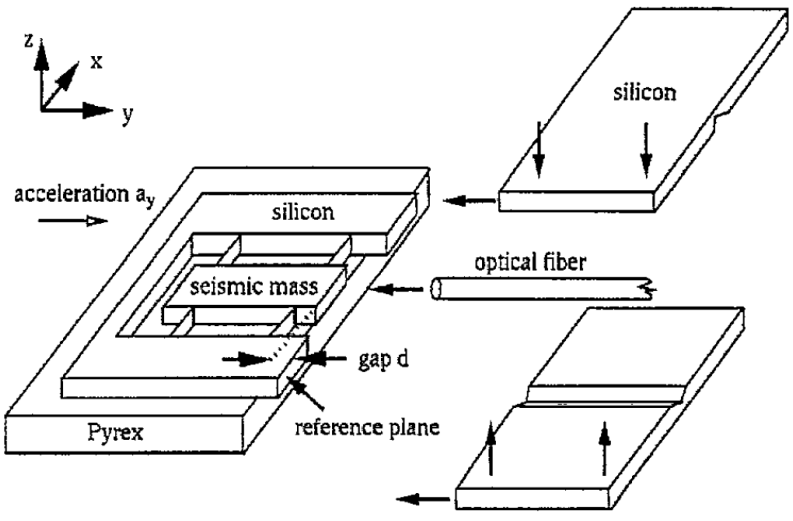

Figure 1-6: Schematic of the FP-based optical accelerometer presented by Schröpfer et al. [26].

A broadband light transmitted through a fiber hits the accelerometer proof mass. The air gap between the accelerometer proof mass and the fiber facet provides a low finesse FP cavity. The deflection of the proof mass relative to the fixed fiber in the presence of an inertial load causes a shift in the transmitted wavelength of the FP interferometer. Device has a low sensitivity due to the low reflectivity of the FP mirrors (fiber facet and seismic mass vertical wall). Sensor resolution is 1 mg for a measurement range of ±10g.

J. John et al. [21] have used a similar structure for the inertial navigation system application in spacecrafts; except that two fibers are employed instead of one at both sides of the seismic mass, providing a differential detection measurement. The seismic mass is a silicon cantilever formed by bulk micromachining technique suspended by four beams (Figure 1-7). Since a differential measurement is used, the signal level is doubled in this configuration. The reported sensitivity is in the mili-g order with a dynamic range of ±12 g.

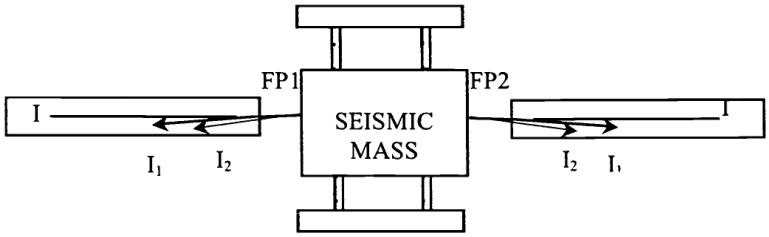

Figure 1-7 : Schematic of the FP-based optical accelerometer presented by J. John et al. [21].

Another optical method to measure the acceleration is based on the measurement of an optical modulation caused by proof mass called variable optical attenuator (VOA). Optical accelerometers based on intensity modulation were proposed [10], [11], [12]. Some of them are unable to detect the acceleration direction [10], [11] or need to be bonded to the traditional fabricated structures [12]. VOAs have been broadly used in dense wavelength division multiplexing (DWDM) systems [43]. MEMS-VOAs are also widely used due to the advantage of their small size and low cost. They are classified into two categories: reflection based and shutter based. In the reflection based, the attenuation consequences from the interferometric superposition of the reflected light beams [22], [23] while in shutter type the signal attenuation is made by blocking a part of light using a shutter [24], [25]. Shutter type VOAs have been developed more extensively since they offer small insertion loss, large attenuation range, and small polarization dependence.

SOI- MEMS VOA-based optical accelerometer with shutter-based modulation was reported by B. Guldimann et al. [14]. Figure 1-8 (a) and (b) show the working principle and scanning electron micrograph (SEM) of the fabricated device respectively. The optical source used is a light-emitting diode (LED). Light from an input fiber is split by a V-shaped gold coated silicon mirror that is attached to the accelerometer proof mass and is coupled simultaneously into the two multimode output fibers. Guided light is then collected by two photodiodes. As the proof mass moves due to the acceleration, more or less light is coupled to the photodiodes. The output signals are then subtracted from the detectors to achieve a differential measurement. This device has a high displacement resolution, however in order to get a linear response, only very small displacements around the zero position (±0.8 µm) are permitted. In addition, their device has a small dynamic range because of its mechanical limitations [43].

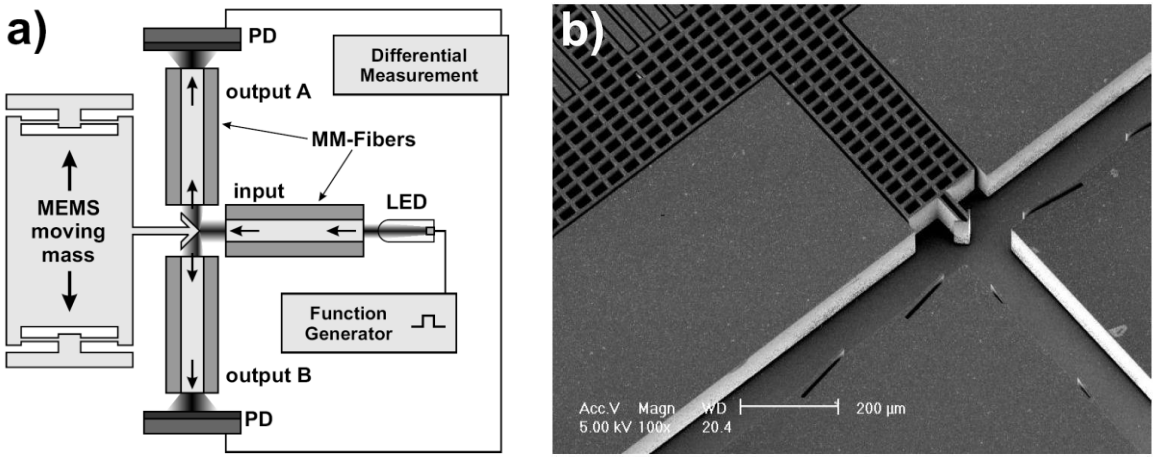

Figure 1-8: a) Schematic of the working principle of the silicon MEMS-based optical accelerometer, and b) SEM image of the fabricated device reported by B. Guldimann [43].

Different types of MEMS-gyros have been reported. Surface micromachined angular rate sensors with different configurations were presented. In most of them, the drive direction is in-plane and the sensing part is designed for the out-of-plane detection purposes. Figure 1-9 shows a capacitive MEMS rate sensor published by K. Tanaka et al. Their device is fabricated using silicon surface micromachining. It is driven laterally by electrostatic force and the capacitance difference between the resonator and its substrate defines the applied angular rate.

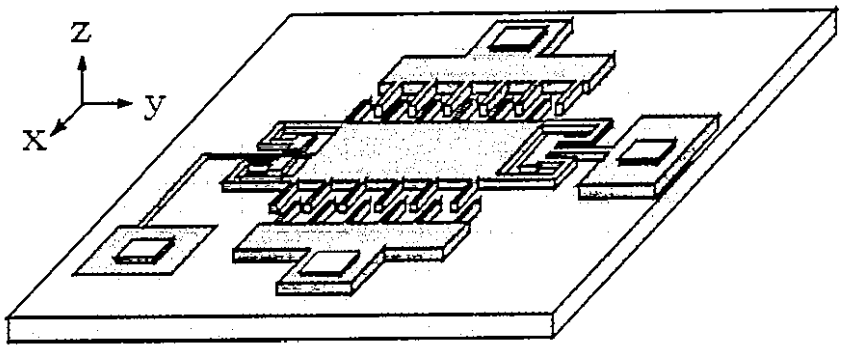

Figure 1-9 : Out-of-plane rotational rate sensor based on capacitance measurement between the movable mass and the substrate [29].

One of the major drawbacks of out-of-plane detection is the big squeeze-film damping which causes a reduction in the sensitivity of the device [30]. As the damping in in-plane movement is caused by slide-film motion which is two-three orders of magnitude smaller than the squeeze-film damping that occurs in out-of-plane movement [30],[31], this particular drawback can be corrected to a large extent by designing the sensor such that the sensing direction could take place in-plane. Also, in-plane design is less sensitive to the residual stresses. M. Lutz et al. used a combination of surface and bulk micromachining to fabricate a yaw rate sensor [32]. A schematic of proposed device is shown in Figure 1-10. The sensor is composed of two identical coupled oscillating masses made by polysilicon surface micromachined suspended on a silicon substrate. An angular rotation around the orthogonal axis (yaw) induces a coriolis force on the oscillating masses. The coriolis force is then detected by the measurement of the difference between the two oscillator's acceleration. The reported sensitivity for the device is 18 mV/s for a range of ±100 °/s over 40° to +85ºC. The sensor represents a good performance however releasing the device layer

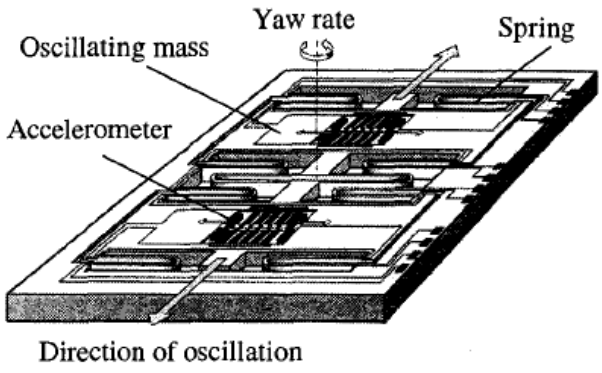

Figure 1-10 : Yaw rate sensor reported by M. Lutz et al. [32].

is difficult due to the mixing of the two surface and bulk micromaching techniques.

MEMS gyros with electrical detection are one of the most important types of silicon-based sensors due to their low-cost fabrication [33], [36]. Although they are relatively inexpensive and easy to fabricate, some have relatively low sensitivity and accuracy and they exhibit some sensitivity to vibration and shock. Integrated CMOS-MEMS capacitive gyroscopes with high resolution and low noise have already been suggested for the space navigation application [33], [35].

STMicroelectronics has recently developed a 3X CMOS-MEMS capacitance gyroscope called "The *Beating Heart*". It is a dual core with very small size (according to them currently the world smallest gyro) and low power consumption (10-15 mW). With the dual core type, the three angular rates (Yaw, Pitch, and Roll) can be read at the same time. Device combines a triple tuning-fork structure with a single vibrating mass. The structure cyclically expands and contracts at a frequency of 20 kHz like a beating heart. The device has high thermal stability, low cross-axis sensitivity, and immunity to acoustic noises. Figure 1-11 shows the 3X gyroscope along with 3X accelerometer fabricated on the same silicon die.

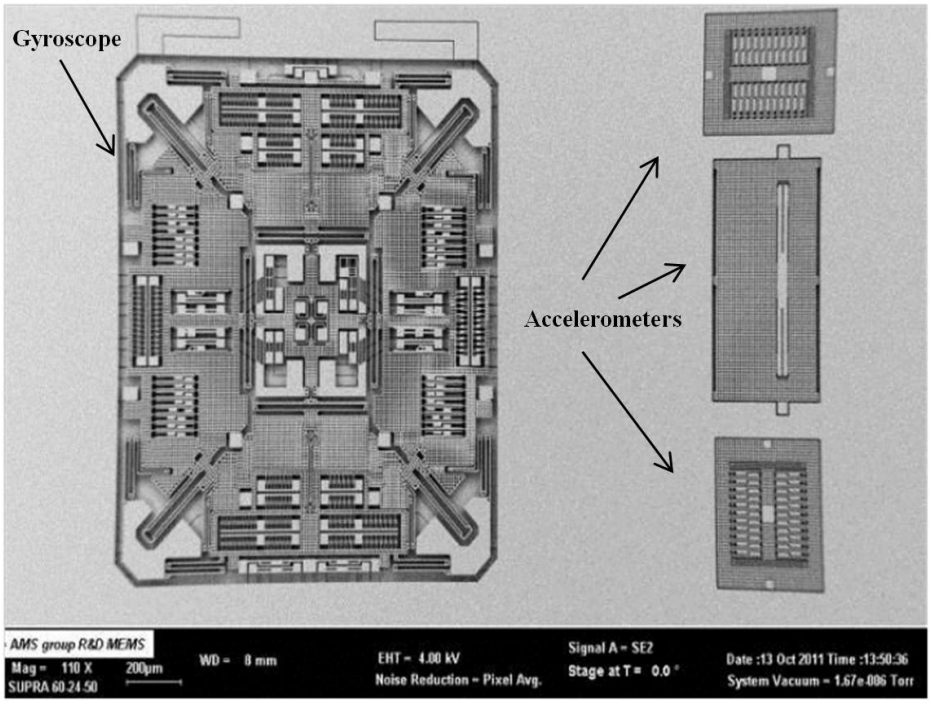

Figure 1-11: 3-axis gyroscope (*Beating Heart)* and 3-axis accelerometer fabricated on the same silicon die [4].

They have also developed an Inertial Six Degree-Of-Freedom Combos (I6XDOF); an integration of tri-axis accelerometers and tri-axis gyroscopes in $3\times5.5\times1\ mm^3$ package [4]. They are currently working on a platform called INEMO™ comprising ten analog building blocks for the future application in smart devices.

The INEMO™ or 10XDOF is a Ten Degree-Of-Freedom Combos platform realized by integrating tri-axis accelerometers, tri-axis gyroscopes, tri-axis magneto-resistive solid state compass and a pressure sensor. Figure 1-12 shows the I6XDOF sensor implemented on two different silicon dice assembled with the companion CMOS chip.

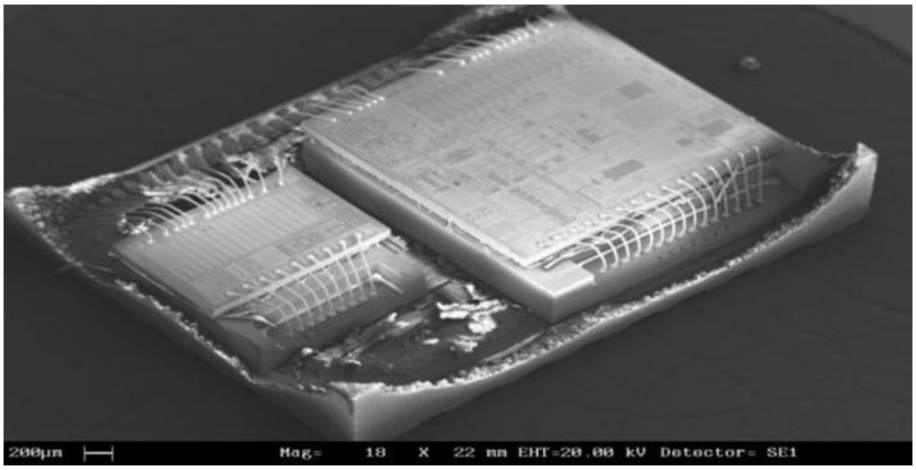

Figure 1-12: 6-axis inertial motion sensor in $3\times5.5\times1\ mm^3$ package fabricated on two different silicon dice and assembled with the companion CMOS chip [4].

Using optical interferometry along with Sagnac effect, rotational rate sensors with no moving parts were presented [38]. Fiber optic gyroscopes (FOGs) are promising candidates for the next generation of gyros. FOGs with integrated optic circuits (IOCs) are predicted to be the next-generation gyros for various aerospace applications because of their high dynamic range and sensitivity. FOG-IOCs are fabricated in $LiNbO_3$. The disadvantage of the $LiNbO_3$-FOG devices is their low optical confinement in the Ti-diffuse waveguides resulting in large waveguide bending radius on $LiNbO_3$ and corresponding high insertion losses.

1.2 Objective of the thesis

A basic spacecraft consists of a bus structure and one or more payloads attached to the bus. The bus structure carries out the basic functions and housekeeping, while the payloads perform

specialized tasks for particular scientific purposes. Since the early 90's, a dramatic change in methodology has occurred inside agencies such as NASA regarding changing from solely performance to performance per unit cost. This paradigm shift, combined with the reduction of budget of different space agencies has put an emphasis on the use of small satellites to accomplish missions at significantly reduced costs.

Over the last decade, as smallsats and microsats application towards full Earth observation, telecom and space science missions increases, their attitude control requirements have evolved towards full three axis stabilization and accurate pointing knowledge and control. This is associated with an increasing requirement for compact, low-power Sun sensors, Earth sensors, gyroscopes and accelerometers. With future planned space missions, the requirements for miniature, low-power attitude sensing for satellite formation flying will further accelerate.

The objective of this thesis is to design, simulate, fabricate and characterize novel highly sensitive low cost in-plane PBG/MEMS-based miniature accelerometers and rotational rate sensors (gyroscopes) on SOI substrate in order to integrate an array of two-axis of them on a single SOI platform in the future providing a microchip for spacecraft navigation purposes. The use of guided-wave optical devices integrated with MEMS on SOI for multichannel/multifunction sensor systems allows the use of multiple sensors to extend the measurement range and accuracy. In the case of electrostatic inertial sensors waveguides are not required to integrate multiple inertial sensor on one chip but in the case of optical inertial sensors light needs to be guided to the sensor or be distributed among other sensors through optical waveguide channels, therefore optical waveguides are required in order to integrate multiple inertial sensors on one single chip if an in-plane detection is intended. However if the detection is intended to be out-of-plane, no optical waveguide is required for integration and light can be coupled out-of-plane to the sensor using optical fibers.

Integration also provides essential redundancy (duplication of functions blocks or devices for increasing the reliability of the system, usually in the case of a backup or device failure) to make long-term reliability in the space environment possible. When MEMS technology is used on silicon, the microfabricated devices are very reliable and robust compared to those fabricated using thin film layers (CMOS). In terms of size, there is no limit that determines the reliability. In our case, as the micro navigator chip is going to be used for microsatellite, smaller the chip is (in terms of size and weight) the better is of course without any compromising on the performance.

The navigator microchip also represents the ability of accommodating diverse attitude and inertial sensors on the same microchip to eliminate the need of many separate sensors. This is a remarkable advantage for small satellites with their limited mass, volume and power resources. Figure 1-13 shows a potential future spacecraft navigation optical MEMS micro-PIC using several basic components or functional blocks that are connected by SOI strip waveguides on a single SOI chip.

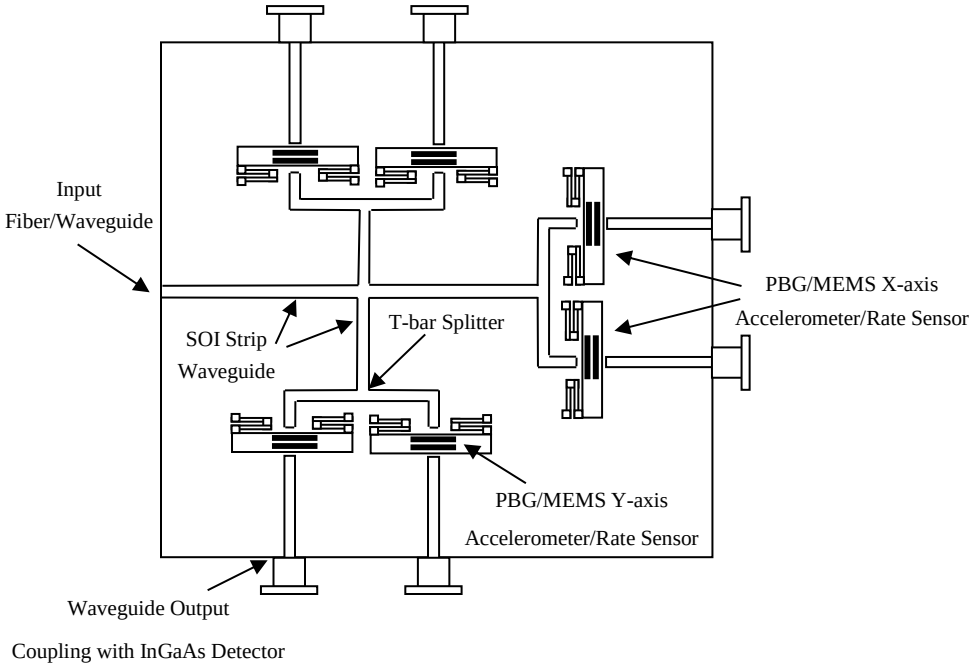

Figure 1-13 : Conceptual design of two-axis spacecraft navigation micro-PIC system.

The basic components consist of:

- Input Fiber/Waveguide Coupler
- SOI Strip Waveguide
- T-bar Splitter
- PBG/MEMS Optical Accelerometer
- PBG/MEMS Optical Rate Sensor
- Waveguide Output Coupling or Hybrid Integration with InGaAs Detectors

Other optical functional blocks such as temperature sensors, radiation sensors, earth and sun sensors could also be integrated on the same chip.

The end product exhibits orders of magnitude reduction in system mass and size. Furthermore, redundancy improves the net performance and precision of the navigation measurement systems.

Since the output is directly coupled to photodetectors, fiber/waveguide output, coupling is not an issue and the signal throughput as well as the Signal-to- Noise Ratio (SNR) can be very high. Two classes of optical accelerometers/gyroscopes are considered as the potentially applicable sensors in the spacecraft navigation system, one based on FP filter and the other based on VOA approach. The FP filter enables a highly sensitive optical detection of displacement at a nanometer scale. MEMS tunable silicon FP filters with DBR mirrors were recently demonstrated [44], [45], [47]. These tunable filters are used for several applications such as optical filtering in telecommunication, microphones, pressure sensors, etc. The main difference between FP-based and VOA-based accelerometers presented here is that the VOA-based sensors do not require high spectral quality sources and the detection is much simpler since the intensity of light is measured at the output instead of wavelength.

1.3 The situation at the beginning of this work

The state-of-the-art of the optical accelerometers and gyroscopes based on optical fiber/MEMS was discussed above. Silicon MEMS-based optical accelerometers provide higher sensitivity and better reliability compared to those based on piezoelectric effect or electrical detection when they are exposed to electromagnetic interferences [20], [43]. Although some attempts were made but none of the reported optical accelerometers offers a simultaneously reliable, high sensitive, in-plane, simple fabrication, low cross-sensitive and compact device. An optical microchip for microsatellite navigation application is still in demand. The following compares our devices with those that could be potentially considered appropriate for the satellite navigation systems. Table 1-2 compares our proposed optical accelerometers with some recent developed capacitance MEMS accelerometers and optical MEMS accelerometers. The main advantage of our proposed optical accelerometers to the conventional ones is that our accelerometers are fully integrated using silicon waveguides without any compromise on the device performance.

µg-resolution optical accelerometers based on FP have been fabricated, but some are out-of-plane, big and expensive to fabricate [37], and some are not integrated and therefore unstable and also not sensitive enough [21], [26], making them inappropriate for microsatellites mission accomplishments. The FP-based optical accelerometer presented here uses DBR mirror along

with silicon strip waveguides integrated with MEMS on a single SOI wafer representing a compact and reliable sensor.

Table 1-2: Comparison between our proposed fully integrated optical MEMS accelerometers with some recent developed capacitance MEMS accelerometers and optical MEMS accelerometers.

	Analog MEMS Capac. ADXL210A 2003 [2]	**MEMS Capac. 7290A 2003** [2]	**CMOS-MEMS Capac. (Y. Zhang) 2012** [3]	**Fiber Optic MEMS (Guldiman) 2002** [43]	**Optical MEMS nano grating based (Krishna) 2008** [16]	**Our Fully Integrated Optical-MEMS Devices**
Detection Direction	In Plane	Out of Plane	In Plane	In Plane	Out of Plane	In Plane
Fabrication	Poly Si Surface	Bulk	SOI Bulk	SOI Bulk	Poly Si Surface	SOI Bulk
Resolution	1.29 mg (100 Hz)	420 μg (100Hz)	1.2 $\mu gHz^{-1/2}$ (186 Hz)	670 μg (65 Hz)	17 $ngHz^{-1/2}$ (1 Hz)	0.1 $\mu gHz^{-1/2}$ (210 Hz) 111 μg for FP-Based (450 Hz) Potential of <10 μg
Immunity to EMI	No	No	No	Yes	Yes	Yes

The FP filter enables a highly sensitive optical detection of at a nanometer scale. Since it is in-plane, it allows the integration of all components (DBR mirrors, optical waveguides, proof masses and suspension beams) on a single substrate, making it compact and reliable.

Among all reported VOA-based optical accelerometers, only Guldimann's device [14] satisfies the main criteria's (immunity to EMI, in-plane, high sensitivity and resolution, simple fabrication, low power consumption) to be used in satellite navigation. The reported device is

very sensitive but it is not fully integrated and therefore has limited reliability because of its alignment sensitivity to vibrations/shocks. Also only very small displacements (±0.8 μm) are allowed in order to obtain a linear response resulting in a small dynamic range for the device [43]. A deposited gold layer is also required for the mirror in order to obtain high reflectivity. In our VOA-based optical accelerometer presented here, the MEMS part of the sensor is integrated with the silicon strip waveguides and the VOA sensing part, making the device more stable, robust and reliable. Compared to Guldimann's device, our device is fully integrated and therefore not sensitive to vibrations/shocks. Also no gold coating is required for the mirror since a DBR mirror is used as the shutter.

Regarding the rate sensor, to the best of our knowledge as of today no integrated optical rate sensor has been reported. Although FOGs represent high sensitivity, they cannot be integrated on the same chip with other inertial sensors. In this work two types of in-plane rotational rate sensors are introduced, one based on FP resonator and one based on VOA.

CHAPTER 2 THEORY

This chapter will discuss the physics of a FP filter with Bragg layers and the optical model of a VOA. Theories of FP-based and VOA-based optical accelerometers/gyroscopes are addressed. Furthermore, the propagation behavior of light inside SOI optical waveguides, coupling losses between optical fibers and silicon waveguides, and the number of optical modes inside SOI waveguides are theoretically studied.

2.1 Fabry-Pérot interferometer with Bragg mirrors

A FP optical filter or etalon consists of two parallel highly reflective mirrors. These mirrors can be made of alternating layers of two different materials with different refractive indexes (Bragg mirrors). When light penetrates from a medium into another medium with a different refractive index, it experiences a phase shift. This phase shift depends on the wavelength of the light and thickness of layers. Therefore the optical filter interferometer can be designed such that light for a specific wavelength could interfere constructively and for the other wavelengths destructively.

2.1.1 Finding the reflection and transmission using transfer matrix method

We are looking for the transmittance and reflection spectrum of the light for a FP interferometer as a function of wavelength. For this, we first find the reflection and transmission coefficient for a single dielectric layer. Considering a dielectric layer with refractive index n_1 and thickness l surrounded by two incident and transmission infinite mediums with refractive indexes n_i and n_t respectively (Figure 2-1). Plane wave approximation is used and normal incident light is assumed. We also assume that all mediums are homogenous i.e. the refractive indexes are constant in each medium. Considering the light as an electromagnetic wave, when a plane wave (E_i) propagating in medium i encounters the interface of the incident and dielectric mediums, a portion of the wave (E_i') is reflected from the interface while the rest is transmitted (E_1). The transmitted light then encounters the interface of the dielectric and transmission medium and again portion of the wave is reflected (E_1') and the rest are transmitted (E_t). Using Maxwell equations and the continuity of the electric fields and magnetic fields at the interfaces (boundary conditions):

Incident/dielectric interface

$$E_i + E_i' = E_1 + E_1'$$
$$H_i - H_i' = H_1 - H_1' \Rightarrow n_i E_i - n_i E_i' = n_1 E_1 - n_1 E_1'$$

dielectric/transmission interface

$$E_1 e^{ikl} + E_1' e^{-ikl} = E_t$$
$$H_1 e^{ikl} - H_1' e^{-ikl} = H_t \Rightarrow n_1 E_1 e^{ikl} - n_1 E_1' e^{-ikl} = n_t E_t$$

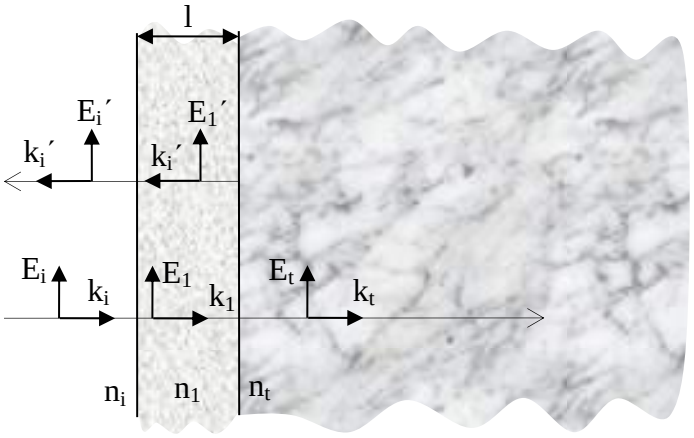

Figure 2-1: Wave vectors and their associated electric fields for the normal incidence case on a single dielectric layer

Eliminating the amplitude E_1 and E_1', the fraction of incident beam that is reflected from the first interface (reflection coefficient) as a function of the fraction of incident beam that is transmitted (transmission coefficient) can be presented with the following matrix equation

$$\begin{bmatrix} 1 \\ n_i \end{bmatrix} + \begin{bmatrix} 1 \\ -n_i \end{bmatrix} \frac{\acute{E}_i}{E_i} = \begin{bmatrix} \cos kl & \frac{-1}{n_1} \sin kl \\ -in_1 \sin kl & coskl \end{bmatrix} \begin{bmatrix} 1 \\ n_t \end{bmatrix} \frac{E_t}{E_i} \tag{2.1}$$

or

$$\begin{bmatrix} 1 \\ n_i \end{bmatrix} + \begin{bmatrix} 1 \\ -n_i \end{bmatrix} r = M \begin{bmatrix} 1 \\ n_t \end{bmatrix} t \tag{2.2}$$

Where $r = \frac{\acute{E}_i}{E_i}$ is the reflection coefficient and $t = \frac{E_t}{E_i}$ is the transmission coefficient and M represent a 2×2 matrix known as transfer matrix of the film:

$$M = \begin{bmatrix} \cos kl & \frac{-1}{n_1}\sin kl \\ -in_1 \sin kl & coskl \end{bmatrix} \tag{2.3}$$

For N layers Eq.(2.2) becomes

$$\begin{bmatrix} 1 \\ n_i \end{bmatrix} + \begin{bmatrix} 1 \\ -n_i \end{bmatrix} r = M_1 M_2 M_3 \ldots . M_N \begin{bmatrix} 1 \\ n_t \end{bmatrix} t = M \begin{bmatrix} 1 \\ n_t \end{bmatrix} t \tag{2.4}$$

where M is the overall transfer matrix and is the product of the individual transfer matrices, that is

$$M_1 M_2 M_3 \ldots . M_N = M = \begin{bmatrix} A & B \\ C & D \end{bmatrix} \tag{2.5}$$

Solving Eq. (2.4) for r and t in terms of A, B, C, D resulting in

$$r = \frac{An_i + Bn_t n_i - C - Dn_i}{An_i + Bn_t n_i + C + Dn_i} \tag{2.6}$$

$$t = \frac{2n_i}{An_i + Bn_t n_i + C + Dn_i} \tag{2.7}$$

The reflectance R and the transmittance T are given by $R = |r|^2$ and $T = |t|^2$, respectively. According to the energy conversation law R+T=1 if the absorption is neglected.

2.1.2 High reflectance films- concept of Distributed Bragg reflectors (DBRs)

A stack of alternate layers of high index, n_H, and low index, n_L, material with the thickness of λ/4 is used to generate high reflectance films called Distributed Bragg Reflectors (DBRs). In this case, the wavelength which is four times the optical path (optical thickness of the layers), is reflected constructively and the layers act as a high reflector. Thus the relation between the wavelength and the thickness of each layer is

$$L = \frac{\lambda}{4n} \tag{2.8}$$

for the first order. However the odd coefficients are allowed for higher orders. Therefore in order to obtain a high-quality reflector, the thickness of each layer has to satisfy the following equation

$$L = \frac{h\lambda}{4n} \tag{2.9}$$

where *h* is an odd integer number. The range of wavelengths that are reflected (forbidden to propagate in the structure) is called the photonic band gap. In this case the transfer matrices of all layers have the same form, and the product of two adjacent ones is

$$\begin{bmatrix} 0 & \frac{-i}{n_L} \\ -in_L & 0 \end{bmatrix}\begin{bmatrix} 0 & \frac{-i}{n_H} \\ -in_H & 0 \end{bmatrix} = \begin{bmatrix} \frac{-n_H}{n_L} & 0 \\ 0 & \frac{-n_L}{n_H} \end{bmatrix} \tag{2.10}$$

and for the stack of 2N layers

$$M = \begin{bmatrix} \left(\frac{-n_H}{n_L}\right)^N & 0 \\ 0 & \left(\frac{-n_L}{n_H}\right)^N \end{bmatrix} \tag{2.11}$$

The reflectance of the multilayer stack according to Eq. (2.6) would be given by

$$R = \frac{n_i n_H^{2N} - n_t n_L^{2N}}{n_i n_H^{2N} + n_t n_L^{2N}} \tag{2.12}$$

where n_i and n_t are the refractive indices of the originating medium and terminating medium respectively.

This equation demonstrates that, increasing the number of layers and the refractive index contrast between them in a DBR increases the reflectivity of the multi-stack layer.

The mirror bandwidth (range of wavelengths where the reflectance is maximum) is given by [45]

$$\Delta\lambda_{BW} = \frac{4}{\pi h} \sin^{-1}\left(\frac{n_H - n_L}{n_H + n_L}\right) \tag{2.13}$$

This equation shows that the bandwidth not only increases with increasing refractive index contrast but is also inversely proportional to the order of Bragg mirror, the lower the order of the Bragg mirror, the larger the bandwidth. Although the 1st order provides the largest bandwidth for the mirror, fabricating such a narrow wall of silicon ($\lambda/_{4n}$ = 112 nm) is impossible with standard microfabrication technology. The combination of silicon and air layers provides high reflectivity for a Bragg mirror because of their high refractive index contrast (n_{si}=3.45, n_{air}=1). Due to this fact even a six-layer stack (N=3) of silicon and air is enough to provide a very high reflectance (R=0.9988 according to Eq. (2.12)). Figure 2-2 shows the relationship between the silicon layers order and the reflection peak bandwidth of one Bragg reflector consisting of three silicon layers and three air layers. As the order of the walls is increased, the reflection peak gets narrower.

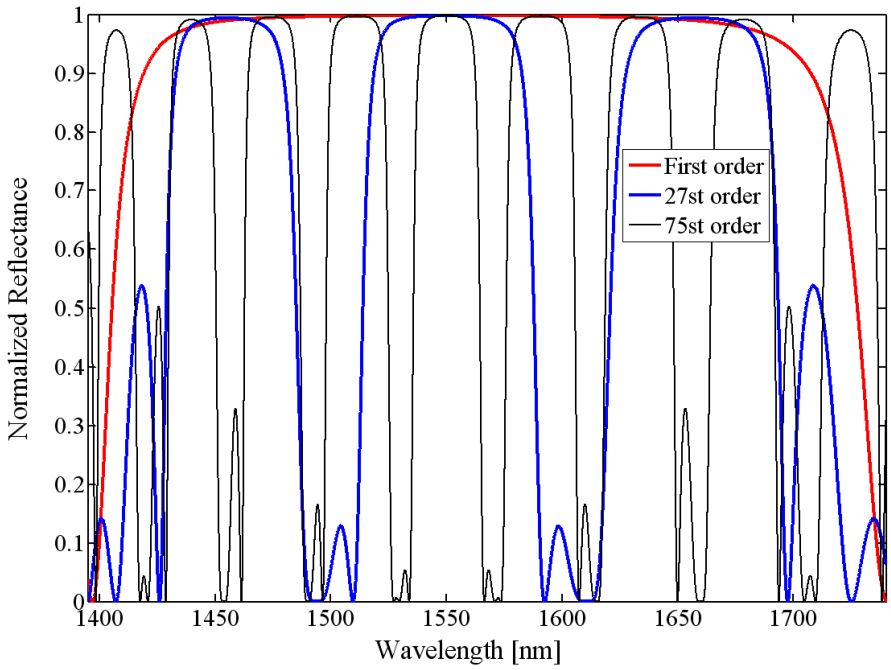

Figure 2-2: Normalized reflectance versus wavelength for a three layer grating with three different orders. The air order was kept constant (=7).

2.1.3 Fabry-Perot Interferometer (FPI) filter

A FP interferometer filter or a FP etalon consists of two partial reflectors (mirrors) separated by an air gap with thickness of an integer multiple of half of the resonance wavelength (Figure 2-3):

$$x = \frac{m\lambda_0}{2} \tag{2.14}$$

where x is the gap between the mirrors and m is the order of FP. The result is a filter that allows only wavelengths that match the optical resonant condition to escape and traverse the device (Figure 2-4). The spectral width of the transmission band depends on the reflection bandwidths of the mirrors. The wider bandwidth the mirrors are, the wider the transmission band is for the FP filter and therefore the wider tuning range is provided for the cavity. A key attribute of the optical characteristics and efficiency of a Fabry-Perot interferometer (FPI) is the finesse. The finesse is defined by the separation of the contiguous fringes (Free Spectral Range or FSR) divided by the fringe width (Full Width of the fringe at Half its Maximum or FWHM). The finesse for a FPI without optical absorption is identified as the reflectance finesse (F_R), which is directly related to the mirror's reflectivity R, as represented in [49]:

$$F_R = \frac{\pi\sqrt{R}}{1-R} \tag{2.15}$$

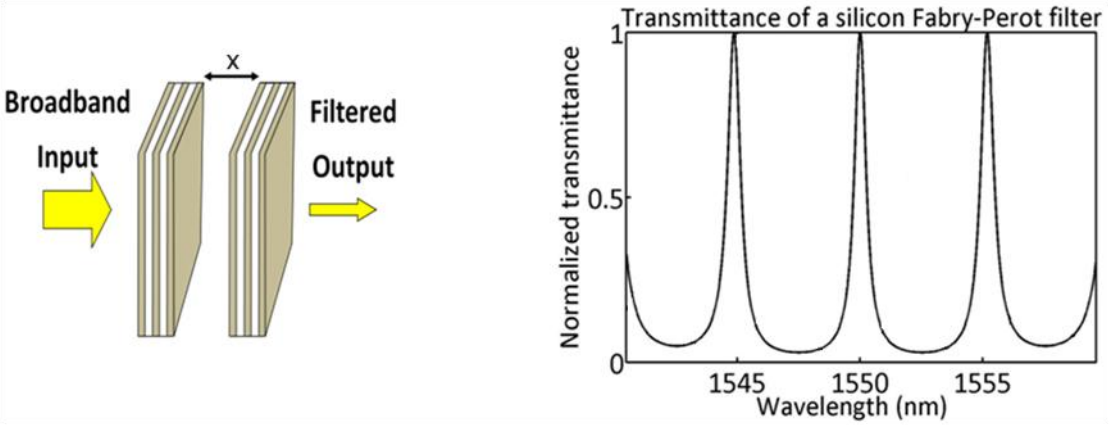

(a) (b)

Figure 2-3: (a) Schematic of a FPI with Bragg mirrors, (b) Transmittance of a FPI filter versus wavelength.

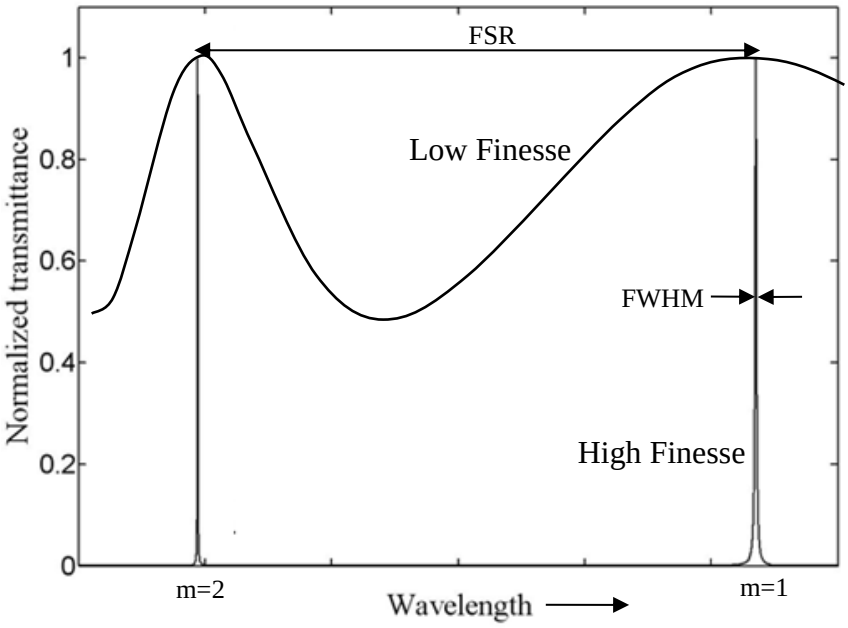

Figure 2-4: The full characteristic transmittance pattern of a FPI.

In order to obtain a high finesse device, both high reflectivity and fine control over Bragg mirror defects and parallelism during the fabrication must be reached. The frequency FSR of the FP filter is the frequency spacing between two resonance frequencies. Considering two adjacent resonant modes *m* and *m+1* from Eq. (2.14) and subtracting them,

$$\Delta f_{FSR} = \frac{c}{2x} \tag{2.16}$$

where *x* is the gap between the mirrors and *c* is the speed of light. The free spectral range in Eq. (2.16) is related to the wavelength free spectral range by

$$\frac{\Delta f_{FSR}}{f_0} = \frac{\Delta \lambda_{FSR}}{\lambda_0} \tag{2.17}$$

where λ_0 is the central wavelength at the spectral region of interest. The wavelength free spectral range can then be written as

$$\Delta\lambda_{FSR} = \frac{\lambda_0^2}{2x} = \frac{\lambda_0}{m} \tag{2.18}$$

According to Eq.(2.18), in order to get a large FSR (and therefore tunning range), smaller FP gaps are required. Using (2.18) and (2.15) and the fact that finesse is the division of FSR and FWHM, the narrowness of the fringe is calculated as follows:

$$\delta\lambda_R = \frac{\lambda_0(1-R)}{m\pi\sqrt{R}} \tag{2.19}$$

According to Eq. (2.19), resonance modes with higher orders have narrower resonances. This can be easily seen in Figure 2-4.

Using higher silicon or air order for Bragg mirrors improves the finesse of the filter [47], however decreases the stopband (Figure 2-2). Therefore there is a trade-off between stopband and finesse in terms of silicon/air walls thickness. Furthermore, the higher number of walls for the Bragg mirrors, the higher reflectivity for the mirrors and therefore the better finesse for the FP cavity (Eq. (2.15)). However due to the fabrication imperfection (section 2.5.1); this will generate more optical losses for the cavity as light experience multiple reflections on each layer of the Bragg mirror. Accordingly, there is a trade-off also between the number of walls and the optical loss generated in the cavity.

2.2 Accelerometers

As shown in Figure 2-5, an accelerometer with a proof mass, *M*, and spring constant, *k*, can be modeled as a second order mass-spring-damper system. The force in this system is given by

$$F = M\ddot{x} + c\dot{x} + kx \tag{2.20}$$

where *x* is the relative displacement with respect to the base, and *c* is the damping coefficient. For a given force this linear differential equation can be solved to determine the system response.

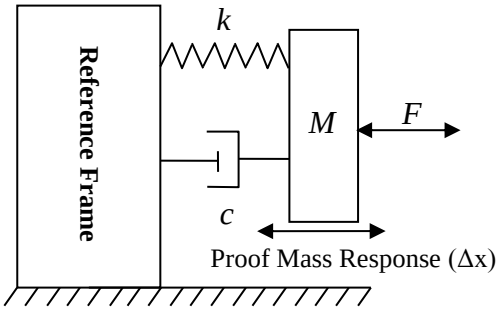

Figure 2-5: Accelerometer modeled as a mass-spring-damper system.

From Newton's 2nd Law, the relationship equation between the measured force and applied acceleration is described as F = Ma. Assuming that the accelerometer proof mass is driven by a force F, in the static condition, and absence of damping, by combining Newton's 2nd Law and Hook's Law the relation between acceleration, *a*, and displacement Δx, is given by:

$$a = -\frac{k}{M}\Delta x \ = -\omega_n^2 \Delta x \tag{2.21}$$

where ω_n is the angular natural frequency of the system in the sensing direction. This assumption is valid as long as resonant frequency is much larger than the frequency of the measured acceleration.

2.3 Damping

Considering $F = F_0 \cos \omega t$ in Eq. (2.20) as the forced vibration function for the viscous-damped, spring-mass system where F_0 is the amplitude of forced vibration; the general solution of Eq. (2.20) is:

$$x(t) = e^{-\gamma t}(C_1 \cos pt + C_2 \cos pt) \tag{2.22}$$

where $\gamma = \frac{c}{2M}$, $p = \omega_n^2 - \gamma^2$ and C_1 and C_2 are constants and they are determined from the initial conditions of the system. A particular solution of Eq. (2.20) is represented by:

$$\mathrm{x} = \mathrm{A}e^{\mathrm{j}(\omega \mathrm{t}+\varphi)} \tag{2.23}$$

where A is the amplitude response of the system and φ the phase angle and are given by:

$$A = \frac{F_0}{k} H(\omega) \tag{2.24}$$

and

$$\varphi = -\tan^{-1}\left(\frac{2\xi\left(\frac{\omega}{\omega_n}\right)}{1-\left(\frac{\omega}{\omega_n}\right)^2}\right) \tag{2.25}$$

in which $H(\omega)$ is the magnification factor or the normalized frequency response of the system and is given by:

$$|H(\omega)| = \frac{1}{\sqrt{\left[1-\left(\frac{\omega}{\omega_n}\right)^2\right]^2 + \left(2\xi\frac{\omega}{\omega_n}\right)^2}} \tag{2.26}$$

where ξ is the damping ratio

$$\xi = c/(2M\omega_n) = c/2\sqrt{Mk} \tag{2.27}$$

In which *c* is the squeeze-film damping between the sensor's proof mass cross section and fixed reference frame (surrounding silicon structure) and for translational squeeze-film damping is given by [48], [111] :

$$c = 0.42\frac{\mu A^2}{d^3} \tag{2.28}$$

where A is the cross section area of the proof mass, μ is the viscosity of the surrounding medium, and d is the distance between the sensor's proof mass cross section and fixed reference frame. The normalized frequency response of the system is plotted in Figure 2-6 for undamped (ζ≅0), critically damped (ζ=0.707), and over-damped systems (ζ>1). Note should be taken that in this analyze, the driving force is assumed to be applied to the proof mass not to the base. So the accelerometer/ gyro is not excited by the base. In the case of base vibration, the response will be different. In our case, for the accelerometer testing, only the static response of the device is measured by applying gravitational force to the mass. Therefore no harmonic excitation is

applied (neither to the proof mass nor to the base). However for the case of gyroscope, the proof mass is driven by a sinusoidal force (again the force is applied to the proof mass not to the base).

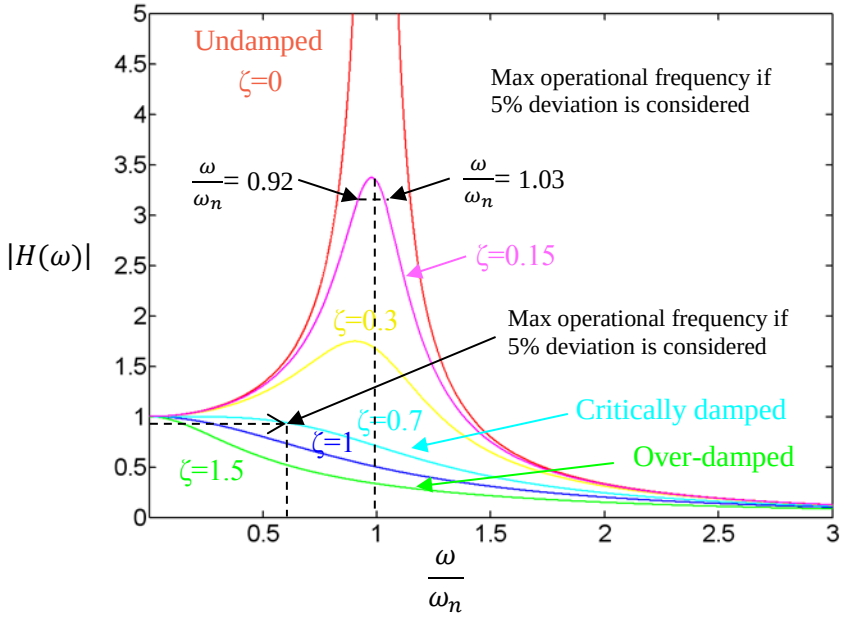

Figure 2-6: Normalized frequency response of a second order system for different damping ratio.

In the case of the undamped system, which is the case for most of micromachined accelerometers, the response is simplified as:

$$|H(\omega)| \approx \frac{1}{\left|1-\left(\frac{\omega}{\omega_n}\right)^2\right|} \tag{2.29}$$

For the case of under damped systems $(0 < \xi < 1)$, the operational frequency bandwidth increases as the damping increases. The maximum normalized frequency for under damped systems with weak damping can be approximated as, $|H(\omega = \omega_n)| = |H(\omega)|_{max} = \frac{1}{2\xi}$. To get an idea of the operational frequency bandwidth of a system, assume that a 5% deviation is considered. For instance, for a system having ζ=0.15, $|H(\omega)|_{max} = \frac{1}{2\xi} = 3.33$, therefore for 5% deviation $|H(\acute{\omega})| = |H(\omega)|_{max} - 0.05\,|H(\omega)|_{max} = 3.16$, substituting into (2.26), the operational frequencies of the system (accelerometer) for 5% deviation frequency are calculated as $\acute{\omega}_1 = 1.03\omega_n$ and $\acute{\omega}_2 = 0.92\omega_n$ (as they are shown in Figure 2-6), providing $\Delta\omega$=$0.11\omega_n$ frequency bandwidth. For the case of critical damping($\xi = 0.7$), the estimation we made earlier

for maximum normalized frequency is not valid anymore as the damping is not weak; instead the maximum normalized frequency occurs at very low frequency (as seen in Figure 2-6) and can be estimated as $|H(\omega)|_{max} \cong 1$. For 5% deviation, $|H(\acute{\omega})| = |H(\omega)|_{max} - 0.05\,|H(\omega)|_{max} = 0.95$, substituting into (2.26), the maximum operational frequency of the system for 5% deviation frequency is $\acute{\omega} = 0.6\omega_n$, or $\Delta\omega$=0.6ω_n frequency bandwidth. The mechanical damping for an accelerometer is typically adjusted to prevent oscillations of the mass in a change of acceleration (ringing).

Basically there are three types of damping: squeezed-film translational damping, slide-film damping and squeezed-film rotational damping. If the proof mass moves perpendicularly to its surface, the gas in the gap between the proof mass and the reference frame will exert a force on the plate leading to a squeezed-film translational damping for the sensor. If the proof mass moves parallel to the squeeze film, the sensor experiences a damping called slide-film damping and in the case where the proof mass rotates around an axis perpendicular to the squeezing direction, the damping is called squeezed-film rotational damping. These three types of damping are illustrated in Figure 2-7 and they will be discussed more in the next chapter.

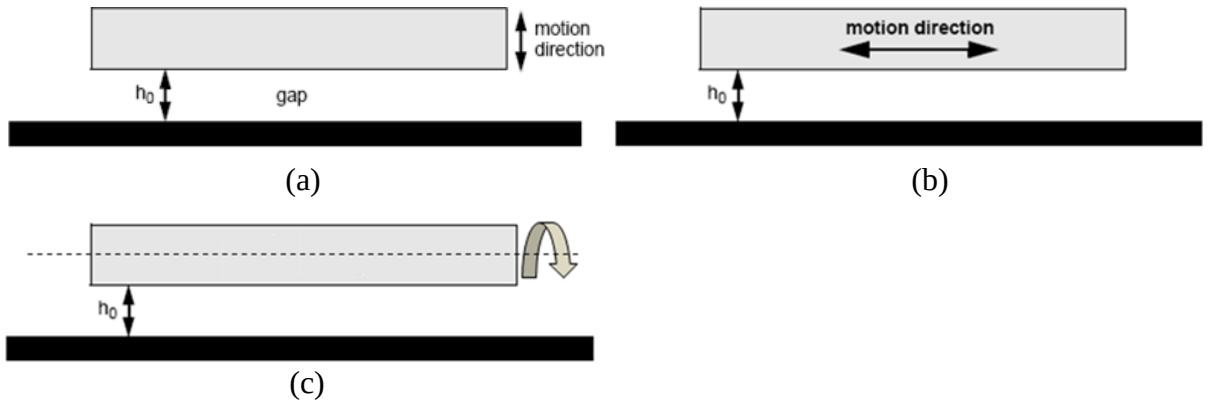

Figure 2-7: Three types of damping: (a) squeezed-film translational damping, (b) slide-film damping, and (c) squeezed-film rotational damping.

2.4 FPI as an acceleration sensor

The resonant condition of an FPI changes as a result of displacing one mirror of FPI relative to the other one (changing the gap between the mirrors) as shown in Figure 2-8(a). This can be adapted to an acceleration sensor by suspending one mirror (which in this case acts as a proof

mass) relative to the other (Figure 2-8(b)). The proof mass displaces in response to an applied acceleration, resulting in a shift of central wavelength of the FPI (Figure 2-8(c)). The static response of such a suspended mass as discussed above is given by Eq. (2.21).

The relationship between the FPI acceleration sensor output and its experienced acceleration is then given by combining equations (2.14) and (2.21):

$$a = -\frac{m\omega_n^2 \Delta\lambda}{2} \tag{2.30}$$

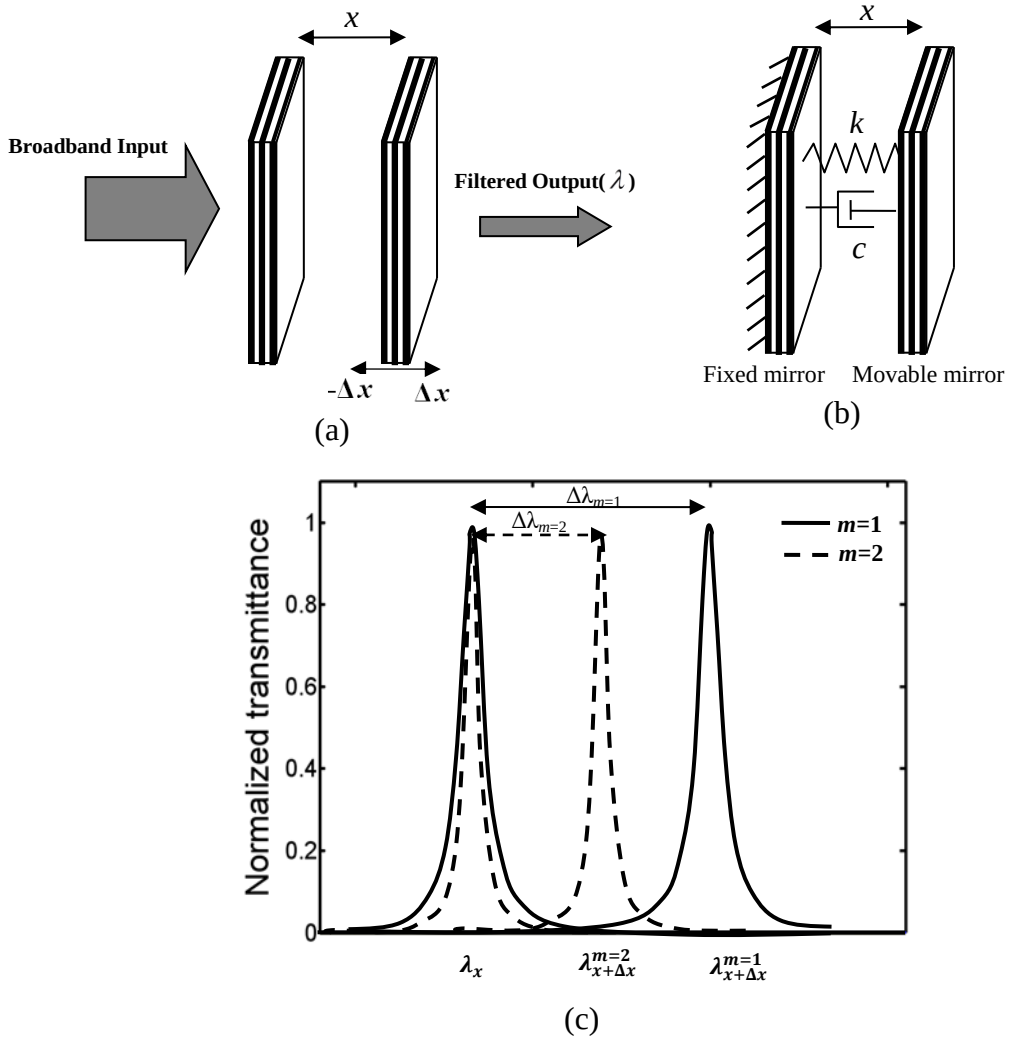

Figure 2-8: (a) FPI with different gap between reflective Bragg grating mirrors, (b) Mechanical block mass-spring-damper model of a FPI-based sensors, and (c) Transmission curve shift of a

FPI due to changes in gap between two mirrors. Two FPI orders are considered (with *m*=1 and *m*=2).

2.5 FP-based accelerometer sensor performance

2.5.1 Effective finesse and imperfections

By considering FWHM ($\delta\lambda_R$) as rough resolution of the FPI sensor and combining Eqs. (2.15), (2.19), and (2.30), the upper limit of the acceleration resolution δa is obtained as follows:

$$\delta a = \frac{\omega_n^2 \lambda_0}{2F_R} \tag{2.31}$$

This equation demonstrate that the resolution (and sensitivity) of a FP-based acceleration sensor in mechanical domain depends on the natural frequency of the suspended mirror, and in optical domain depends on the FP finesse.

The reflectance finesse (F_R), for any actual system due to the fabrication imperfection is not measurable. In fact what is measured in practice is the total effective finesse (F_{eff}) which is the total effective finesse of the system by accounting all the defects generated during the fabrication [50] and is defined as [51]:

$$\frac{1}{F_{eff}^2} = \frac{1}{F_R^2} + \frac{1}{F_D^2} \tag{2.32}$$

where F_D is the effective defect finesse and is defined as

$$\frac{1}{F_D^2} = \frac{1}{F_S^2} + \frac{1}{F_{GRMS}^2} + \frac{1}{F_P^2} \tag{2.33}$$

where F_S , $F_{GRMS,}$ and F_P are the surface roughness, deviation from parallelism, and spherical bowing defect finesse respectively (Figure 2-9 (c)) and can be computed as [51]:

$$F_S = \frac{\lambda}{2\delta t_s} \qquad F_{GRMS} = \frac{\lambda}{4.7\delta t_{GRMS}} \qquad F_P = \frac{\lambda}{1.7\delta t_P} \tag{2.34}$$

where δt_s, δt_{GRMS}, and δt_P are spherical bowing defects, surface roughness, and deviation from parallelism respectively.

From Eq. (2.32), the F_{eff} reduces with increasing mirrors surface roughness, mirrors walls spherical bowing, and deviation from parallelism between the two mirrors.

Figure 2-9 shows the decrease in finesse experienced by an FPI with high reflectivity mirrors in the presence of mechanical errors.

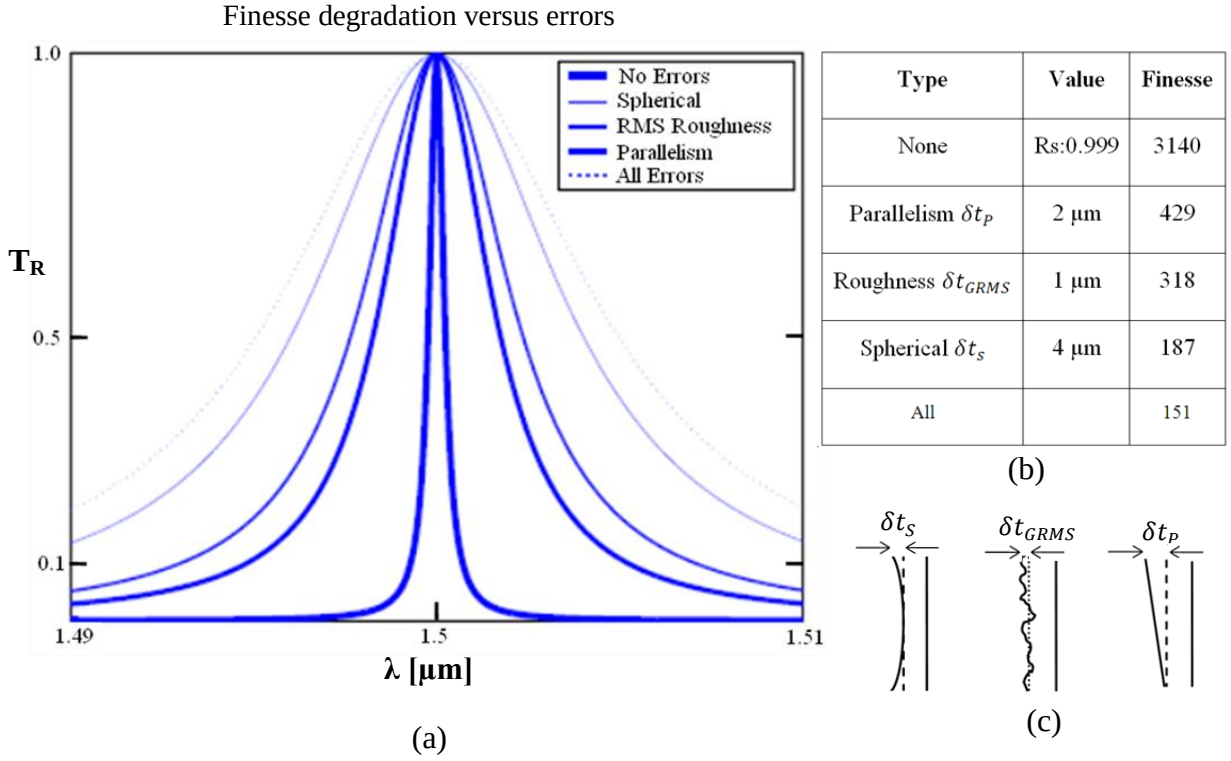

Type	Value	Finesse
None	Rs:0.999	3140
Parallelism δt_P	2 µm	429
Roughness δt_{GRMS}	1 µm	318
Spherical δt_s	4 µm	187
All		151

Figure 2-9: (a) Transmission versus wavelength of a resonance with mechanical defects of the mirrors (parallelism, roughness, spherical bowing), (b) List of values for each defect type and finesse. PS: as finesse value increases, the fringe becomes narrower, (c) Schematic of different types of mechanical defects [50].

In the specific case of Figure 2-9 (b), the finesse decreases by three orders of magnitude. It should be mentioned that in this example, values are based on two silicon wafers forming a FP mirrors.

In the case of high reflectance systems ($F_R \gg F_D$), from Eq. (2.32), the effective finesse is $F_{eff} \approx F_D$, meaning that the system is influenced strongly by mechanical errors.

2.5.2 Sensor Dynamic Range

In FP-based sensors the range of the device is limited to half of free spectral range (FSR), therefore from Eq. (2.30), the maximum dynamic range is calculated as:

$$\Delta a_{max} = \frac{m\omega_n^2}{2} \cdot \frac{FSR}{2} \tag{2.35}$$

It should be mentioned that the displacement of the movable mirror is so small (nm scale) that using one FSR can cover all the required tuning range. Also as discussed earlier, the tuning range not only increases by using smaller gap (Eq. (2.18)) but also increases with the spectral width of the mirrors. On the other hand, as discussed in section 2.1.2 the spectral width of the Bragg mirrors depends on the order of the Bragg mirrors (Eq. (2.13)). The lower the order of the Bragg mirror (thinner silicon/air layer) is, the larger the bandwidth is. In summary, the dynamic range of the sensor increases by decreasing the FP gap and the Bragg mirror walls width.

2.5.3 Sensor Sensitivity

According to Eq. (2.30), the sensitivity of the sensor depends on two factors: the mechanical part (ω_n) and the optical part ($\Delta\lambda$). In other words, the sensor requires low resonant frequencies (larger mass and softer springs) and high optical quality (high finesse) in order to attain high sensitivity. Sensor sensitivity also depends on the system architecture and signal detection techniques. Sensors with low resonant frequencies exhibit better sensitivities, however as discussed in section 2.3 this will reduce the frequency bandwidth of the sensor.

2.5.4 Sensor Resolution

Device has been designed such that the FP has x=30 μm gap (to enable its future interrogation using a tunable laser with 30 nm dynamic range), providing a resonance order of m=52 for the FP

microcavity. The designed resonant frequency for the system is 409 Hz. From (2.30) and considering an optical spectrum analyzer with a wavelength resolution of Δλ =10 pm and assuming that we are only limited by the optical spectrum analyzer resolution; the resolution δa of our device is calculated as (Eq. (2.30):

$$\delta a = \frac{52(2\pi 409)^2 \times 10\ pm}{2} = 175\ \mu g \tag{2.36}$$

This can be improved 52 times ($\delta a = 3.4\ \mu g$) if the FP order m is reduced to 1. This demonstrates the potential of a FP based optical accelerometer. In other words, the device resolution can go below 10μg if small gap is used for the FP cavity.

2.6 Variable optical attenuator-based accelerometer

VOA-based optical accelerometer presented here uses the shutter modulation based on transmission mode to modulate the beam intensity of a multimode strip silicon waveguide. A DBR mirror is used as a shutter to block the light. The shutter is moved perpendicularly to the central propagation axis of two multimode strip silicon waveguide separated by a small gap (Figure 2-10). As the shutter displaces sideways (due to acceleration), less or more light is coupled from the input to the output waveguide. In order to model the structure we must first study the propagation and coupling theory of multimode waveguides. Geometrical optics (ray optics) approximation can be used when the wavelength is much smaller than the feature size. Since the core diameter of a multimode waveguide (10-20μm in our case) is much larger than the wavelength of light (λ=1.55 μm), many characteristics of light propagation in multimode waveguides including coupling loss can be described by ray optics.

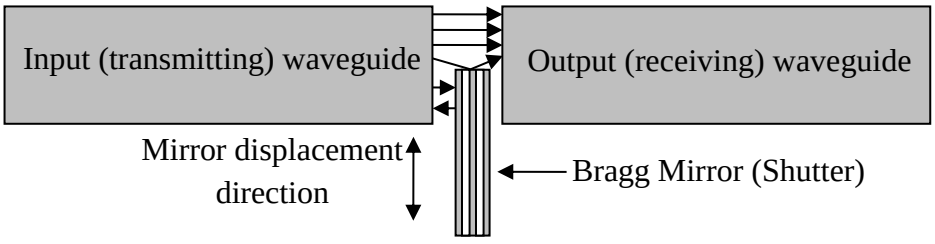

Figure 2-10: Shutter modulation based on transmission mode

2.6.1 Sources of loss in an optical waveguide

There are two different types of loss that must be distinguished when an optical waveguide is measured, insertion loss and propagation loss. The propagation loss is the loss related to the propagation in the waveguide, whereas the insertion loss is the total loss of the waveguide including both the inherent loss and the coupling losses. The propagation loss in an optical waveguide originates from three sources, namely, scattering, absorption and radiation. Each of the contributions of these three sources to loss will be discussed here.

Scattering

There are two types of scattering loss in an optical waveguide: 1-volume scattering originated from imperfections in the waveguide material, such as crystalline defects, contaminant atoms, or voids and 2- scattering due to the waveguide sidewall roughness or interface scattering. The volume scattering has usually less contribution compared to interface scattering [52].

Absorption

Band edge absorption and free carrier absorption are two main sources of absorption loss in waveguides. When a photon with energy greater than the band gap of the waveguide core (in our case silicon) travels in the waveguide, it gets absorbed by the band gap and excites the electrons from the valence band to the conduction band. To avoid that, the energy of the travelling photon must be lower than the material band gap. Silicon has a band gap of 1.1 ev or band edge wavelength of 1.1 μm. Above this band edge, silicon can be used as waveguide material, however below it; silicon can be used as a good absorber. Band edge absorption loss of silicon at wavelength of $\lambda = 1.55$ μm is below 0.004 dB/cm.

Radiation

Ideally, radiation loss of a straight waveguide should be very small. This type of loss denotes leakage from the waveguide due to imperfections (such as slight damage on waveguide due to fabrication mask defects) into the surrounding media or for a rib waveguide, leakage of higher order modes into the planar adjacent region. The mode scattered from the defect can be coupled to another mode and get lost if that mode is leaky. Another source of radiation loss can be due to the leakage of light into the cladding. For example for the case of SOI substrate if the buried oxide layer is not sufficiently thick enough, the guided mode can penetrate into the oxide layer

and lose energy by radiating from the oxide layer into the substrate. The minimum required thickness for the buried oxide layer varies from one mode to another and it also depends on the size of waveguide. As the thickness of a planar waveguide reduces, less confined is the fundamental mode and therefore the more the mode tail extends into the cladding. Therefore the thinner the waveguide is, the thicker cladding is required to prevent the mode of leaking into the substrate from the cladding.

2.6.2 Modeling of multimode waveguide coupling with shutter modulation

To model the shutter modulation, we must first study the coupling behavior between two multimode waveguides. This is a common case in telecommunications particularly in fiber optic connectors or splices. Calculating losses in the output waveguide (receiving waveguide) due to the large number of modes, diverse loss, and unknown coupling coefficient of each mode in a multimode waveguide, is tremendously difficult. The refraction profile of the waveguides have step index profile. The ability of a step index multimode waveguide to accept optical energy or numerical aperture is given by

$$NA = \sin\theta_{max} = \sqrt{n_{cor}^2 - n_{cl}^2} = \sqrt{n^2 - 1} \tag{2.37}$$

where θ_{max} is the maximum acceptance angle by the fiber, n_{cor} is the core refractive index of the waveguide, and n_{cl} is the refractive index of the waveguide cladding (see Figure 2-11). Eq. (2.37) gives the maximum acceptance angle with respect to the waveguide axis at which light rays can propagate and still be guided by total internal reflection. Any light entering that point of the core at angles greater than θ_{max} will be quickly lost through radiation modes (modes that are lost locally at the splice) or leaky modes (modes that are lost within a certain travelling distance). Orange ray in Figure 2-11shows a leaky mode. Assuming two identical aligned waveguides with no gap, θ is identical for both waveguides end facet and does not change across the interface. For splices with air gap, the reflection losses at the interface must also be taken into account. Another important parameter that should be considered for the model is the optical power distribution over the waveguide core surface. For step index waveguides, each mode exclusively corresponds to the angle of propagation in the waveguide core. Therefore the angular power distribution at any point on the core is directly related to the modal power distribution.

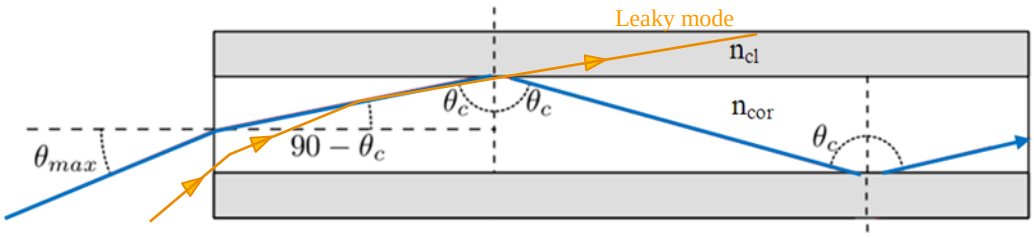

Figure 2-11: Schematic of light propagation in a step index waveguide. θ_{max} is the maximum acceptance angle with respect to the waveguide axis at which light rays can propagate and still be guided by total internal reflection. Any light entering with angles greater than θ_{max} will be quickly lost through radiation or leaky modes.

2.6.2.1 Optical power distribution model for multimode silicon waveguide

Since the sidewall roughness are periodic along the waveguide, the scattering loss is affected not only by the amplitude of the roughness, but also by the distance period of the roughness (mean distance between the scattering points), called autocorrelation length. The surface roughness is usually modeled with two autocorrelation functions: exponential and Gaussian. For waveguides that their sidewalls are defined with photolithography process, the exponential function best describes their autocorrelation [62]. These two autocorrelation functions are defined as follows [62]:

$$C(u) = \bar{\sigma}^2 \exp\left(-\frac{u}{L_c}\right) \quad , \quad C(u) = \bar{\sigma}^2 \exp\left(-\frac{u^2}{{L_c}^2}\right)$$

where $C(u)$ is the autocorrelation function of real roughness function of the sidewalls, $\bar{\sigma}$ and L_c are standard rms deviation of the roughness and autocorrelation length respectively. According to Marcuse [53] for a multimode dielectric slab waveguide, the power distribution is uniform over the slab waveguide core if the waveguide is sufficiently long. The power profile depends on the correlation length (L_c or sometimes is abbreviated as D) of the roughness. If the ratio of correlation length to the slab half width (d) is large enough (≥ 35), regardless of initial excided modes, the power distribution settles down to a steady state distribution. He explains his theory as follows:

"For very long correlation length each mode carries an equal amount of power regardless of the shape of the power versus mode distribution at the beginning of the guide. This is due to the fact

that for long correlation length only the high-order guided modes lose power directly to the radiation field while the guided modes couple in such a way that only next neighbors exchange power. For small correlation lengths, as D/d decreases more power is carried by the lower-order modes. For very small values of D/d (less than unity) essentially all the power is contained in the lowest order mode. This can be explained as the fact that for very short correlation length all guided modes couple directly to radiation. Higher order modes lose power by this mechanism at a higher rate than lower order modes. In addition, each guided mode couples to all the other guided modes. Since the lowest order mode loses the least power to radiation it is the one that survives after all the other modes have lost nearly all of their power".

In reality, waveguides do not have perfectly smooth walls due to the fabrication imperfections (mask and etching errors) and have roughness on their sidewalls (Figure 2-9 (c)). In our case, the waveguides have roughness only along z direction generated by the roughness of mask edges and scalloping during DRIE process (Figure 2-12).

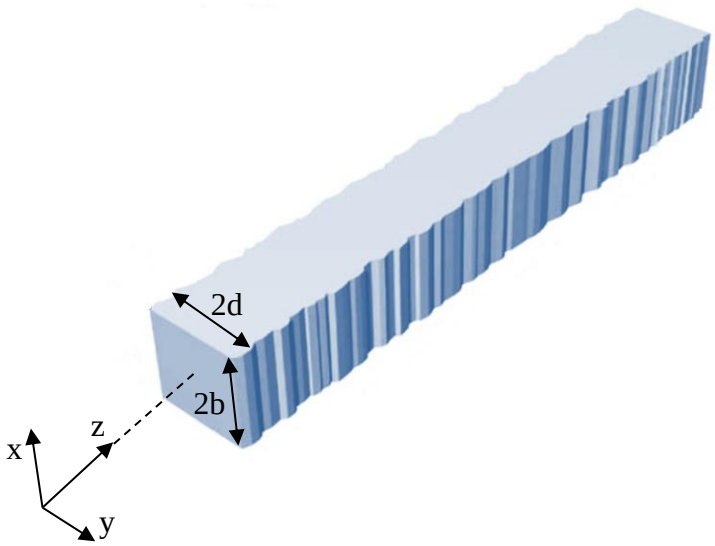

Figure 2-12: Schematic view of our multimode rectangular waveguide. The top and bottom walls are smooth and only the sidewalls have roughness.

Due to the presence of side wall roughness, as light travels, guided modes exchange power between each other continuously. This leads to the coupling between guided modes and radiation modes. As a result they radiates from the waveguide core into the cladding leading to scattering loss for the waveguide. Especially when the autocorrelation length is close to the operational wavelength, the sidewalls of waveguide act as a grating and generate higher losses. If the

autocorrelation length approaches one quarter of the operational wavelength, the scattering losses can be very large.

Marcuse [53]-[61] stated in his coupling theory and coupled power theory that as modes propagate in a waveguide with wall roughness they meet to a specific distribution called steady state distribution where the average power ratio between modes remains constant although the instantaneous power ratios might fluctuate. The power distribution between the modes depends on the amplitude of roughness and the autocorrelation length. As modes propagate in the transition region, their propagation loss and power distributions vary before reaching the steady state distribution. The required distance to reach the steady state distribution is called equilibrium length. This is very important as at the steady state, the power distribution is uniform independent of the initial field that excited the waveguide.

Many people tried to investigate the propagation loss or power distribution in a rectangular cross section waveguides. Some used 2-D effective refractive index approximation [62], [63] while others approximated the radiation modes with the free-space cladding modes [64]-[66]. However both methods were based on approximation and even invalid in some cases. Many other methods have been used such as volume current method [65]-[70] and ray tracing [71] but they were either dealing with single mode operation [65]-[70] or only propagation loss [71].

High index contrast waveguides have been studied and precise analysis have been reported [69], [72]. However the studied waveguide in [72] is single mode and they only focused on the propagation loss. A three dimensional exhaustive analysis on different types of rectangular waveguides with any refractive index contrast including silicon rectangular waveguides were reported in [69], however they only focused on the single mode operation. Papakonstantinou et al. [73] studied for the first time the radiation and guided modes propagation in a highly multimode rectangular strip waveguide with sidewall roughness using new method called Radiation mode Fourier Decomposition Method (RFDM). Using coupled mode theory they calculated the radiation modes, equilibrium loss, length and more interesting, the power distribution of a 50μm×50μm waveguide (supporting 1052 bound modes) as a function of wall roughness and autocorrelation length. The waveguide core has a refractive index of 1.5249 and cladding of 1.5560 for the operational wavelength of λ=850 nm. They showed that modes with different symmetry do not interact with each other in the presence of sidewall roughness. As a

result, two sets of modes propagate independently inside the waveguide and gradually converge to two uncorrelated distributions at steady state. In their simulation they used a waveguide with 4 μm autocorrelation length (L_c) and sidewall roughness deviation ($\bar{\sigma}$) in the range of 10nm-100nm. They showed that, as the roughness increases, the steady state loss increases for both mode symmetries. High sidewall roughness causes guided modes to be coupled more strongly to the radiation modes, leading to a larger propagation loss at equilibrium. Despite steady state loss, the equilibrium length decreases as roughness increases. This is due to the guided-to-guided modal coupling increment adding to existence of guided-to-radiation coupling. More guided modes are coupled to each other, faster they exchange energy and in shorter length the equilibrium is reached. Authors cannot yet explain why the steady-state loss for the odd–odd (electric field with odd-odd mode number), even–odd (electric field with even-odd mode number), group is higher than that of the even–even (electric field with even-even mode number), and odd–even group (electric field with odd-even mode number). What is more interesting is that, only fundamental mode (first even-even mode or 00 mode) out of 537 modes belonging to even–even/odd–even group modes and the first even-odd mode (01 mode) out of 515 belonging to the odd–odd/even–odd group modes survive at equilibrium. Equilibrium length for example for a waveguide with L_c=4 μm and side wall roughness of 30 nm according to their result is 43.1 m. Authors [73] showed that this dual-mode operation is expected for all autocorrelation lengths and roughness deviations. They also examined the effect of the autocorrelation length of the roughness on the steady state loss for different mode groups for $\bar{\sigma}$=25 nm. Their result was a confirmation to what Marcuse [[55], p. 187] predicted: the steady-state loss reaches a maximum value when the width of the slab (or the radius of the fiber) is 0.3–0.4 times smaller than the autocorrelation length.

A. D. Donato et al. [74], have also studied the stationary mode distribution and sidewall roughness effects in multimode polymeric optical waveguides. In their study, they considered a waveguide with roughness in three dimensions and showed that higher orders of modes are more affected by roughness. This is a confirmation on Papakonstantinou results. They also showed that for a waveguide with top and bottom smooth walls (Figure 2-12), the power between the guided modes are distributed relatively uniform. However lower modes are less affected by the roughness in propagation direction (z direction).This is valid for our case, as we only have roughness along the propagation light direction (z) whereas top and bottom surfaces are smooth.

It has also been shown that in a multimode fiber if all the modes are excited equally, the power distribution at any point on the core is uniform and the distribution of power exiting the fiber end has the similar shape as the index profile [77]. Many authors have used uniform power distribution model to calculate the splice loss [78]-[84].

Some other people used another method called Gaussian power distribution model ([85], [86]) which was able to compute the splice losses in fibers more precisely. This model assumes that the power distribution within the solid angle defined by the numerical aperture at any point on the fiber core has a Gaussian form. This model was verified by Metter [86] for different source of losses such as refractive index mismatch and transversal misalignment (Figure 2-25) between the transmitter fiber and receiver fiber. The difference between the calculated loss and the measured loss in the case of refractive index mismatch was less than 0.04 dB and in the case of transversal misalignment was 0.1 dB.

Lenz et al. [87], studied the modal power loss coefficient of highly overmoded rectangular dielectric waveguides (30 μm×30 μm), in the presence of sidewalls roughness. They approximated the radiation modes with free space modes. They validated their method by comparing their results with a slab waveguide for which its exact loss coefficient and radiation loss based on free space modes are known (reported by Marcuse [57], and Wang [88]). The refractive index of the core and cladding are chosen to be 1.01 and 1 respectively in their simulation for $\lambda = 1$ μm. They used Guassian autocorrelation function in their model with correlation length of D=0.05d/2=750 nm. They also showed that the mode loss coefficient increases as the mode number increases, i.e. higher modes experience more loss than lower modes. As they explain, this is because the difference between the propagation constants of a higher order mode and a radiation mode is smaller than that of a radiation mode and a lower order mode. As a result, this matching offers better coupling efficiency to radiation modes for higher modes.

In conclusion, for a multimode waveguide having side wall roughness at the interface between core and cladding, as light travels, higher order modes experience more scattering loss with a higher rate than lower order modes. As a result not only they constantly exchange power to their next neighbors but also after a certain length (called correlation length) they are coupled to

radiation modes and get lost. Since the lowest order mode loses the least power to radiation, it is the one that survives after all the other modes have lost nearly all of their power.

2.6.2.2 Modeling

In the previous section, the power distribution over a multimode waveguide (MMW) was considered. The stationary power distribution model was studied by many people with different methods and has given a good agreement with experiments. Light propagation in the existence of side wall roughness is a complex topic, particularly in multimode waveguides, as energy continually redistributes itself between the guided modes and radiates from the core of waveguide into the cladding due to the coupling between guided modes and radiation modes. The correlation length seems to be a key factor that determines the limit between non-stationary and stationary modal power distribution inside the waveguide. When a Bragg mirror is introduced in the air gap between two MMW, more extrinsic loss will be generated for the system. When a Bragg mirror is placed in the light path between two perfectly aligned MMW, the light beam from the transmitting MMW (from now on it will be called input waveguide) is partially blocked by the mirror and is then diffracted to the facet of the receiving MMW (from now on it will be called output waveguide) and coupled into the output, leading to the modulation of the transmitted power to the output waveguide. In our case, since both MMW are identical and perfectly aligned (another advantage compared to Guldimann [14] configuration), most of the transmitted light is captured by the output waveguide except the part that might be reflected or scattered from the Bragg mirror and reaches the output waveguide out of its NA. The other way can also occur, i.e. non-coupled light beams can be coupled into the output waveguide due to scattering or reflection from the edge of the mirror. However, as the mirror is thin (6-8 μm), this scattered light has small contribution to the overall coupled power and is neglected.

In order to model our sensor, the following assumptions are made for the VOA sensing junction:

- Due to the large NA of the MMWs compare to the operational wavelength, the ray optics approach is valid to estimate the transmitted power.
- Light emitting from the input waveguide facet is at its stationary state since the MMW length (4 mm as can be seen in Figure 4-27) is much greater than the correlation length (100 nm).

- At stationary state, the fundamental mode is considered as the only guided mode in the input and output waveguides (argued below).
- Fundamental mode profile can be approximated with a Gaussian beam [107].

In the case of silicon waveguides fabricated with DRIE, the typical sidewalls roughness and correlation lengths depend on the process and can vary from 10 nm and 50 nm [62], [69], [89] to 2nm and 50 nm [96]. Our fabricated waveguides have periodic sidewall roughness of 30 nm with typical correlation length of 100 nm. According to Marcuse, ratio of correlation length to waveguide half width D/d <1 is sufficiently small whose steady state distribution would only consist the fundamental mode. This ratio in our case is at the order of 0.017 (D=100 nm, d=6 µm) which satisfies the Marcuse condition. Contrary to Marcuse, Papakonstantinou predicts dual-mode operation for D/d less than unity but as it will be discussed in the following; only the fundamental mode has significant contribution to the signal modulation.

According to Papakonstantinou, the first two modes of the waveguide always survive in the presence of side wall roughness. Figure 2-13 shows optical simulations demonstrating the intensity distribution of two first TE modes of a multimode SOI strip waveguide simulated by FemSIM. The width of the waveguide is 12 µm and the height is 30 µm.

The size of the intensity profile at the MMW output depends on the cross section size of the waveguide. The larger the waveguide cross section, the broader the total intensity profile. This is clear because from ray optics point of view, as the width (or height) of the waveguide increases, beams travel more parallel, leading to the increment of the total intensity profile size. In our case, we are more concerned about the width of the waveguide, as power is only modulated in the lateral direction.

Although the superposition of both modes intensity in the case of dual-mode operation provides relatively uniform intensity profile along the X direction, it predicts a nearly (approximated) Gaussian intensity profile in the Y direction (along waveguide width). Since both guided modes have approximately the same lateral mode size, and also due to the profile of the power distribution of the second mode (zero power at the center and maximums at the sides), the total intensity (superposition of both modes intensity) around the center of waveguide offers approximately the same lateral intensity profile as the fundamental mode. Therefore from now on we consider the fundamental mode as the only guided mode in our simulations.

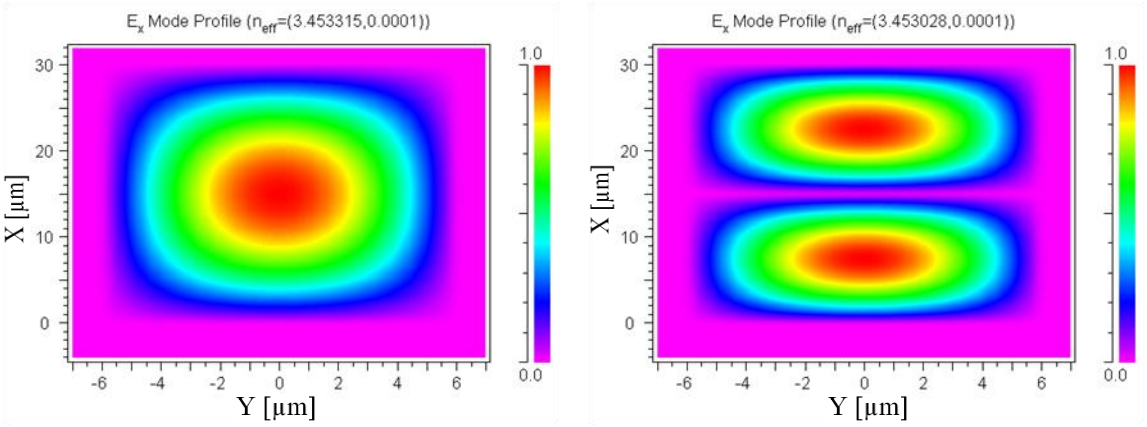

(a) (b)

Figure 2-13: Simulated intensity distribution of first two modes of a multimode SOI strip waveguide with 2d (width) =12 µm, 2b (height) = 30 µm: (a) Fundamental mode, (b) first even-odd mode (01 mode).

- Since the Bragg mirror is thin (6-8 µm), its width will not be taken into account in the model. Therefore the scatered or reflected light from the edge of the mirror (and coupled into the output waveguide) are neglected.

In the simulations, the effect of Bragg mirror on the mode power distribution after the mode is blocked by the mirror is neglected since the mirror is thin. In other words, since the mirror is thin, the contribution of scattered or reflected light from its edge is negligible. Note should be taken that calculating the exact contribution of scattered/reflected light caused by mirror thickness in the overall output power is very complex as the mirror surface roughness should also be taken into account.

- The coupling loss due to the existence of the air gap (longitudinal offset) between the two input and output waveguides (15-25 µm) can be neglected as the generated longitudinal loss in this case is very small.

To validate this assumption, we will study the coupling loss between two Gaussian beams using coupling theory. Coupling coefficient η between two Gaussian beams having beam waist radius of w_0 and w_1 or two single mode waveguides caused by longitudinal misalignment z between them is given by [91]

$$\eta = \frac{4w_0^2 w_1^2}{\left[(w_0^2 + w_1^2)^2 + \left(\lambda z/\pi\right)^2\right]} \tag{2.38}$$

Assuming both waveguides having equal beam waist radius $w_0^2 = w_1^2$,

$$\eta = \frac{4w_0^4}{4w_0^4 + \left(\lambda z/\pi\right)^2} = \frac{4z_R^2}{4z_R^2 + z^2} \tag{2.39}$$

yielding a longitudinal coupling loss of

$$L_{lc} = -10\log\frac{4z_R^2}{4z_R^2 + z^2} \tag{2.40}$$

where Z_R is the Rayleigh range $z_R = \frac{\pi w_0^2}{\lambda}$. Figure 2-14 shows the longitudinal coupling loss variation as a function of longitudinal distance between two beams for three different beam radiuses.

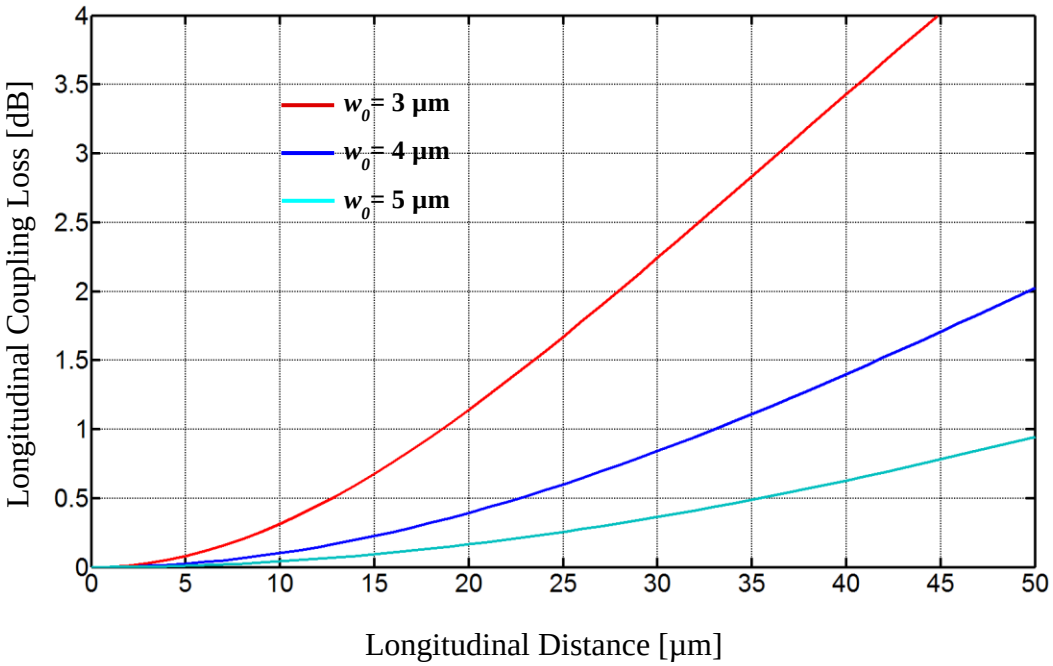

Figure 2-14: Longitudinal coupling loss variation as a function of longitudinal distance between two Gaussian beam having equal beam radius for three different beam radiuses.

As seen, the smaller the beam radius is, the higher the longitudinal coupling loss is for a certain distance. However for small gaps, the generated loss is very small. From Figure 2-14, in our case, the longitudinal coupling loss for our used gap (15-25 μm) is less than 0.75 dB for the guided mode with beam radiuses greater than 4 μm. The beam radius of the fundamental mode in a silicon waveguide depends on the waveguide width and can only accurately be determined with analysis methods. From Figure 2-13 the beam radius of a waveguide having 12 μm widths is extracted to be 4 μm.

It is worth noticing that although increasing the gap between input and output waveguides will generate more coupling loss, increasing the gap between the input waveguide and Bragg mirror can increase the usable linear range. The reason for that as can be seen in Figure 2-16 is, as the mode leaves the input waveguide end facet and starts propagating in the free space, its spot size (beam diameter) begins to diverge (due to non-existence guiding medium for the mode), leading to a broader uniform power region available at the Bragg mirror position. The beam divergence of a Gaussian beam with an initial beam diameter (beam waist) of $2w_0$ is given by [108]:

$$w_1 = w_0\sqrt{1+\frac{z_1^2}{z_R^2}} \tag{2.41}$$

where w_1 is the waist size of the beam at position z_1 and z_R is the Rayleigh range. Figure 2-15 shows the evolution of beam radius as it travels in free space.

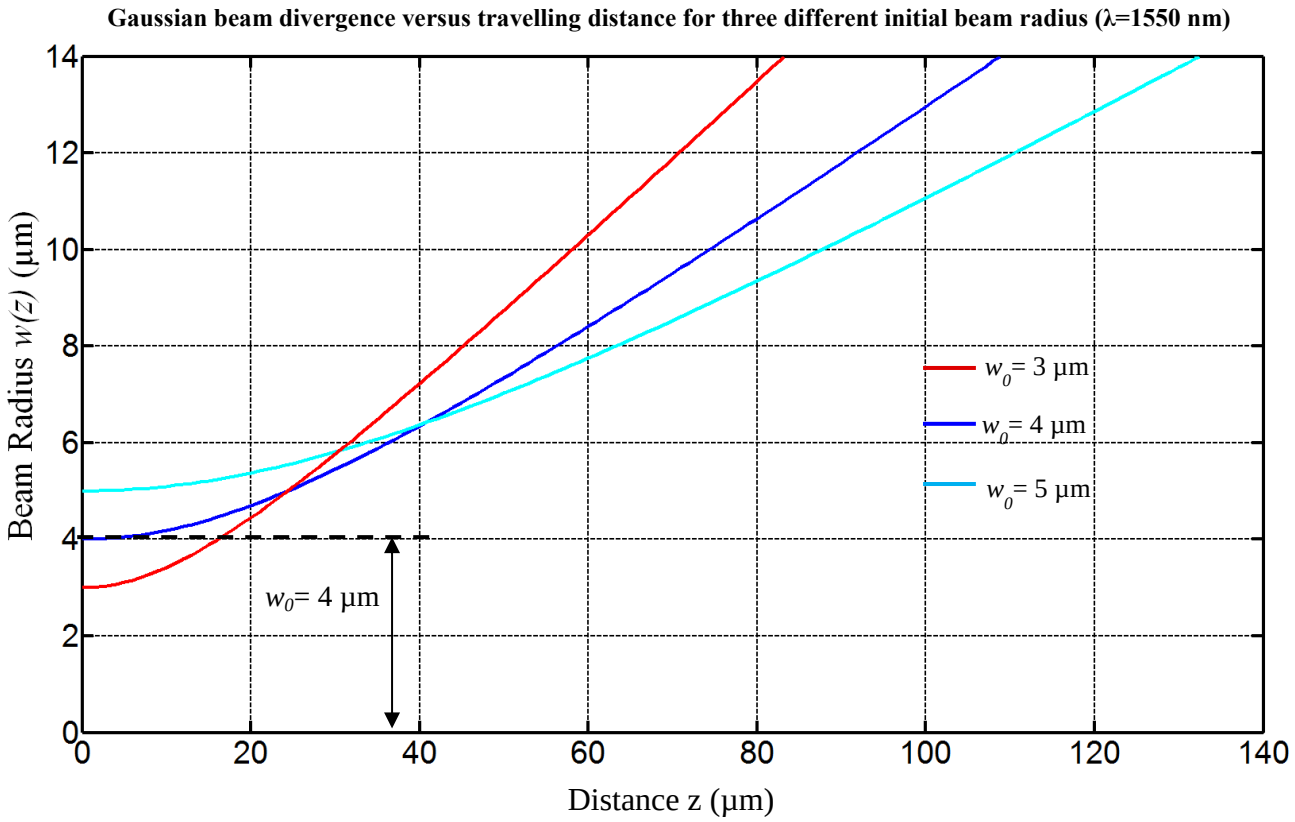

Figure 2-15: Divergence of a Gaussian beam as it travels for three different value of initial beam radius (λ=1550 nm).

Now let's study the absolute attenuated output power caused by mirror displacement. A. Q. Liu et al. [90], have optically modeled a MEMS-VOA with shutter modulation using two single mode fibers as input and output. Although Liu's method is accurate, it is very complex. We would like to estimate our coupled output power with a simple analysis using scalar optical theory without missing too much information about the output signal.

Figure 2-16 shows the diagram of our optical model similar to Liu's model. Light beam of transmitting silicon MMW (input waveguide) is partially blocked by the Bragg mirror and then is diffracted to the facet of the receiving silicon MMW (output waveguide) and coupled into the output.

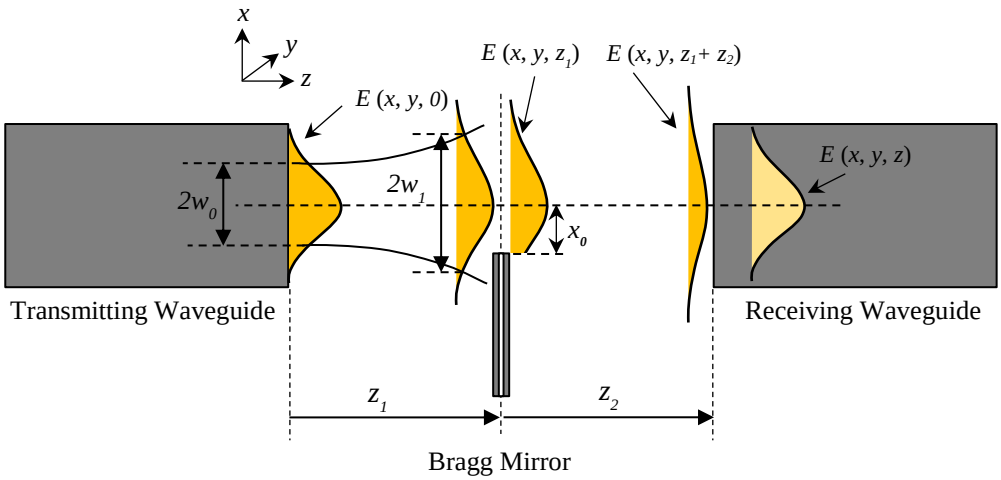

Figure 2-16: Schematic of the optical model for VOA-based sensors

Note that according to ray optics, the incoming mode can be considered as a superposition of plane waves propagating in different angles. Since the width of output waveguide is greater than the spot size of incoming light (fundamental mode of input waveguide), ideally all light power of the beams propagating within the numerical aperture of the output waveguide can be captured by the output waveguide.

The coordinates of the input fiber, the plane after the mirror, and the output fiber facet are represented by $(x, y, 0), (x, y, , z_1)$, and $(x, y, z_1 + z_2)$ respectively. The electric field profile of the guided mode at the input waveguide end approximated with a Gaussian beam is given by,

$$E(x, y, 0) = E_0(x, y) = exp\left(-\frac{x^2 + y^2}{w_0^2}\right) \tag{2.42}$$

where w_0 is the beam waist radius. Electrical amplitude do not contribute to the final result (transmission loss), therefore it is considered to be unity. The field distribution of the beam right before the mirror (distance z_1) can be represented as a Gaussian beam with new beam waist size w_1:

$$E(x,y,z_1) = exp\left(-\frac{x^2+y^2}{w_1^2}\right) \tag{2.43}$$

where w_1 is defined in (2.41). Therefore, the field distribution right after the mirror can be expressed as (neglecting the mirror width):

$$E(x,y,z_1) = \begin{cases} exp\left(-\frac{x^2+y^2}{w_1^2}\right) & x > -x_0 \\ 0 & x < -x_0 \end{cases} \tag{2.44}$$

where x_0 is the initial position of the mirror (mirror top edge distance from the waveguides optical axis). Power distribution right after the mirror is then given by:

$$P(x,y,z_1) = exp\left(-\frac{2(x^2+y^2)}{w_1^2}\right) \tag{2.45}$$

As mentioned previously, since the width of output waveguide is greater than the spot size of incoming light (fundamental mode of input waveguide), and since the gap between the mirror and the output waveguide is small, beams that are propagating within the numerical aperture of the output waveguide can be captured by the output waveguide. Therefore we can consider the same power function as (2.61) for the transmitted power to the output waveguide. The transmitted power P_0 to the output waveguide when no acceleration is applied ($x_0 = 0$) is therefore represented by,

$$P_0 = \int_{-\infty}^{+\infty}\int_{0}^{+\infty} exp\left(-\frac{2(x^2+y^2)}{w_1^2}\right) dxdy.$$

Term $\int_{-\infty}^{+\infty} exp\left(-\frac{2y^2}{w_1^2}\right) dy$ will be eliminated at the end as the transmission loss is going to be calculated (ratio of powers). Therefore the lateral transmitted power P_{l0} is:

$$P_{l0} = \int_{0}^{+\infty} exp\left(-\frac{2x^2}{w_1^2}\right) dx.$$

Knowing that,

$$\int_{0}^{+\infty} dx\, e^{-\alpha x^2} = 1/2 \int_{-\infty}^{+\infty} dx\, e^{-\alpha x^2} = 1/2\sqrt{\frac{\pi}{\alpha}} \tag{2.46}$$

$$P_{l0} = \frac{1}{2} \cdot \sqrt{\frac{\pi}{2}} w_1 \tag{2.47}$$

Lateral transmitted power to the output waveguide P_{lx_0} (if the divergence of beam from z_1 to z_2 is small) when mirror is moved to position x_0 (due to applied acceleration) is:

$$P_{lx_0} = \int_{x_0}^{+\infty} exp\left(-\frac{2x^2}{w_1^2}\right) dx\ .$$

Knowing,

$$\int_{x_0}^{+\infty} dx\, e^{-\alpha x^2} = \frac{1}{2}\sqrt{\frac{\pi}{\alpha}} Erf\left(\sqrt{\alpha} x_0\right) \tag{2.48}$$

where $Erf\left(\sqrt{\alpha} x_0\right)$ is the error function. Therefore,

$$P_{lx_0} = \frac{1}{2}\sqrt{\frac{\pi}{2}} w_1 \left[Erf(+\infty) - Erf\left(\frac{\sqrt{2}}{w_1} x_0\right)\right] = \frac{1}{2}\sqrt{\frac{\pi}{2}} w_1 \left[1 - Erf\left(\frac{\sqrt{2}}{w_1} x_0\right)\right] \tag{2.49}$$

Figure 2-17 shows the normalized transmitted power to the output waveguide as a function of mirror position x_0 for three different beam radiuses (at mirror position) of 3 μm, 4 μm, and 5 μm. Lines fitted on the curves at $x_0 = 0$ are shown with solid lines. Lines with 5% deviation from fitted lines are also shown (dotted lines), representing the maximum linear range with 5% uncertainty. As seen in Figure 2-17, curves have maximum slope (maximum sensitivity for the sensor) at the center. This is the reason why mirror is designed to be positioned at the center of waveguide when no acceleration is applied. Another reason is that, the sensor has linear response only around the center of the waveguide (propagation axis) due to its uniform power distribution around the center. The range of linearity depends on the beam radius and increases as the beam radius increases. For instance for a structure with input waveguide having w_1=3 μm beam radius at the mirror position, the sensor has a linear response between -1 μm to +1 μm (linearity better

than 0.5%), providing a linear displacement range of ±1µm. This rage is increased to ±1.7 µm for the case of w_1= 5 µm (indicated with vertical dashed line).

The maximum displacement of a moving mass with dimensions of 1000 µm×1000 µm (proof mass displacement for applied acceleration with the magnitude of gravity) depends on the springs dimensions and varies from 0.16- 2.2 µm as represented in Table 3-2. The width of the waveguide therefore should be chosen based on the proof mass MEMS design such that, the maximum displacement of the proof mass due to the gravity would fall into the linear range determined by the waveguide width (or guided beam radius).

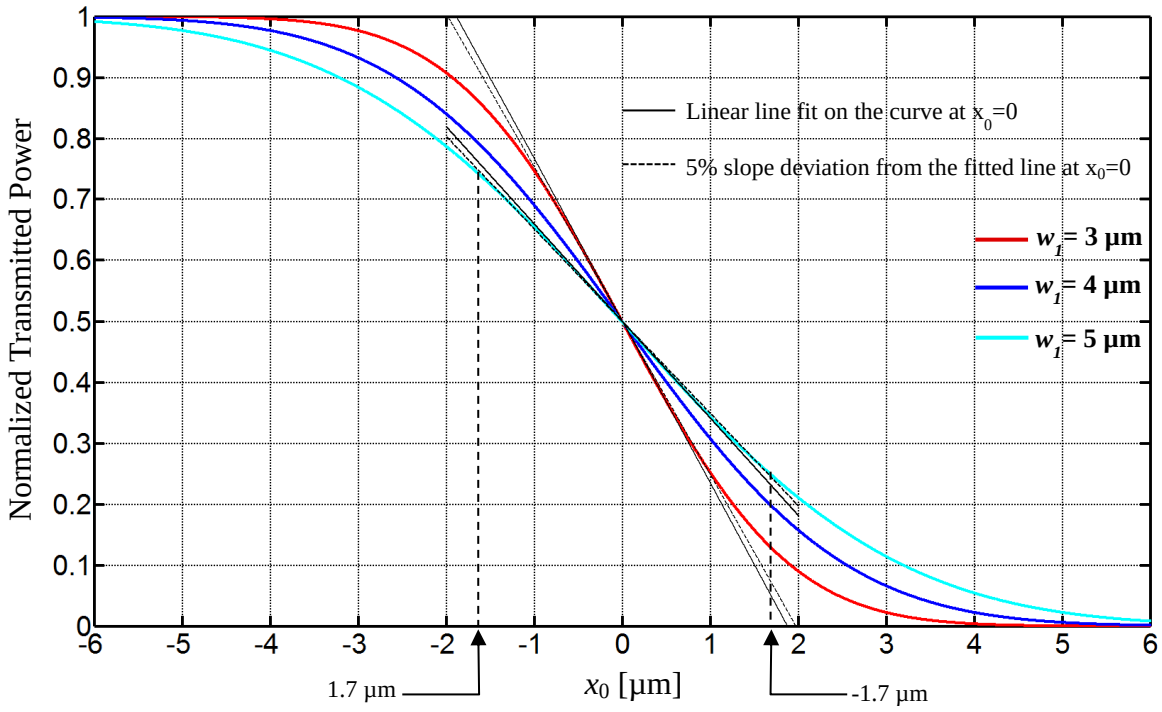

Figure 2-17: Normalized transmitted power as a function of mirror position for three different beam radiuses seen at the mirror position. Black solid lines are the lines fitted on the curves at the initial mirror position $x_0 = 0$. Dotted lines are the lines fitted on the curves to calculate the linear range response of device with 5% uncertainty.

The attenuation L_a (ratio of the lateral transmitted power to the initial lateral transmitted power in decibel) is given by,

$$L_a = -10\ log \frac{P_{lx_0}}{P_{l0}} \tag{2.50}$$

Substituting (2.47) and (2.49) into (2.65),

$$L_a = -10\ log \frac{P_{lx_0}}{P_{l0}} = -10\ log \left[1 - Erf\left(\frac{\sqrt{2}}{w_1} x_0\right)\right] \tag{2.51}$$

Figure 2-18 demonstrates the evolution of output power attenuation caused by mirror movement as a function of position of the Bragg mirror for three different beam radius values of 3 μm, 4 μm, and 5 μm. As seen, the attenuation per mirror displacement or optical sensitivity inversely increases (as predicted before) with the size of the lateral mode seen by the mirror at the mirror position. As an example, if the initial beam radius (in the input waveguide) is 3 μm and the gap between the input waveguide and the mirror is 15 μm, the new beam radius at the mirror position from Figure 2-15 will be 4 μm. If the mirror displaces 1 μm (x_0=+1) from its initial position (x_0=0) due to an applied acceleration, from Figure 2-18, ΔL_a=2.1 dB, leading to 2.1 dB/μm optical sensitivity. On the other hand the mirror displacement sensitivity depends on the proof mass-MEMS architecture design. For example from Table 3-2, for a device having a proof mass of 1000 μm×1000 μm fabricated on a SOI wafer with 75 μm thickness and spring parameters listed on the last row of the table, the proof mass displacement sensitivity is 2.2 μm/g leading to total 4.6 dB/g sensitivity for the device.

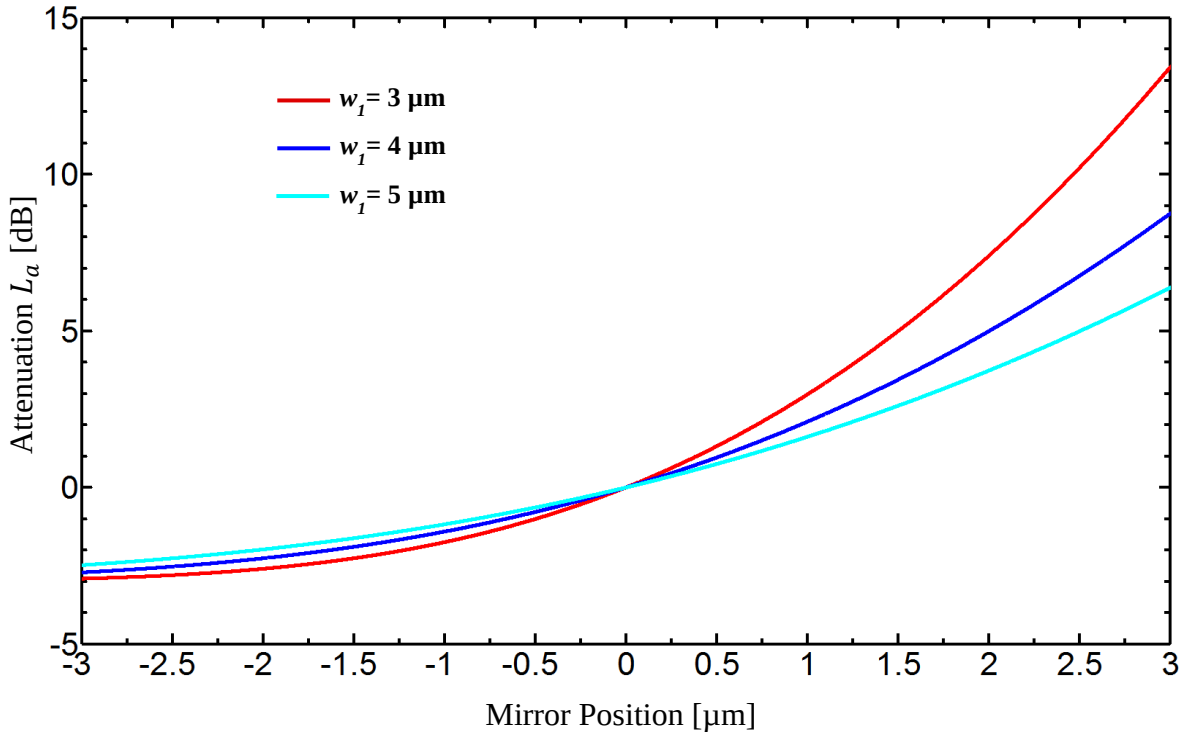

Figure 2-18: Attenuation in power output versus mirror position for VOA- based sensor devices for three different beam radiuses seen at the mirror position.

2.6.3 Sensor Dynamic Range

The tuning range of VOA-based devices is determined by the lateral guided mode size at the mirror location which is directly related to the waveguide width at the VOA junction. On the other hand, the linear response range is determined by the regions where the power of the guided mode is uniform. These are the regions nearby the optical axis of the waveguide. For instance, for a beam having a beam radius of 3 µm, a linear range from +1 µm to -1µm with 5% uncertainty is extracted from Figure 2-17, providing a total linear dynamic range of 2 µm. This range is increased to 3.4 µm when the beam radius is increased to 5 µm. Although increasing the waveguide width at the VOA junction enlarges the mode size and as a result, provides a larger tuning range for the device, it reduces at the same time the sensitivity of the device (Figure 2-18); unless the proof mass displacement is increased accordingly by lowering the resonance frequency. Therefore there is a trade-off between the sensor linear dynamic range and the device optical sensitivity.

2.6.4 Sensor Sensitivity

The total sensitivity of a VOA-based device is the result of multiplication of both device mechanical sensitivity or proof mass displacement sensitivity and device optical sensitivity and is: 1- inversely proportional to the system resonant frequency and, 2- inversely proportional to the lateral guided mode size in the waveguides (which is related to the waveguides width) at the VOA junction (more intensity modulation for unit displacement).

2.7 SOI waveguides

A SOI waveguide is a waveguide that is created with a silicon layer atop of the oxide layer (device layer) on a SOI substrate (Figure 2-19). In this case, the core of the waveguide is the silicon layer that is surrounded by air on top and the oxide layer underneath called buried oxide (BOX). Air and the BOX layer both have lower refractive index compared to silicon, acting as the waveguide cladding. There are mainly two types of SOI waveguides that are commonly used in microphotonics integrated circuits, namely rib waveguides and strip waveguides. Figure 2-19 shows the schematic of a SOI rib and a strip waveguide.

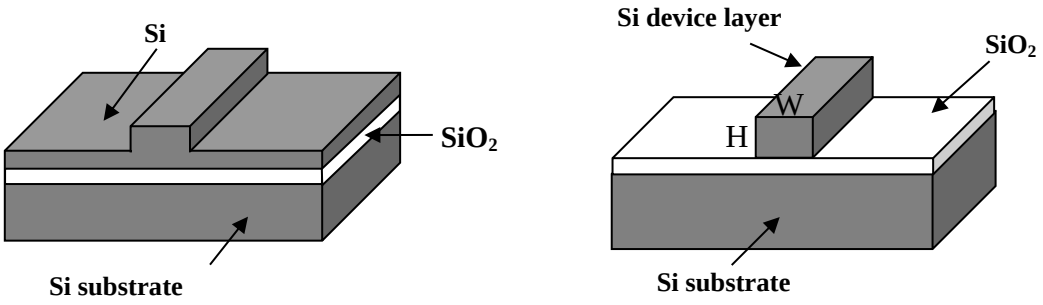

(a) (b)

Figure 2-19: Various types of SOI waveguides: (a) rib waveguide; (b) strip waveguide

Since the required dimensions for being SM for a SOI strip waveguide is small (order of sub-micrometer) compare to that of fiber, the coupling efficiency is very low for fiber–waveguide coupling in this case [97].

Silicon rib waveguides are often used as SM optical waveguides in microphotonics integrated circuits. These kinds of waveguides are large (compared to SM strip waveguides) and do not create high confinement like strip waveguides. Their advantage is their large size which eases

coupling (to the optical fibers), reduces scattering losses and increases fabrication tolerances. SOI rib waveguides with large cross sections (several micrometers) have been developed [92], [93]. Unlike strip waveguides, rib waveguides can be SM even at dimensions over 10μm. For rib waveguides, the higher order modes escape into the surrounding slab regions (i.e., Region II in Figure 2-20(a)) during the propagation and consequently equivalent SM propagation in the rib region is realized. SM condition for SOI waveguides was studied in 1991 by Soref et al. in [95] and is given by

$$r > 0.5 \qquad \text{(a)} \qquad (2.52)$$
$$t < \frac{r}{\sqrt{1-r^2}} + 0.3 \qquad \text{(b)}$$

where r and t are called normalized rib height and normalized rib width, respectively and are given by $r = h/H$, and $t = W/H$ (Figure 2-20 (a)). Due to the Soref's width limitation (Eq. (2.52)-b), all higher order horizontal modes acquire higher effective index than the fundamental mode, hence leaking into the one dimensional slab waveguide that surrounds the rib. On the other hand Eq. (2.52)-a guarantees that all higher order vertical modes will leak into the slab and become radiative.

Optical simulations were carried out to map the modal power distribution in the waveguide. A mode solver that uses finite element method (FemSIM) is used to find the power distribution and the number of guided modes in the waveguide. Results agree with the Soref's theory showing that the fundamental TE mode is the only guided mode in the waveguide. Figure 2-20 (b) shows the intensity distribution of the guided mode in the SM SOI rib waveguide. Losses in SM strip waveguides typically range from 0.2 to 5 dB/cm [96]. On the contrary, rib waveguides, due to their larger dimensions, typically have lower losses (< 0.1 dB/cm [92]).

SOI waveguides have been previously integrated with other micro optical components for different applications [98]-[105]. Single mode SOI strip waveguides have been integrated with micro-ring cavities for bio sensing purposes [98], [99]. Rib waveguide have also been integrated with Bragg reflectors to form Gires–Tournois interferometers [100] or tunable in-plane FP cavities [101]-[105].These tunable in-plane FP cavities have been used for thermo-optic tuning [104] and refractive index measurement [105].

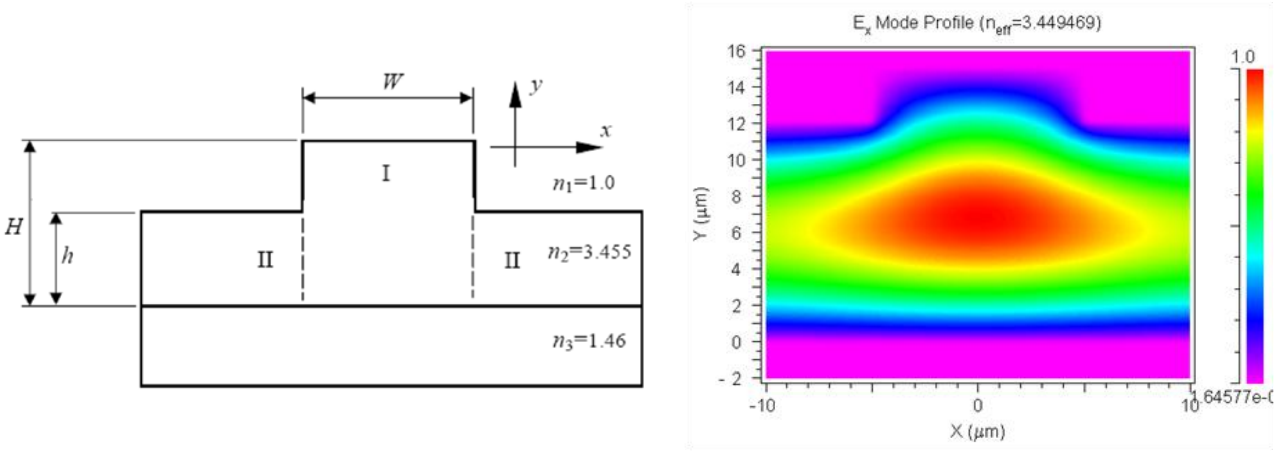

(a) (b)

Figure 2-20: a) Cross section of rib waveguide, b) Simulated intensity distribution of the fundamental TE mode of a single mode SOI rib waveguide with W=10 µm, H= 15 µm, and h=12 µm.

2.7.1 Scattering loss estimation in a strip multimode SOI waveguide

Let's now evaluate the interface scattering loss for our multimode strip SOI waveguides. We can only consider the vertical side walls of the waveguide as the main sources of interface scattering loss since the upper and lower waveguide interfaces have smooth surfaces. As a result, we can approximate it with a planar waveguide constituting sidewalls as it is shown in Figure 2-21.

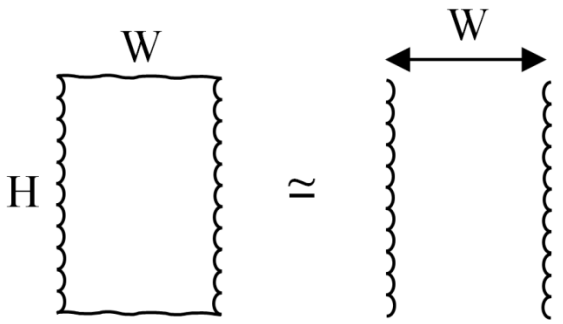

Figure 2-21: In a silicon strip waveguide fabricated on SOI substrate, upper and lower interfaces of waveguide have smooth surfaces compared to sidewalls. As a result to estimate the scattering loss, the waveguide can be approximated with a planar waveguide constituting of sidewalls.

The loss coefficient of a mode propagating in a planar waveguide due to interface scattering studied by Tien [93] is approximated with [52], [93]:

$$\alpha_s = \frac{\cos^3\theta}{2\sin\theta}\left(\frac{4\pi n_{cor}(\sigma_u^2+\sigma_l^2)^{1/2}}{\lambda_0}\right)^2\left(\frac{1}{W+\frac{1}{k_{yu}}+\frac{1}{k_{yl}}}\right) \tag{2.53}$$

where θ is the propagation angle of the mode (Figure 2-22), n_{cor} is the refractive index of core, σ_u and σ_l are the variance of the upper and lower surface roughness (or r.m.s roughness) respectively, λ_0 is wavelength where the loss is going to be measured for, W is the planar waveguide width, and k_{yu} and k_{yl} are the decay constants perpendicular to the waveguide surface ($k_y = n_{cor}k_{0y} = n_{cor}k_0\cos\theta$ where $k_0 = {}^{2\pi}/_{\lambda_0}$) in the upper and lower surfaces respectively.

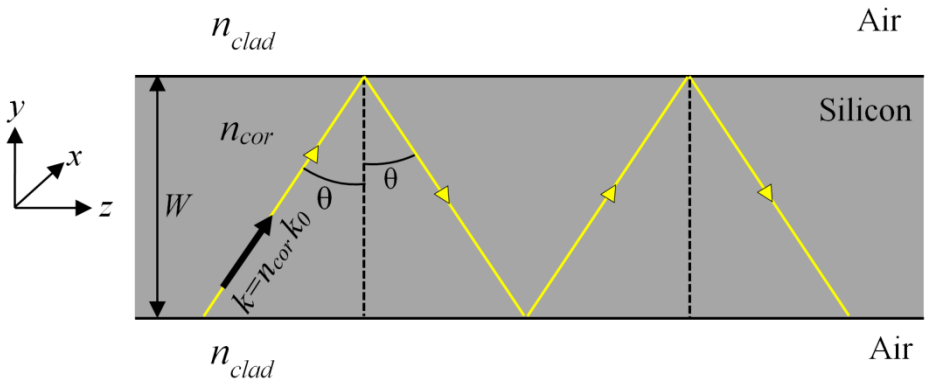

Figure 2-22: Propagation of mode in a planar waveguide.

The propagation angle θ of a TE mode m of a symmetrical planar waveguide (our waveguide in the lateral dimension is surrounded by air n_{clad}=1, therefore it is a symmetrical planar waveguide) can be calculated from the following equation [52]:

$$k_0 n_{cor} W\cos\theta - m\pi = 2\tan^{-1}\left(\frac{\sqrt{\sin^2\theta-\left({}^{n_{clad}}/_{n_{cor}}\right)^2}}{\cos\theta}\right) \tag{2.54}$$

In our case W=12 µm.

For comparison, if only fundamental mode TE_0 (m=0), first TE mode TE_2 (m=2) and fifth TE mode TE_{10} (m=10) are considered, for λ_0=1.55 µm and n_{cor}=3.5, and if both right and left hand side of equation (2.54) are plotted versus cos θ, the intersection of them will determine the value of θ for the corresponding mode. The values extracted from the curve are 89 º, 86.9 º, and 78.5 º for TE_0, TE_2, and TE_{10} respectively. The fundamental mode has therefore higher propagation angle than the first TE mode, resulting in less divergence for the fundamental mode as it propagates along the waveguide compared to the first TE mode. More interesting, if W=1µm, from (2.54) the propagation angle for the fundamental mode will be 79 º, i.e., the narrower the waveguide, the less confined the mode will be.

Decay constants in the waveguide cladding are given by:

$$k_{yi}^2 = \beta^2 - k_0^2 n_i^2$$

where $\beta = k_0\ n_{cor}\ sin\theta$. Since waveguide is symmetric, decay constants of upper and lower surfaces are equal $k_{yu} = k_{yl} = k_y$. Decay constants are calculated as 13.59 μm^{-1}, 13.57 μm^{-1}, and 13.3 $\mu m^{-1}$for TE_0, TE_2, and TE_{10} respectively. Typical roughness of waveguides sidewalls after DRIE is 30 nm. Substituting corresponding values in (2.53), loss coefficients of 0.3 cm^{-1}, 9.26 cm^{-1}, and 472.7 cm^{-1} are calculated for TE_0, TE_2, and TE_{10} respectively. Expressed in decibels, these are equivalent to losses of 1.3 dB/cm, 40.2 dB/cm, and 2053 dB/cm. The term $\frac{\cos^3\theta}{2\sin\theta}$ plays a very crucial role in Eq. (2.53) even for slight changes in propagation angle. Higher order modes suffer more loss due to the scattering generated by the side wall roughness than the fundamental mode. This is due to two reasons: first, the fundamental mode is more optically confined than higher order modes, and second, since it has the largest propagation angle, it experiences less reflection per unit length as it propagates. This is also a confirmation on what was discussed in section 2.6.2.1 regarding modal power distribution in a multimode waveguide (higher order modes experience more scattering loss with a higher rate than lower order modes therefore the lowest order mode loses the least power to radiation and as a result it is the one that survives after all the other modes have lost nearly all of their power).

2.7.2 Optical coupling to silicon waveguides

There are four main sources for coupling loss between a SM fiber and a Si waveguide, namely scattering, reflection, modal mismatch and misalignments (longitudinal, transversal, and tilt).

Figure 2-25 shows a schematic of coupling loss sources between a SM fiber and a Si waveguide. Surface roughness in the junction, for both optical fiber and Si waveguide especially at the end facet of the Si waveguide, generate scattering losses. Thus, the waveguide facets must be well polished, cleaved or etched. Reflections appear at all dielectric interfaces, and are significant especially at the Si waveguide's end facet due to the high refractive index contrast between fiber and silicon. Reflections from the waveguide end face and the fiber facet for one light round trip (during the light coupling from fiber to waveguide) is determined by the refractive indices of the media engaged in coupling from one medium to another, and is described by the Fresnel equations [108]. For a light ray propagating in a medium *i* with refractive index n_i, and reflecting from a medium t with refractive index n_t for the case of normal incidence (Figure 2-23), the reflectance is given by [108]:

$$R = \left(\frac{n_t - n_i}{n_t + n_i}\right)^2 \tag{2.55}$$

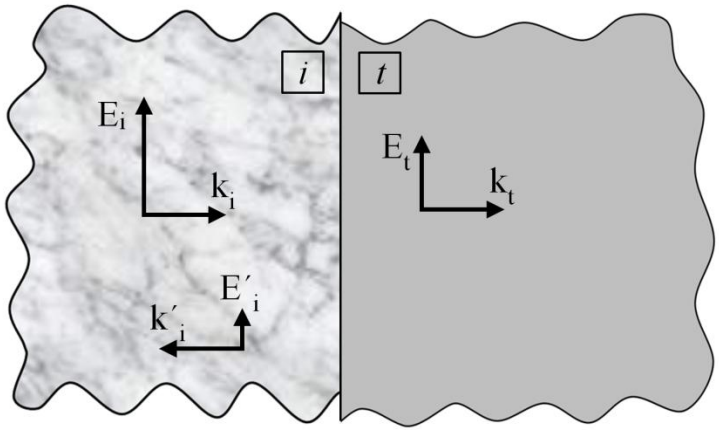

Figure 2-23: Reflection and transmission for the normal incidence case at the interface of mediums *i* and *t*. Wave vectors and their associated electric fields are shown.

The reflection loss caused by the reflection of light at the interface of mediums *i* and *t* is given by

$$\begin{aligned} Reflection\ loss &= 10log_{10}\left(\frac{P_t}{P_i}\right) = 10log_{10}\left(\frac{E_t}{E_i}\right)^2 = 10log_{10}T \\ &= 10log_{10}(1-R) \end{aligned} \tag{2.56}$$

where P_t and P_i are the transmitted and incident powers, and E_t and E_i are the transmitted and incident electric fields respectively. T and R are the transmittance and reflectance and are defined

in section 2.1.1. Therefore for one round trip of light, traveling from fiber to waveguide (air-silicon and air-fiber) the total reflection loss is

$$L_{ref} = -10\left\{log_{10}\left[1-\left(\frac{n_{fiber}-n_{air}}{n_{fiber}+n_{air}}\right)^2\right]+log_{10}\left[1-\left(\frac{n_{si}-n_{air}}{n_{si}+n_{air}}\right)^2\right]\right\} \quad (2.57)$$

Considering n_{fiber}=1.5 and n_{si}=3.5, this leads to 1.8 dB reflection loss for one time reflection between fiber and silicon, however due to the air gap between the waveguide and the fiber, multiple reflections occur.

Coupling coefficient between two Gaussian beams or an incident Gaussian beam and a SM waveguide in the case of longitudinal, transversal, and angular misalignments is given by [91]:

$$\eta = \kappa exp\left[-\kappa\left(\frac{x_0^2}{2}\left({}^1\!/_{w_0^2}+{}^1\!/_{w_1^2}\right)+\frac{\pi^2\theta^2}{2\lambda^2}(w_0^2(z)+w_1^2)-\frac{x_0\theta z}{w_0^2}\right)\right] \quad (2.58)$$

As shown in Figure 2-24, w_0 is the beam waist of the incident beam, w_1 is the beam waist of the SM waveguide, z is the longitudinal distance between the incident beam waist and the SM waveguide end, and and x_0, θ are the lateral and angular misalignments of the fiber axis relative to the waveguide beam axis respectively. The coefficient κ is given by

$$\kappa = \frac{4w_0^2w_1^2}{\left[(w_0^2+w_1^2)^2+\left({}^{\lambda z}\!/_{\pi}\right)^2\right]} \quad (2.59)$$

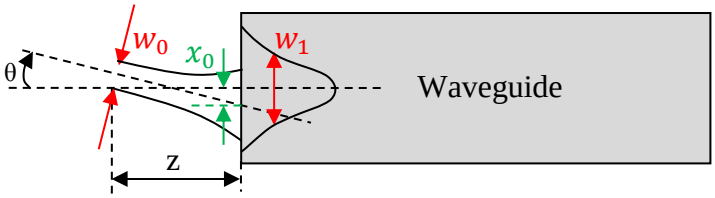

Figure 2-24: Coupling between two Gaussian beams. In this case, the incident beam is the output beam of a SM fiber coupled to the mode of a SM waveguide.

In the case of having multimode waveguide as recipient, the modal power of the incident beam is coupled to different modes of the waveguide with different coupling efficiencies. This case will be studied in next section.

In the beginning of this work, single mode silicon rib waveguides were used to guide the light from the single mode fiber to the sensor, but because of the fabrication complexity this was

avoided and multimode strip waveguides were employed instead. The reason why fabrication of rib waveguides is complex is because two step lithography and etching are required to create rib waveguides, requiring photolithography and etching on a surface with pre-existing high topography (surfaces with high topography are usually called for surfaces having deep trenches, for instance trenches etched in silicon with 10 µm, 20 µm or 100 µm height). Therefore in the following section, only the coupling between a SM fiber and multimode strip waveguides is studied.

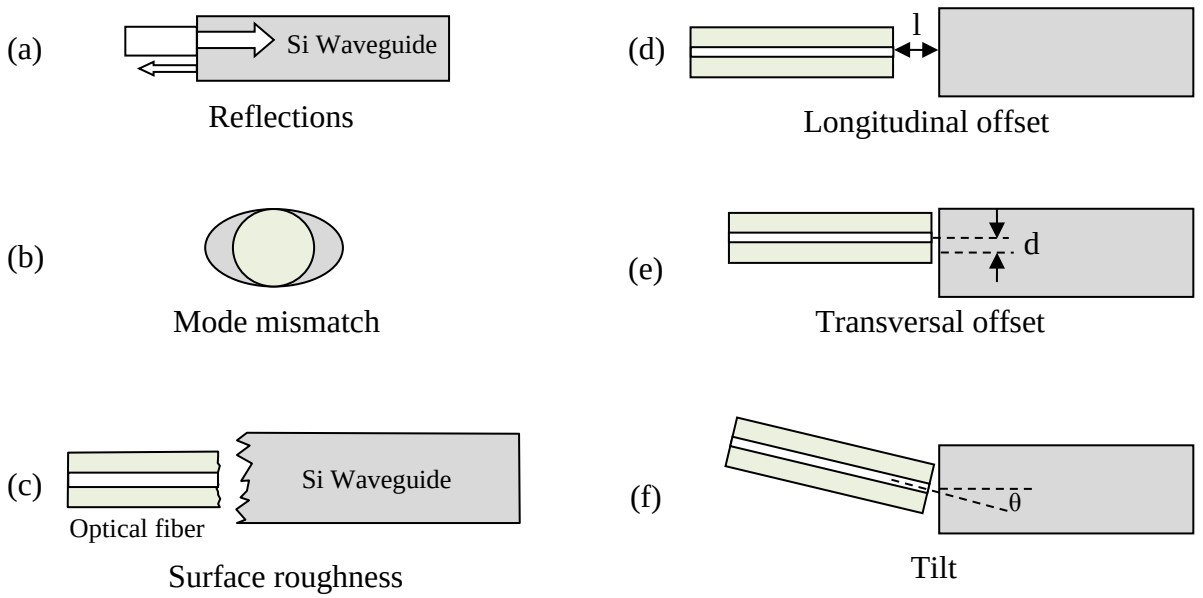

Figure 2-25: Different sources of optical coupling loss from an optical fiber to a Si waveguide: (a) reflection loss caused by reflections between fiber and waveguide facets, (b) mode mismatch between coupled modes, (c) silicon waveguide facet roughness causing scattering loss, (d) loss due to longitudinal offset between fiber and waveguide, (e) loss generated by transversal offset between fiber and waveguide, and (f) loss generated by angular misalignment between fiber and waveguide.

2.7.3 Coupling efficiency between a SMF and a multimode waveguide (MMW)

In order to estimate the optical coupling efficiency between a SMF and a MMW, the electric field function inside a MMW has to be determined. As the BOX layer is partially etched away after

releasing the sensor structure (Figure 4-13) and the refractive index of silicon dioxide is close to air, the refractive index of remaining BOX layer is approximated to have the same refractive index as air and therefore the surrounded medium of the waveguide or cladding is considered to be air. After using Maxwell equations and applying boundary conditions for a rectangular dielectric waveguide with cross dimension of 2a by 2b and waveguide refractive index of n_1 that is surrounded by a medium (air) with refractive index of n_2 (Figure 2-26), the electric field can be calculated as [112],

$$E(x,y,z)=\sum_{p=1}^{M}\sum_{q=1}^{N}A_{pq}u_{pq}(x,y)\exp(-j\beta_{pq}z) \tag{2.60}$$

where A_{pq} is constant, β_{pq} is the propagation constant of the mode pq in the z direction, $u_{pq}(x,y)$ is the transverse electrical field distribution, and M and N are the total number of modes in x and y directions. Transversal electrical field distributions for different regions are specified as following:

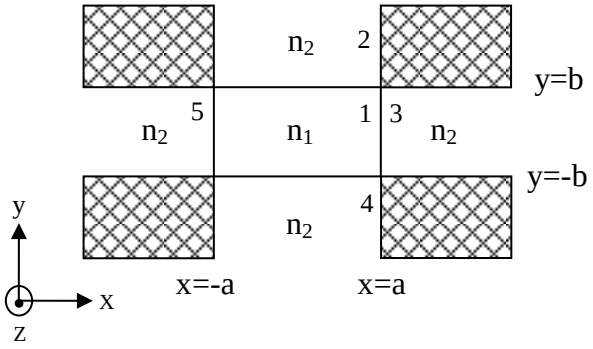

Figure 2-26: Geometry of the rectangular dielectric waveguide

$$u_{pq}(x,y)=\begin{cases} A_1\cos(k_x x+\alpha_1)\cos(k_y y+\alpha_2) & region\ 1\\ A_2\cos(k_x x+\alpha_1)\exp\left(-\gamma_y(y-b)\right) & region\ 2\\ A_3\cos\left(-\gamma_x(x-a)\right)\cos(k_y y+\alpha_2) & region\ 3\\ A_4\cos(k_x x+\alpha_1)\exp\left(\gamma_y(y+b)\right) & region\ 4\\ A_5\exp(\gamma_x(x+a))\cos(k_y y+\alpha_2) & region\ 5 \end{cases} \tag{2.61}$$

where α_1 and α_2 are constant and

$$k_x^2 + k_y^2 + \beta^2 = k_0^2 n_1^2$$

$$k_x^2 - \gamma_y^2 + \beta^2 = k_0^2 n_2^2 \tag{2.62}$$

$$k_y^2 - \gamma_x^2 + \beta^2 = k_0^2 n_2^2$$

$$k_x a = tan^{-1}\left(\frac{n_1^2 \gamma_x}{n_2^2 k_x}\right) + \frac{(p-1)\pi}{2} \qquad p = 1,2,.. \tag{2.63}$$

$$k_y b = tan^{-1}\left(\frac{\gamma_y}{k_y}\right) + \frac{(q-1)\pi}{2} \qquad q = 1,2,\ldots$$

$$\gamma_x^2 = k_0^2(n_1^2 - n_2^2) - k_x^2 \qquad \gamma_y^2 = k_0^2(n_1^2 - n_2^2) - k_y^2 \qquad \beta_{pq}^2 = -\left(k_x^2 + k_y^2\right) - k_0^2 n_1^2$$

For a rectangular waveguide with a large number of modes, the number of modes in each dimension is proportional to $\left(\frac{2d}{\lambda}\right) NA$ [93], where d the length of waveguide in that dimension and NA is is the numerical aperture defined by (2.37). The total number of modes including both TE and TM polarization is given by [93]

$$M \approx \frac{\pi}{2}\left(\frac{2d}{\lambda}\right)^2 NA^2 \tag{2.64}$$

For instance for a rectangular multimode silicon strip waveguide with 12 μm width a wavelength of λ=1.55 μm, NA=3.3, hence the number of modes are 2050. Figure 2-13 shows the optical simulation demonstrating the intensity distribution of the two first TE modes of a multimode SOI strip waveguide simulated by FemSIM.

At z=0 (where the optical fiber is coupled to the waveguide), the electric field of MMW has to match the field of SMF.

The transverse field distribution of a the fundamental mode of a fiber LP_{01} can be approximated by a Gaussian profile as [107], [55]

$E(r,z)= exp(-r^2/w_0^2)exp(-i\beta_0 z)$, at $z=0$ $E(r)= exp(-r^2/w_0^2)$.

where w_0 is the spot size of the Gaussian beam.

The electric field in the cladding can be ignored since all the optical field of MMW is confined in the center of waveguide due to the high index contrast between silicon and air. From (2.60) and (2.61),

$$E(x,y,z)=\sum_{p=1}^{M}\sum_{q=1}^{N}A_{pq}\cos(k_p x+\alpha_1)\cos(k_q y+\alpha_2)e^{-j\beta_{pq}z} \tag{2.65}$$

Applying the matching condition

$$E_{MMW}(x,y,z)|_{z=0}=E_{fiber}(r,z)\big|_{z=0}$$

$$E(x,y,0)=\sum_{p=1}^{M}\sum_{q=1}^{N}A_{pq}\cos(k_p x+\alpha_1)\cos(k_q y+\alpha_2)=e^{-\frac{x^2+y^2}{w_0^2}}$$

Assuming $\alpha_1=\alpha_2=0$

$$A_{pq}=\int_{-\infty}^{+\infty}e^{-x^2/w_0^2}\cos k_p x dx\int_{-\infty}^{+\infty}e^{-y^2/w_0^2}\cos k_q y dy$$

Knowing that

$$\int_{-\infty}^{+\infty}e^{-ax^2}\cos bx dx=\sqrt{\frac{\pi}{a}}e^{-\frac{b^2}{4a}}$$

$$\Rightarrow A_{pq}=\pi w_0^{\,2}\exp\left(-\frac{w_0^{\,2}}{4}(k_p^{\,2}+k_q^{\,2})\right) \tag{2.66}$$

Only symmetrical modes in the MMW are excited due to the boundary condition (the input field (mode of the optical fiber) is a symmetric wave).

Coupling efficiency to pq th mode of MMW is then represented by:

$$\eta_{pq}=\frac{\left|\int_{-\infty}^{+\infty}E(r)\,u_{pq}(x,y)dxdy\right|^2}{\int_0^{+\infty}|E(r)|^2 rdr\int_{-\infty}^{+\infty}|u_{pq}(x,y)|^2 dxdy}$$

$$\eta_{pq} = \frac{\left| \int_{-\infty}^{+\infty} e^{-\frac{x^2+y^2}{w^2{}_0}} \cos(k_p x)\cos(k_q y)dxdy \right|^2}{\int_0^{+\infty} \exp\left(-\frac{2r^2}{w_0{}^2}\right) r dr \int_{-\infty}^{+\infty} \cos^2(k_p x)\cos^2(k_q y)dxdy}$$

The nominator was calculated in above (A_{pq}). Also knowing

$$\int_0^{+\infty} \exp\left(-\frac{2r^2}{w_0{}^2}\right) r dr = \frac{w_0{}^2}{4}$$

$$\int \cos^2(ax)dx = \frac{x}{2} + \frac{\sin 2ax}{4a} \Rightarrow \int_{-a}^{+a} \cos^2(k_i x)dx = a + \frac{\sin 2k_i a}{2k_i}$$

$$\eta_{pq} = \frac{4\pi^2 w_0{}^2 \exp\left(-\frac{w_0{}^2}{2}(k_p{}^2 + k_q{}^2)\right)}{\left(a + \frac{\sin 2k_p a}{2k_p}\right)\left(a + \frac{\sin 2k_q a}{2k_q}\right)} \tag{2.67}$$

where k_p and k_q can be determined from (2.62) and (2.63),

$$k_p a = \tan^{-1}\left(\frac{n_1{}^2}{n_2{}^2} \cdot \frac{\left(k_0{}^2(n_1{}^2 - n_2{}^2) - k_p{}^2\right)^{1/2}}{k_p}\right) + \frac{1}{2}(p-1)\pi$$

$$k_q a = \tan^{-1}\left(\frac{\left(k_0{}^2(n_1{}^2 - n_2{}^2) - k_q{}^2\right)^{1/2}}{k_q}\right) + \frac{1}{2}(q-1)\pi$$

Finally zeros of the derivative of the coupling coefficient with respect to the mode number will determine the peak of the coupling efficiency associated with that specific mode number where the mode has the highest coupling efficiency.

Coupling efficiency between SMF and MMF has been studied by W. S. Mohammed et al. [109]. Figure 2-27 shows the coupling efficiency curve between a SMF and two different MMF with core radii of 52.5 µm and 92.5 µm as a function of mode number.

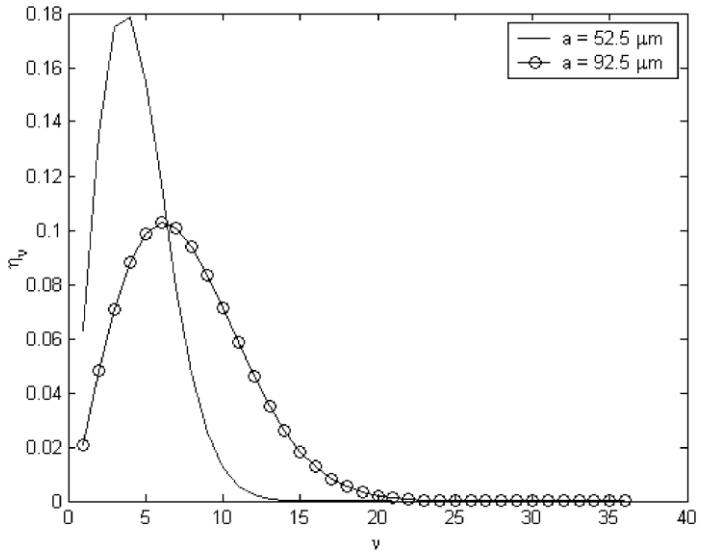

Figure 2-27: Coupling efficiency between a SMF and two different MMF with core radii of 52.5 µm and 92.5 µm as a function of mode number [109].

The radial mode number that has the highest coupling efficiency is different from one fiber to another depending on the fiber core radius. For the MMF with 52.5 µm core radius, 5^{th} mode has the highest coupling efficiency and for the MMF with 92.5 µm, the highest coupling efficiency takes place for mode number 7. In conclusion only few numbers of modes with low orders will get excited in a MMW when it is excited with a SMF. However as described in section 2.6.2.1, this modal power distribution does not remain constant as modes exchange their power with higher order modes due to scattering generated by fabrication imperfections such as side wall roughness. Therefore the number of excited modes in a MMW when light is coupled from a fiber to the waveguide is not constant and changes after light travels in the waveguide.

2.8 Gyroscopes

The working principle of a vibrating gyroscope is based on the Coriolis effect. When a structure moves in a rotating reference frame, it experiences a force, called Coriolis force. This Coriolis force is given by:

$$\overrightarrow{F_C} = -2m\vec{\Omega} \times \vec{v}$$

where m is the mass of the structure, v is the velocity of the moving structure, and Ω is the rotation rate of the rotating reference frame. A vibrating gyroscope consists of a mass suspended by four springs along two perpendicular directions as shown in Figure 2-28.

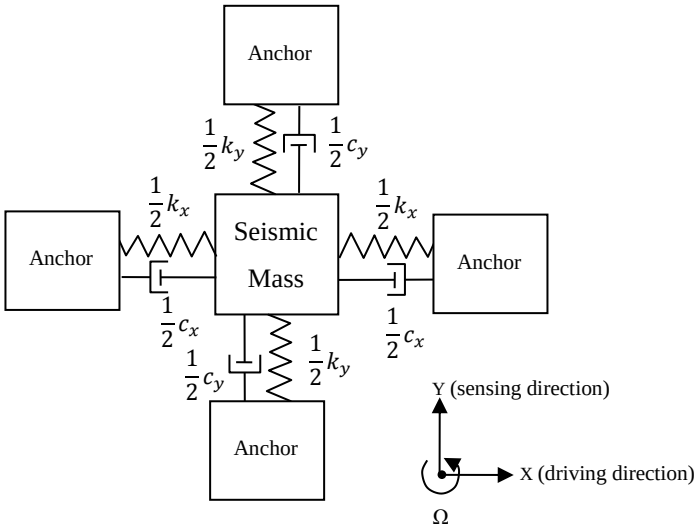

Figure 2-28: Working principle of a MEMS gyroscope

The system is a two dimensional vibration system with two vibration modes, ω_x and ω_y. When the suspended mass m is excited by an electrostatic force (F_D) caused by a comb drive in the x-direction, in the presence of an angular rotation (Ω) in z direction, the mass experiences the Coriolis force in the y-direction:

$$|F_C| = 2m\Omega \times \dot{x} \tag{2.68}$$

where $\dot{x}$ is the velocity of the mass along the driving direction. The electrostatic force is in a sinusoidal format:

$$F_D = F_{0D} \cos \omega_D t \tag{2.69}$$

where F_{0D} is a constant driving force and ω_D is the driving frequency. Considering the system as a damped system, the governing differential equations of the system are:

$$\begin{aligned} m\ddot{x} + c_x\dot{x} + k_x x &= F_D \quad \text{(a)} \\ m\ddot{y} + c_y\dot{y} + k_y y &= F_C \quad \text{(b)} \end{aligned} \tag{2.70}$$

The steady-state solution of the first differential equation as discussed in section 2.3 is,

$$x = Ae^{j(\omega_D t+\varphi_x)} \tag{2.71}$$

where

$$A = \frac{\frac{F_{0D}}{k_x}}{\sqrt{\left(1-\frac{\omega_D^2}{\omega_{0x}^2}\right)^2+\left(2\xi_x\frac{\omega_D}{\omega_{0x}}\right)^2}} \tag{2.72}$$

and

$$\varphi_x = -\tan^{-1}\left(\frac{2\xi_x\frac{\omega_D}{\omega_{0x}}}{1-\frac{\omega_D^2}{\omega_{0x}^2}}\right) \tag{2.73}$$

In which ξ_x is the damping ratio and were previously defined (Eq.(2.27)) and $\omega_{0x} = \sqrt{\frac{k_x}{m}}$.

Eq. (2.71) is the drive mode time-domain response of the system. Figure 2-29 shows the variation in the phase angle φ_x with the frequency ratio $\frac{\omega_D}{\omega_{0x}}$ simulated for several levels of damping. When damping is present, there is a continual change in φ_x as the ratio $\frac{\omega_D}{\omega_{0x}}$ increases. Also, regardless of the amount of damping, $\varphi_x = {}^{\pi}/_{2}$ is found at resonance. $\frac{F_{0D}}{k_x}$ in Eq. (2.72) is the system response (deflection) to a constant DC force of F_{0D}, i.e. the system in AC mode is amplified with the factor of,

$$|H(\omega_D)| = \frac{1}{\sqrt{\left(1-\frac{\omega_D^2}{\omega_{0x}^2}\right)^2+\left(2\xi_x\frac{\omega_D}{\omega_{0x}}\right)^2}} \tag{2.74}$$

In fact $|H(\omega_D)|_{max}$ represents the quality factor of the resonator which is a very important parameter for the characterization of the system. The resonance frequency of the system occurs at,

$$\omega_R = \omega_{0x}\left(1-2{\xi_x}^2\right)^{1/2} \tag{2.75}$$

providing the following quality factor for the resonator in the x-direction,

$$Q_x = |H(\omega_D)|_{max} = \frac{\left(1 - {\xi_x}^2\right)^{-1/2}}{2\xi_x} \tag{2.76}$$

with the phase,

$$\varphi_Q = -\tan^{-1}\left(\sqrt{\frac{1 - 2{\xi_x}^2}{{\xi_x}^2}}\right)^{1/2} \tag{2.77}$$

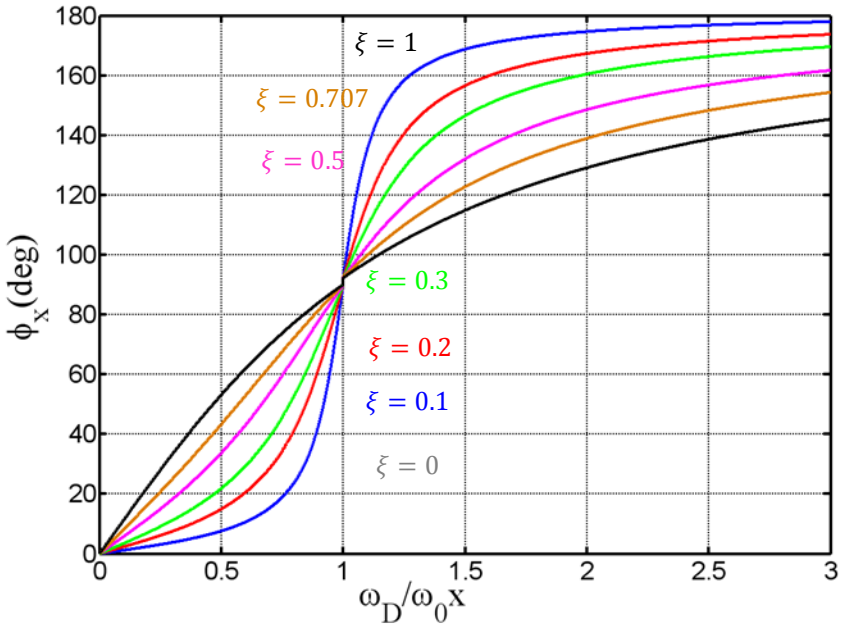

Figure 2-29: Phase angle plotted against the frequency ratio for various levels of damping

According to Eq. (2.75), increasing damping decreases the resonance frequency and therefore the maximum response of the resonator (Figure 2-6) and also the phase difference (Figure 2-29). As we will demonstrate with simulations in section 3.2.1, the system is operating in weak damped region. In drive mode resonance, assumption of weak damping ($\xi_x \ll 1$) leads the assumption of resonance at ω_{0x}.Thus, the quality factor from (2.76) can be estimated as,

$$(Q_x)_{weak\ damping} = \frac{1}{2\xi_x} = \frac{\sqrt{mk_x}}{c_x} \tag{2.78}$$

From (2.72) and (2.74), $A = \frac{F_{0D}}{k_x}|H(\omega_D)| \Rightarrow A_{max} = \frac{F_{0D}}{k_x}|H(\omega_D)|_{max} = \frac{F_{0D}}{k_x}Q_x$.

Hence, the vibration amplitude is,

$$(A_{max})_{weak\ damping} = \frac{F_{0D}}{k_x}(Q_x)_{weak\ damping} = \frac{F_{0D}}{2\xi_x k_x} \tag{2.79}$$

This corresponds to $\omega_D = \omega_{0x}$ in (2.72) i.e., maximum displacement in x diection is achieved when the system is drived with a frequancy equal to its natural frequency in the x direction. This is also clear in Figure 2-6. The phase from (2.77) for weak damping is:

$$\varphi_Q = -\tan^{-1}(\infty) = -\frac{\pi}{2} \tag{2.80}$$

Let's now calculate the magnitude of the Coriolis force. From (2.68):

$$|F_C| = 2m\left|\vec{\Omega} \times \vec{\dot{x}}\right| = 2mA\omega_D\Omega Sin(\omega_D t + \varphi_x) = F_{C_{max}} Sin(\omega_D t + \varphi_x) \tag{2.81}$$

where

$$F_{C_{max}} = 2mA\omega_D\Omega \tag{2.82}$$

Substituting in Eq. (2.70)-b yielding similar answers as (2.71) and (2.72), i.e.

$$Y = B\ e^{j(\omega_D t + \varphi_y)} \tag{2.83}$$

where

$$B = \frac{\frac{F_{C_{max}}}{k_y}}{\sqrt{\left(1 - \frac{\omega_D^2}{\omega_{0y}^2}\right)^2 + \left(2\xi_y \frac{\omega_D}{\omega_{0y}}\right)^2}} \tag{2.84}$$

is the sense mode amplitude and

$$\omega_{0y}^2 = \frac{k_y}{m}\ \ and\ \xi_y = \frac{c_y}{2m\omega_{0y}} \xRightarrow{weak\ damping} = \frac{1}{2Q_y}$$

Eq. (2.84) represents the sensor response that exhibits the sensor sensitivity. Substituting $F_{C_{max}}$ from (2.82):

$$B = \frac{\frac{2mA\omega_D\Omega}{k_y}}{\sqrt{\left(1-\frac{\omega_D^2}{\omega_{0y}^2}\right)^2+\left(\frac{\omega_D}{Q_y\omega_{0y}}\right)^2}} \tag{2.85}$$

Assuming that the structure will be drive with its natural frequency in x direction ($\omega_D = \omega_{0x}$) to get the maximum displacement (as discussed in (2.79)). Together with the weak damping assumption and recalling: $\omega_{0y}^2 = \frac{k_y}{m}$, the sense mode amplitude becomes,

$$B = \frac{2A\omega_{0x}\Omega}{\omega_{0y}^2}\cdot\frac{1}{\sqrt{\left(1-\frac{\omega_{0x}^2}{\omega_{0y}^2}\right)^2+\left(\frac{\omega_{0x}}{Q_y\omega_{0y}}\right)^2}} \tag{2.86}$$

The gyroscope displacement sensitivity (DS_g) is defined as the sensing vibration amplitude of the proof mass in response to unit angular velocity. It is therefore expressed as,

$$DS_g = \frac{dB}{d\Omega} == \frac{2A\omega_{0x}}{\omega_{0y}^2}\cdot\frac{1}{\sqrt{\left(1-\frac{\omega_{0x}^2}{\omega_{0y}^2}\right)^2+\left(\frac{\omega_{0x}}{Q_y\omega_{0y}}\right)^2}} \tag{2.87}$$

Equation (2.87) can be expressed in a normalized way as:

$$DS_{ng} = \frac{\omega_{0y}}{2A}DS_g = \frac{\frac{\omega_{0x}}{\omega_{0y}}}{\sqrt{\left(1-\frac{\omega_{0x}^2}{\omega_{0y}^2}\right)^2+\left(\frac{\omega_{0x}}{Q_y\omega_{0y}}\right)^2}}$$

or

$$DS_{ng} = \frac{\frac{\omega_{0x}}{\omega_{0y}}}{\sqrt{\left(1-\left(\frac{\omega_{0x}}{\omega_{0y}}\right)^2\right)^2+\frac{1}{{Q_y}^2}\left(\frac{\omega_{0x}}{\omega_{0y}}\right)^2}} \tag{2.88}$$

where, $DS_{ng}$is normalized displacement sensitivity. The gyroscope displacement sensitivity is then expressed as

$$DS_g = \frac{2A}{\omega_{0y}} DS_{ng} \tag{2.89}$$

Figure 2-30 shows the variation of the normalized displacement sensitivity versus $\frac{\omega_{0x}}{\omega_{0y}}$ for different values of Q_y. The maximum of normalized displacement sensitivity occurs at $\omega_{0x} = \omega_{0y}$. This is called matching condition where the sensor is mechanically designed symmetrically so that $\omega_{0x} = \omega_{0y}$ [110], [111]. As seen from Figure 2-30, as the quality factor in y direction increases, the peak gets narrower, leading to higher displacement sensitivity.

Equation (2.89) in the case of matching condition is simplified to:

$$DS_g = \frac{2AQ_y}{\omega_{0y}} \tag{2.90}$$

Higher displacements for both VOA-based and FP-based sensors corresponds to higher sensitivity for the sensors, as for the VOA-based more input signal gets modulated and for the FP-based, the FP gap changes more, leading to larger shift in the wavelength at the output (Eqs. (2.14) and (2.21)). According to (2.88) and (2.89), to attain a highly sensitive rate sensor, it is necessary to have a high quality factor, high amplitude of vibration, and matching between resonance frequencies of the driving mode and the sensing mode.

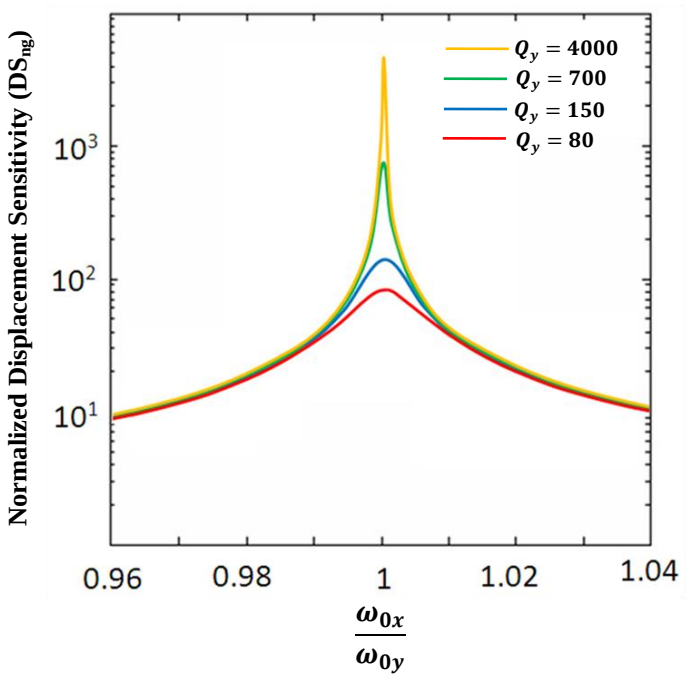

Figure 2-30: Normalized displacement sensitivity of the gyroscope versus ω_{0x}/ω_{0y} for different values of Q_y

2.9 Conclusions

Theory of FP-based and VOA-based devices (accelerometers and gyroscopes) was studied. When a FP-based device is actuated (by either applied acceleration or angular frequency), the FP resonance wavelength is modulated as a result. The FP microcavity consists of two distributed Bragg reflectors (DBR), in which one DBR mirror is attached to the proof mass of the system. As a consequence of acceleration/rotation, the relative displacement of the movable mirror with respect to the fixed mirror changes the cavity length (or gap) and modifies the FP resonance. Device has a linear response (linear shift in the FP resonance wavelength) to both applied accelerations and angular frequencies. Device can be tuned over its FSR which is inversely proportional to the cavity length. The tuning range increases not only by using small gap but also with the spectral width of the mirrors. The spectral width of the Bragg mirrors depends on the order of the Bragg mirrors. The lower the order of the Bragg mirror (thinner silicon/air layer) is, the larger the bandwidth . As a result, the dynamic range of the sensor increases by decreasing the FP gap and the width of Bragg mirror's walls. The sensitivity of the sensor is proportional to the finesse of FP resonance peak and inversely proportional to the mechanical resonance frequency. In other words, the sensor requires low resonant frequencies (larger mass and softer springs) and high finesse to attain high sensitivity. However using low resonant frequencies will reduce the frequency bandwidth of the sensor. Sensor has the potential to achieve μg resolutions.

The VOA-based device is a MEMS variable optical attenuator (VOA)-based sensor. A Bragg mirror that is attached to the sensor proof mass is positioned in the middle of the gap of two multimode waveguides: transmitting (input) and receiving (output) waveguides. When the device is actuated by the applied acceleration, the intensity of the transmitted light to the output waveguide is modulated by the displacement of the Bragg mirror. The modal power distribution in a multimode waveguide was studied in this chapter. As light travels in a multimode waveguide (due to the presence of side wall roughness) high order guided modes exchange power continuously between each other faster than low order modes. As a result, higher order modes radiate from the waveguide core into the cladding leading to scattering loss for the waveguide. A model called stationary power distribution was verified (by reviewing the state-of-the-art) and used to model the modal power distribution in the multimode waveguide. According to this model, the power distribution in a waveguide after travelling distances longer than the correlation

length of waveguide (measured from sidewall roughness) reaches a stationary state where all guided modes couple to radiation modes except the lowest order mode (fundamental mode) that loses the least power and survives. Applying this model to the VOA-based sensor, device sensitivity depends not only on the resonance frequency but also the lateral fundamental mode size in the waveguide at the VOA sensing junction. A low resonance frequency and small lateral mode will result in a better sensitivity for the sensor. Sensor shows linear response for small displacements around the waveguide optical axis. The required displacement range to attain linear response depends on the intensity profile of the fundamental mode which is directly related to the width of the waveguide at the VOA sensing junction.

Regarding the gyroscopes, when the proof mass of the sensor is driven along the x-axis in the presence of an applied angular rotation which is perpendicular to the sensor plane (z-axis), a Coriolis force induces, causing the proof mass and the attached VOA/FP movable mirror to displace along the y-axis, modulating the VOA actuator/FP gap and the resultant transmitted optical signal/wavelength respectively. Higher displacements for both VOA-based and FP-based sensors correspond to higher sensitivity for the sensors. In order to attain a highly sensitive rate sensor, it is necessary to have a high quality factor, high amplitude of vibration, and matching between resonance frequencies of the driving mode and the sensing mode.

CHAPTER 3 SYSTEM DESIGN AND SIMULATIONS

In this chapter, the design details of the fabricated accelerometers and gyroscopes including architect model of the structures, flexion designs and simulations, mode shapes, and resonance frequencies are presented.

3.1 FP-based optical accelerometer

Figure 3-1 shows the schematic of the FP-based optical accelerometer. Device is based on an in-plane FP with two distributed Bragg reflectors (DBR) mirrors utilizing strip silicon waveguides, in which one DBR mirror is attached to two suspended proof masses. As a consequence of

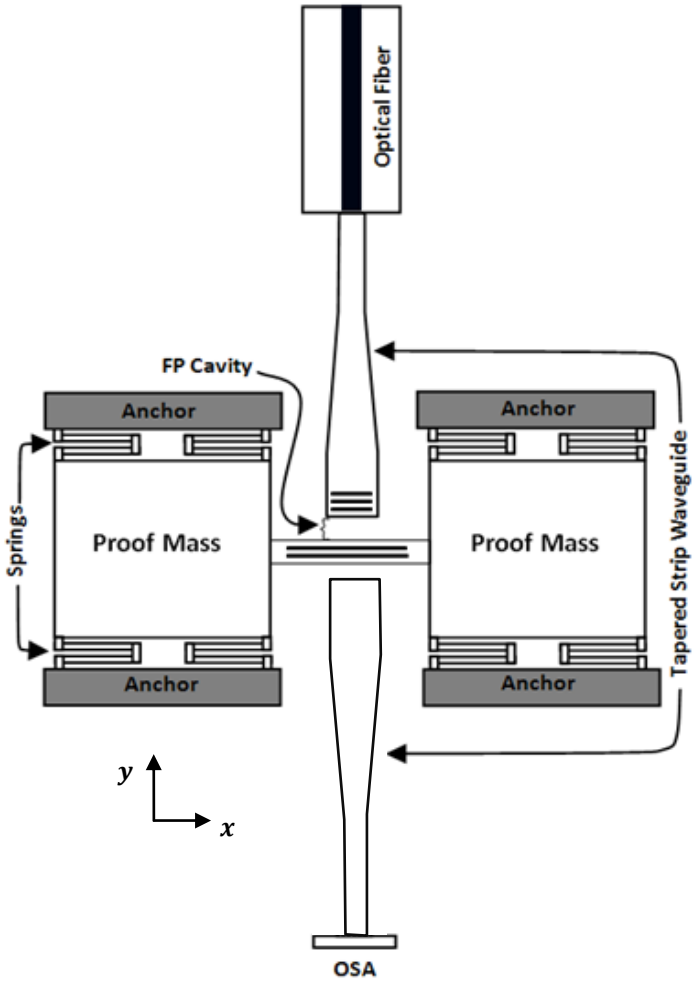

Figure 3-1: Schematic of the optical accelerometer based on FP filter

acceleration, the relative displacement of the movable mirror with respect to the fixed one changes the cavity length and modifies the Fabry-Perot resonance. The accelerometer is symmetrical and consists of two proof masses suspended by eight serpentine flexures beams. Although fixed-fixed springs can also be used at the sides of proof masses but that will make the size of sensor larger in the x direction. In addition, the proof masses will be only anchored from their sides not center where in the case of using serpentine flexures beams, the proof mass is also anchored from the center, leading to more stability for the sensor and therefore less bending in the z direction (lower z-axis cross sensitivity both translational and rotational). Finite element method (using Coventor Ware 2010) is used to model the mechanical behavior of the device as shown in Figure 3-2. The mechanical responses of sensor are also analyzed theoretically and will be discussed later. As shown in Figure 3-2, serpentine flexure beam consists of two span beams and three connector beams. As discussed in section 2.5.3, the mechanical sensitivity of the device depends on the natural resonance frequency of the device. Table 3-1 lists some of considered dimensions for serpentine beams components and their overall simulated stiffness. The thickness of SOI wafer used to fabricate the device is 30 µm.

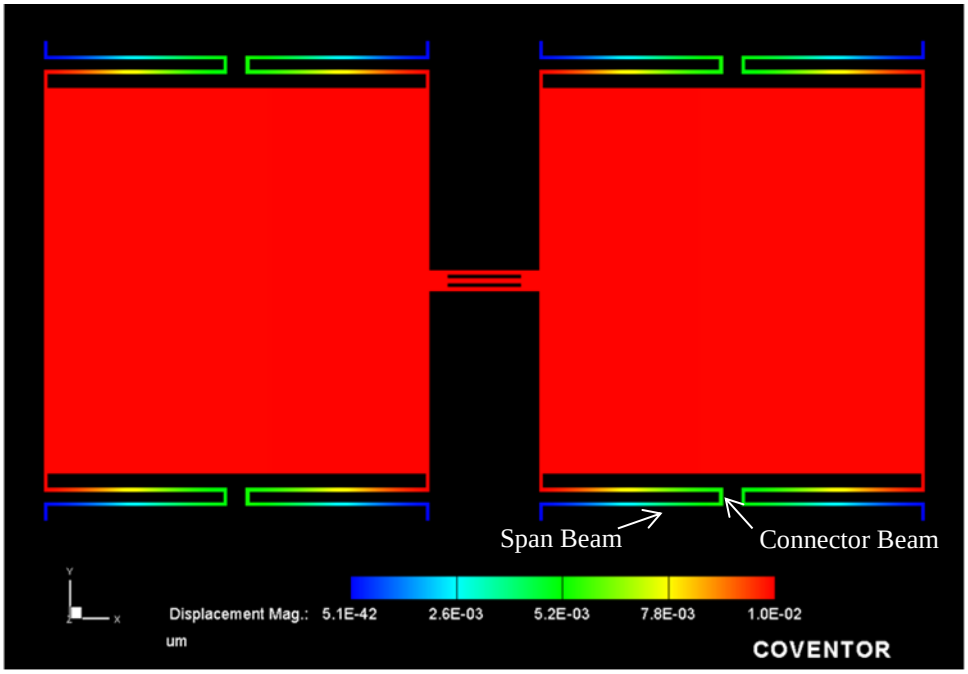

Figure 3-2: Finite element simulation of the optical accelerometer structure containing eight serpentine flexures beams. The red region is proof mass of the sensor.

Accelerations parallel to the wafer plane and perpendicular to the DBR mirrors force the proof masses to move in the wafer plane. The static response of such a suspended mass in y direction is defined by Eq. (2.21),

$$a_y = -\frac{k_y}{M} = -\omega_{ny}^2 \Delta y$$

where Δy is the sensor displacement in y-direction, M is the total mass, k_y is the device spring stiffness in y-direction, and $\omega_{ny}$is the angular natural frequency of the system in the y-direction.

Using basic beam theory, the spring constant of a fixed-end beam with the length of l, width of w and thickness of t are given by:

$$k_y = \frac{Etw^3}{l^3} \tag{3.1}$$

$$k_x = \frac{2Etw}{l} \tag{3.2}$$

$$k_z = \frac{Ewt^3}{l^3} \tag{3.3}$$

where E is the Young's modulus (~ 150 GPa for silicon).

Table 3-1: Serpentine beams components dimensions and the overall simulated stiffness.

Thickness (µm)	Span beam length (µm)	Span beam width (µm)	Connector beam length (µm)	Connector beam width (µm)	Overall spring constant (N/m)
30	152	2	10	2	20
	198	2	10	2	7.6
	248	2	10	2	4
	470	3	10	10	6.1
	500	3	15	15	5.5

The two proof masses have 8.1×10^{-7} kg mass in total. The considered dimensions for each serpentine flexures beam component are as follows:

Span beam length: 470 µm

Span beam width: 3 µm

Connector beam width=connector beam length= 10 µm

Since the width of the connector beams are much larger than the width of the span beams, we can consider a serpentine flexure beam as a serial of two fixed-end beams. The effective spring constant k_s k_s of two springs that are connected in series is then given by:

$$\frac{1}{k_s}=\frac{1}{k_1}+\frac{1}{k_2}=\frac{2}{k_i}\ \Rightarrow\ k_s=\frac{k_1}{2}=\frac{Etw^3}{2l^3}=0.62\ N/m \tag{3.4}$$

where k_1, k_2 k_1 k_2 are the spring constant of two fixed-end beams which are equal in this case. Since the device consist of eight serpentine springs in parallel the total effective spring constant of the device is,

$$K_{tot}=8k_s=4.8\ N/m \tag{3.5}$$

The spring constant of the device simulated by Finite Element Modeling using Coventorware 2010 found to be K=6.125 N/m. The difference between theory and simulation originates from the estimation (considering a serpentine flexure beam as a serial of two fixed-end beams) we have made for the serpentine spring.

The main challenge in designing accelerometers is the manufacturing of a sensor which is sensitive to acceleration in the desired direction but insensitive to all other cross-axis directions. Cross-sensitivity of the device is investigated using modes analysis. Figure 3-3 shows the first four possible modes of the structure. Thanks to the optical characteristics, the sensor is insensitive to excitations that result in parallel motion of the Bragg mirrors (modes 2 and 4) since the length of the FP microcavity remains unchanged. However it is sensitive to the angular or trunnion deflection (mode 3) since the optical path of light in the FP microcavity changes in this case (Figure 3-4.b). Although under the excitation of the resonant trunnion mode, no wavelength shift is generated, the transmitted power through the device at the resonant wavelength is modulated due to the finesse reduction of the microcavity caused from parallelism deviation.

Since the frequency of this mode is well above the sensor working bandwidth, it can be suppressed over the sensing bandwidth. Figure 3-5 presents the simulated frequency response of the system to a constant acceleration for normal and trunnion modes.

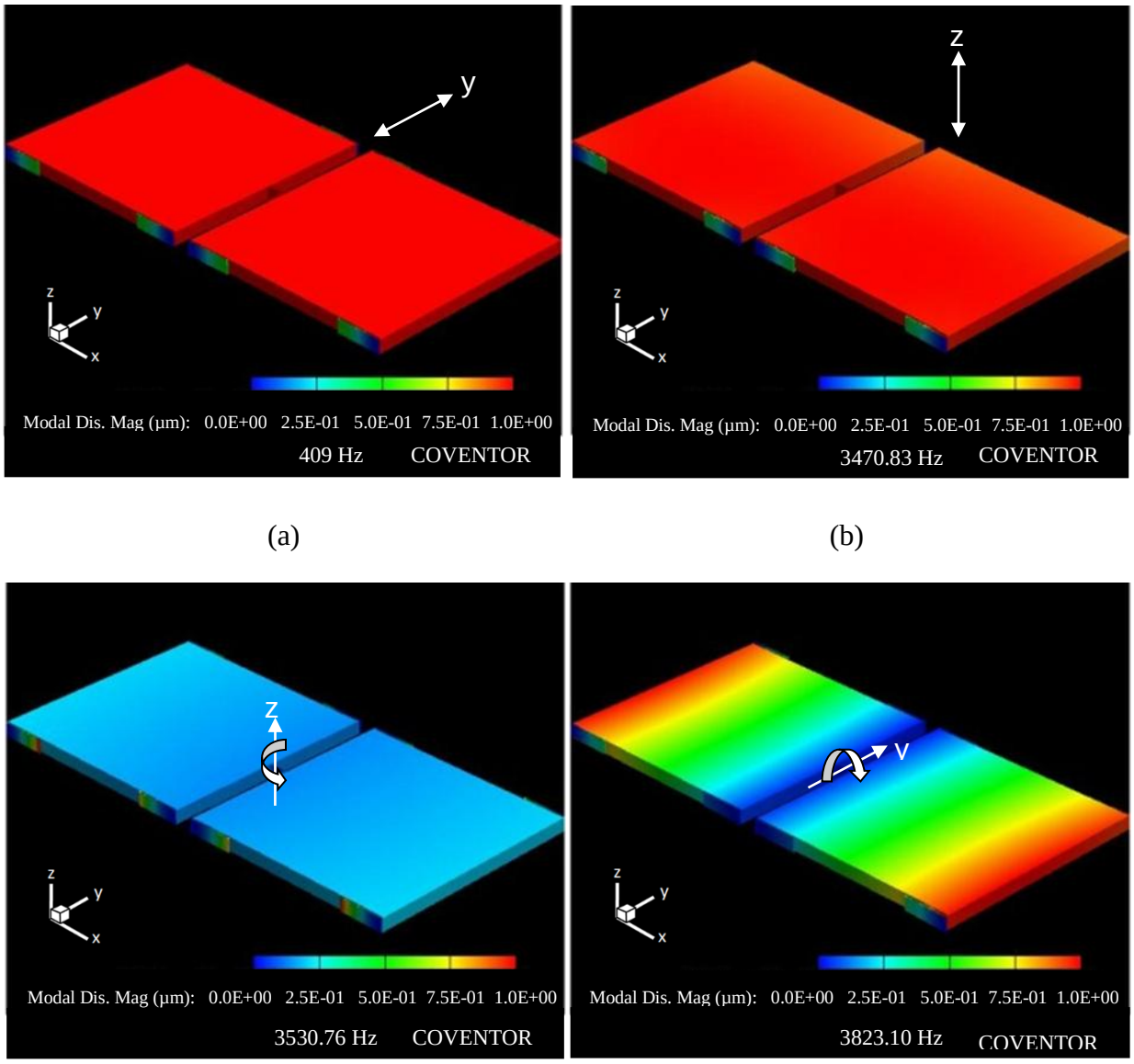

(a) (b)

(c) (d)

Figure 3-3: Simulated first four modes of the device: a) Normal mode (excited at 409 Hz), b) Second mode (excited at 3.48 kHz), c) third mode or trunnion mode (excited at 3.53 kHz), and d) Forth mode (excited at 3.82 kHz). The arrows in the pictures show the displacement (or rotation) for each mode.

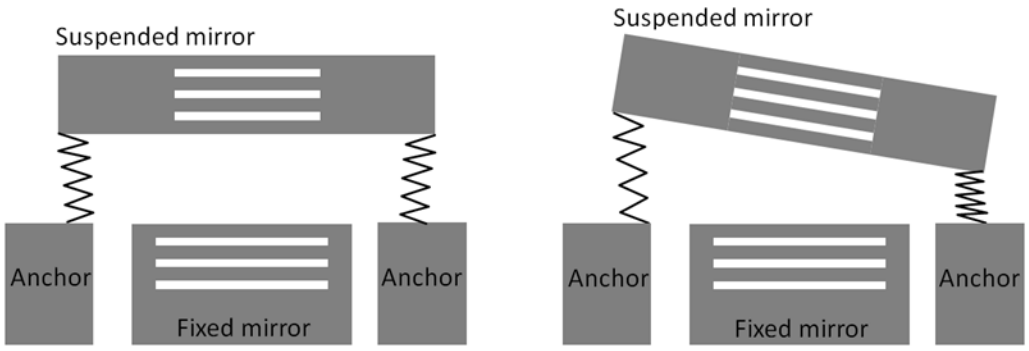

(a) Normal mode (b) Trunnion mode

Figure 3-4: Two expected sensitive modes for the sensor.

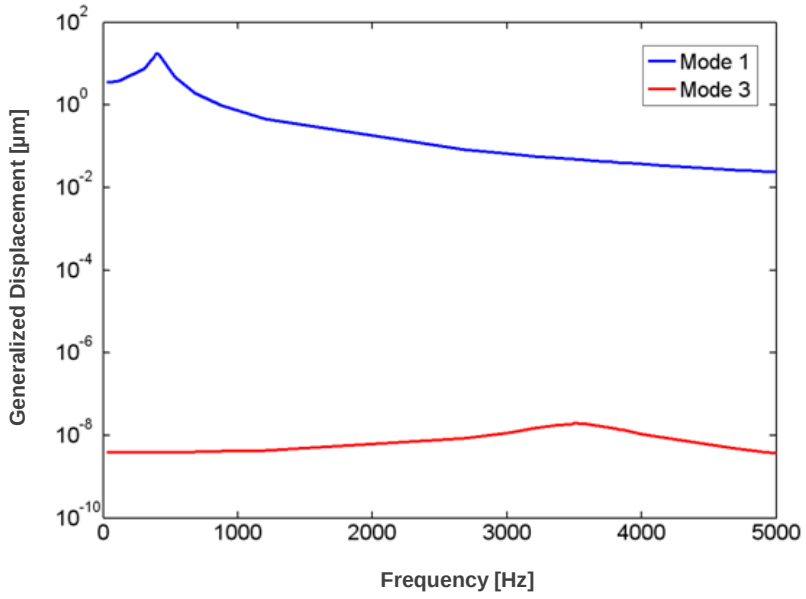

Figure 3-5: Simulated frequency response of the system to a constant acceleration for the normal and trunnion modes.

3.2 VOA-based optical accelerometer

Figure 3-6 shows the schematic of the proposed VOA-based optical accelerometer. Light is launched from a single mode optical fiber through an integrated SOI U-groove to a multimode SOI strip waveguide and then is split by a T-bar waveguide splitter into two arms: sensing arm and reference arm. The light emitted from the sensing arm hits a movable Bragg mirror, which is attached to the sensor proof mass that is suspended by springs (span beams). The position of the

mirror edge is designed to be at the center of the waveguide when no acceleration is applied. A similar mirror is placed in the reference arm at the same position as the other mirror in order to have similar optical length. This second mirror is fixed and used as a reference so the reference signal does not change with the applied acceleration. It is used to compensate the measurements for any variation in the optical source signal and any temperature effect. The displacement of the Bragg mirror relative to the nominal signal detected by the reference in the presence of an inertial load modulates the coupled optical intensity from the transmitting multimode waveguide (input waveguide) to the receiving multimode waveguide (output waveguide). Finally the output power is detected and the magnitude of the applied acceleration is measured.

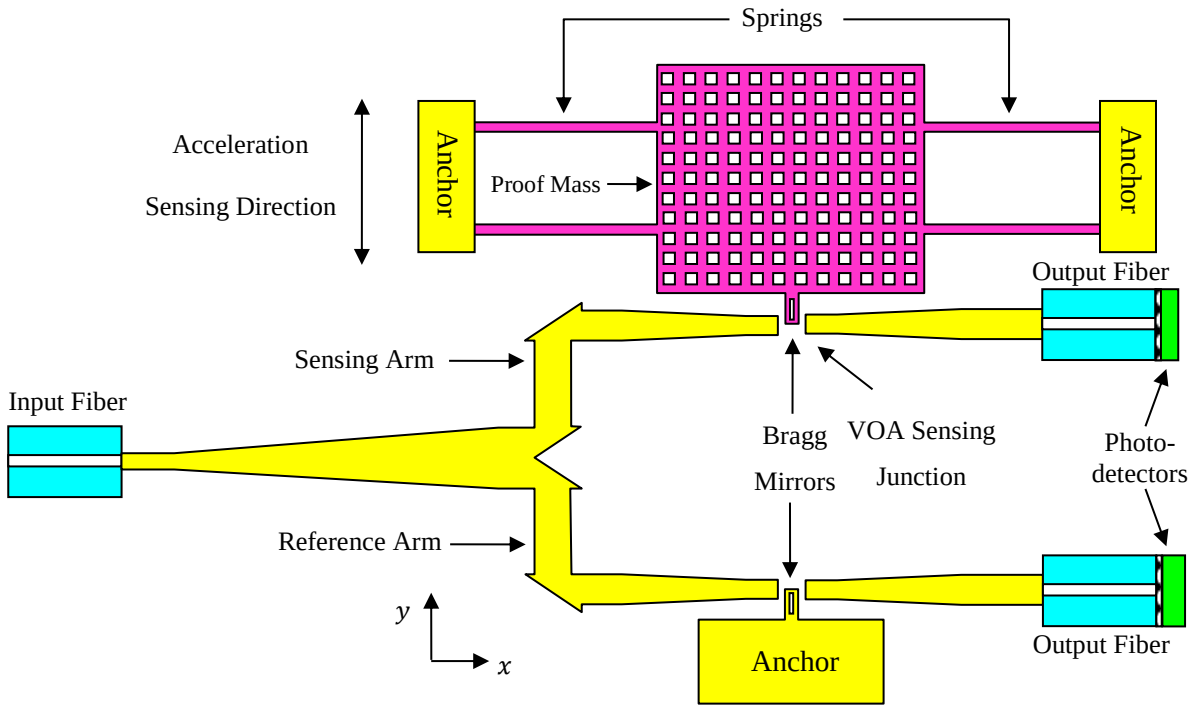

Figure 3-6: Schematic of the optical accelerometer based on VOA.

The overall spring's constant of a structure with N span beams is given by (Eq. (3.1)),

$$k_y = \frac{NEtw^3}{l^3} \tag{3.6}$$

where E is the Young's modulus, and l, w, t are the length, width, and thickness of the beam.

Span beams with different sizes were simulated using Finite element method (Coventorware).

Table 3-2 lists some of the results. Typical applied accelerations to satellite in space are of the order of gravity, therefore the MEMS architecture has to be designed such that the proof mass can moves in micrometer scales when accelerations in the order of gravity are applied to the sensor. Maximum moving mass (proof mass) displacement caused by maximum applied acceleration (gravity) can be calculated from the Hook's law:

$$F_y = Ma_y = k_y y \Rightarrow F_{y_{max}} = Mg = k_y y_{max} \Rightarrow y_{max} = \frac{Mg}{k_y} \tag{3.7}$$

where *M* is the mass of the proof mass. Substituting (3.6) into (3.7),

$$y_{max} = \frac{\rho_{si} l_p w_p l_b^3}{N E w_b^3} . g \tag{3.8}$$

where ρ_{si}, l_p, w_p, l_b, and w_b are representing the silicon density, proof mass length, proof mass width, beam length, and beam width respectively. In fact y_{max}/g represents the displacement sensitivity of the sensor. Note that the displacement is independent of the device thickness as long as the sensor proof mass has the same thickness as the springs. According to (3.6), in order to achieve soft springs, beams have to be long and narrow. However beams sizes are restricted by the fabrication limitations such as lithography resolution.

As expected, from Eq. (3.7) the displacement sensitivity increases by using large proof mass or soft springs (low resonance frequencies). The maximum MEMS displacement of a sensor with a proof mass of 1000 µm×1000 µm for different device thicknesses (SOI thickness) were simulated and are given in Table 3-2. The overall spring constant has to be small enough so that the proof mass can displace few micrometers to be able to block partially (or completely) the light at the VOA sensing junction arm when forces of the order of proof mass weight are applied to the system. The required amount of displacement that can significantly modulate the signal also depends on the lateral supported mode size in the waveguide at the VOA junction arm, which is directly related to the width of the waveguide. In other words, the sensor sensitivity not only increases with displacement, it is also inversely proportional to the waveguide width at the VOA sensing junction. Depending on the MEMS design, an appropriate width for the waveguides at the VOA sensing junction has to be chosen in order to effectively modulate the signal at the device output. For instance for a 75 µm thick device with a proof mass of 1000 µm×1000 µm and

four span beams of 1000 µm×2 µm (last row in Table 3-2), the maximum displacement due to gravity is 2.2 µm, representing 2.2 µm/g displacement sensitivity for the sensor.

Table 3-2: Span beams dimensions and the overall simulated stiffness. The maximum MEMS displacement for a proof mass with dimensions of 1000 µm×1000 µm is also given.

Thickness (µm)	Number of Beams	Beam Length (µm)	Beam Width (µm)	Overall Spring Constant (N/m)	Max. Mass Disp. (displacement per gravity in µm)
30	4	1100	5	1.9	0.37
	4	800	3	1.2	0.58
	4	1320	5	1.1	0.63
	4	1000	3	0.56	1.25
	4	1200	3	0.5	1.4
47	6	400	2	7	0.16
	6	600	2	3	0.4
	4	400	2	5	0.22
75	4	1000	3	1.6	1.1
	4	800	2	1.2	1.5
	4	1000	2	0.8	2.2

3.2.1 Damping

Any accelerometer is a resonant structure and needs to be damped in order to increase its useful operational frequency bandwidth (refer to section 2.3) and also diminish the risk of breakage. Proof mass immerged in a gas or a liquid can result in a linear response over a wide frequency range. The viscosity of the damping fluid and the thickness of the damping layer determine the

damping characteristics. Three types of damping, squeezed-film translational damping, slide-film damping, and squeezed-film rotational damping were illustrated in section 2.3 (Figure 2-7). In this section some of the simulation results are discussed.

Squeeze film theory is based on the fact that for fluid films, the damping force is proportional to the velocity of the displacement $\boldsymbol{F}=c\boldsymbol{v}$ where c is the damping coefficient. Bold characters and those shown with a bar will be representing complex quantities. On the other hand, a squeezed film fluid also has a spring effect: $\boldsymbol{F}=c\boldsymbol{v}+k\boldsymbol{x}$ where k is the spring constant. By analyzing this system in the sinusoidal steady state, i.e. assuming:

$\boldsymbol{F}=\bar{F}e^{j\omega t}$, $\boldsymbol{x}=\bar{x}e^{j\omega t}$ => $\boldsymbol{v}=j\omega\bar{x}e^{j\omega t}$ => $\bar{F}=j\omega c\bar{x}+k\bar{x}$.

Therefore damping (also called viscous damping) and spring forces are the imaginary and real parts of $\bar{F}$ respectively. The damping coefficient is a function of frequency extracted from the imaginary part of $\bar{F}$.

Finite element method is used to simulate the damping response of the structure. A mass with the dimensions of 1000 µm×1000 µm ×550 µm is considered as the damping proof mass of the accelerometer for the simulations. The gas is air with viscosity of 1.86×10^{-5} kg/m s. Figure 3-7 shows the simulated response of squeezed-film translational damping for two different gaps of 150 µm and 20 µm. The damping peak occurs at 36 MHz for 150 µm gap. The spring force rises rapidly. The air captured in the cavity is squeezed (like gas compressed by a piston in a cylinder). As at low frequencies there is no closed cavity, air can run away with little resistance and the force is small. At high frequencies (here above 36 MHz) air is imprisoned as there is not enough time for the air to flee out of the way as the structure oscillates. The air compresses, resulting in a spring force. As the damping force is caused by viscous stresses, if the gas compresses and does not move too much, the damping force decreases. Imagine a gas compressed by a piston in a cylinder. If there is no way for the air to escape in the cylinder when the piston is pushed down, the air gets compressed and only thing you feel is a spring force resisting with your pushing force. The system cannot be damped in this way as there is no viscous stress. This explains why the damping force gets weaker as the frequency increases above 36MHz. This behavior is only applicable for gases; liquids behave in a different way because they are practically incompressible. Reducing the gap (Figure 3-7(d)) increases the damping (compare to Figure 3 7(c)) as predicted in Eq. (2.28). Figure 3-8 (a) shows the damping coefficient as a function of frequency for the case of slide-film damping for gap=100 µm, and Figure 3-8 (b) shows the

squeezed-film rotational damping simulation results for gap=20 μm. For the slide-film damping, the damping coefficient increases all the way up and rises rapidly above 1 MHz. Squeezed-film rotational damping is significant at high frequencies which is very far from the operational frequency of the sensor and therefore can be ignored at low frequencies. From Eq. (2.28), gases with higher viscosity provide more damping for the sensor. Different gases are considered in the squeezed film damping simulations in order to understand the amount of effect of viscosity on the damping. Table 3-3 compares the results. As more viscous gas is used, the damping force frequency peak shifts towards lower frequencies. This is due to the fact that the more viscous the fluid is, the lower frequency is needed to give enough time to the fluid to escape. Again as explained above, the damping force is caused by the viscous stresses. If the frequency is not low enough to give enough time to the gas to escape, the damping force will be small.

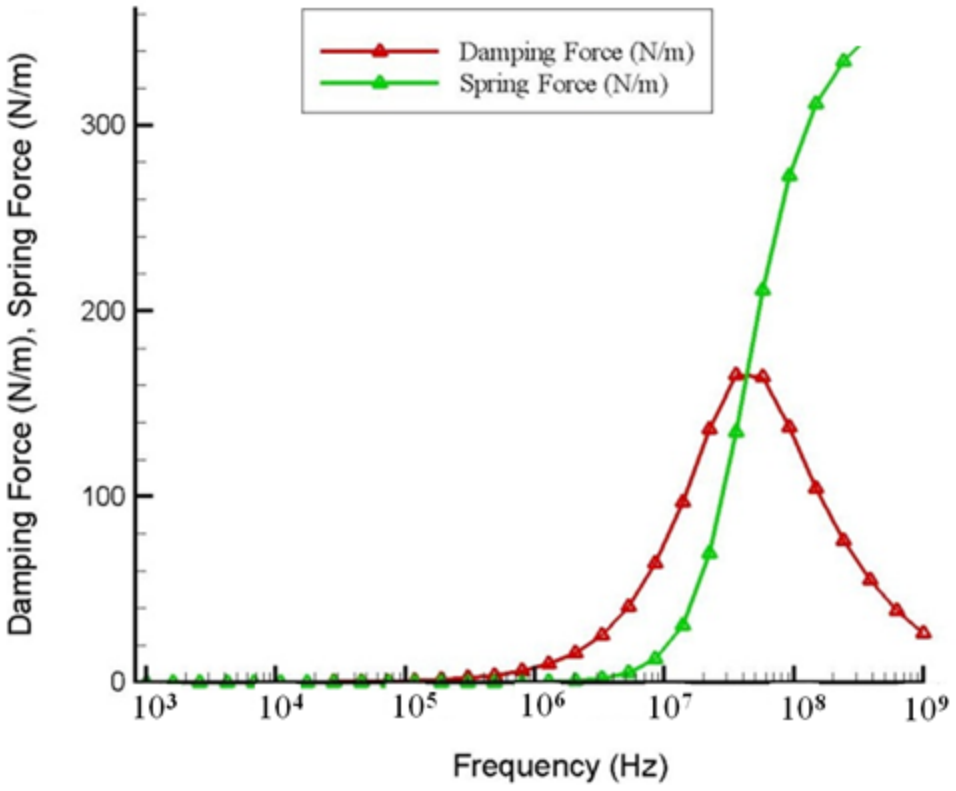

(a) Damping force and spring force versus frequency for gap=150 μm.

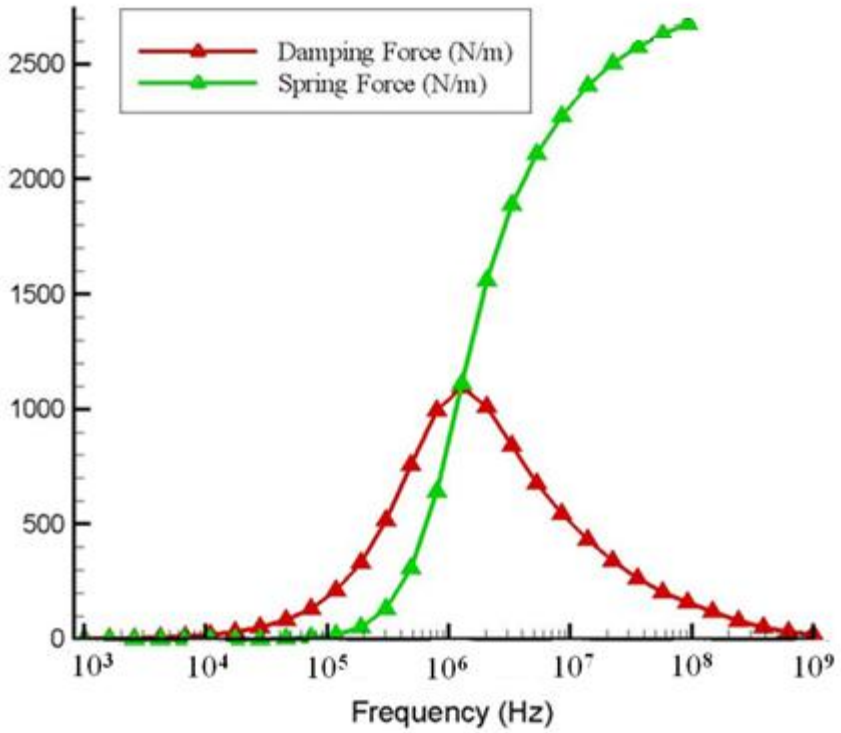

(b) Damping force and spring force versus frequency for gap=20 µm.

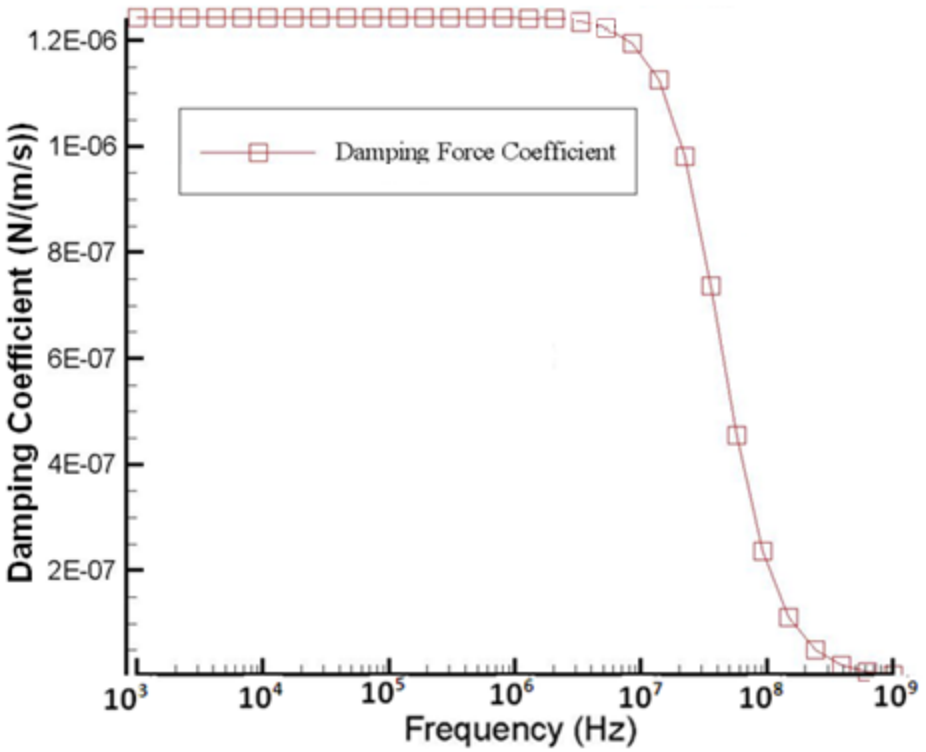

(c) Damping coefficient versus frequency for gap=150 µm.

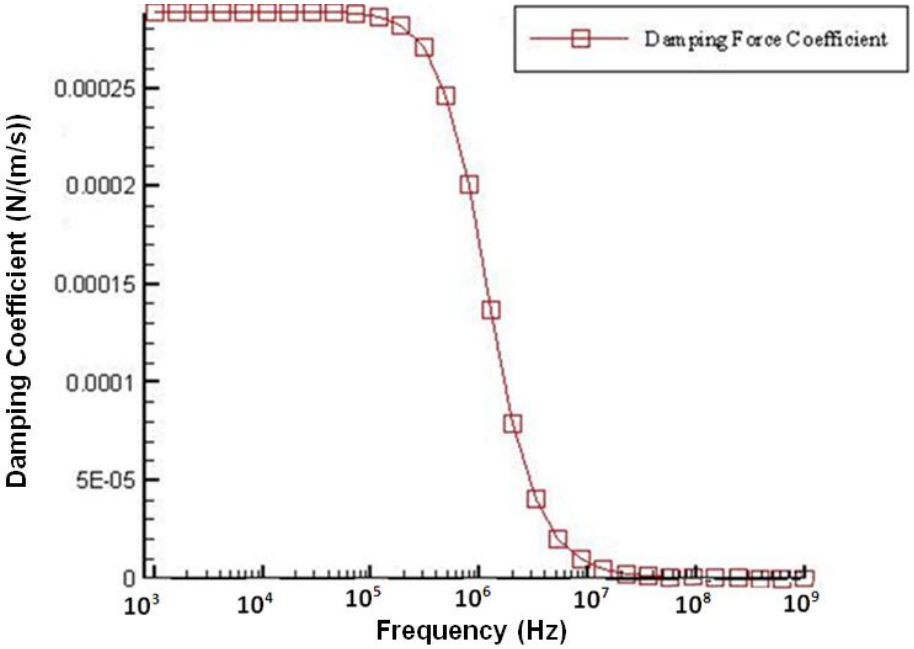

(d) Damping coefficient versus frequency for gap=20 µm.

Figure 3-7: Simulated damping force, spring force, and damping coefficient of squeezed-film translational damping as a function of frequency for two different gaps: (a), (c) 150 µm and (b), (d) 20 µm, gas: air.

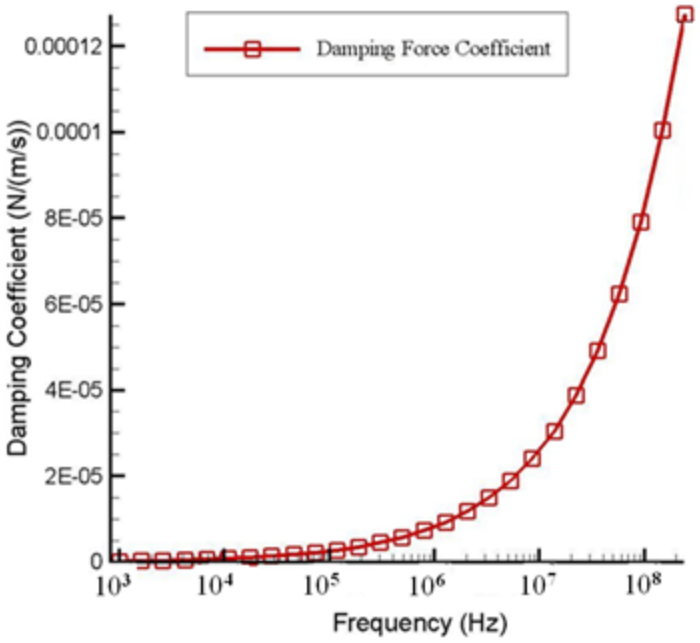

(a)

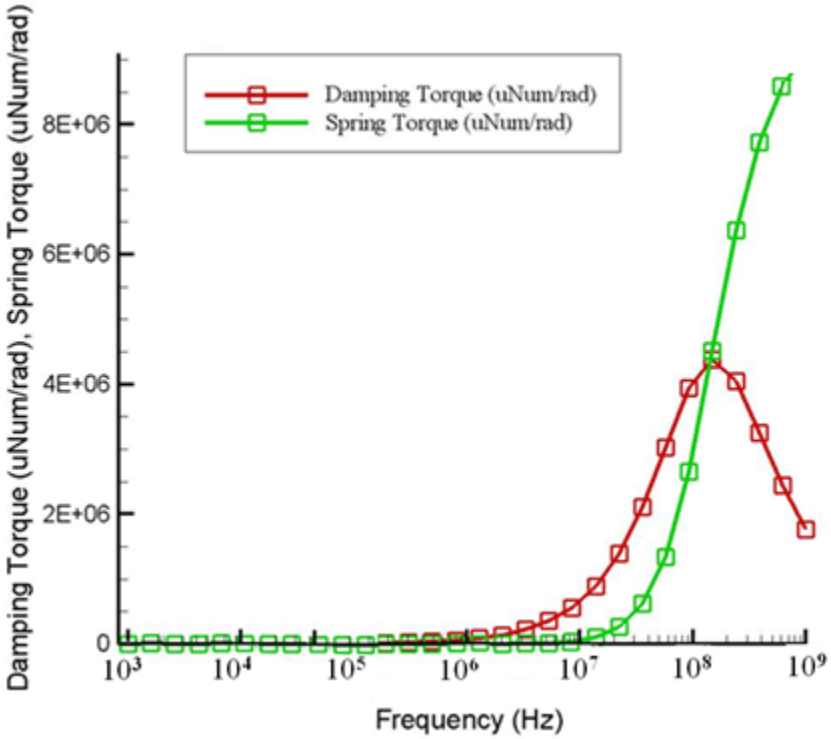

(b)

Figure 3-8: (a) Damping coefficient as a function of frequency in the case of Slide-Film Damping (gap=100 µm), and (b) Damping and spring torque as a function of frequency for the case of Squeezed-Film Rotational Damping (gap=20 µm), gas: air.

Table 3-3: Damping force frequency peak versus gas viscosity.

	Air	Nitrogen	Helium	Neon
Viscosity (kg/µm s)	1.8e-11	1.86e-11	2e-11	3.21e-11
Damping force frequency peak (Hz)	5.76e7	3.56e7	3.56e7	2.26e7

In conclusion, in the case of squeezed-film translational damping, reducing the gap between the sensor's proof mass and fixed reference frame can significantly increases the damping. Using a gas with higher viscosity will also increase the damping however the impact is not as significant as reducing the gap. The effect of slide-film damping is less than squeezed-film translational

damping at low frequencies for the structure proposed here; however changing the structure geometry (such as having etch holes in the proof mass) can affect the damping response.

3.3 Rate Sensor

Like accelerometers, rate sensors can be based on either VOA or FP. Figure 3-9 shows the designed optical rate sensor based on FP. As discussed in section 2.8, in order to maximize the sensor response (maximum sensing displacement), the resonance frequency in the driving direction has to be equal or close to that in the sensing direction, meaning the structure design has to be symmetrical.

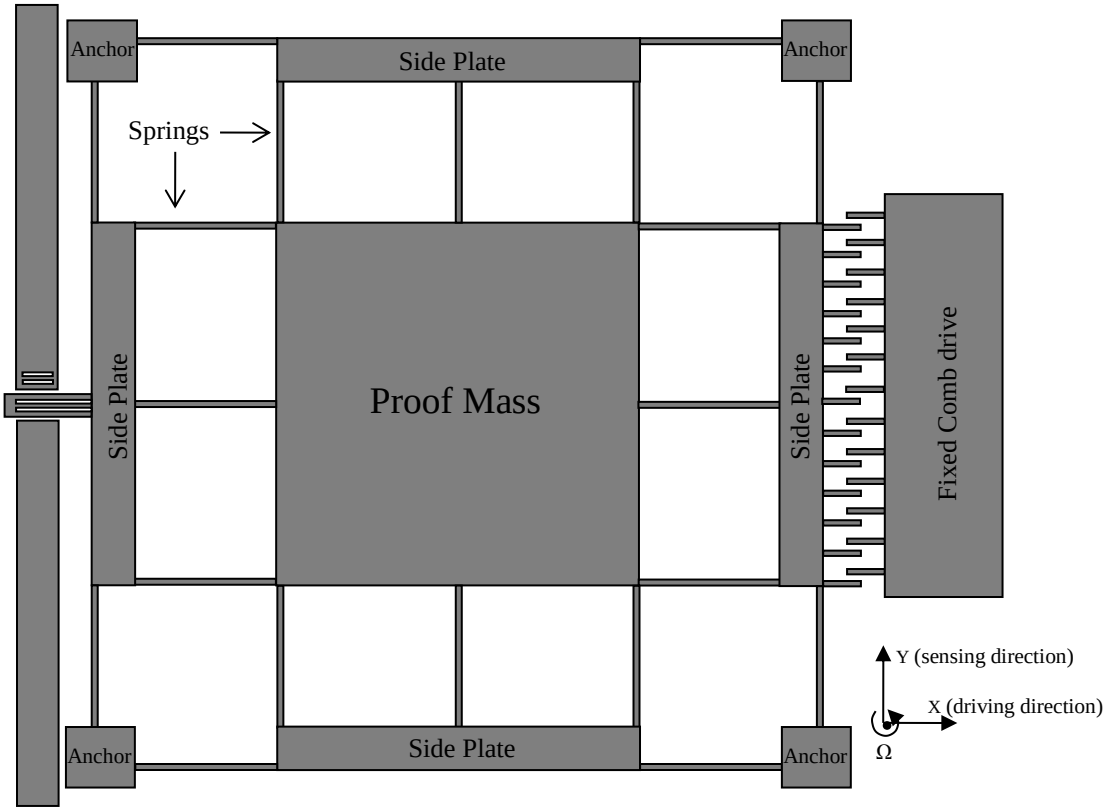

Figure 3-9: Schematic view of the designed rate sensor based on FP

Side plates are used to uncouple their motion from the proof mass. They are connected to the proof mass through separate beams. A comb drive is placed on one of the side plates in order to drive the structure. In the drive mode, the springs along the drive direction do not deform due to their high stiffness along the drive direction. In the same way, in the sense mode, the beams along

the sense direction do not deform. Therefore the overall design leads to the decoupling of the driving mode from the sensing mode. When sensor is excited in driving direction (x), the gap of the FP does not change. As a result, the sensor is not sensitive in this direction however it is sensitive to the Coriolis force (y direction). For the VOA-based rate sensor, similar structure is used to drive the proof mass (Figure 3-10). The Bragg mirror that modifies the transmitted light at the VOA junction is attached to the top side plate as shown in Figure 3-10. As the structure is displaced in y direction due to the Coriolis force, the attached Bragg mirror moves vertically and modulates the signal at the VOA junction (Figure 2-10).

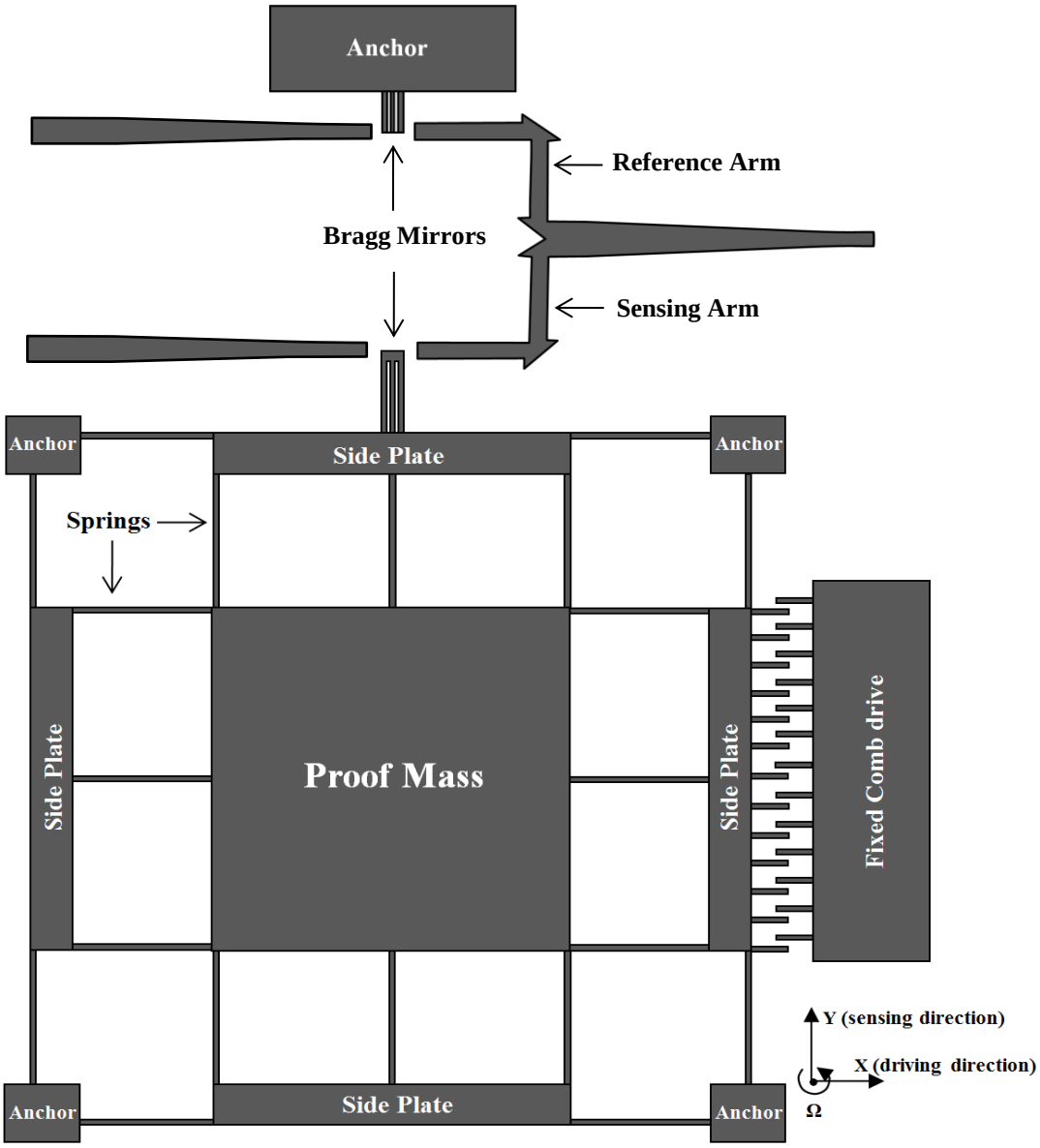

Figure 3-10: Schematic view of the designed rate sensor based on VOA

According to (2.90), the gyroscope displacement sensitivity under the matching condition ($\omega_{0y} = \omega_{0x}$) is given by:

$$DS_g = \frac{2AQ_y}{\omega_{0y}} \tag{3.9}$$

Therefore, the displacement sensitivity is proportional to the sensor quality factor in sensing mode (y direction) and the displacement in driving mode (x direction) and is inversely proportional to the sensor resonance frequency. Therefore in order to get a sensor with high sensitivity, high quality factor in y direction, high driving displacement and low resonance frequency are required. The working resonance frequency was chosen to be in kHz range, as very low frequencies will make the system unstable. Also lowering frequency will lower the quality factor ($Q=\omega/\Delta\omega$), leading to a lower sensitivity for the sensor. Therefore, there is a trade-off between the resonant frequency and the displacement sensitivity.

To achieve a resonance frequency in the order of kHz, a proof mass with dimensions of 1000 µm× 1000 µm×550 µm (m=1.3×10^{-6} kg) suspended by springs with total spring constant of 77 N/m is used. This provides a natural resonance frequency of ω_0= 7.7 kHz, or resonance frequency of f_0=1.2 kHz for the sensor. Thick mass is used to get larger mass, leading to smaller resonance frequency. The spring constant can be lower but using very soft springs generate in-plane cross sensitivities, resulting in coupling between driving and sensing modes. Also it generates z-cross sensitivity and bends the structure.

Let's now calculate the displacement sensitivity. First, from (2.28), the squeeze-film translational damping in y direction is expressed as:

$$c_y = 0.42\frac{\mu A^2}{d^3} \tag{3.10}$$

where A is the cross section area of the proof mass (damped plate in y direction), µ is the viscosity of the surrounding medium (air= 1.86×10^{-5} kg/ms), and d is the gap between the proof mass cross section and the fixed reference frame. The damped plate dimension is 1000 µm×550 µm. For a gap of 20 µm, c_y is calculated as 3×10^{-4} N.s/m, which is in a good agreement with simulation (Figure 3-7 (d)). The quality factor is then calculated from (2.78):

$$Q_y = \frac{\sqrt{mk_y}}{c_y} = 33$$

This is a very low quality factor leading to low sensing displacement sensitivity (as discussed in section 2.8). The gyroscope displacement sensitivity given by (3.9) is calculated as:

$DS_g = \frac{2AQ_y}{\omega_{0y}} = 8.6 \times 10^{-3} \left[\frac{1}{second^{-1}}\right] \times A$.

This requires a high driving displacement in the order of hundreds micrometer (which is practically impossible to achieve) to induce a sensing displacements in the order of micrometer. However by decreasing the damping coefficient in y direction, the quality factor can be significantly increased. From (3.10) a lower c_y can be achieved if the gap is increased or viscosity is reduced. For example for a gap of 150 µm, c_y =1×10^{-6} N.s/m (Figure 3-7 (c)), providing Q_y=10^4 and DS_g=2.6 [1/(sec)$^{-1}$]×A. This means, if for example we could get a displacement of 1 µm in the x direction due to the driving, we can induce 2.6 µm/ (sec)$^{-1}$ displacement for unit angular velocity. It should be recalled that, the required y-displacement depends on the lateral guided mode size in the waveguide (which is directly related to the width of the waveguide) at the VOA sensing junction, as discussed in section (3.2). Therefore, the total sensitivity of the gyroscope can be defined as the ratio of the displacement sensitivity to the waveguide width at the VOA junction, i.e.

$$\text{Sensitivity of gyroscope: } S_g = \underbrace{\frac{1}{W_w}}_{\text{Optical}} \times \underbrace{DS_g}_{\text{Mechanical}}$$

where, W_w is the width of waveguide at the VOA junction. It should be noted that, for the FP-based, even nanometer displacements can effectively modulate the FP resonance peak.

Used dimensions of each element of the sensor are listed in Table 3-4. According to Eq. (3.6), the net stiffness in either type of motion is given by (considering N=10):

$$k_x = k_y = \frac{10Etw^3}{l^3} \tag{3.11}$$

Resulting in 77N/m stiffness in drive and sensing direction for the sensor.

Table 3-4: Dimensions of each element used in the sensor

	Number	Length (μm)	Width (μm)	Thickness (μm)
Proof Mass	1	1000	1000	550
Beams	20	200	2	47
Side Plates	4	500	50	47

3.3.1 Comb Drive Design

Interdigitated-finger comb-drives are electrostatic actuators. They are made of two conductive combs, a fixed comb and a movable comb (Figure 3-11). The attractive electrostatic forces between the two combs are generated when a voltage is applied between the fixed and moving combs. These forces cause the moving comb to be drawn to the fixed comb. Generated force by a comb drive is given by [113],

$$F_{comb} \approx \frac{n_f t \varepsilon_0 V^2}{\mathrm{d}} \tag{3.12}$$

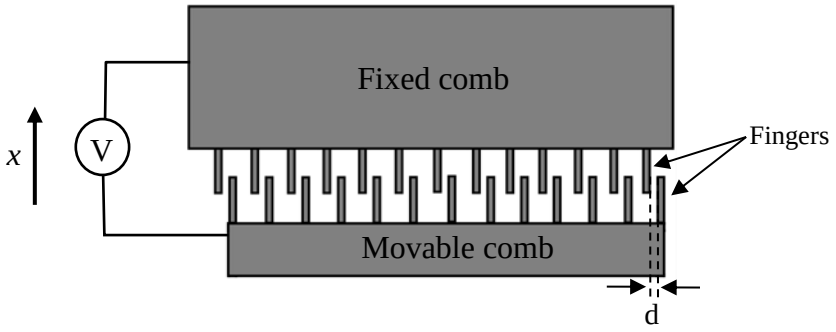

Figure 3-11: Schematic of an interdigitated-finger comb drive

where n_f is the number of fingers, t is the thickness of the comb drive (in our case, device layer thickness of the SOI wafer), ε_0 is the vacuum permittivity (8.85×10^{-12} F/m), d is the space

between the fingers (between fixed comb finger and movable comb finger), and V is the applied voltage.

For weak damping, the maximum driving displacement is defined from (2.79) as:

$$(A_{max})_{weak\ damping} = \frac{F_{0D}}{k_x}(Q_x)_{weak\ damping} \tag{3.13}$$

where $F_{0D} = F_{comb}$ is the force generated by the comb drive. First let's verify if we are at the weak damping regime. From (2.27), the damping ratio in x-direction is defined as:

$$\xi_x = c_x/2\sqrt{mk_x} \tag{3.14}$$

Showing that maximum damping ratio is achieved from maximum damping coefficient. As the structure is symmetric, we can use the same values of c_y calculated in previous section. Maximum c_y was achieved for the gap of 20 μm as $c_y = 3\times10^{-4}$ Ns/m. Note should be taken that damping in the comb drive is neglected in this analyze. Substituting this value in (3.14), ξ_x is calculated ξ_x=0.015. Referring to Figure 2-6, this corresponds to a weak damping condition. The space between the fingers of the comb drive d, is set to be 3 μm in our design as we are limited to the lithography resolution (a thick resist (3 μm) is used to selectively be able to etch 47 μm thick silicon layer). Although the number of fingers is proportional to the generated force by the comb drive, the effect of applied voltage is more significant, as it is in power of two in (3.12). Also the number of fingers is limited by the length of the proof mass. In our design we used 42 fingers; along with t= 47 μm, and d=3 μm, the driving force produced by the comb drive from (3.12) is calculated as a function of voltage as

$$F_{comb} = 6\times10^{-9}\left(\frac{Newton}{(Volts)^2}\right)\times V^2 = 6\times10^{-3}\left(\frac{Micro-Newton}{(Volts)^2}\right)\times V^2 \tag{3.15}$$

Backing to Eq. (3.13), knowing k_x=77 N/m, the maximum driving displacement is calculated as:

$$A_{max} = 7.8\times10^{-5}\left(\frac{Micro-Newton}{(Volts)^2}\right)\times V^2 Q_x \tag{3.16}$$

Figure 3-12 shows how the maximum driving displacement varies as a function of applied voltage for three different quality factors. What is interesting here is that, unlike the sensing

mode, the driving mode does not require a very high quality factor to induce displacements in the order of micrometers. For example the quality factor of 33 seems to provide enough displacement for small values of applied voltages.

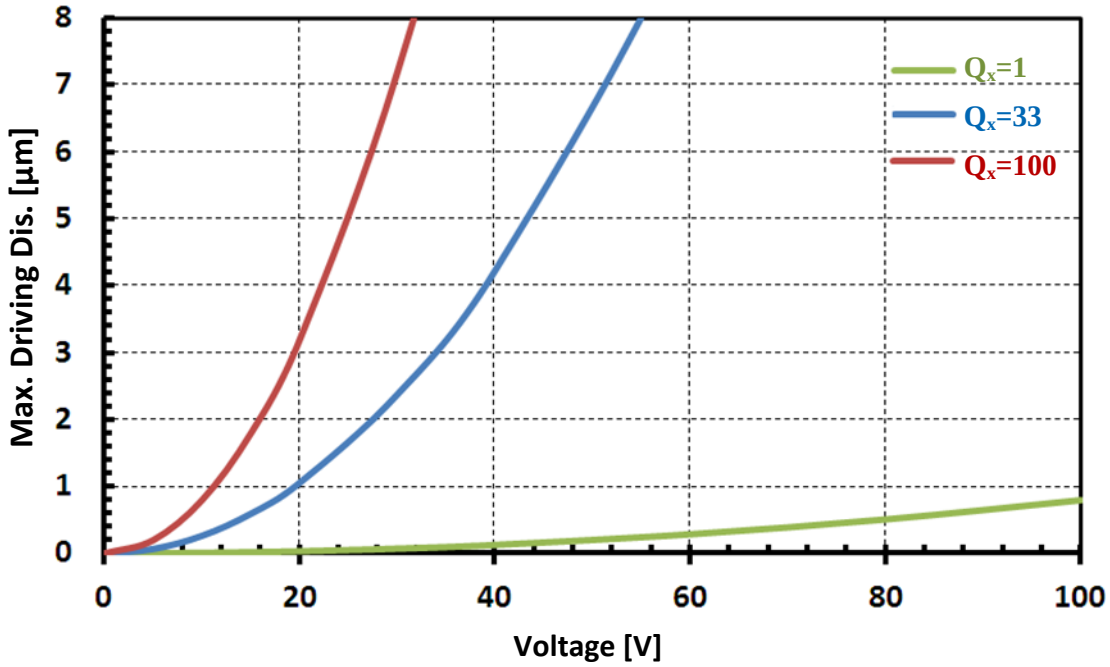

Figure 3-12: Maximum driving displacement of the sensor versus the applied voltage to the comb drive for three different values of quality factors in driving direction.

Finite element simulations were performed using Coventoreware 2010 at the stationary (or quasistatic) state to verify the results. Table 3-5 shows the results. In addition to the maximum displacement in x-direction, maximum displacements in y and z direction are listed in order to check the cross sensitivity of the device.

The ratio of maximum sensing displacement to maximum driving displacement for unit angular velocity is obtained from (2.90), i.e.

$$\frac{DS_g}{A} = \frac{2Q_y}{\omega_{0y}} \tag{3.17}$$

For example for Q_y=33, and ω_{0y}=7.7 kHz, this ratio is 8.6×10^{-3} $(rad/s)^{-1}$. Therefore the sensing displacement is very small when a sensor with low quality factor in sensing direction is used. As

a result even very small motions coupled from the drive mode to the sense mode can be added and be read as the rotation signal.

Table 3-5: Proof mass displacements versus applied voltage to the comb drive in the stationary (quasistatic) regime.

Voltage (v)	40	50	100	150	200
Maximum x displacement (μm)	0.12	0.2	0.78	1.7	2.1
Maximum y displacement (μm)	0.002	0.002	0.01	0.02	0.07
Maximum z displacement (μm)	0.0001	0.0001	0.0004	0.001	0.008

These coupled motions can arise from cross sensitivity or fabrication imperfections. Consequently, highly symmetric design, control on cross sensitivity, and process fabrication are required to minimize the coupling. For example if due to the fabrication imperfection, small motions from x direction are coupled into the sensing direction, the horizontal position of the Bragg mirror at the VOA junction changes, modifying the longitudinal coupling (due to the divergence of the beam in free space) and leading to the power change in the transmitted light (Figure 3-13).

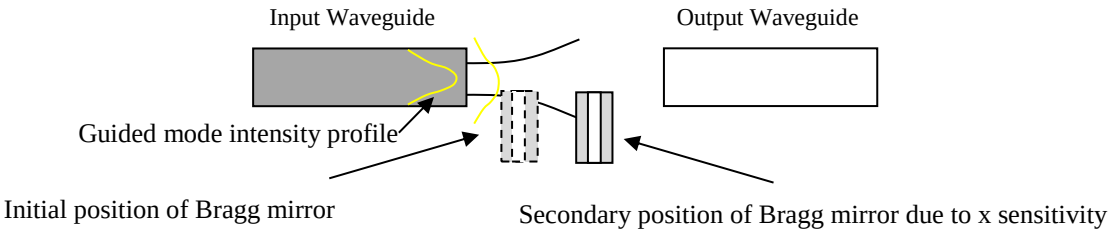

Figure 3-13: Effect of x-cross sensitivity on the transmitted light at the VOA junction.

Cross sensitivity can also come from the comb drive. Due to fabrication imperfection (Figure 4-5), there may be small geometric mismatches of a comb drive that can generate additional electrostatic forces in the cross-axis y direction.

As seen in Table 3-5, the values of the maximum y and z displacements compared to the maximum x displacement are two and three magnitudes of order smaller respectively, providing very low cross sensitivity for the sensor.

At stationary (quasistatic) condition, the generated force by the comb drive is balanced with the Hooke's force i.e.:

$$F_{comb} = k_x x \tag{3.18}$$

Substituting k_x from (3.11), and (3.12) in to (3.18), the displacement is achieved as:

$$x = \frac{n_f \varepsilon_0 V^2}{10Ed} \cdot \left(\frac{l}{w}\right)^3 \tag{3.19}$$

Note that the displacement is independent of the SOI thickness. This equation is the simplified form of (3.16) for Q_x=1.

The maximum x displacement achieved from the finite element simulations listed in Table 3-5 are in very good agreement with the values calculated from analytical calculations (Figure 3-12 for Q_x=1). Figure 3-14 shows a finite element simulation of the sensor using Coventoreware 2010. In this simulation 200 volts is applied to the comb drive, resulting in 2.1 μm displacement in driving direction for the structure.

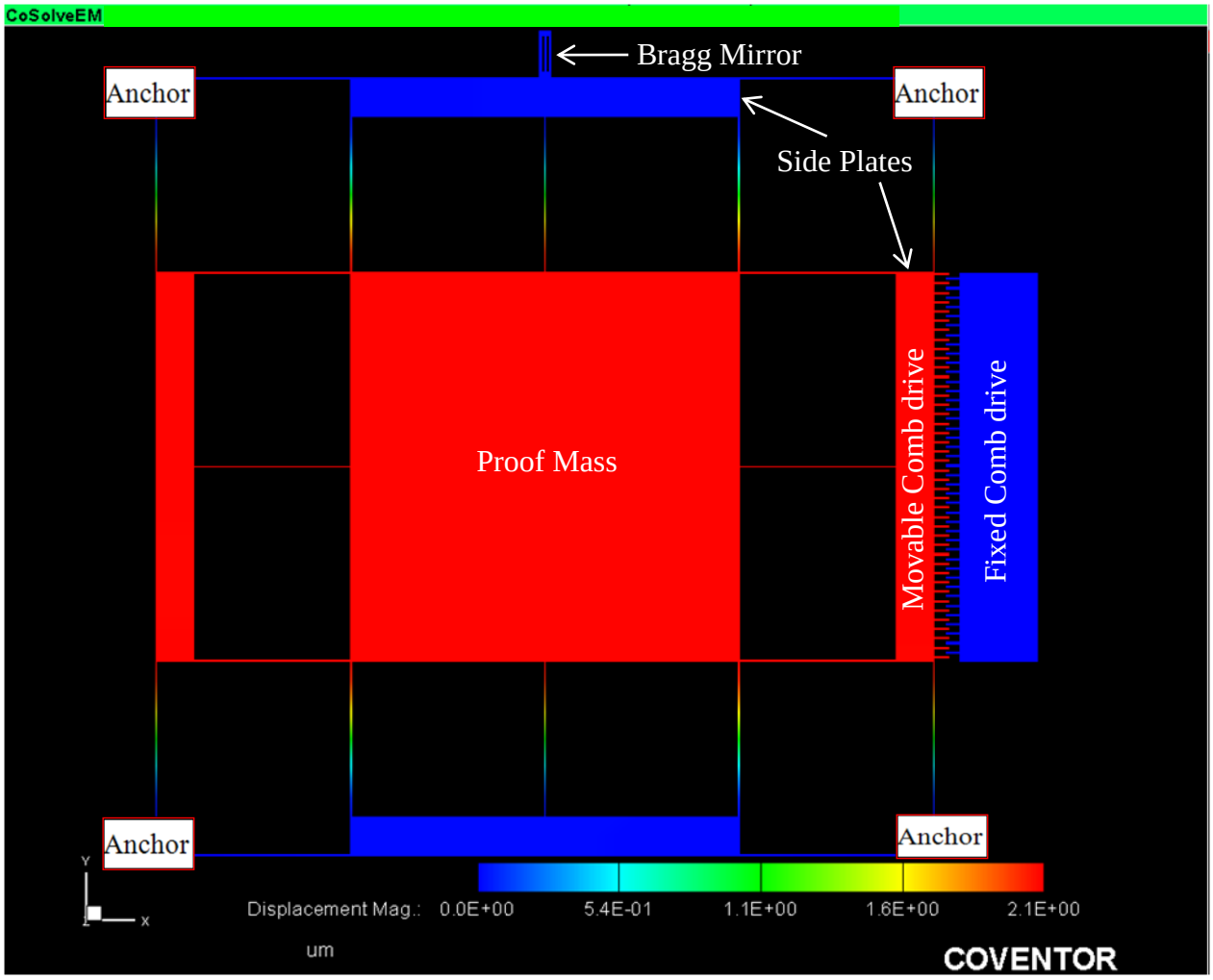

Figure 3-14: Electrostatic simulation result of the rate sensor. Maximum x displacement of the structure is 2.1 µm when 200 volts voltage is applied.

3.3.2 Compliant Mechanisms

If for any reason (such as fabrication imperfections) the matching condition (where the resonance frequency in x direction is equal to the resonance frequency in y direction) is not satisfied, the sensing displacement would be very small (Figure 2-30). Even with the matching condition this displacement for systems with low Q_y can be very small. For example from Eq. (3.16) for Q_y=33, when 60 V is applied to the comb drive, A_{max}=9 µm, substituting in to (3.17), for ω_{0y}=7.7 kHz, DS_g= 0.1 µm (rad/s)$^{-1}$. For FP-based gyroscope, this can effectively modulate the transmitted resonance peak of the FP but for VOA case, the required displacement depends on the lateral mode power distribution of the output of the input waveguide at the VOA junction. For

example from Figure 2-17 for a waveguide having diverged beam waist radius of 3 μm at the mirror position, for a linear response, the required displacement is +/-1 μm. Increasing the Q_y by decreasing the damping seems to resolve the problem but only in the case of matching condition. As achieving a fully symmetric structure is extremely difficult because of the fabrication imperfection (such as non-uniformity of photolithography caused by non-planar spun resist or having non ideal contact during exposure or deviation causing from DRIE such as notching (4.1.1)), satisfying matching condition is very difficult, leading to a shift between x and y resonance frequencies. A possible solution is to amplify the sensing displacement using compliant structures. In the following, a brief discussion about the compliant structures using micro-leverage mechanism along finite element simulations is presented. Although, it is found that these structures can significantly amplify the sensing displacement, they may also disturb the matching condition by modifying the structure stiffness in y direction. Further studies should be carried out to investigate the possible arising issues.

A single stage micro-leverage mechanism usually consists of four parts: lever arm, pivot beam, input and output systems as shown in Figure 3-15(a). Single-stage micro-leverage mechanism can be classified into three types (Figure 3-15), depending on the relative positions of the pivot, the input and output systems on the lever arm. The first type micro-lever can either amplify displacement or force, depending on the respective distances between the pivot and the input or output. It can also be used to change the direction of force. While the second type is only used to amplify force, the third type is typically used to amplify displacement. For example micro-tweezers are made of joining the pivots of two third-type micro-levers. Analyzing the compliant micro-leverage mechanisms is beyond the scope of this thesis. For more information readers can refer to [114], [115].

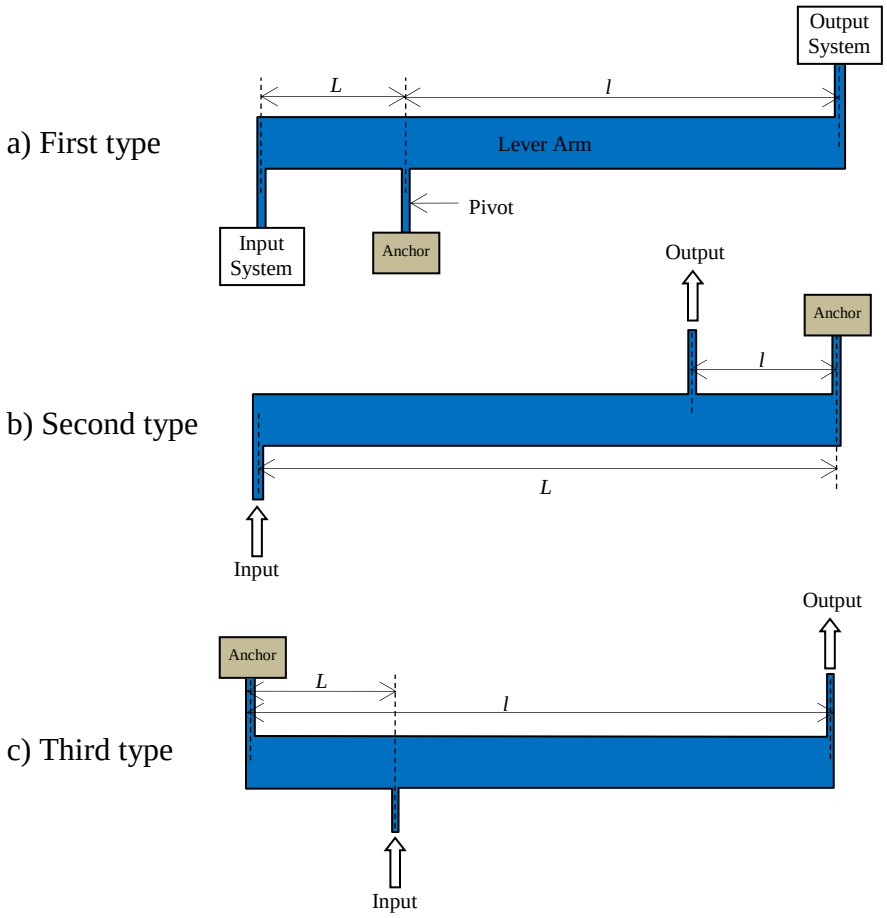

Figure 3-15: Classification of three kind of micro-lever

The amplification factor $A = l/L$ is the maximum amplification factor that a leverage mechanism can achieve where l, L are the distances between the anchor and output and input respectively. If only a single micro-lever is used, for high amplifications, the lever ratio needs to be high, leading to a very long lever arm. Since in micro technology one is limited to the design area, multiple stages of micro-levers are used in series to obtain high amplification factor. The total amplification factor, A, is then the product of the amplification factor of each individual stage. Adding more stages increases the amplification factor, however from energy conservation point of view; more energy is consumed at the pivot and the beams that connect the stages. Therefore, in optimum case, it is better to use minimum number of lever stages. In our case two stages will provide enough displacement amplification for the sensor. First type and third type of micro-levers were used in series to form our micro-lever stage. There are three main parameters that have to be optimized, l, L and the length and width of the pivot. The lever arm width does not

have any effect on the amplification and has to be designed large enough to be kept rigid and not bend under applied forces. Many different dimensions are used and simulated to obtain high displacement amplification. Figure 3-16 shows the optimized dimensions for the two micro-lever stages, leading to 7 x amplification as shown in Figure 3-17. Pivots have 2 µm widths. Their lengths are 12 µm and 100 µm for the first stage and second stage pivots respectively. In Figure 3-17 same forces are applied to the proof mass of the gyroscope without and with leverage mechanisms. The structure responses without and with leverage mechanisms to the applied force are 1.7 µm and 12 µm respectively, resulting in 7 x displacement amplification.

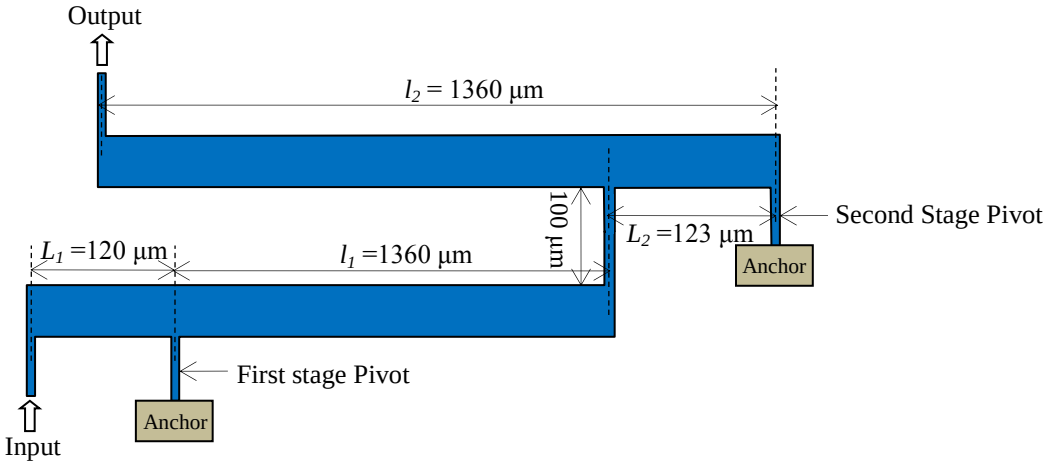

Figure 3-16: Two-stage micro-lever used dimensions

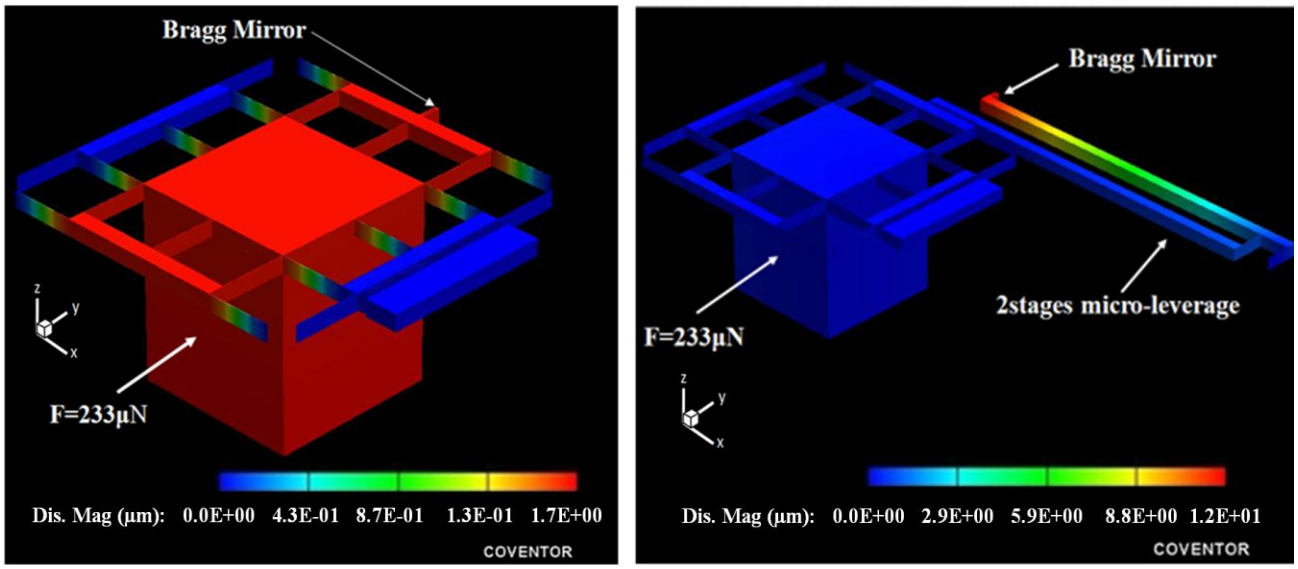

(a) (b)

Figure 3-17: FEM simulation of the rate sensor, (a) without and (b) with two stage micro-lever. Same forces are applied in both cases. The structure response without and with leverage mechanisms to the applied force is 1.7 μm and 12 μm respectively, resulting in 7 x displacement amplification.

Figure 3-18 shows a SEM picture of the designed two stage micro-lever integrated with gyroscope fabricated on 47 μm SOI.

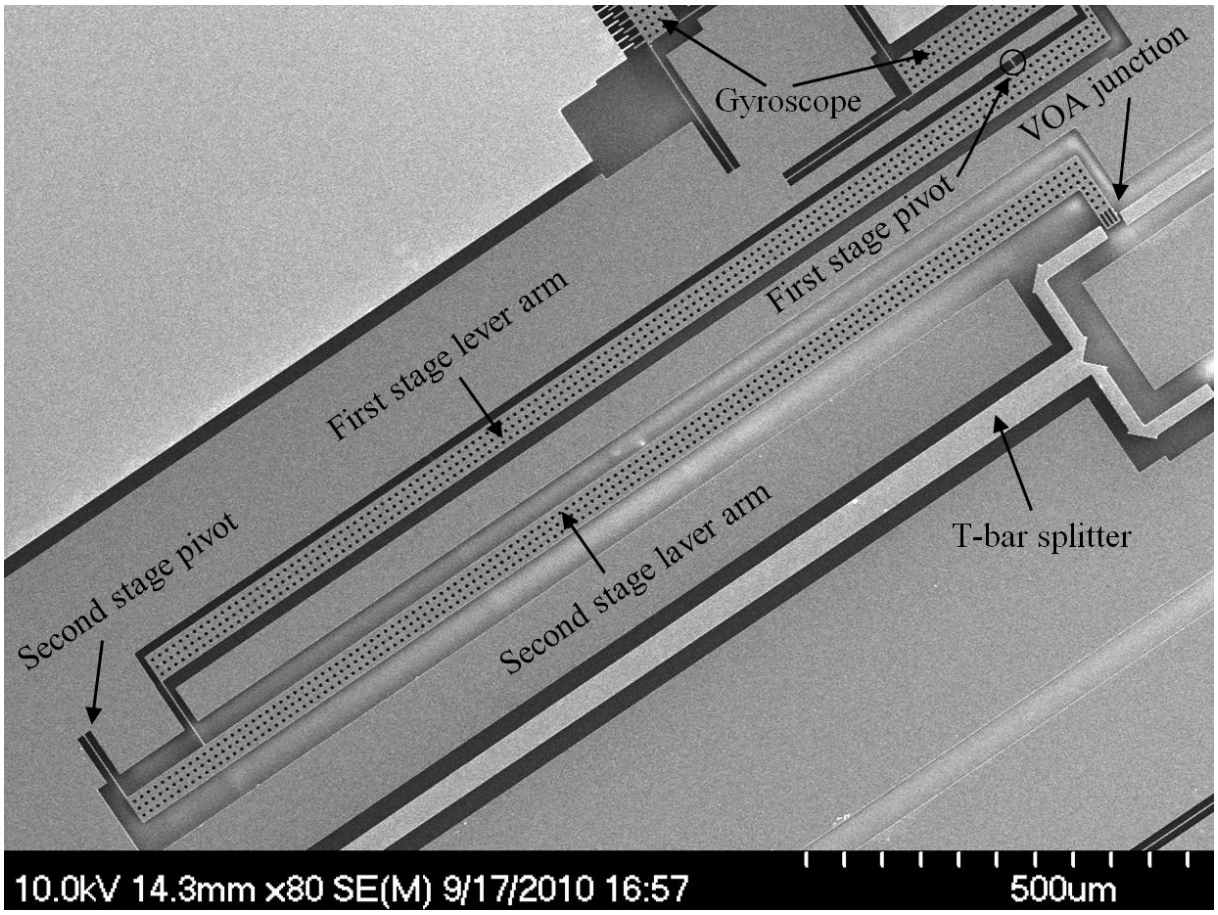

Figure 3-18: Two stage micro-lever integrated with gyroscope (fabricated on 47 μm SOI).

3.4 Conclusions

The design details and simulations of FP-based and VOA-based optical accelerometers and gyroscopes were presented. Finite element method is used to model the mechanical behavior of the devices. FP-based device is based on an in-plane FP with two distributed Bragg reflectors (DBR) mirrors utilizing strip silicon waveguides, in which one DBR mirror is attached to two

suspended proof masses. As a consequence of acceleration (or rotation), the relative displacement of the movable mirror with respect to the fixed one changes the cavity length and modifies the Fabry-Perot resonance. The accelerometer is symmetrical and consists of two proof masses suspended by eight serpentine flexures beams. In the VOA-based device, a Bragg mirror that is attached to the suspended (by span beams) proof mass is positioned in the middle of the gap between two input and output multimode strip waveguide. When the device is actuated by the applied acceleration (or rotation), the intensity of the transmitted light to the output waveguide is modulated by the displacement of the Bragg mirror. Both FP-based and VOA-based sensors sensitivity is inversely proportional to the system resonance frequency. This means, not only springs with low spring constant are required, but also large proof mass is needed to increase the sensor sensitivity. FP-based device is highly sensitive even with nanometer displacements, as it is based on wavelength detection (interferometry). On the other hand to obtain a relatively high sensitive VOA-based sensor, displacements in the order of few micrometers are required (requiring softer springs and larger proof mass for the device compared to FP-based), as the lateral transmitted intensity of the mode is modulated instead of wavelength. Device sensitivity is also inversely proportional to the lateral mode size in the input waveguide at the VOA sensing junction which is directly proportional to the waveguides width. Effects of different types of damping on the device performance were also studied. Accelerometers frequency bandwidth increases with damping and shows a maximum in the case of critical damping.

For the case of gyroscopes, a MEMS electrostatic comb-drive is used to drive the sensor proof mass along the x-axis. An applied angular rotation perpendicular to the sensor plane (z-axis) induces the Coriolis force, causing the proof mass and the attached VOA/FP movable mirror to displace along the y-axis, modulating the VOA actuator/FP gap and the resultant transmitted optical signal/wavelength. A matching condition between resonance frequencies in driving (x) and sensing (y) directions is required to obtain high displacement sensitivity for the gyroscope. The gyroscope displacement sensitivity is also proportional to the driving displacement (caused by comb-drive), the mechanical quality factor of the sensor in y direction (Q_y), and inversely proportional to the device resonance frequency. In other words, in order to obtain a sensor with high displacement sensitivity, a matching condition between the resonance frequencies in driving and sensing directions, high driving displacement, high quality factor in y direction, and low resonance frequency are required. The quality factor increases inversely with damping.

Consequently, in order to get a high quality factor in y direction, the sensor needs to be weakly damped in y direction. The driving displacement not only depends on the comb-drive characteristics but also directly relates to the quality factor in the driving direction (Q_x). However despite the sensing direction, not very high quality factor in driving direction is required to obtain displacements in the order of micrometers for applied voltages below 100 V. Although reducing the spring constant can increase the driving displacement, but it will make the system unstable and can also generate some cross sensitivities leading to the motion coupling from the drive mode to the sense mode, resulting in errors (noise) to the system. On the other hand, the sensitivity of the gyroscope is inversely proportional to the lateral guided mode size in the waveguide at the VOA sensing junction; therefore the mechanical and optical designs both have to be taken into account.

If for any reason (such as fabrication imperfections) the matching condition is not satisfied, the sensing displacement will be very small. To overcome this problem, a compliant micro-leverage mechanism was introduced to amplify the sensing displacement. A two stage micro-lever mechanism was proposed, leading to 7 x displacement amplification. In the case of FP-based gyroscope, a compliant structure is not required as displacements in the order of nanometers can effectively modulate the transmission peak of the FP.

CHAPTER 4 FABRICATION

In this chapter, the fabrication processes of the designed devices are discussed and their challenges and proposed solutions are addressed. Silicon on insulator (SOI) wafers with different thickness are used based on required device performance. At the beginning of this work we start with 30 μm thick SOI to be able to inject light from optical fibers into input silicon strip waveguides using butt coupling method. Then 47 μm thick SOI wafer is employed to passively integrate SM optical fibers with 80 μm diameter to the chip using U-grooves helping us to eliminate the misalignment issues and signal instabilities. Finally, 75 μm thick SOI wafers are employed allowing us to integrate standard SM optical fibers to the chip through U-grooves. Finite element simulations and corresponding mask layout design were carried out for each thickness.

4.1 Deep Reactive Ion Etching (DRIE)

Deep reactive ion etching (DRIE) is a dry etching technique that is based on plasma etching and is used to anisotropically etch materials (here silicon) with a high aspect ratio (ratio of geometric depth to width). It is a combination of plasma etching (chemical etching) and ion milling etching (physical reaction). Plasma etching uses gases (typically fluorine radicals) and the energy of plasma to chemically etch the material, and ion milling bombards the surface of material/wafer and physically etches the surface using momentum transfer. With this technique trenches with very vertical sidewalls can be achieved. There are two main technologies for DRIE, namely cryogenic and Bosch. Bosch process using inductively coupled plasma (ICP) is used (Figure 4-1) in our case and is based on two steps: passivation and etching. A layer of polymer is created on the substrate using a source gas (here C_4F_8) prior to etching. Then in second step, the surface is etched using different source gas (here SF_6). The polymer is sputtered away by ion milling, but only on the horizontal surface of the substrate and not the sidewalls. Ions are accelerated vertically relative to the substrate surface using a potential. The polymer has low etching selectivity (low etch rate compared to silicon) to the chemical part of etching, resulting to a protection for the sidewalls. As a result, etching aspect ratios up to 30 to 1 (or higher depending on the process) can be achieved. These two steps are repeated alternatively until the desired depth for etching is obtained. The typical etching rate is 3μm/min [117]. It can be lower or higher

depending on the process parameters such as pressure, plasma power, the ratio of etching step length to the passivation step length.

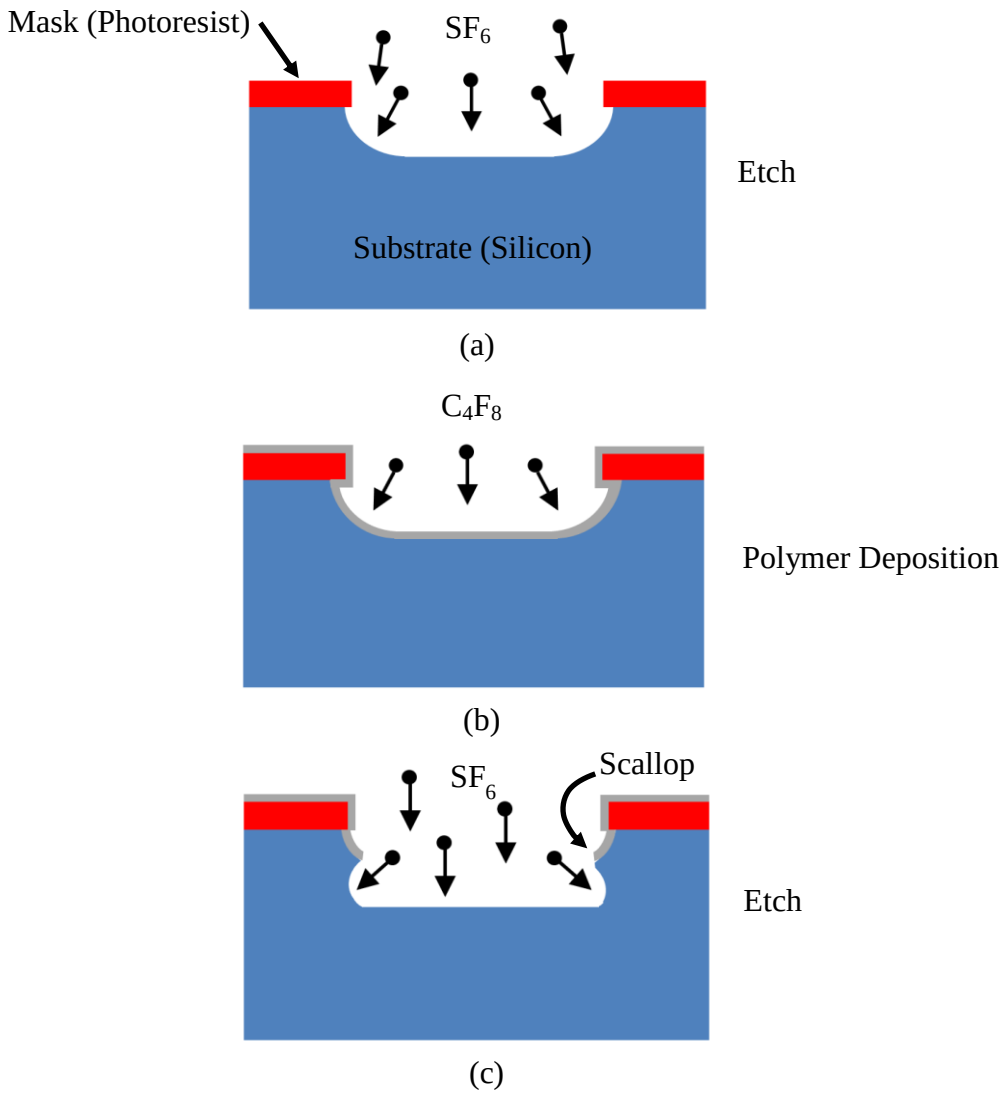

Figure 4-1: Schematic of Bosch process in DRIE: (a) Etch step using SF_6 gas, (b) Side wall passivation using C_4F_8, (c) Etch cycle using SF_6 gas after passivation.

Therefore deep etching can be accomplished in a relatively short time. Process has a high selectivity to photoresist depending on the process and can be up to 75:1 [116]. Table 4-1 shows the parameters that we used for DRIE. The etching was performed at 20 ºC and 15 mTorr pressure. These parameters are not fixed and had to be adjusted depending on the type (single or double SOI) and the thickness of the SOI substrate. Small amount of oxygen is added to the

etching step to improve the profile of the sidewalls (verticality) [116]. It also improves the etch rate uniformity [118] and surface roughness (smoother sidewalls) [117]. However care should be taken as oxygen reacts with resist, resulting in a lower etch selectivity.

Table 4-1 Parameters used in DRIE etching

Step	ICP Power (W)	RF Power (W)	C_4F_8 (sccm)	SF_6 (sccm)	O_2 (sccm)	Time (sec)
Deposition	450	10	65	1	0	4
Pause	0	0	0	0	0	2
Etching	450	25	1	65	5	4

4.1.1 DRIE-Challenges

The key challenges of deep silicon etch are to attain high etch rate and selectivity, high aspect ratio, smooth and vertical sidewall, bottoms (silicon and BOX interface) free of micro-grasses and notching. Following we will address these challenges and their possible solutions.

1- Verticality

The profile of the etched walls depends on geometry of the pattern on the mask and the set process parameters. The verticality of the walls can often be controlled by adjusting the etch to deposition time ratio. The verticality of the walls is important for the Bragg mirrors to get a high reflectance, leading to high finesse for the FP resonance peak (Figure 2-9). Figure 4-2 (a) shows an array of trenches with poor verticality etched in SOI (negative sidewall profile). As seen the width of the walls have decreased with depth. This means that the length of etching has to be decreased compared to the deposition length. By doing this, verticality can be significantly improved as shown in Figure 4-2 (b).

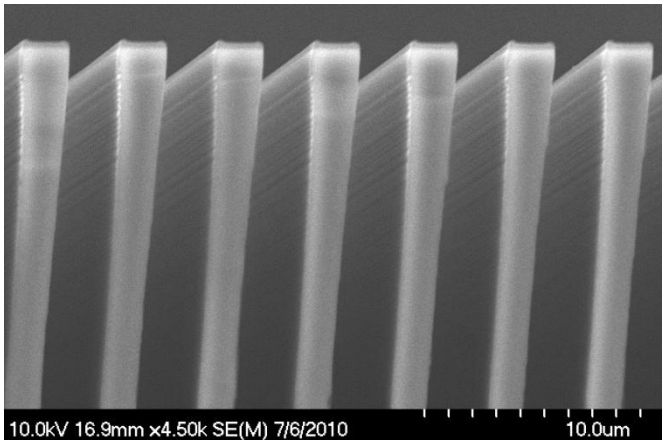

(a)

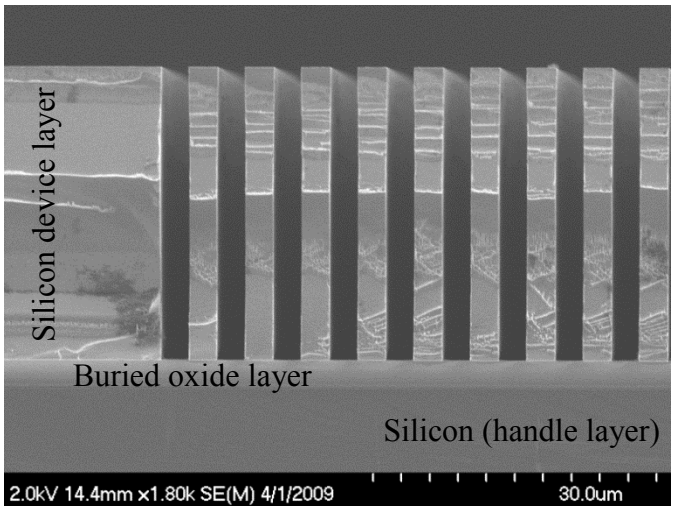

(b)

Figure 4-2: Etched trenches into SOI substrate: (a) sidewalls with poor verticality, and (b) good verticality

2- Scalloping

Scalloping occurs as a result of the alternating etch and passivation steps, as shown in Figure 4-1(c). It can be reduced by decreasing the etching time in the etch step, however that leads to low etch rate. Scalloping has major optical impacts, as the generated roughness effects on the mode/modes power exchange in the optical waveguide. Reducing the roughness is desirable, leading to less scattering loss for the system. Figure 4-3 (a) shows the scalloping formed on trench sidewalls after etching. Figure 4-3 (b) shows the presence of scalloping on the sidewalls of a rib waveguide etched by DRIE.

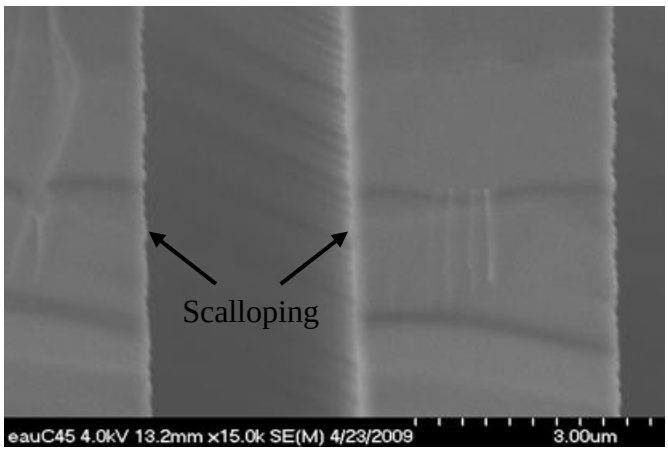

(a)

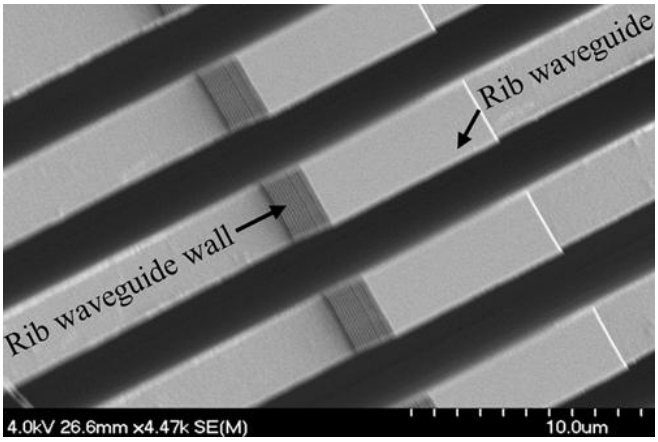

(b)

Figure 4-3: Scalloping phenomenon in DRIE: (a) An etched trench in silicon, (b) Etched rib waveguide, the scalloping can be seen on the rib waveguide's side walls.

3- High aspect ratio structures etch more slowly leading to notching when SOI is used

As seen in Figure 4-4 (a), structures with high aspect ratios are etched more slowly than those with low aspect ratio. This is due to the fact that the number of accelerated ions that reach the bottom of the trenches with smaller opening area (trench width w_1) is lower than those with larger opening area (trench width w_2). When a SOI substrate is used, the buried oxide (BOX) layer acts as an etch stop as the etching rate of oxide is much lower than silicon (<150:1) [116]. One issue that arises here is a lateral etching caused by the existence of oxide layer once the oxide layer is reached. The silicon starts to be etched laterally at the silicon and oxide interface as shown in Figure 4-4 (b).

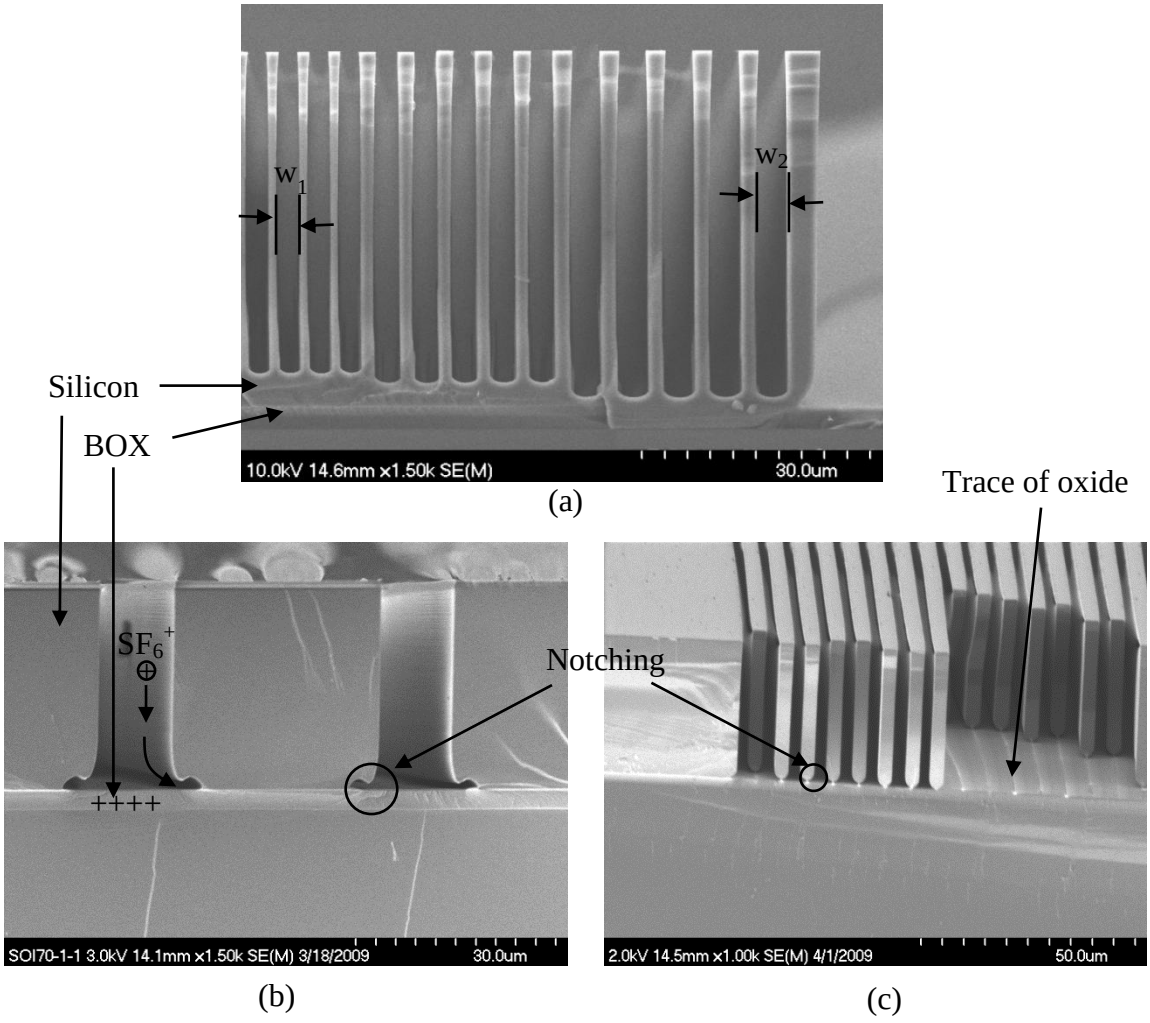

Figure 4-4: Trenches etched in SOI substrate, (a) High aspect ratio structures etch more slowly, leading to notching (b) at the silicon and oxide interface when a SOI wafer is used. This can result in an unwanted releasing of small features in the pattern (c).

This is due to the charging of oxide layer, leading to deflection of SF_6 ions towards the bottom of the sidewalls as demonstrated in Figure 4-4 (b). This lateral etching can result in unwanted releasing of small features in the pattern as shown in Figure 4-4 (c). This phenomenon can be inhibited by increasing the level of oxygen in the gas mixture [116]. As the whole pattern on the mask has to be etched at the same time, and the size of features are different, the total etching time is the time needed for the smallest feature to be etched and reach the BOX layer. During this time, features with lower aspect ratio have already reached the BOX layer and therefore the notching starts to occur for them. This can have high impact on the device performance. For

example a notching for the comb drive as seen in Figure 4-5 can generate y-displacement and affect the output signal as discussed in section 3.3.1. So the notching effect should be minimized as much as possible.

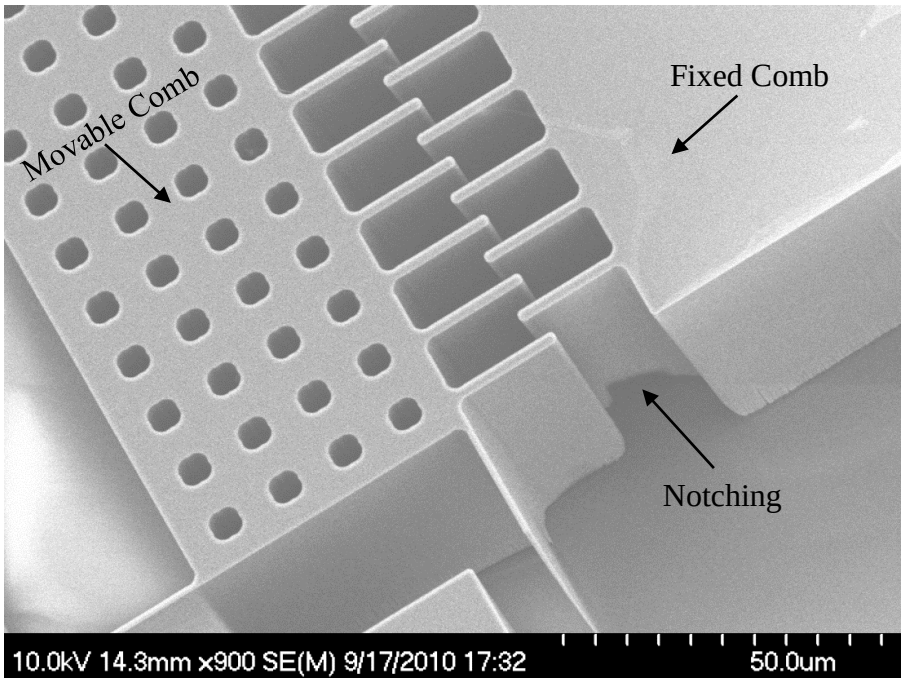

Figure 4-5: Notching observed on the finger of the comb drive of a rate sensor.

3- Micro-Grasses (Black silicon)

Particles coming from the contaminations inside the chamber can be deposited on the sample during the etching process and act as etching micromasks, leading to creation of some micro-grasses known as “black silicon” and as a result, stopping the etching process (Figure 4-6 (b)). This phenomenon happened many times for us during the etching (Figure 4-6 (a)). In reality, it is preferable to adjust the steps of etching and deposition in order to obtain walls deviating slightly from the vertical to prevent the formation of these micrograsses. If the etching cycle is set to be slightly longer, the walls profile will tend to have negative slope such as shown in Figure 4-2 (a), causing the micrograsses to be etched away during the etching (both side of steps meet at the bottom). Micrograsses can also be avoided by increasing the ion density [116]. However this will reduce the selectivity to the mask. Black silicon formation also depends on other parameters such as, temperature, pressure, and ICP power [117].

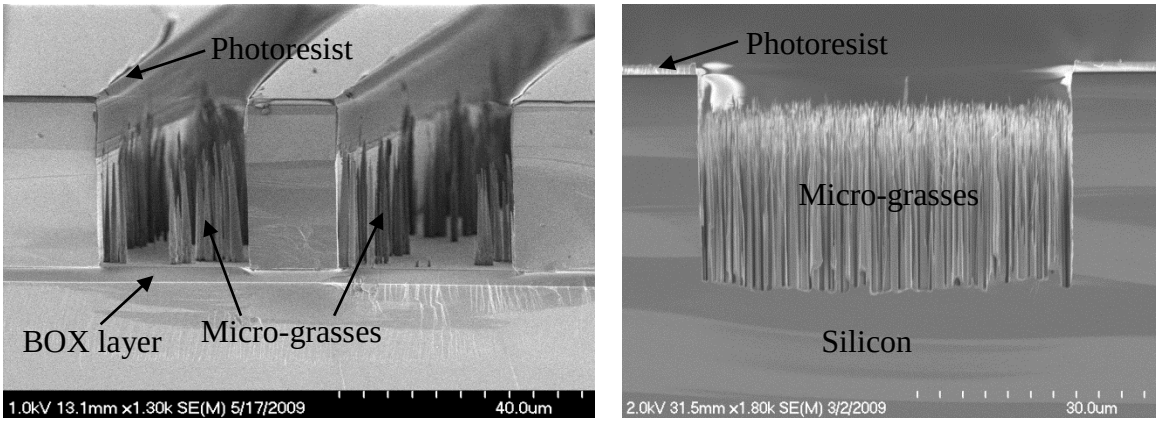

(a) (b)

Figure 4-6: Formation of micro-grasses in (a) SOI, and (b) Silicon substrate. As seen in (b), this can stop the etching process.

4.2 Fabrication Methodology, results and discussion

4.2.1 30 µm thick SOI process

Fabry-Perot (FP) and variable optical attenuator (VOA) based optical accelerometers are fabricated on 30 µm SOI wafers with the following specifications:

Type/Dopant: P doped/Boron

Orientation: <100>

Device Resistivity: > 1000 Ω-cm

Handle Thickness: 500 µm

Handle Resistivity: 1-10 Ω-cm

Buried Oxide (BOX) Thickness: 3 µm

Silicon device layer with 30 µm thickness is used to provide bigger proof mass for the sensor resulting in better sensitivity (see section 2.5.3). Suspension beams, proof masses, DBR mirrors, and waveguides are fabricated by deep reactive ion etching (DRIE). After wafer saw-cut dicing and polishing, which are critical processes for having waveguides with good quality edges and

facets, the remaining BOX is removed using vapor HF etching to release the structure and prevent the devices from sticking to the substrate.

There were two approaches for the waveguides to be used, single mode rib waveguide and multimode strip waveguide (Figure 2-19). Rib waveguides are single mode with large cross section, however they exhibit more scattering loss generated by the waveguide side walls roughness. On the other hand in a strip waveguide, since the waveguide is totally surrounded by air, the refractive index contrast between the silicon waveguide and cladding is high and the mode is more confined than in a rib waveguide as were shown in Figure 2-20 and Figure 2-13. On the other hand in terms of fabrication, rib waveguides do not lift up during the releasing process and are easier to dice and polish since they are connected to the device layer contrarily to strip waveguides. However two step lithography and etching are required to create the rib waveguides which makes the fabrication process more complicated. Especially photolithography on high topography surfaces with depth layer greater than 30 micron is almost impossible. Figure 4-7 shows the fabrication process flowchart for the case where rib waveguides are used. We start with a SOI substrate with 30 μm thick device layer (a), then photolithography with 2.8 μm thick resist (b), followed by 30 μm DRIE (c). The basics parts of the sensor are defined at DRIE step such as, Bragg mirrors, proof mass, and springs. After that, the etched surface is covered with a thick resist layer to protect the structure (d), followed by pholtolithography to define the rib waveguide (e). 6 μm DRIE followed by vapor hydrofluoric acid (HF) releases the structure and completes the process (f). Figure 4-8 shows an optical image of an accelerometer based on FP after second lithography (step e in Figure 4-7). The structure is completely covered with a thick resist. The measured thickness of resist at flat areas was 6 μm. The thickness is not uniform everywhere and depends on the distance between topographic features [116]. The edges of features were well covered by resist since a thick resist was used. The fabricated device is shown in Figure 4-9. The reason why the waveguide at second DRIE is etched 6 μm is to ensure that the first single mode condition in equation (2.52) is fulfilled ($r=h/H$=24/30=0.8, which is greater than 0.5). The width of the rib waveguides at the FP cavity are designed to be 40 μm (inset of Figure 4-9) providing broad mode (large lateral mode waist), leading to less diffraction for the mode while oscillating in the FP cavity. This width size (40 μm) at the same time satisfies the second single mode condition (2.52-b). Note that the width of the rib waveguide at the input is 12 μm. The reason for choosing this width for the waveguide at the input is to have a mode that its

size is close to the size of the mode in the fiber (9 μm) and therefore minimizing the mismatch coupling loss but at the same time satisfying the second single mode condition (2.52-b). Figure 4-10 shows the fabrication process for the case where strip waveguides are employed. The device is fabricated using one single DRIE step. Suspension beams, proof masses, DBR mirrors, and strip waveguides are all defined by one single step DRIE.

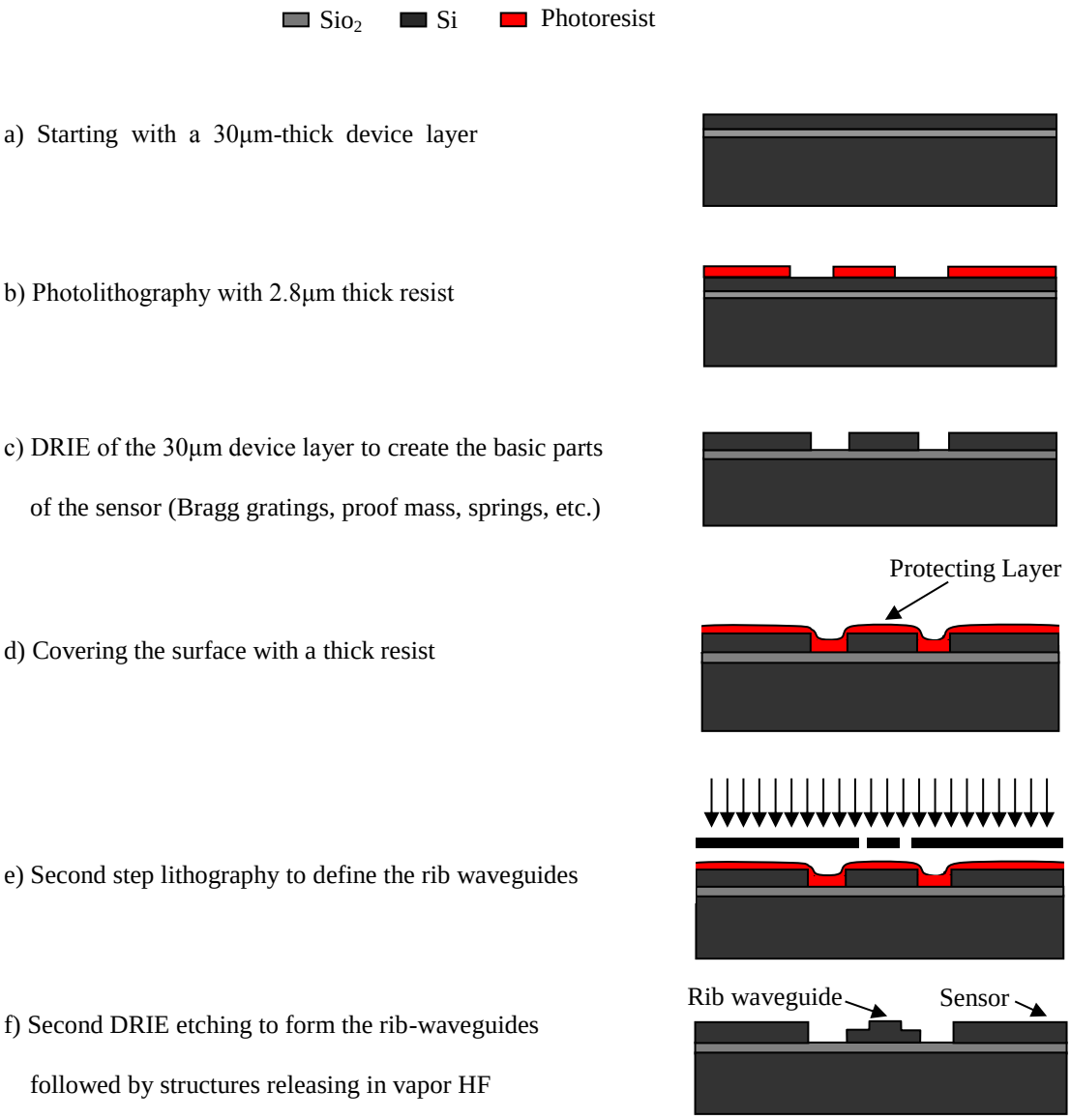

Figure 4-7: Fabrication process of optical accelerometers integrated with rib waveguides. Devices are fabricated on a SOI substrate with 30μm-thick device layer.

A FP-based accelerometer fabricated device is shown in Figure 4-11. In this figure two proof masses (8.1×10^{-7} kg) are suspended on eight springs having a designed overall stiffness of 6.125 N/m providing 2.75 kHz resonant frequency.

The movable DBR mirror is displaced when exposed to acceleration, producing a reduction in the length of the air gap of the FP filter. The other DBR mirror is positioned at the end of a waveguide collimator. The waveguide collimator is used to reduce the numerical aperture of the beam in the horizontal direction, reducing the divergence of the input beam. A gap of 27.1 μm was considered for the FP cavity to enable its future interrogation using a tunable laser with 30nm dynamic range.

The impact of fabrication imperfections on the effective finesse (F_{eff}) of FP cavity was studied in section 2.5.1. Scallops created on silicon sidewalls resulting from DRIE process introduces surface roughness defect to the system and reduces the effective finesse of FP cavity. Due to the scattering loss that light experiences at each round trip while it oscillates in the FP cavity, the life time of resonance photon in the cavity decreases, leading to the reduction in the optical quality factor and therefore widening the resonance peak. Deviation from parallelism and spherical bowing also contribute to reduction in effective finesse. Due to these fabrication imperfections, the real dimension of fabricated micro-structures (such as the width of silicon and air walls in the Bragg mirror and the FP gap) deviates from what is designed in the mask layout. This could be problematic if a very narrow band laser source is used, as the Bragg mirrors only act as a reflector for their design wavelength. If the width of silicon and air layers after fabrication do not satisfy the reflectance condition (Eq. (2.9)), the Bragg mirrors do not reflect the wavelength of the laser source. On the other hand, if a broad band source is used, the wavelength within the spectrum which is four times the optical thickness of the walls is reflected constructively and the layers act as a high reflector for that wavelength. This is the reason why a broad band source is used in our experiment. The same story for the FP gap is valid. The wavelength among the wavelength spectrum of the broad band laser source that satisfies the FP resonance condition (2.14) resonances and traverse the device and is detected in the optical spectrum analyzer.

SOI waveguides end facet polishing was done using lapping and polishing technique with Ultrapol End& Edge machine. A rotating lapping plate polishes the surface that is in direct contact with the lapping plate. Abrasive films bonded to the lapping plate with different grains

were used at different steps. First we started with coarse film having 20 µm abrasive diamond particles leading to 20 µm surface roughness for the silicon edge facet. The abrasive film was then replaced by films with smaller abrasive particle size ranging from 10 µm to 0.1 µm. The final polishing step with a film having 0.1 µm particle size is the most important and crucial step. The lapping needs to be done at low rotating speed (typically 60 rpm) for a longer time. Figure 4-12 (a) shows the SOI waveguide facet after polishing and Figure 4-12 (b) is the three-dimensional Atomic Force Microscopy (AFM) image of the surface profile of the waveguides facet after the polishing. The rms roughness of the facet surface is approximately 3.5 nm which is good enough when telecommunication wavelength range is used [119].

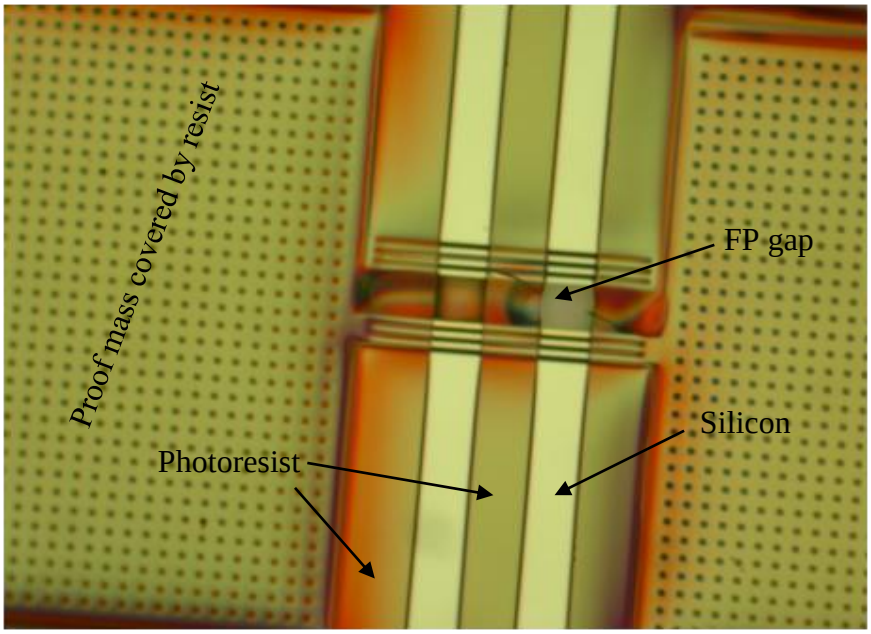

Figure 4-8: A FP-based optical accelerometer after second photolithography

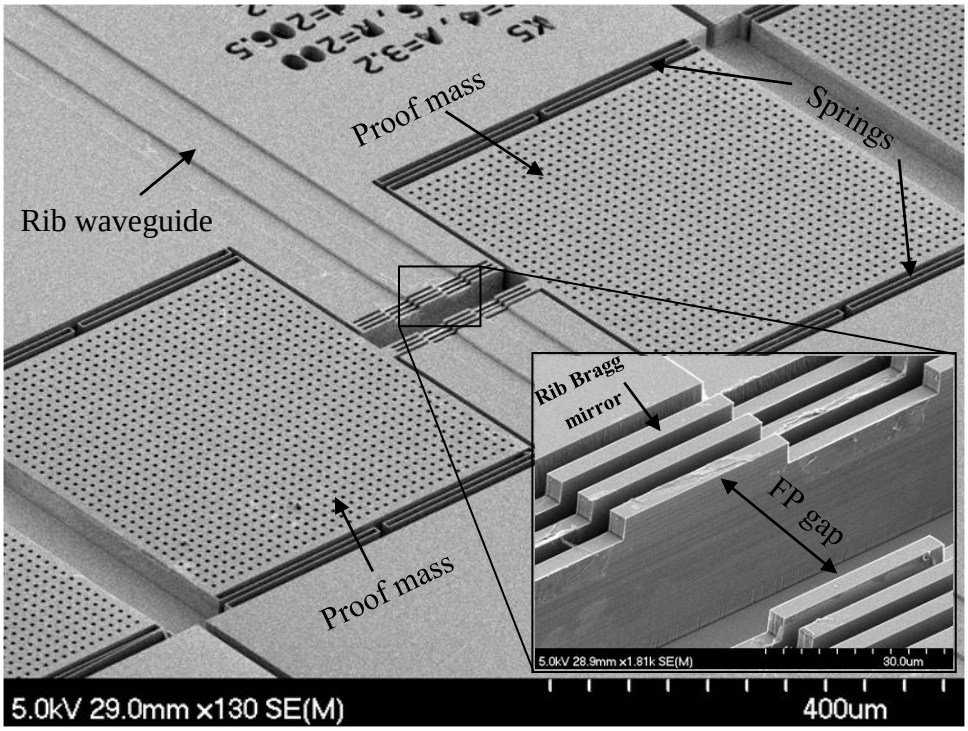

Figure 4-9: Fabricated FP-based optical accelerometer integrated with rib waveguides. Inset: Fabry-Perot cavity close-up view.

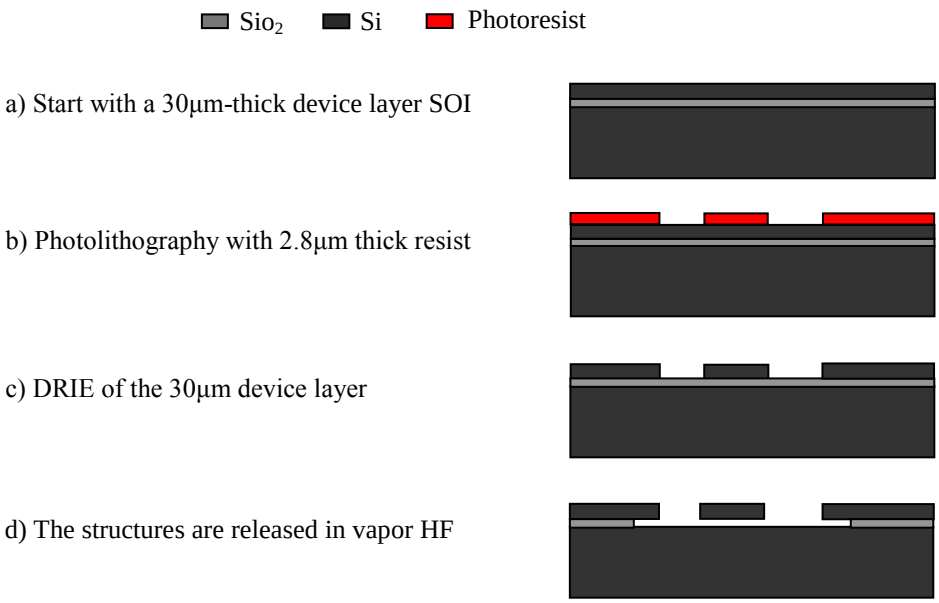

Figure 4-10: Microfabrication steps for the FP and VOA based accelerometers integrated with strip waveguides, fabricated on SOI substrate with 30μm-thick device layer.

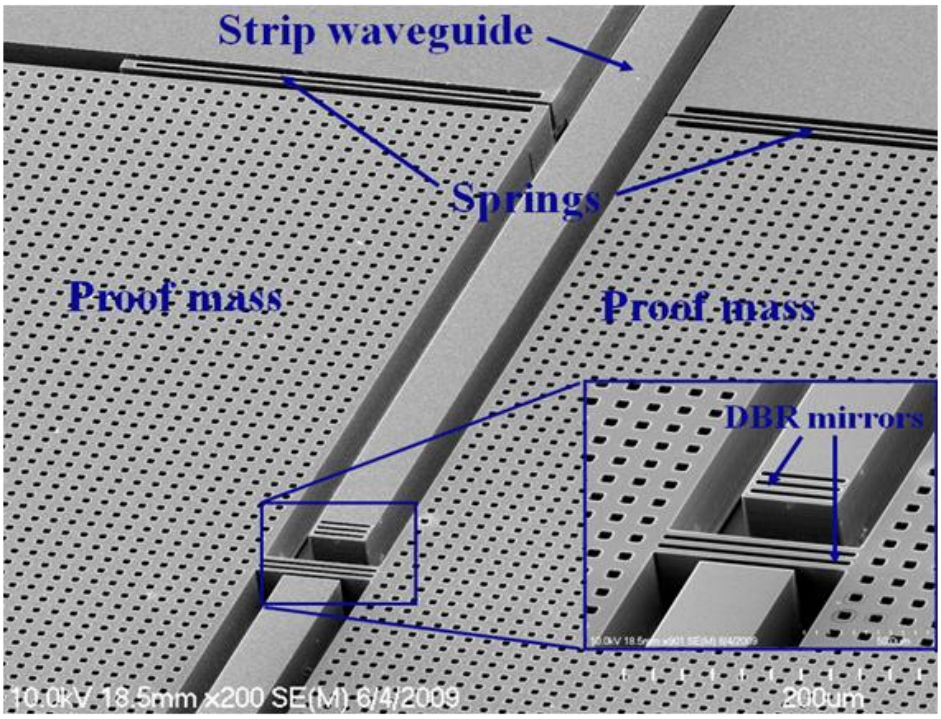

Figure 4-11: SEM photograph of the silicon microfabricated FP-based accelerometer integrated with strip waveguides.

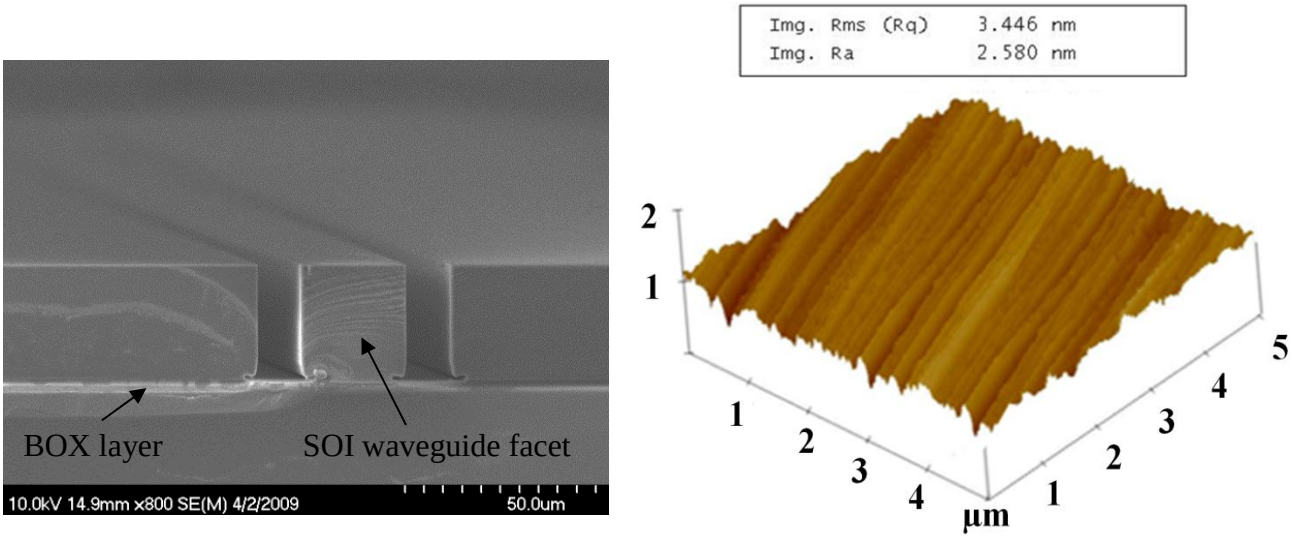

(a) (b)

Figure 4-12: (a) SOI waveguide facet after polishing, and (b)Three-dimensional AFM image of the waveguide's facet surface profile after polishing.

As mentioned above, the main challenge with strip waveguides is the waveguides lifting during the oxide releasing process. Thus the releasing process has to be carefully optimized so that the oxide layer under the strip waveguides will not be released while the proof masses are released. For that, etch holes with dimensions of 5 µm × 5 µm and 6 µm spacing are designed on the proof mass. The space between the two adjacent holes should be smaller than the width of the strip waveguides at the VOA junction (this is the part of waveguide with the smallest width of 12 µm), so that the proof mass can be released before they are released. If narrower waveguide is used at the VOA junction, the space between the two adjacent etch holes have to be reduced accordingly. After releasing the devices, they were checked mechanically by pushing the proof mass with a needle (using probe station) to ensure that the masses are completely released. Figure 4-13 shows optical images of two samples after the device releasing with different releasing time. Figure 4-13 (b) is an image of a sample with a broken waveguide showing that the oxide layer under the waveguide has not been completely released and Figure 4-13 (a) shows another sample where the waveguides are lifted up due to being over exposed to vapor HF.

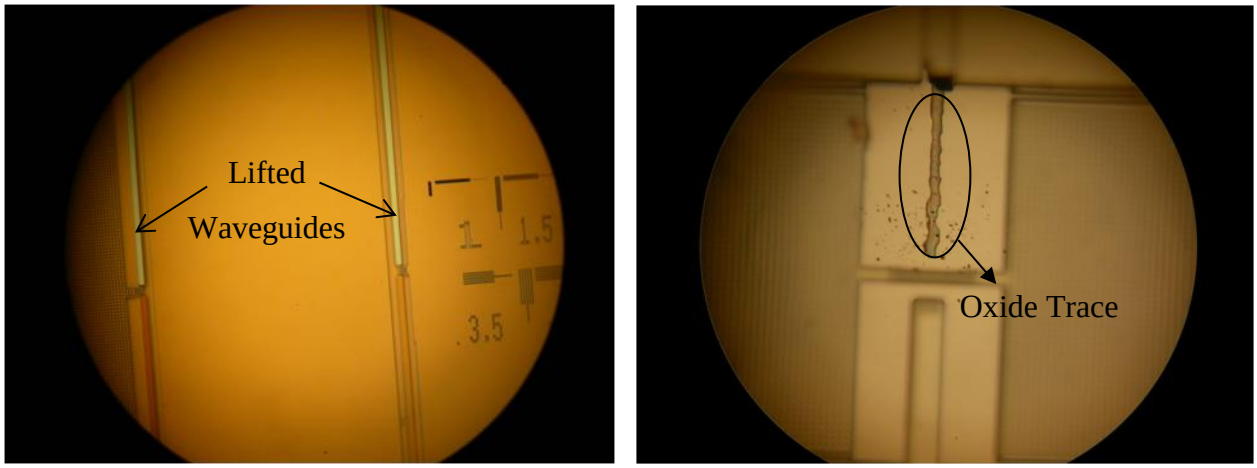

(a) (b)

Figure 4-13: Optical images of two different samples after releasing process (a) sample was exposed to vapor HF for long time leading to waveguides lift up, and (b) Sample that has been released with optimized releasing time. A part of waveguide was broke to check the remaining oxide layer under the strip waveguide.

4.2.2 47 µm thick SOI-VEM accelerometer process

In order to improve the coupling alignment instability between optical fibers and waveguides (that was observed when butt coupling method is used), U-grooves integrated with sensors were used to eliminate the tilt and transversal misalignment issues (Figure 2-25), allowing an easy alignment between the fiber core and the input/output waveguides. This also allows us to avoid the complicated and time consuming polishing. To determine the required thickness for the SOI substrate, there are three parameters that should be considered: fiber cladding diameter, fiber core diameter, and the divergence of the beam at the fiber output at a certain distance. The divergence of the beam should be considered, as there might be a gap between the fiber and the input of the waveguide after aligning the fibers via U-grooves. This is inevitable especially in our case where the fiber has to be bonded using ultra-violate (UV) curing optical adhesives. Because the generated stress by the glue while is dried by the UV exposure can create a gap between the fiber and the waveguide input and induce a longitudinal offset misalignment (Figure 2-25(d)) as for example can be seen in Figure 5-18 (b).

The optical fiber we used was a standard single mode (SM) fiber with 125 µm cladding diameter and 9 µm core. If the mode profile in the fiber is approximated by a Gaussian beam [107], the new beam waist radius w_1 at a distance z_1 from the fiber end facet having an initial beam waist radius w_0 is given by (2.41). For λ=1.55 µm and w_0 =9 µm, z_R=164 µm. Assuming that the separation distance between the fiber end facet and input waveguide is 100 µm (typical longitudinal offset misalignment that we experienced), providing w_1=10.5 µm. This difference (1.5 µm) should be compensated by the thickness of the SOI, to ensure that the entire beam leaving the fiber at this position (z_1=100 µm) will be completely captured by the input waveguide as shown in Figure 4-14. As the distance from the fiber cladding surface to the upper fiber core edge is 67 µm, the minimum required thickness including the oxide layer considering the beam divergence is 68.5 µm for the case of having longitudinal offset of z_1=100 µm. Deducting the oxide thickness (3 µm), the minimum required device layer would be 65.5 µm.

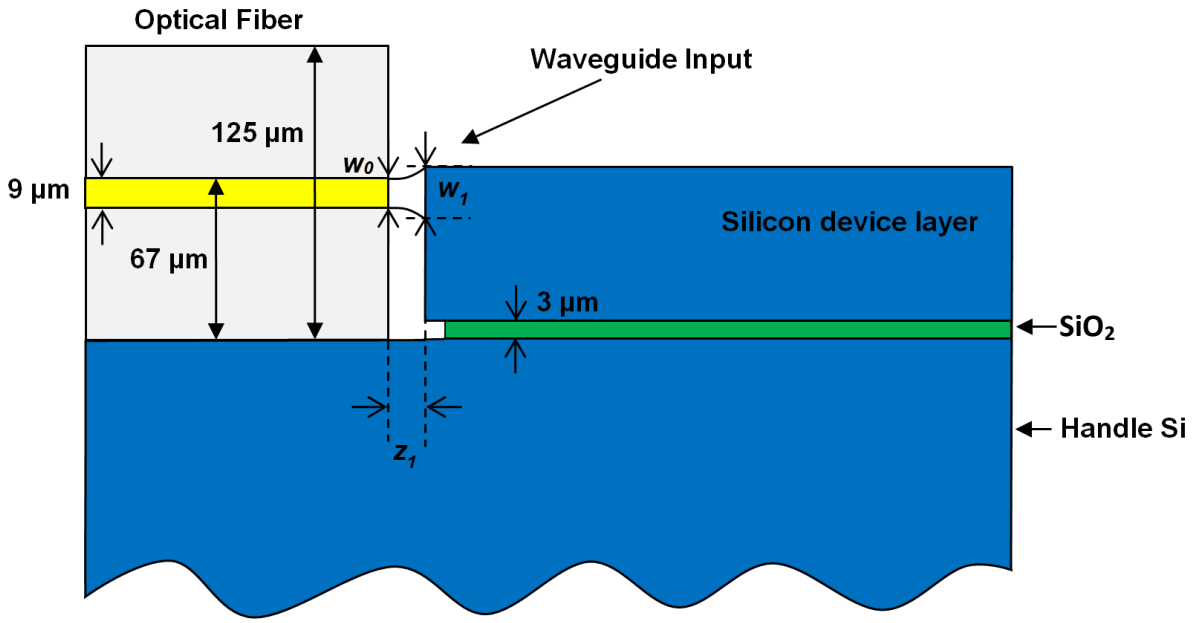

Figure 4-14: Alignment between fiber and input waveguide

Etching small features on a thick device layer is extremely challenging. The thicker the device layer, the thicker, the required resist thickness to etch the layer. This is because the resist mask is also etched during the silicon etching. In other words, resist shows selectivity to the DRIE process. The ratio of the silicon etching rate to the resist etching rate depends on the recipe used for DRIE. It was found that, this ratio is 13 for our recipe (Table 4-1). The thicker the resist, the lower the resolution one can get from the photolithography. Also etching features with high aspect ratio when SOI substrates with thick device layers are used is more challenging. Therefore we wanted to start with thinner device layer to minimize the risk of fabrication. 80 µm diameter SM fibers are commercially available. Let see what would be the required silicon device thickness if we use these types of fibers. In this case the distance from the fiber cladding surface to the upper core edge would be 44.5 µm. Therefore the minimum required thickness including the oxide layer, considering the beam divergence is 46 µm for the case of having longitudinal offset of z_1=100 µm. Deducting the oxide thickness (3 µm), the minimum required device layer in this case is 43 µm. We used SOI substrates with 47 µm-thick device layer to ensure that the beam is entirely coupled to the waveguide input. In this case the fiber core center is going to face the part of waveguide where it is 10 µm below the SOI surface. Single SOI and double SOI wafers are both used. Single SOI wafer as shown in Figure 4-14 consists of only one single device layer on top of an oxide layer. However a double SOI wafer consists of two device layer

separated by an additional oxide layer as shown in Figure 4-15. Double SOIs are used to guide the light only inside the top device layer providing thinner waveguides hence lowering optical loss by scattering from the side-walls roughness generated during DRIE process. Also with this configuration the notching phenomenon (Figure 4-4 (b)) at the bottom of the waveguides is minimized as the thickness of middle oxide layer is chosen to be thin (0.3 µm). Thinner the BOX layer, the less time is needed to etch a trench through the BOX layer, and therefore less time for deflection of SF_6 ions towards the bottom of the sidewalls. In other words, the thicker the oxide layer, the longer it takes to etch the oxide layer and therefore, the longer the oxide layer is charged, leading to longer time for deflection of SF_6 ions towards the bottom of the sidewalls and as a result generating more notching at the bottom of the trenches (Figure 4-4 (b)). Single SOI wafer are used to compare the results. The double SOI wafer consists of a thin and low doped (high resistivity) top Si layer that will be used for the optical part where the light is propagating, middle Si layer with lower resistivity, and the handle Si layer (Figure 4-15) separated by SiO_2 layers. Middle layer has lower resistivity because in the case of gyroscope, the sensor needs to be actuated with the comb drive and for that reason this part needs to be electrically conductive.

Figure 4-15 shows the dimensions of used double SOI wafer, having the following specifications:

15 µm thickness low doped top Si device layer

0.3 µm top SiO_2 layer

32µm middle Si device layer

3 µm bottom SiO_2 layer

500 µm Si-handle layer

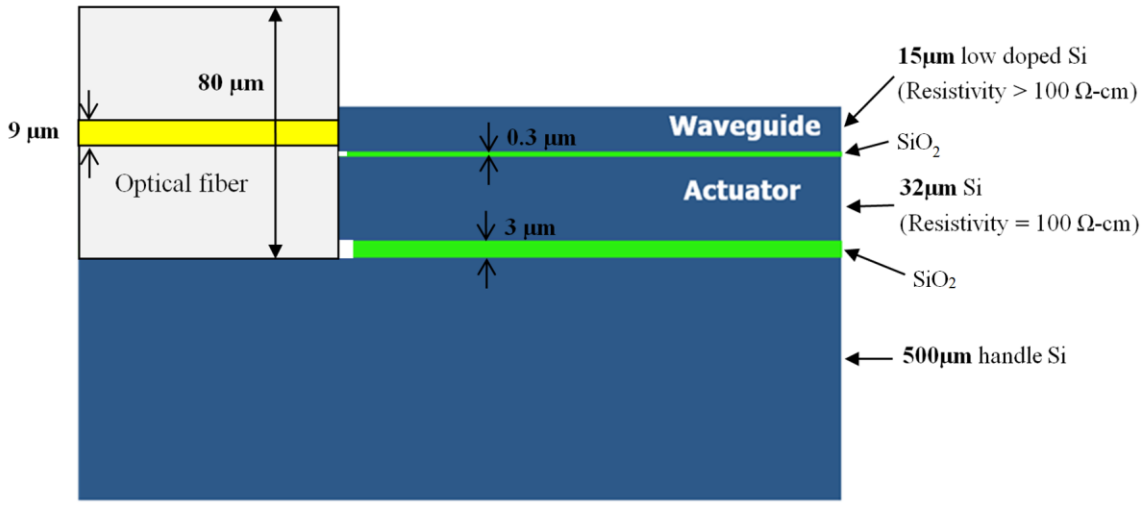

Figure 4-15: Dimensions of used double SOI

Figure 4-16 illustrates the device fabrication process. The device is fabricated using two masks.

The single SOI wafer has the following specifications:

47 µm thickness Si device layer (resistivity=100 Ω-cm)

3 µm SiO_2 layer

500 µm Si-handle layer

The attainable proof mass was extended further by adding mass from the Si handle layer to the device layer as illustrated in Figure 4-16. From now on, we will call this method "Vertically Extended Mass" (VEM). This approach presents a three dimensional structure for the device and maximizes the attainable proof mass and can provide the highest achievable acceleration sensitivity. Since there is no underlying substrate, the VEM- MEMS approach also provides the lowest achievable stiction. The proof mass is composed of all five layers. First, 2 µm-thick oxide layer is sputtered on the front side of the wafer (on the top device layer) to protect the front side surface during the back side fabrication (a), followed by Cr deposition and lift-off on the backside (b). Then DRIE on the backside is carried out to reach the bottom BOX layer (c). The sputtered oxide is then removed followed by photolithography on the front side (device mask is aligned with the Cr mask at this point) (d). Next, the patterned device resist mask was etched using DRIE all the way down to the bottom BOX layer (e). Finally, resist stripping; followed by

proof mass releasing using vapor HF from the backside (f) completes the fabrication process. Releasing the structure from the backside prevents the strip waveguides of being directly exposed to the vapor and being lifted up as the result. Waveguides, U-grooves, springs and the device structure are patterned at step (e) and the substrate mass-adding to the sensor proof mass (providing higher sensitivity) is undertaken at step (c). Many tests were done to optimize the DRIE process of the device layer. In many cases micro- grasses (section 4.1.1) appeared at the bottom of the etched trenches as shown in Figure 4-17. This is believed to be due to the presence of the top oxide layer that acts as a mask for the middle device layer. This slows down the etching process and stops it at some point. This phenomenon was eliminated by increasing the etching time in the DRIE process.

The 500 µm backside DRIE in silicon was the most challenging part of the fabrication. At the beginning, the front side etching was carried out prior to the backside etching. The etched front side (including 2 µm wide flexure springs) was protected by a thick layer of resist (SPR 220-7.0) and was mounted on a silicon support wafer coated with a very thick resist as shown in Figure 4-18. The caused stress led to the spring's breakage. Therefore to avoid this issue, the front side etching was performed after the backside etching as explained in Figure 4-16. Figure 4-19 (a) and (b) show the SEM photograph of the etched 500 µm backside. In order to speed up the etching process, etching to deposition ratio time was increased (20:8). This will cause some roughness and angling on the Si side walls (Figure 4-19. b), but this is not critical to the device operation since only the top Si structures (waveguides and MEMS comb electrodes/flexures) are participating in the device optics and sensing.

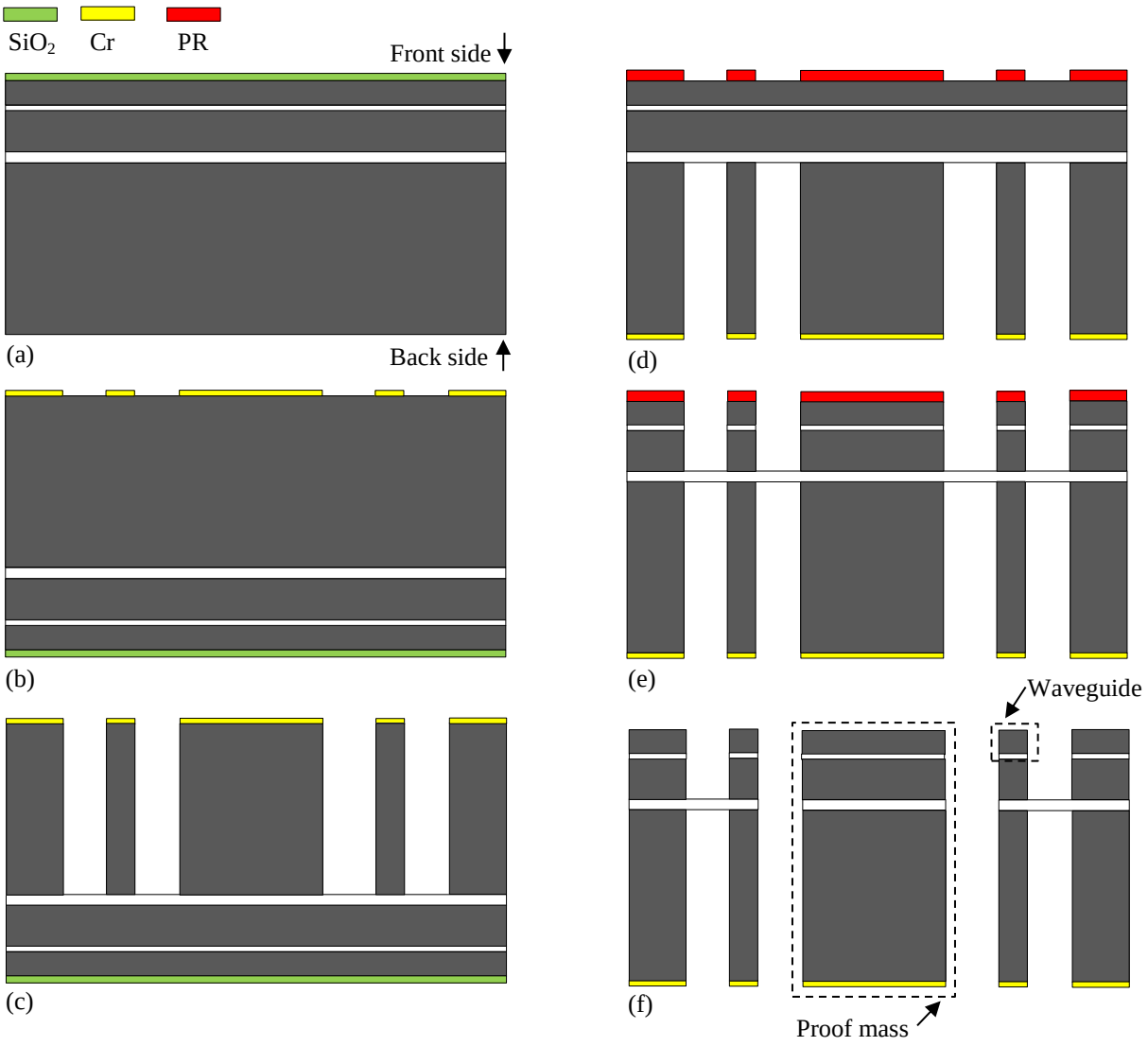

Figure 4-16: Fabrication process for optical accelerometers using double SOI: (a) 2 µm oxide layer deposition on the front side of the wafer to protect it during the fabrication on the backside, (b) Cr deposition and lift-off on the backside, (c) DRIE on the backside until the bottom BOX layer is reached, (d) removing the sputtered oxide protection layer followed by photolithography on the front side, (e) DRIE on the front side until the bottom BOX layer is reached, and finally (f) resist stripping followed by proof mass releasing using vapor HF from the backside.

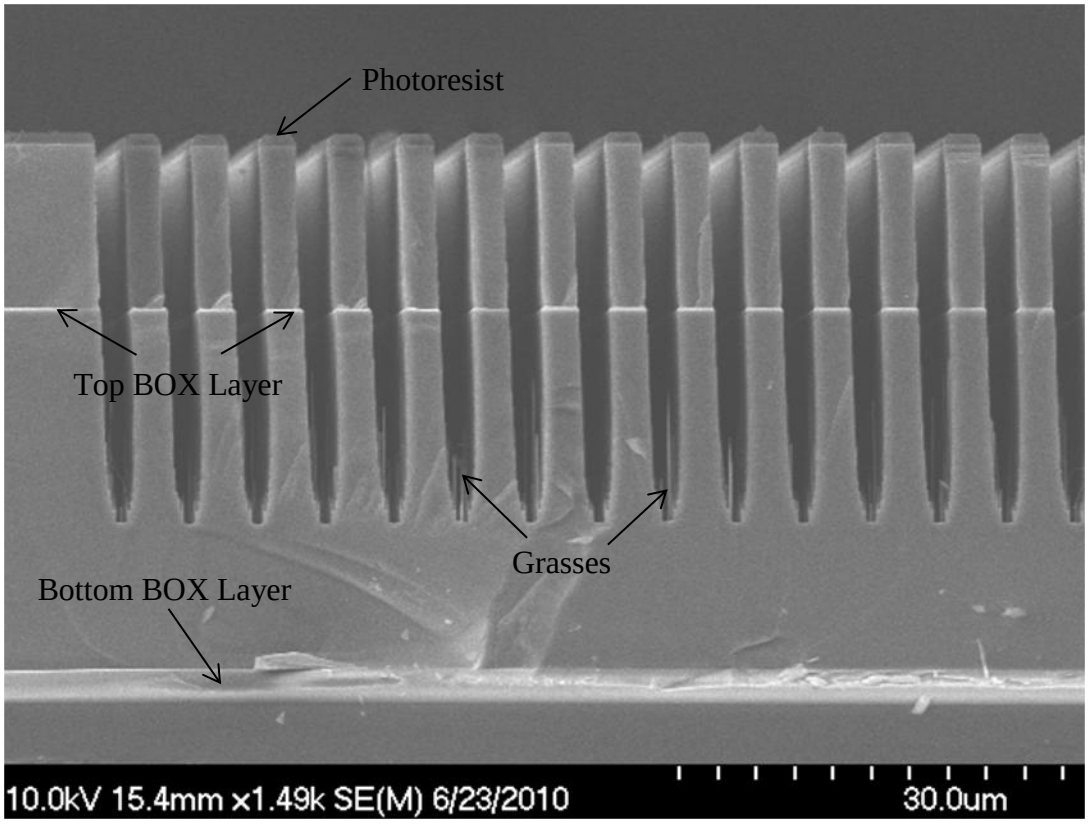

Figure 4-17: An array of 2 μm etched trenches. Presence of grasses at the bottom of the trenches slows down the etching process.

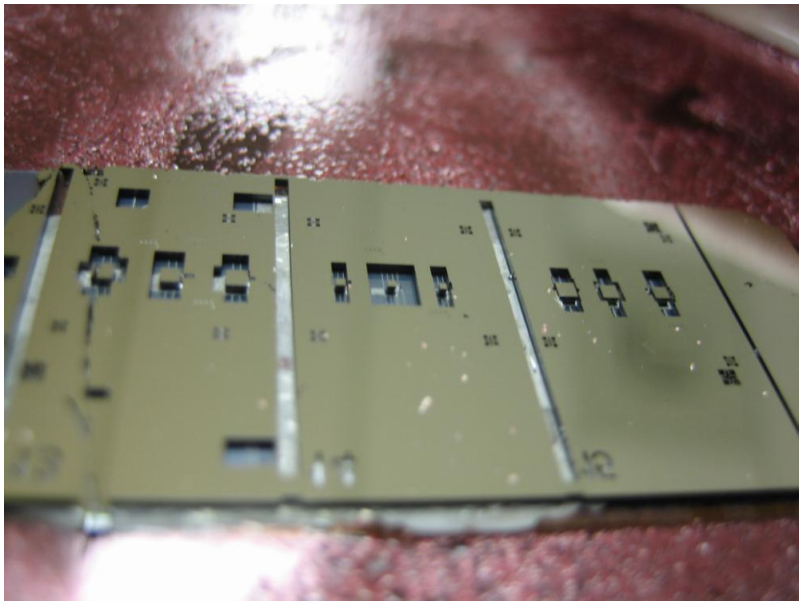

Figure 4-18: Photograph of several VOA accelerometer devices after the 500 μm backside DRIE of SOI for the case of VEM approach.

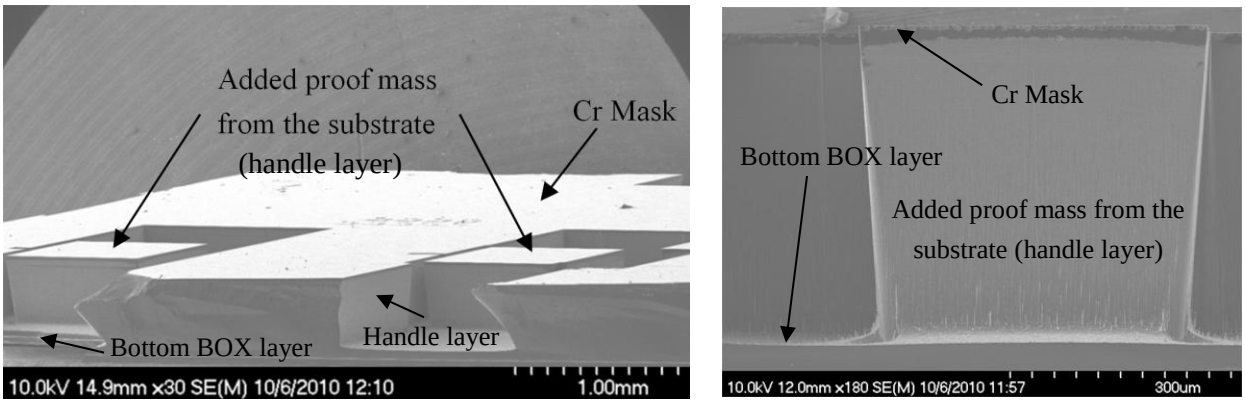

(a) (b)

Figure 4-19: SEM photograph of 500 µm backside DRIE of SOI for VEM approach, (a) Side view, (b) Front view.

Figure 4-20 shows a VEM fabricated VOA-based optical accelerometer.

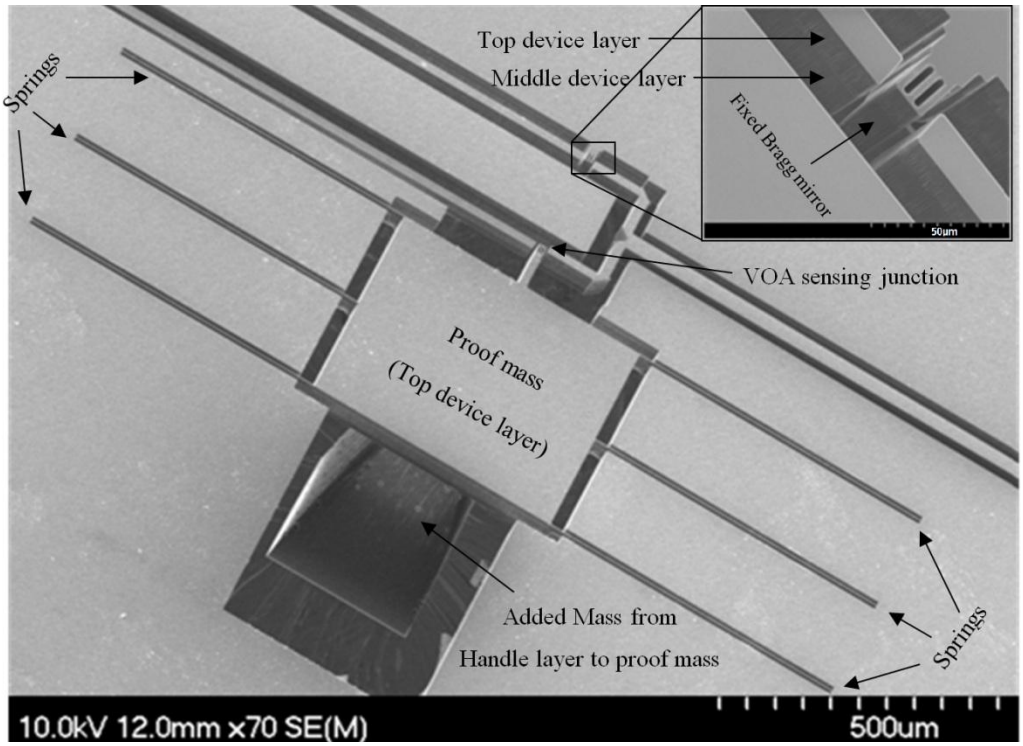

Figure 4-20: SEM photograph of the fabricated VEM VOA-based optical accelerometer with added mass from Si handle on 47 µm double SOI. Inset: close up view of the Bragg shutter. The width of the input and output waveguides are 20µm.

Figure 4-21(a) shows the integrated input U-groove. For device characterization, the input and output fibers need to be bonded using UV-curing optical adhesives. In order to prevent epoxy flow into the MEMS structure, 2 µm-wide staggered dams are used at the input and output waveguides. Due to the presence of the top oxide layer, the side walls on the middle 32 µm device layer are not smooth (Figure 4-21.b). This does not affect the device optics performance since only the top Si layer is contributing to the device optical performance.

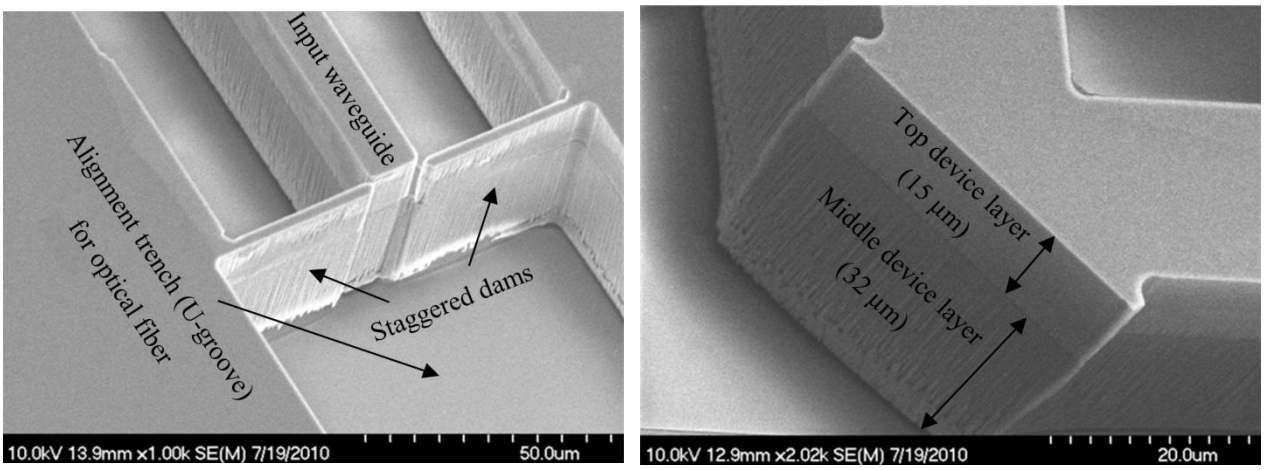

(a) (b)

Figure 4-21: (a) Integrated input U-groove with added staggered dams, and (b) Right-angle waveguide bend, showing smooth waveguide sidewalls in the 15 micron top Si device layer with some roughening in the lower 32 micron-thick middle Si device layer.

Figure 4-22 and Figure 4-23 show the fabricated VOA-based gyroscopes on double SOI and single SOI substrates respectively. For the gyroscope fabricated on double SOI, the structure needs to be actuated by the comb drive and as the top Si layer is not electrically conductive enough, we need to reach the middle layer in order to apply the voltage, meaning additional photolithography and etching steps. The problem here is to uniformly cover photoresist on top of such a high topography surface. There have been many efforts with different recipes and resists to uniformly cover the structure. Thick SPR 220-7.0 resist is used with different spinning and baking recipes. The main issue was the bubbles formation after resist soft baking (Figure 4-24 (a)). Also some air cavities were observed after resist spinning and soft bake as shown in Figure 4-24 (b). The bubbles formation is believed to be due to the expansion of air in the air cavities

and the resist solvent evaporation during the soft baking [120]. The formation of air cavities and bubbles can be explained as follows:

During resist spinning, due to the centrifugal force that resist experiences (and also the resist viscosity), resist cannot flow down along the sidewalls of trenches with high aspect ratios, leading to the formation of air cavities.

The volume thermal expansion change of air is given by $\Delta V = V_0 \beta \Delta T$, where V_0 is the initial volume of trapped air, β is thermal expansion coefficient of air, and ΔT is the change in temperature. Trench length, width, and depth are 1 cm, 5 μm, and 40 μm respectively, providing $V_0 = 2 \times 10^5 \mu m^3$. Air thermal expansion coefficient at room temperature ($T_0 = 293\ °K$) is $\beta = 3.4 \times 10^{-3} 1/°K$. Resist was baked at 100º C or 373 º K, yielding $\Delta T = 80\ °K$ resulting in $\Delta V = 5 \times 10^4 \mu m^3$. From Figure 4-24 (a), the total volume of the three bubbles (assuming they are all lining up in one trench) is approximately $6 \times 10^6\ \mu m^3$ (considering each bubble as a hemisphere with radius of 100 μm). This is approximately two orders of magnitude smaller than volume change caused by thermal expansion. This leads to the conclusion that the bubbles are formed mainly by the evaporation of resist solvent during baking.

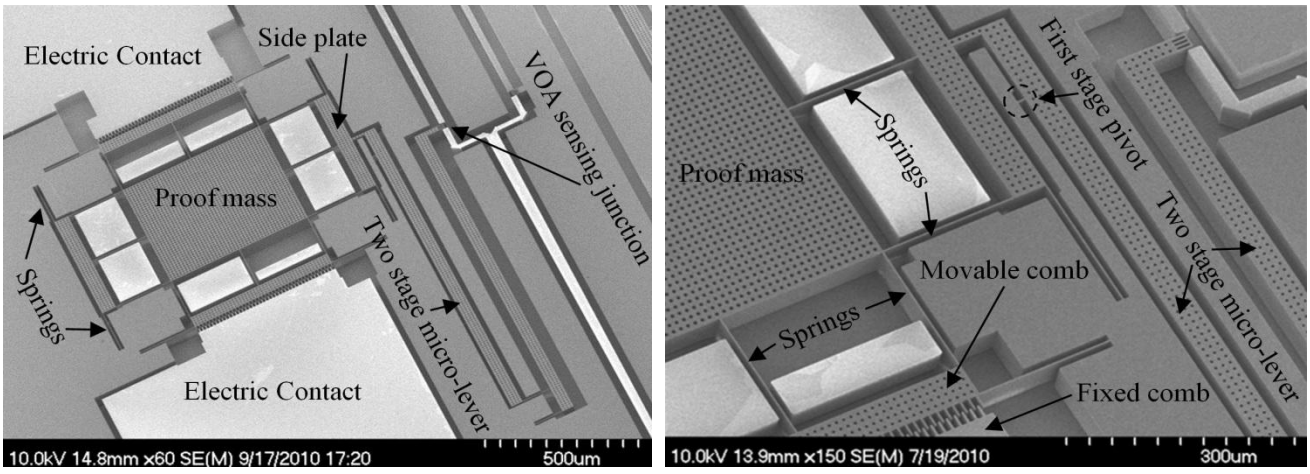

(a) (b)

Figure 4-22: (a) Fabricated VOA-based gyroscope integrated with two stage micro-lever on 47 μm double SOI, (b) close up of the device.

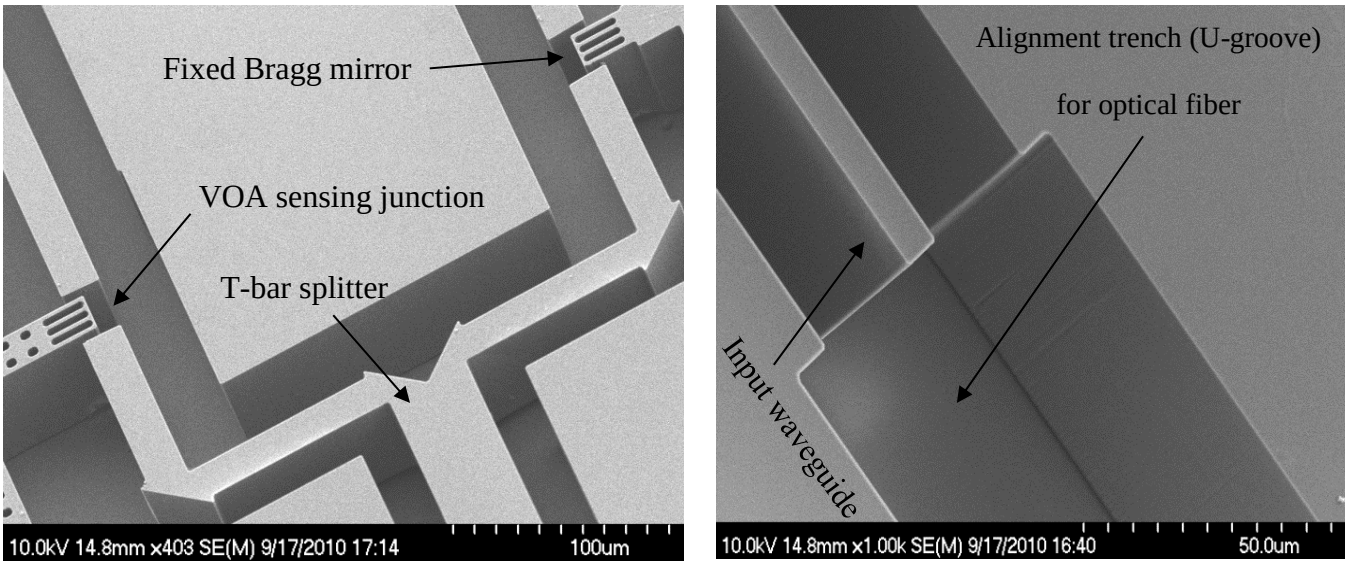

(a) (b)

Figure 4-23: (a) Close up of the VOA sensing junction of the fabricated VOA-based gyroscope on 47 µm single SOI, (b) Input waveguide and its associated U-groove (for optical fiber to silicon waveguide light coupling).

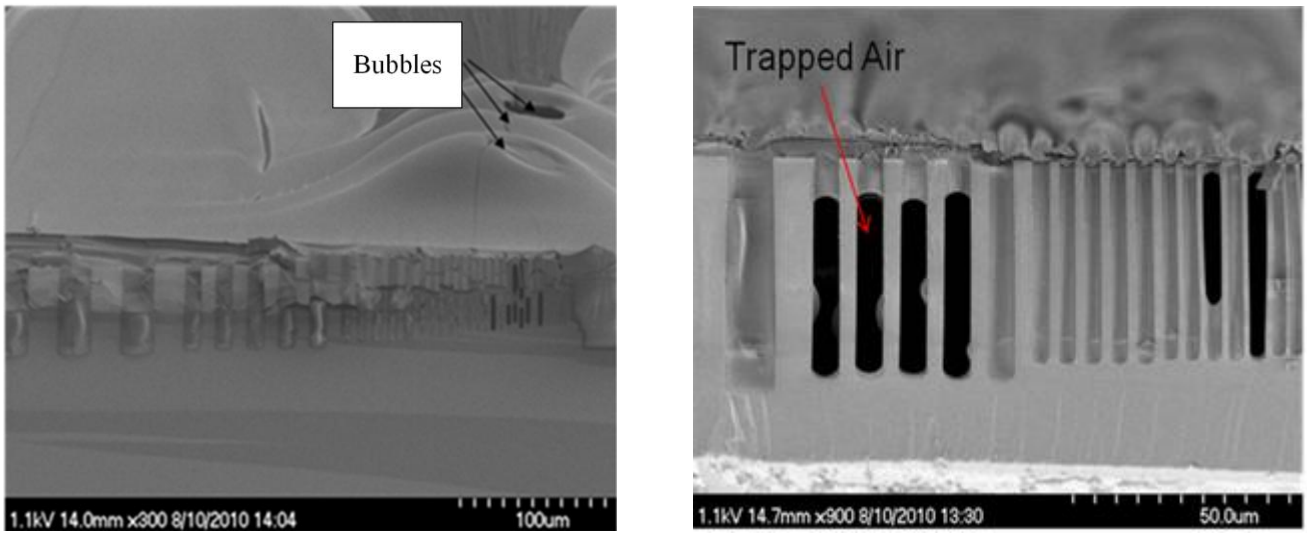

(a) (b)

Figure 4-24: An array of trenches with 50 µm depth and different widths covered by a thick layer of resist SPR 220-7.0. (a) Bubbles are formed after soft baking due to resist solvent evaporation. (b) Some cavities are observed after resist spinning and soft bake.

These bubbles are exploded during the DRIE process, causing damages on the protected areas. Figure 4-25 (a) and (b) show a sample after UV-exposure and DRIE respectively.

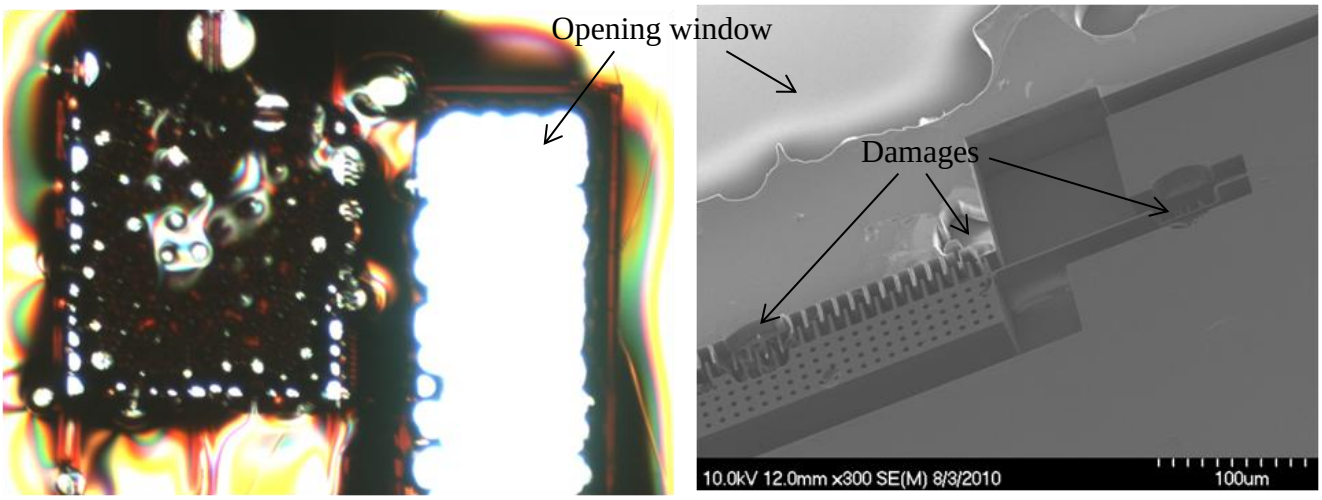

(a) (b)

Figure 4-25: (a) Photograph of a sample with 47 µm topography coated with thick resist after UV-exposure, (b) Same sample after DRIE.

Another issue is the spring's breakage during the spinning step caused by the centrifugal force. Figure 4-26 is a photograph of a sample after resist spinning.

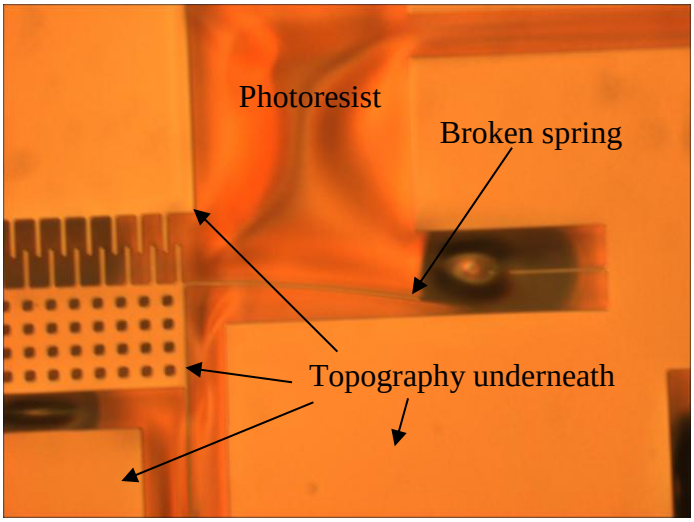

Figure 4-26: Photograph of a sample after resist spinning. Springs get broken due to the centrifugal force.

In order to overcome these issues, a new method of coating on high topography surfaces called Dynamic Surface Tension (DST) coating was investigated and successfully implemented (see section 4.3).

4.2.3 75 µm thick SOI Process

As described in previous section, for the VEM approach, 80 µm fibers were used to couple light to the sensor. Cleaving 80 µm fibers were very challenging since most commercial cleavers have been designed for standard 125 µm diameter SM fibers. Although the VEM approach maximizes the attainable proof mass and can provide higher acceleration sensitivity, the fabrication requires two separate DRIE steps and the resulting fabrication yield is low, requiring additional process optimization. In the next phase of this work, 75 µm-thick SOI wafers were used to overcome these two challenges. First of all it allows us to integrate standard 125 µm telecom optical fibers to the chip and secondly it provides a thicker device layer helping to get thick enough proof mass without adding mass from the wafer backside (handle layer). However etching 75 µm silicon is more challenging and requires thick resists as the mask. The problem with using a thick resist is that it limits the lithography lateral resolution. The lithography process was optimized to get the highest possible resolution. 6 µm-thick resist is used as a mask for the DRIE. The best conditions resulted in 1.5 µm lateral resolutions for the lithography which was good enough for our application as the minimum feature size was 2 µm (spring's width). As the MEMS structure displacement is in the order of micrometers, the strip waveguides widths at the VOA sensing junction interface are gradually tapered to 12 µm in order to increase the signal intensity variation leading to better sensitivity for the device (Figure 4-27). As seen in Figure 4-28, waveguides at the sensing junction are anchored to the substrate preventing them from lifting after releasing the oxide layer. These anchors will introduce some optical loss to the system but they will have no impact on the device optical performance. Figure 4-27 and Figure 4-29 show the fabricated accelerometer and gyroscope based on VOA. After etching, the remaining resist is stripped off. The oxide underneath (BOX layer) is then removed (using vapor HF) to release the structure.

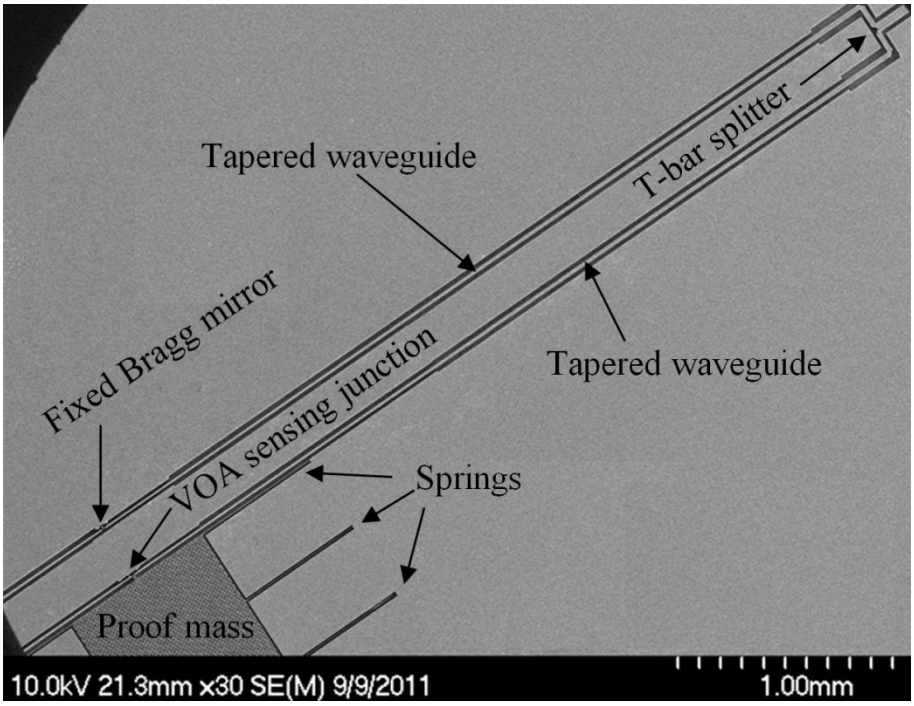

Figure 4-27: SEM photograph of the VOA-based optical accelerometer fabricated on 75 µm SOI. Strip waveguides widths at the VOA sensing junction interface are tapered to 12 µm to increase the sensor sensitivity.

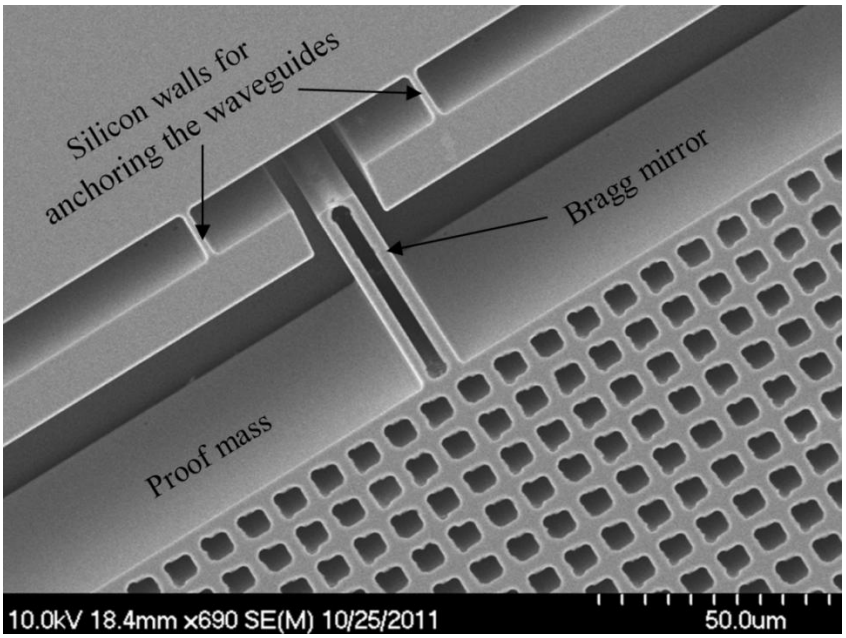

Figure 4-28: SEM photograph of the VOA sensing junction fabricated on 75 µm SOI. Strip waveguides at the VOA sensing junction interface are anchored to the substrate to prevent them from lifting after releasing the oxide layer.

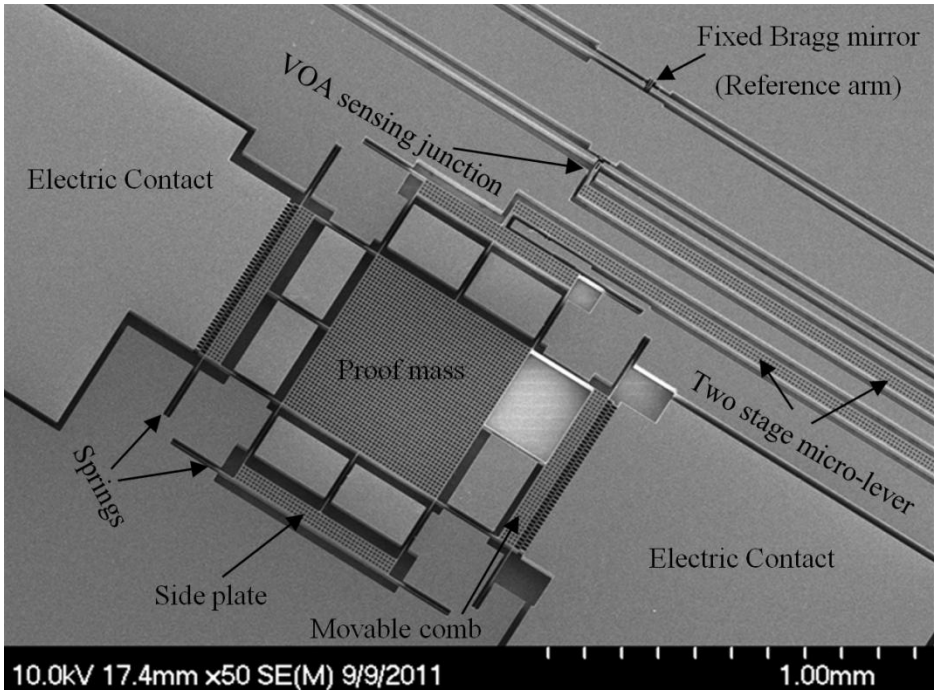

Figure 4-29: VOA-based gyroscope integrated with two stage micro-lever fabricated on 75 µm SOI.

4.3 New Photoresist Coating method for high topography surfaces

Surfaces with high topography are usually called for surfaces having deep trenches, for instance trenches etched in silicon with 10 µm, 20 µm or 100 µm heights. With the development of MEMS and the growing use of three dimensional microstructures, new techniques are required to fulfill the demand for uniform photoresist coverage over non-planar surfaces with high topography, like trenches, V-grooves, and cavities. Thus, the conformal photoresist coating of wafers with three dimensional microstructures becomes a critical step in the integration process. In the MEMS fabrication process of devices, there are three main different photoresist coating techniques: spin coating, electrodeposition (ED) coating [124], and spray coating [122]. Several efforts to obtain a conformal coating layer by using spin coating have been reported [122], [123]. Although spin coating is an established technique for resist deposition, it is often not suitable for applications with high topography on silicon or glass surface because of defects generated in the resist layer during the process. More specifically, the photoresist flows down along the sidewalls of trenches due to gravity, gathers at the bottom corners, and is detached at the top corners, as shown in Figure 4-30. This figure shows an array of trenches that were fabricated in silicon by

using deep reactive ion etching (DRIE) process, and were further coated with commercial photoresist shipley SPR 220-3.0 using spin coating method.

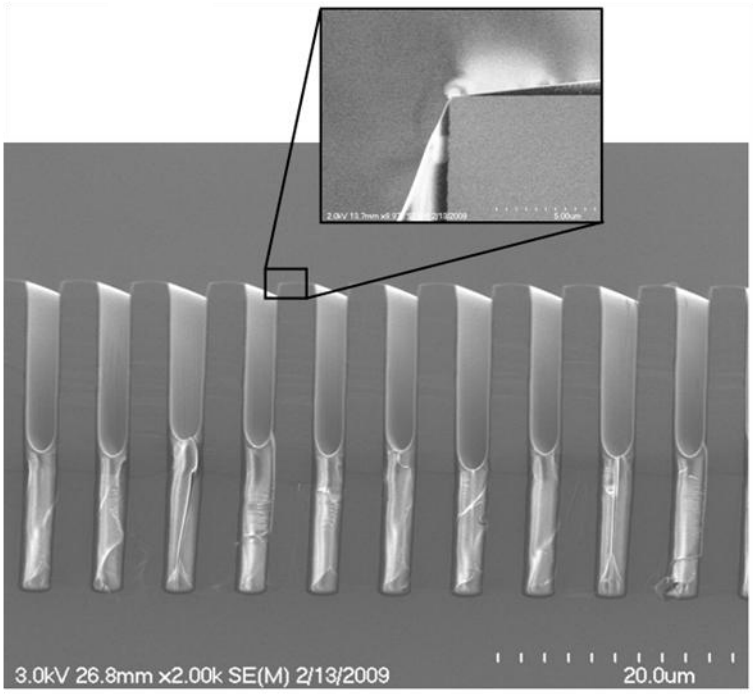

Figure 4-30: An array of trenches with resist coated by spinning method.

Electrodeposition of photoresist has been reported as a useful method for three dimensional stacks of chips [124] but it requires a conductive layer. In the case of spray coating, no commercial photoresist exist that could be used without being diluted. Also the diluted photoresist is thick (9μm) not allowing to get a good resolution, the thickness of photoresist is not uniform and depends on the geometry. For instance, if coating an array of cavities, only those cavities having the same size would be covered with the same thickness of photoresist [124]. Here we report a new method that is based on the Nanometrix Inc. [125] technology, called Dynamic Surface Tension (DST) [128]. We used a commercial photoresist (Shipley SPR 220-3.0) to achieve uniform photoresist coverage not only on planar surfaces, but also on a micromachined surface with high topography. Photoresist has the same thickness (1.5μm) everywhere independent of the geometry of the patterned surface. Table 4-2 shows a comparison of this new technique with the three other existing ones.

Table 4-2: A comparison between DST technique and three others techniques.

	SPIN COATING	ED COATING	SPRAY COATING	DST COATING (Nanometrix)
Process	Simple Geometry dependent	Complicated	Simple Geometry dependent	Simple Geometry independent
Substrate material	Conductor or Insulator	Only conductor	Conductor or Insulator	Conductor or Insulator
Photoresist	Commercial	Specific ED resist	Not commercial 8μm resolution	Commercial 1.5 μm resolution
Resist uniformity	Not uniform on pre-existing topography	Uniform	Depends on geometry	Uniform

The DST deposition method that Nanometrix uses can be briefly described as follows. Resist is poured on a surface of a liquid, called carrier liquid (here water) that has a greater surface tension (than resist) in the presence of a gas (here air). The spread resist is driven by a surface tension force (called driving force) on the substrate that is placed on a movable handle, called wafer handling unit (WHU). Key parameters that influence the thickness, uniformity and quality of the photoresist layer are:

- Solid content of the solution
- Solvent evaporation rate and miscibility
- Temperature
- Gas pressure
- Speed of WHU

Since this technique has been developed by Nanometrix Inc. and is not a part of this work, the details of the work cannot be stated here. For more information readers are referred to [129].

Most conventional photoresists cannot be used directly for DST coating because of their high viscosity. Therefore they have to be diluted with solvents in order to lower their viscosity. Basically the DST coating system can be operated using solutions with viscosity lower than 470 cP. Using too viscous photoresists cause small driving force and therefore create non uniform layer. Several photoresist solutions have been investigated in order to find the most appropriate one for the purpose of coating high topography surfaces.

We have investigated AZ9260 resist solutions that are diluted from the original photoresist by adding solvents. Also SPR 220-3.0 resist was used without dilution.

4.3.1 Experiments and results

Several <100> silicon samples containing array of trenches with different widths etched by DRIE, were prepared for the DST coating experiments. Water and air are used as the carrier liquid the gas in the experiments. Unlike other coating methods, in DST coating photoresist is coated on top (stacked) of the trenches.

Figure 4-31 shows SEM pictures of a sample coated with AZ9260 resist diluted with butyl alcohol using DST method. As seen, the coating is not uniform. The thickness of photoresist is 4μm at the top of steps whereas at the corners is almost zero, meaning the deposited film is not planar.

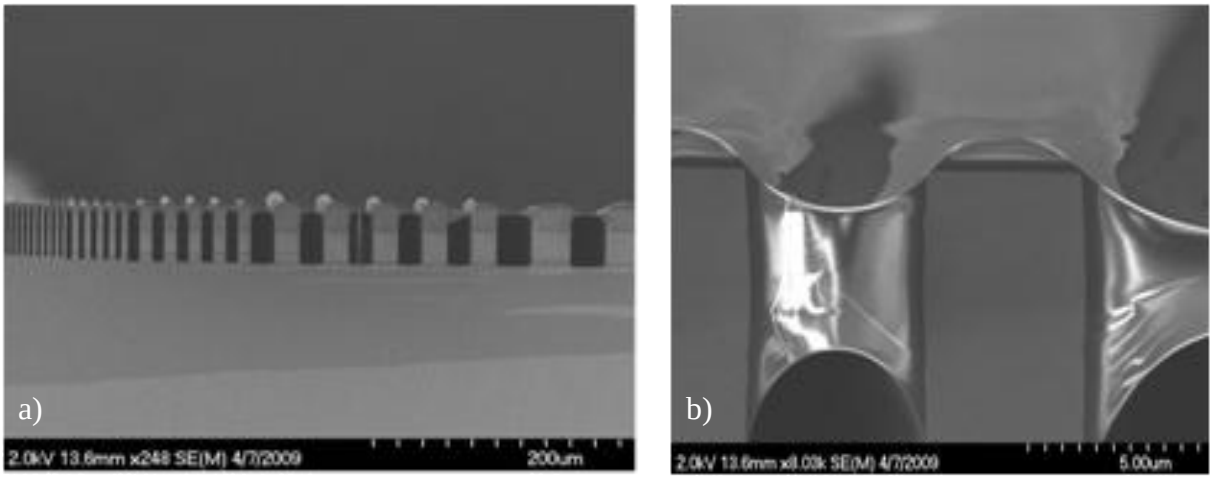

Figure 4-31: a) Coated AZ9260 resist diluted with butyl alcohol, b) zoom on one trench.

We define the degree of planarization (DOP) as:

DOP= $\acute{h}/_{h}$×100,

where $\acute{h}$ is the thickness of photoresist at the corner of steps and h is the thickness of photoresist on top of steps, respectively, as shown in Figure 4-32. Clearly, when $h \doteq h$, DOP is 100%.

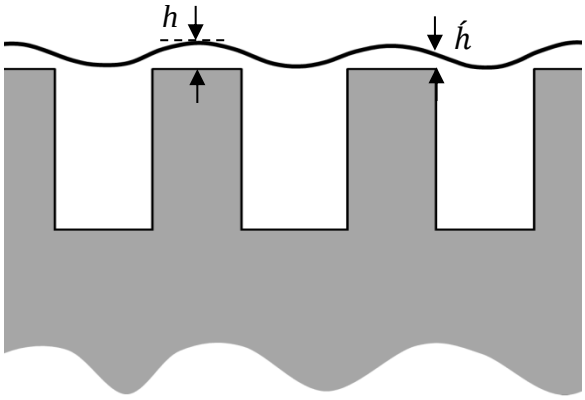

Figure 4-32: Schematic of the coated film profile.

The degree of planarization increases with decreasing distance between trenches (or steps) and with increasing film thickness (high viscosity photoresist) when spin coating method is used [130]. In DST method, planarization is independent of trench (or steps) height which is a great advantage over other methods. As the coated film flow deeper, $\acute{h}$ decreases leading to a poorer planarization. From Figure 4-31, $\acute{h}$=0, leading to zero planarization. Figure 4-33 shows a more uniform coating realized with AZ9260 photoresist diluted in acetone.

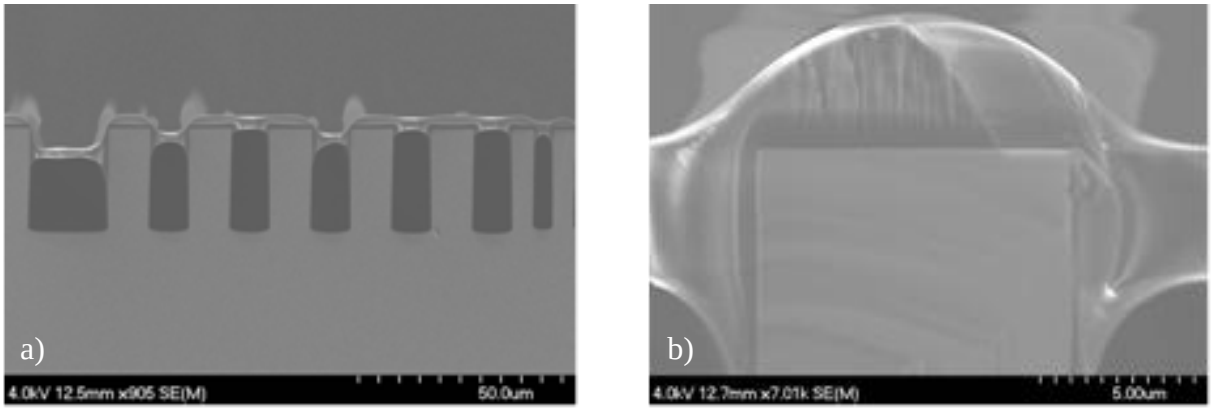

Figure 4-33: a) Coated AZ9260 resist diluted with acetone, b) zoom on one trench.

The thickness of photoresist is 4.7μm on the top of steps and 1.8μm at the corners, providing 38% planarization.

Another sample was coated with SPR 220-3.0 photoresist. Since this type of photoresist has low viscosity, we did not dilute it with any solvents. The resulting coated profile is shown in Figure 4-34. The coated photoresist on top of the steps and trenches are uniform and has the same thickness as that at the corners ($\acute{h} = h$), providing 100% planarization. The thickness of photoresist is 1.5 μm everywhere and is independent of trench (or cavity) depth. The resist is suspended over the trenches due to the resist surface tension. Since the coated photoresist is thin, lithography with high precision (1.5 μm) is feasible. It should be noted that, while the DST coating is independent of the trench depth, it is limited by trench width. The maximum required width to get the resist uniformly coated on the trench, was not investigated but as seen in Figure 4-34, trenches up to 50 μm have uniformly coated. Figure 4-35 shows the entire left edge of the trench array. As seen in this case, the resist layer has collapsed on the bottom of trench.

In the next step, the coated sample was patterned using photolithography with a mask containing lines with different widths as illustrated in Figure 4-36. Then the sample with the patterned resist was etched by DRIE and as a result the patterns were transferred to the bottom of the trenches (or top of the steps). Figure 4-37 shows the same sample after photolithography and etching. The bottom of trenches and the top of steps have been perfectly etched while preserving the masked areas. This technique can be used to overcome the photolithography problem on the structures with initial topography that we faced for the gyroscopes fabrication on double SOI (Figure 4-25). The 47 μm-thick structure can be easily covered with SPR 220-3.0 photoresist using this technique if the limit on the trench width is applied in the structure design. It should be mentioned that the DST technique was not finally used on the devices as the final devices were fabricated on single SOI.

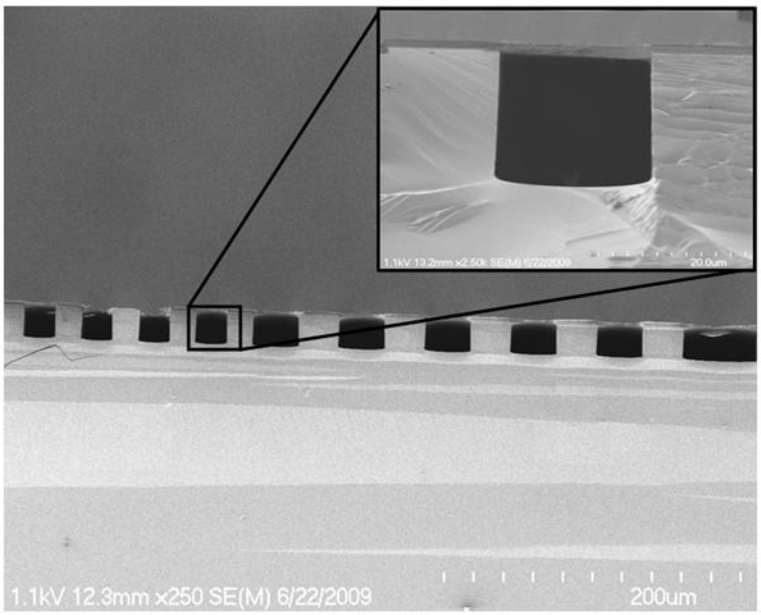

Figure 4-34: Coated SPR 220-3.0 resist.

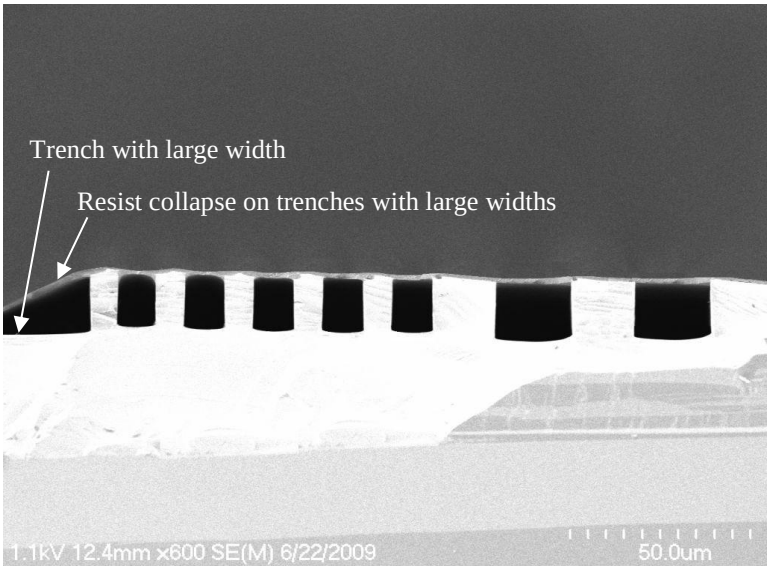

Figure 4-35: The entire edge of an array of trenched. Resist cannot be suspended over the trenches with large widths.

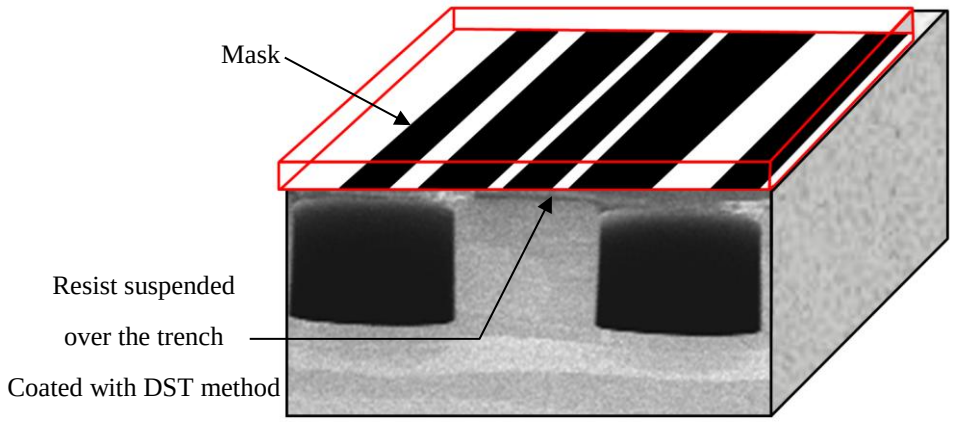

Figure 4-36: Photolithography on the suspended resist over the trenches coated by DST method.

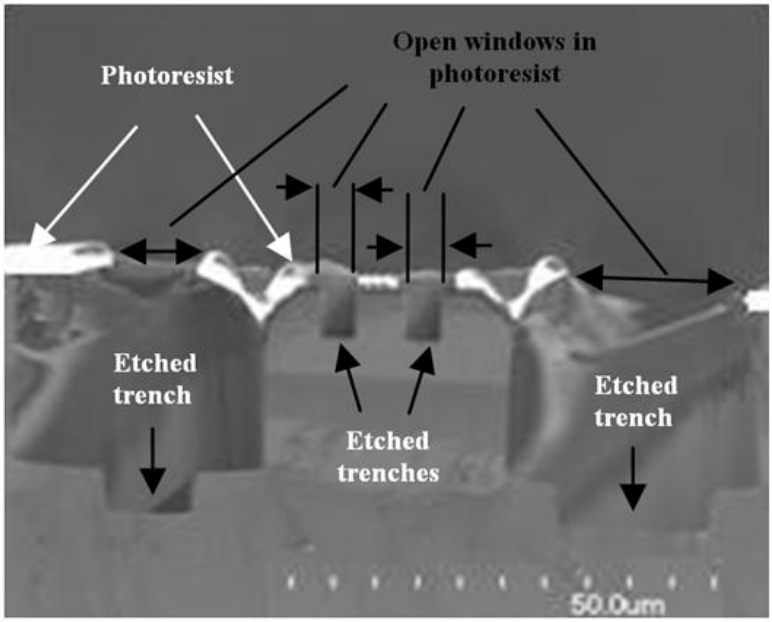

Figure 4-37: Etched sample after photolithography and DRIE.

Figure 4-38 (b) shows a different sample after stripping the photoresist. The edges of the trenches are sharp demonstrating the uniformity of the coating. Figure 4-38 (a) is the schematic of the photolithography process on the coated SPR 220-3.0 photoresist on the array of trenches shown in Figure 4-38 (b).

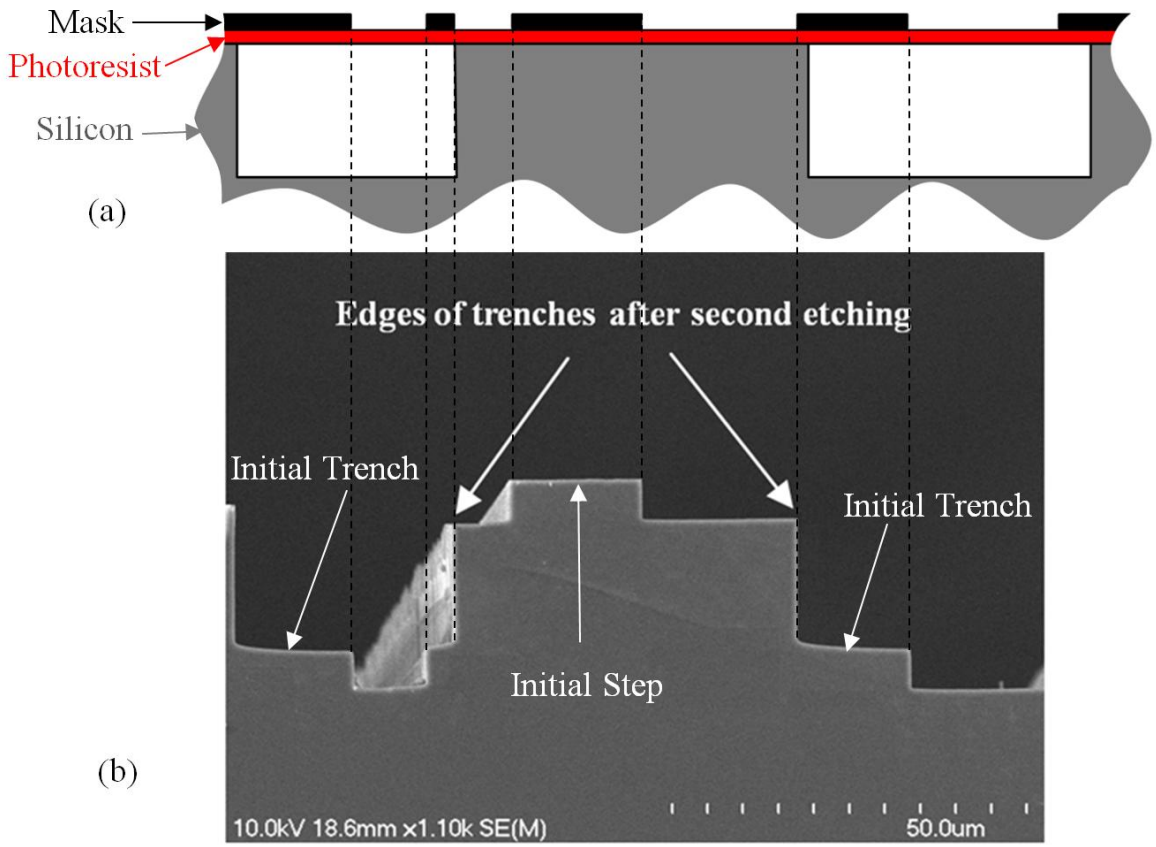

Figure 4-38: (a) Schematic of the photolithography process on the coated SPR 220-3.0 photoresist (using DST method) on a structure with pre-existing topography (array of trenches), (b) Sample after photolithography, DRIE and resist stripping.

In conclusion we have successfully coated uniformly a commercial photoresist on a surface with high topography. Solid content of the solution, solvent evaporation rate and miscibility, temperature, gas pressure, and speed of WHU are the key parameters that play important roles in the coating process. Photolithography on the coated resist on top of trenches was successfully performed, followed by etching on the sample with the patterned mask (patterned suspended resist on top of trenches). The resist uniformity is independent of the depth of the trenches; however it is restricted by trenches widths. The DST coating method can be used to overcome the photolithography problem on the micromachined structures with high topography that we faced for the gyroscopes fabrication on double SOI wafers. Since the etching ratio of resist to silicon is 1:13 for our DRIE recipe (Table 4-1), 1.5 µm resist can easily survive during the 15 µm (thickness of the top device layer) DRIE of the top device layer.

CHAPTER 5 CHARACTERIZATION

5.1 Mechanical characterization

To ensure that the structure is completely released, each sample was mechanically tested using a probe station (Figure 5-1). The tip of a needle which is attached to a micro stage is placed on the side of the device proof mass. The proof mass is then displaced by pushing it by the needle tip using the micro stage. Figure 5-2 shows a released VOA accelerometer that is pushed by the needle. As seen in this figure, bended springs after pushing the proof mass demonstrate that the sample is successfully released.

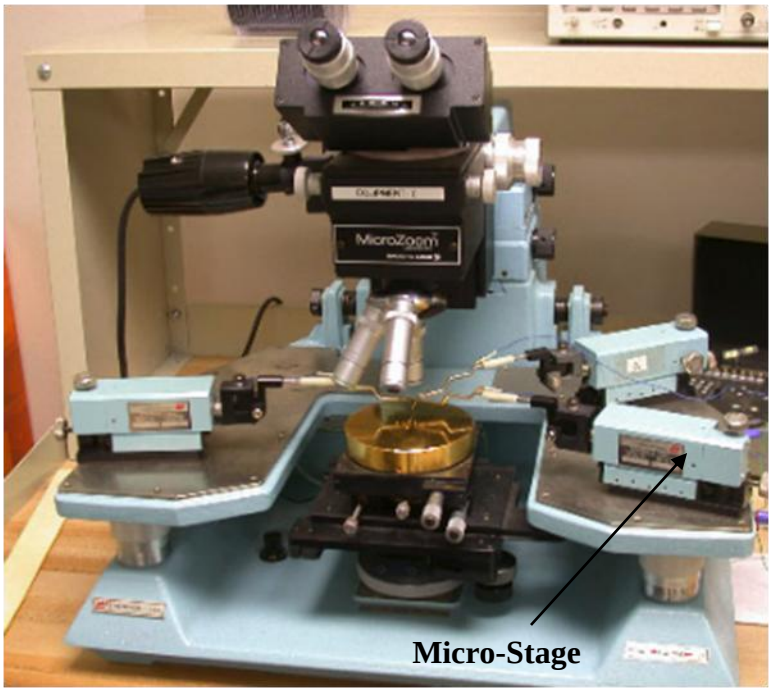

Figure 5-1: Probe station setup for sample release testing.

Vibration tests are also accomplished by actuating the samples with a piezo actuator. Figure 5-3 demonstrates a VOA accelerometer response to different actuator frequencies. The piezo actuator frequency is tuned and the accelerometer displacement is measured. As the actuator frequency approaches the resonant frequency of the device, the proof mass displacement amplifies. According to Figure 5-3, the resonant frequency of the accelerometer is 1.4 kHz which was slightly different from the theory (1 kHz). The difference arises from the fabrication deviations

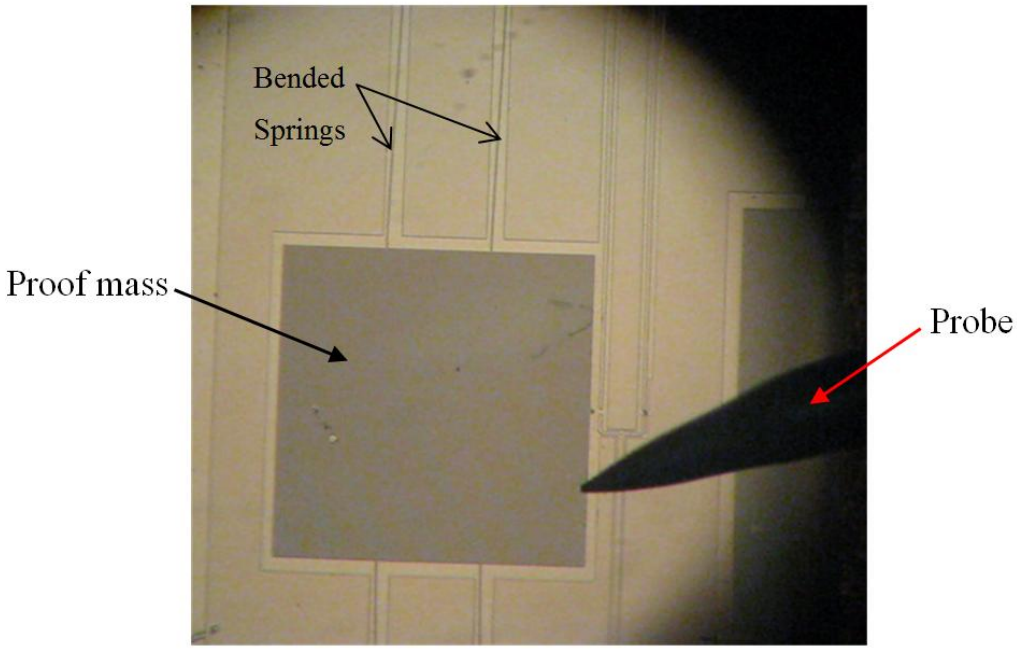

Figure 5-2: Release testing of a VOA accelerometer with a needle.

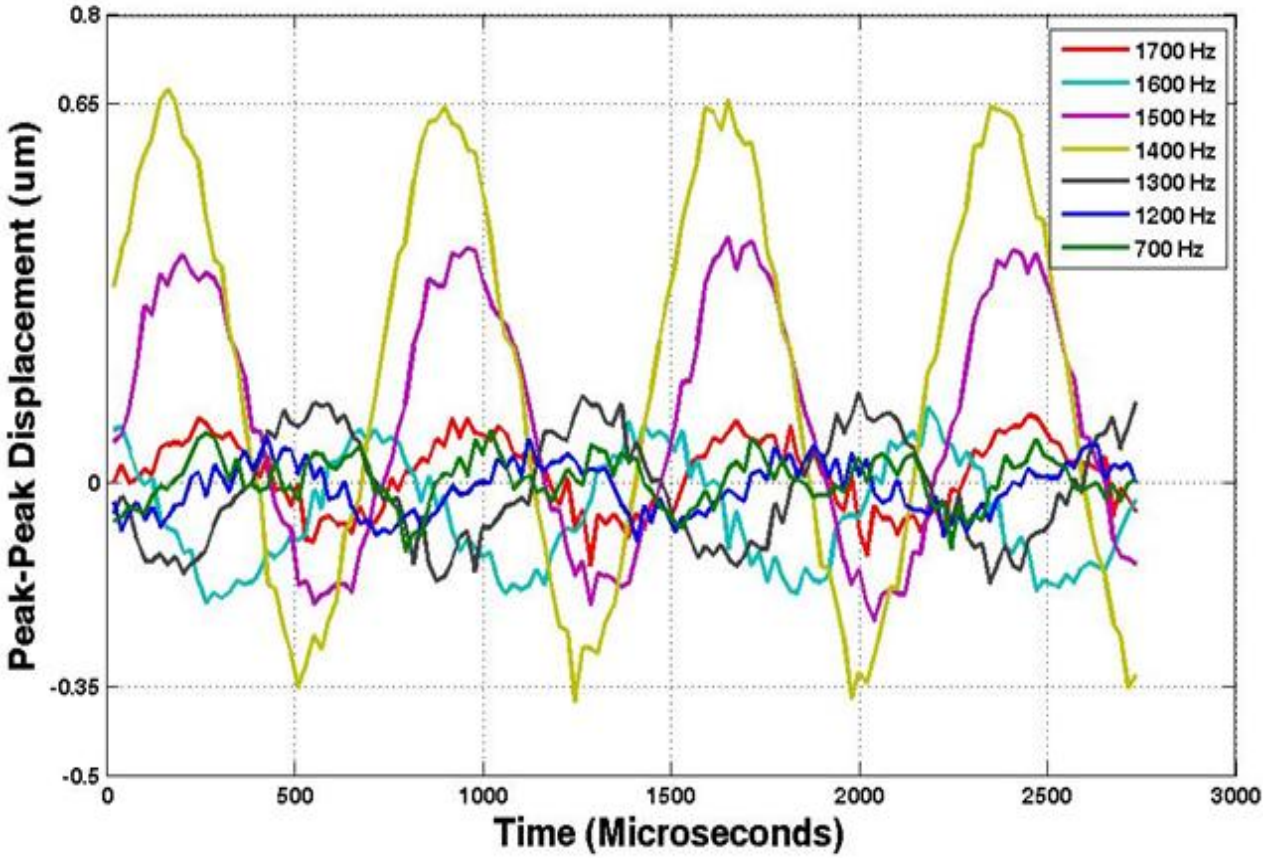

Figure 5-3: Mass displacement of a VOA accelerometer for different actuator frequencies.

such as notching phenomenon and photolithography diffraction. Figure 5-4 shows the corresponding acceleration versus the actuation frequency.

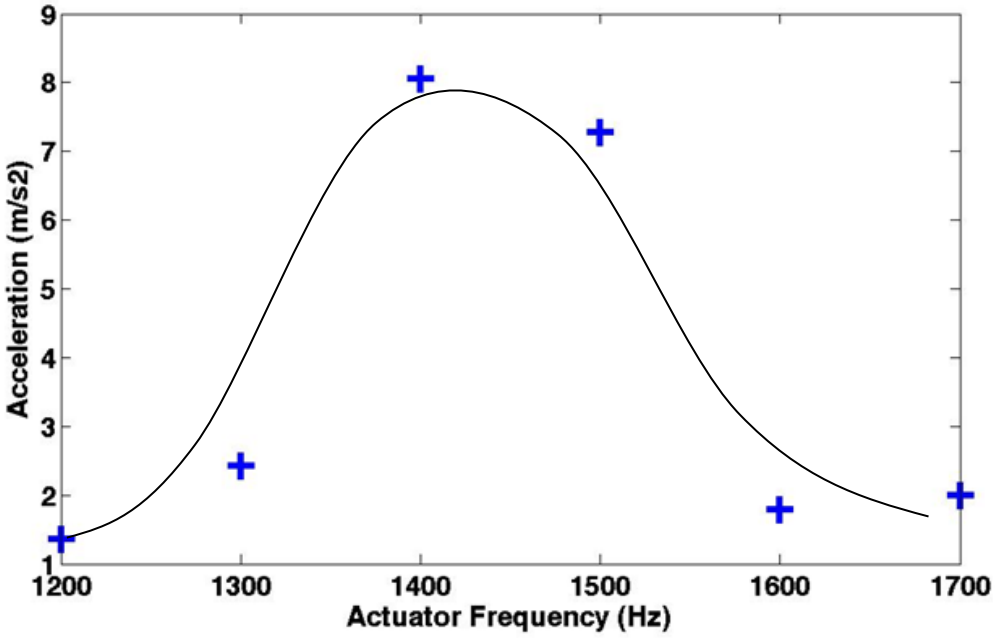

Figure 5-4: Experienced acceleration versus the actuator frequency.

5.2 Optical characterization

5.2.1 30 µm thick SOI accelerometers

FP-based accelerometer integrated with strip waveguides

Experimental setup for the FP-based accelerometer testing is shown in Figure 5-5. Light from a broadband source (1520nm-1620nm) is transmitted using butt coupling into the input waveguide through an optical fiber. The transmitted light is collected by a second optical fiber, which is butt coupled to the output tapered waveguide on one side and to an optical spectrum analyzer on the other side. The whole setup is attached to an inclinable board that can be tilted. Acceleration is applied to the device as a consequence of gravity by tilting the board ($g\ sin\theta$). The transmission peak of the FP shifts to shorter wavelength, while increasing the angle of inclination (sensing accelerations from 0 to 0.83g). Two proof masses (1.36×10^{-7} kg) are suspended on eight springs (Figure 4-11) having a designed overall stiffness of 15 N/m providing ω_n=10.5 kHz natural

frequency. Figure 5-6 compares the measured and simulated transmission spectra of the device. The initial transmission peak is 1589.33nm. As acceleration is increased, the air gap between the two Bragg reflectors is decreased resulting in transmission peak shift toward shorter wavelengths. The filter can be tuned continuously down to 1559.33nm for a total tuning range of 30nm. A larger tuning range could be achieved by using a smaller gap since it would provide a larger free spectral range. The FWHM of the peak is 2.4 nm. A transfer matrix method (Eq. (2.4)) is used to simulate the transmitted light across the FP filter by considering a plane wave incident beam. Due to the fabrication imperfections (deviation of lateral dimensions generated by photolithography and etching processes (such as notching)), the measured peaks are not exactly located at the same locations predicted by the simulations.

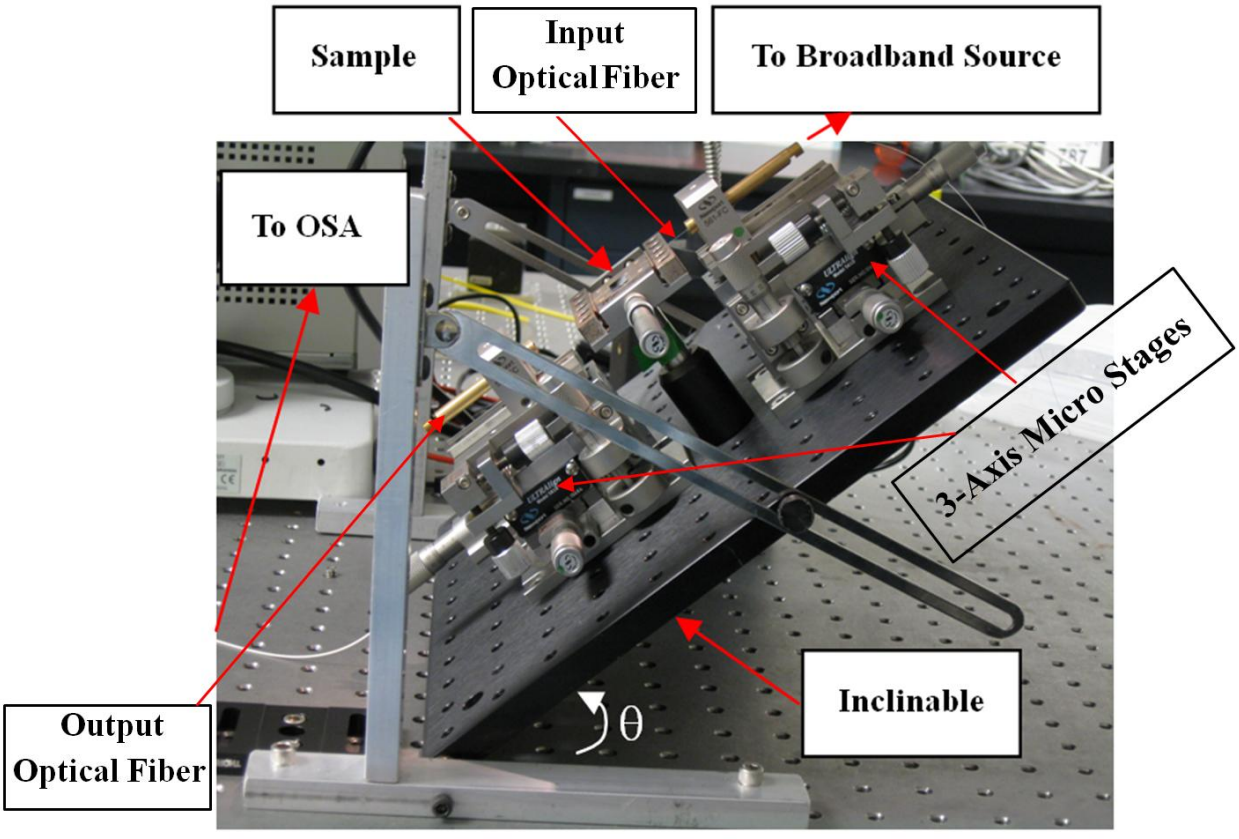

Figure 5-5: Optical setup for the characterization of the accelerometers.

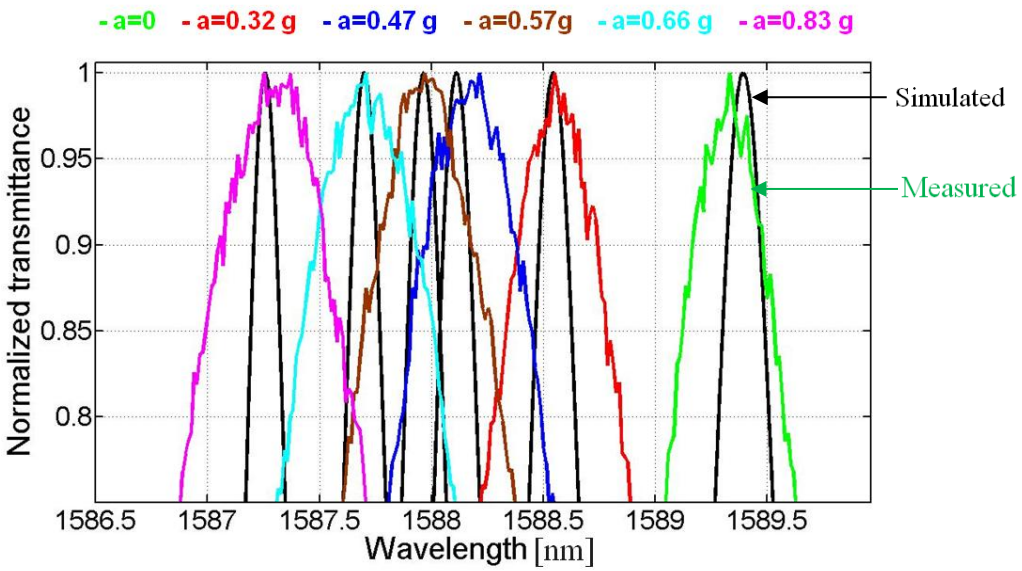

Figure 5-6: Measured (colored curves) and simulated (black curves) transmission spectra of the FP-based accelerometer integrated with strip waveguides for various accelerations (ω_n=10.5 kHz).

Figure 5-7 shows the applied acceleration versus the resonant wavelength shift of the FP filter with ω_n=10.5 kHz (two proof masses (1.36×10^{-7} kg) suspended on eight springs (Figure 4-11), having an overall stiffness of 15 N/m). 2.5 nm/g sensitivity is extracted from the curve leading to 4 mg resolution for the sensor (for an OSA with 10 pm wavelength resolution).

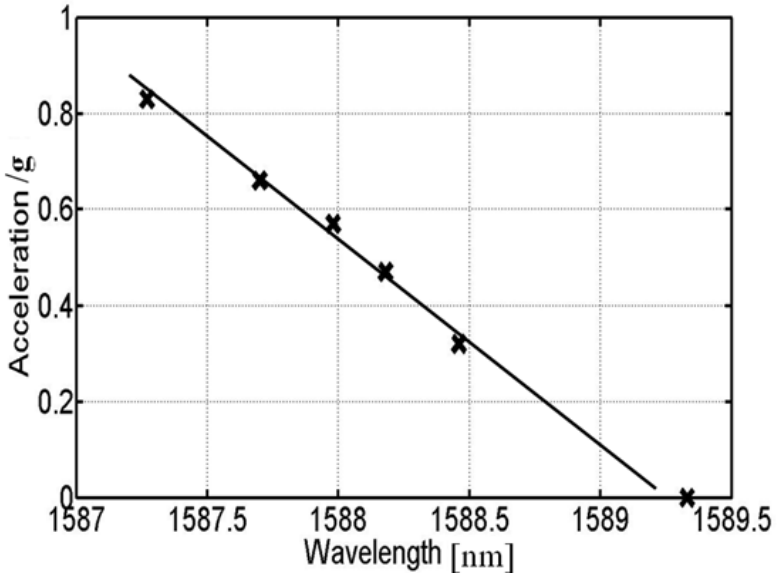

Figure 5-7: Measured wavelength shift versus applied acceleration of the FP-based accelerometer integrated with strip waveguides (ω_n=10.5 kHz).

According to Eq. (2.30) better resolution and sensitivity can be achieved if the natural frequency is lowered. To achieve that, a device with larger proof mass and smaller spring constant was designed and fabricated. The mechanical sensor model was described in section 3.1. Table 5-1 summarized the used dimension (on the mask layout) for the device.

Table 5-1: Accelerometer design parameter used in Figure 4-11.

Span beam length	470 µm
Span beam width:	3 µm
Connector beam width=Connector beam length	10 µm
Number of beams	8
Proof mass thickness	30 µm
Length of proof mass	288 µm
Width of proof mass	2884 µm
Etch-holes dimension	5 µm ×5 µm
Distance between etch-holes	4 µm
Mass of proof mass	8.1×10^{-7} kg
FP gap	27.1 µm
Silicon wall width of the Bragg mirror	3.8 µm
Air wall width of the Bragg mirror	2.5 µm
Waveguide width at the input and output	12 µm
Waveguide collimator length	4000 µm
Waveguide width at the end of collimator	40 µm

The device has a mass of 8.1×10^{-7} kg with a spring constant of 6.125 N/m resulting in ω_n= 2.75 kHz natural frequency. The device response is measured with the same setup (Figure 5-5). Figure 5-8 compares the measured and simulated transmission spectra of the device. The initial transmission peak is 1534.5 nm while 0.18 g acceleration is applied. The gap of the FP cavity is 27.1 µm, leading to 30 nm FSR for the sensor. Therefore the filter can be tuned continuously over 30 nm. The full width at half maximum (FWHM) of the peaks is 3nm. As seen once more due to the fabrication imperfections (generated by photolithography and etching processes), the measured peaks are not exactly located at the same locations predicted by the simulations.

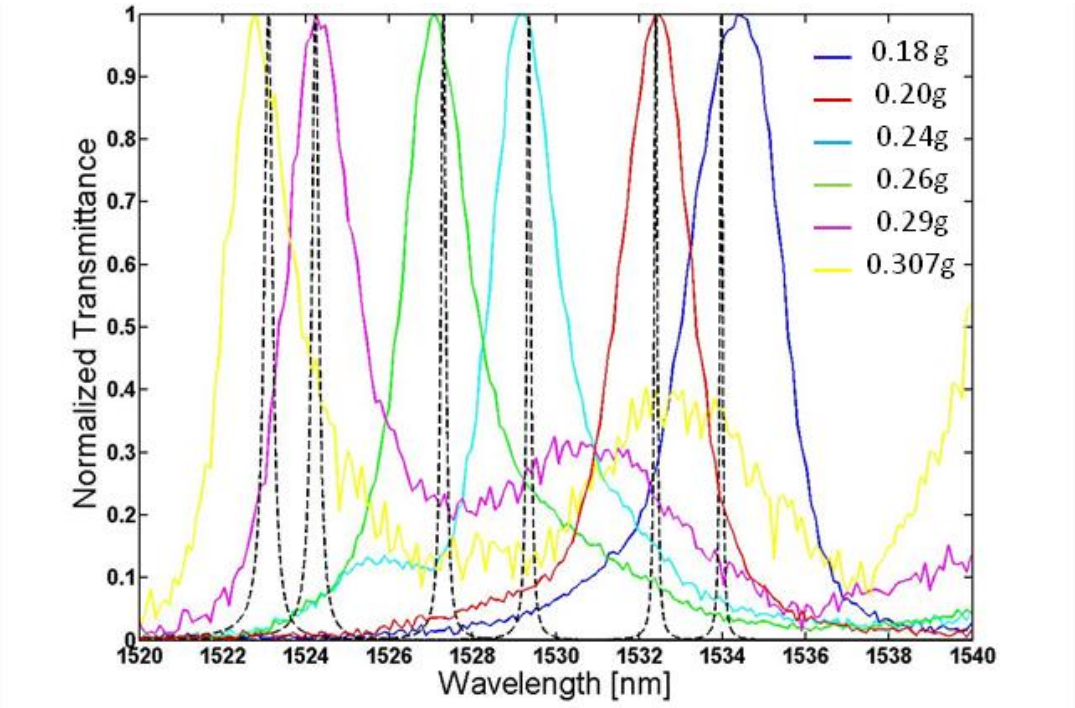

Figure 5-8: Measured (colored curves) and simulated (black-dashed curves) transmission spectra of the FP based accelerometer integrated with strip waveguides for various accelerations (ω_n= 2.75 kHz).

Figure 5-9 shows the applied acceleration versus the resonant wavelength shift of the FP filter with ω_n=2.75 kHz (two proof masses (8.1×10^{-7} kg) suspended on eight springs, having an overall stiffness of 6.125 N/m). 90 nm/g sensitivity is extracted from the curve leading to 111µg resolution for the sensor. Using (2.18) and (2.35), sensor has a maximum dynamic range of 295 mg.

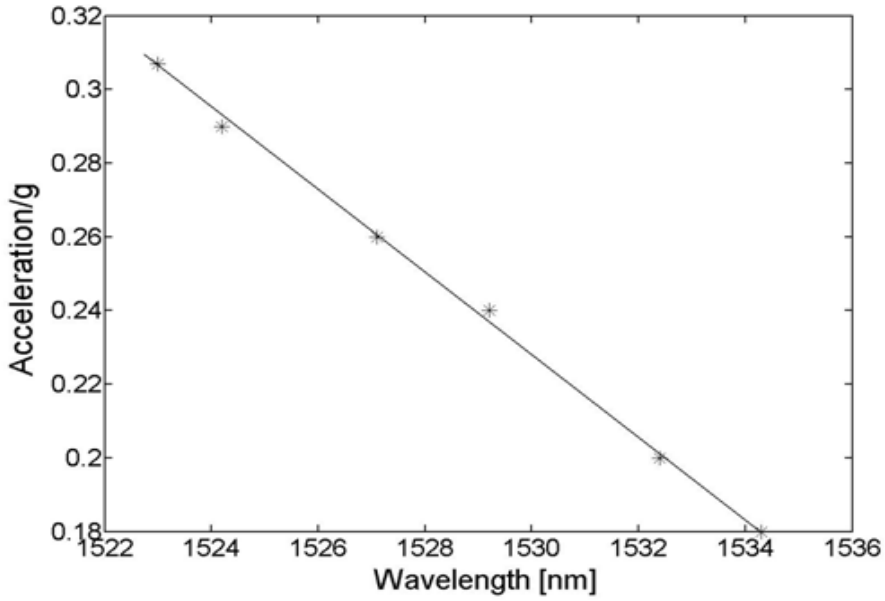

Figure 5-9: Measured wavelength shift versus applied acceleration of the FP-based accelerometer integrated with strip waveguides (ω_n= 2.75 kHz).

FP-based accelerometer integrated with rib waveguides

FP-based accelerometers integrated with rib waveguides (Figure 4-9) were also optically characterized. Using rib waveguides provides two advantages compared to strip waveguides as discussed in section 4.2.1: first of all, they are single mode so the profile of guided mode inside the waveguide is known and second, the SiO_2 layer under the waveguide is not removed while the structure is released in vapor HF. The device has a mass of 2.24×10^{-8} kg with overall spring constant of 7 N/m resulting to ω_n= 17.7 kHz natural frequency.

Figure 5-10 shows the response of the device. The initial transmission peak is 1595 nm while no acceleration is applied.

Figure 5-11 shows the applied acceleration versus the resonant wavelength shift of the FP filter. 1.5 nm/g sensitivity is extracted from the curve leading to 6.7mg resolution for the sensor.

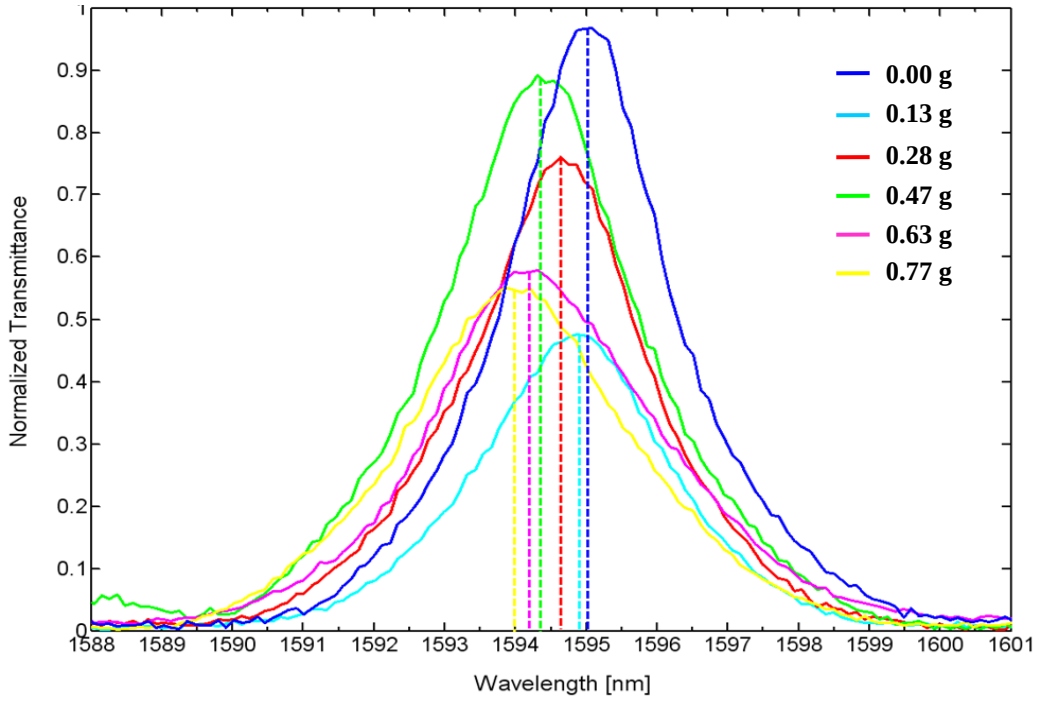

Figure 5-10: Measured transmission spectra of the FP-based accelerometer integrated with rib waveguides (ω_n= 17.7 kHz).

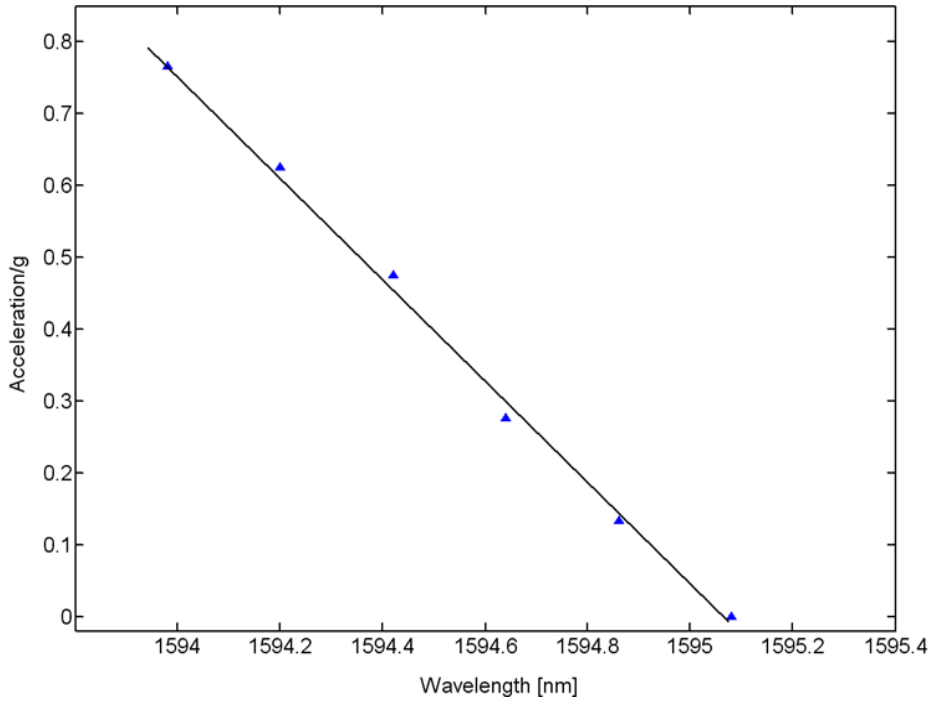

Figure 5-11: wavelength shift versus applied acceleration of the FP-based accelerometer integrated with rib waveguides (ω_n= 17.7 kHz).

As discussed in section 2.5.3, the sensor sensitivity is inversely proportional to the resonance frequency of the device and the finesse or quality factor of the FP cavity. However both of these parameters are independent of the modal distribution in the waveguide. The resonance frequency is a mechanical parameter that depends on the sensor proof mass and spring constant and the quality factor of microcavity depends on the optical characteristics of the cavity such as reflectivity of Bragg mirrors and fabrication imperfection (section 2.5.1). Therefore, using rib or strip waveguides do not affect the device performance.

5.2.2 47 µm thick SOI-VEM accelerometer

The static responses of the Vertically Extended Mass (VEM) VOA-based accelerometer fabricated on double SOI (Figure 4-20) were measured by exposing it to gravity. The accelerometer has 1.32×10^{-7} kg proof mass and is suspended by six span beams having a designed overall stiffness of 2.2 N/m providing 4.1 kHz natural resonance frequency. The widths of the waveguides at the VOA junction are 20 µm.

Light (λ=1550 nm) from a 4 mW laser source (Agilent 8164 B) is transmitted into the input waveguide (top device layer) through a 80 µm diameter single mode optical fiber aligned in an input U-groove. The transmitted light is collected by the second optical fiber, which is coupled to the untapered end of the output waveguide (Figure 3-6) at one end and to a photodetector at the other end. Fibers were bonded to the U-grooves using UV-curing optical adhesives (Thorlabs NOA63). Fiber to waveguide coupling is quite challenging as light has to be coupled to the thin top device layer (Figure 4-15). The whole setup is attached to an inclinable board that can be tilted (Figure 5-5). Acceleration (towards the fixed Bragg mirror) is applied to the device as a consequence of gravity by tilting the board ($g\sin\theta$).

Figure 5-12 shows the detected output power versus applied acceleration. Power decreases, as the angle of inclination increases while the acceleration is applied towards the fixed Bragg mirror (the movable Bragg mirror in Figure 3-6 moves towards the fixed Bragg mirror and blocks more light leading to less coupling light from the input waveguide to the output waveguide at the VOA junction). Due to the coupling loss from optical fibers to waveguides and from waveguides to waveguides, the measured output power is low (from Eqs: (2.55) and (2.56), 1.6 dB for each silicon/air interface and 0.2 dB for each fiber/air interface). Sensor response repeatability is checked for three different accelerations and is described as follows. Three arbitrary angles are

chosen: 0 º, 25º, and 45º. When for example the output power of the device is recorded at 0º, the angle is set to 25º and 45º and after recording the power at these angles, it is returned to 0º and the output power is measured again. Slight fluctuations at the output power were observed for each of the measurement as seen in Figure 5-12. The error arising from the board height measurement (reading error or uncertainty) is also indicated in this graph. The average fluctuation of the output powers were approximately 0.003 µW (0.178 dB). These fluctuations are believed to be coming from the produced stress on the fiber generated from the glue (UV-curing optical adhesive). The reading power uncertainties (the accuracy of reading of power by the photodetector) are very small compared to the power fluctuations arising from the fiber stress and therefore can be neglected. The sensor response to the acceleration ranging from 0 to 0.7 g is approximately linear with1.47±0.25 dB/g sensitivity. Sensitivity can be improved by using bigger proof mass and softer springs.

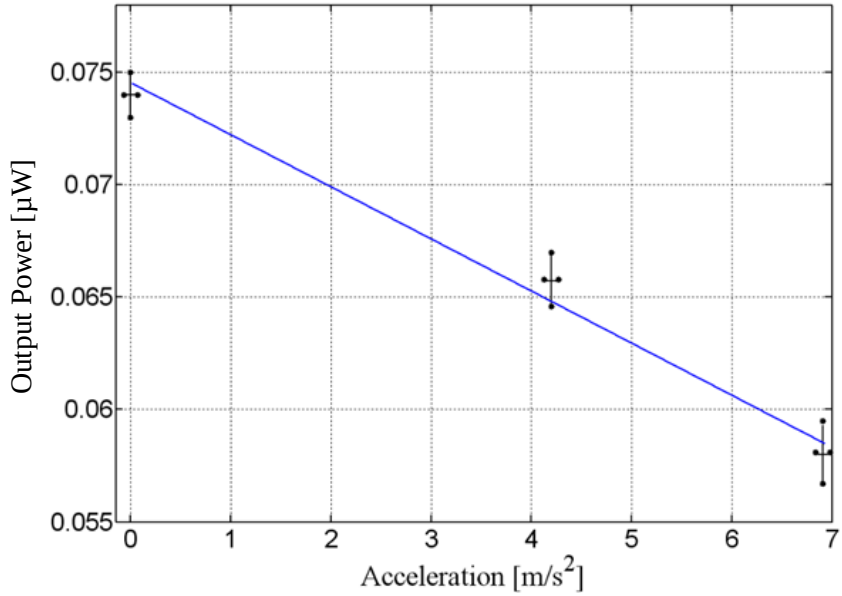

Figure 5-12: Static response of the VEM VOA-based accelerometer to applied acceleration (ω_n= 4.1 kHz).

5.2.2.1 Gyroscope drive mode validation

Gyroscopes actuation in the drive mode was successfully tested by applying differential voltage between the movable part (attached to the system proof mass) and the fixed part of the comb drive. Driving displacement of gyroscopes fabricated on 47 µm-thick single SOI were measured using optical profilometer when 100 V is applied to the electrical pads of the gyroscopes (Figure

5-13 (a)). Only double SOI test structures with 2 beams (one side plate with dimensions of 500 µm×50 µm suspended by two span beams with dimensions of 200 µm×2 µm) were tested, as all springs could not survive at the end of fabrication due to the fabrication issues that were discussed in section 4.2.2 (Figure 4-25). Figure 5-13 (b) shows this test structure. Proof mass has the same thickness as the springs (47 µm). Proof mass displacement for the single SOI structure excited at 10 Hz frequency for an applied voltage of 100 V was measured to be 3 µm. Sensor has a mass of 4×10^{-8} kg suspended by 10 springs with overall constant of 77 N/m (3.11), providing 44 kHz natural resonance frequency for the system. The ratio of driving frequency to resonance frequency ($\frac{\omega_D}{\omega_{0x}}$) is 1.4×10^{-3}; the driving force produced by the comb drive is calculated from (3.15) to be 60 µN. The damping ratio of the sensor can be extracted from (2.72), since the ratio of the driving frequency to the resonance frequency is very small; referring to Figure 2-6 the effect of damping is very small (also discussed in section 3.2.1), leading to weak damping situation for the sensor. Maximum displacement of proof mass for weak damping from the simulations is 0.78 µm (Table 3-5). The difference between measurement (3 µm) and simulation arises from microfabrication imperfections. Especially notching can make a big difference in the comb drive performance (Figure 4-5). It also changes the expected resonance frequency of the device. As discussed in § 2.8, in order to obtain a highly sensitive rate sensor, it is necessary to have high amplitude of vibration which entails weak damping and matching between driving frequency and device resonance frequency in driving direction (2.72). In the case that we are studying here, the matching condition is not satisfied and to be so, the driving frequency has to be increased. However at high frequencies, the damping effect is more significant. Damping can be lowered by increasing the gap between the oscillating plate and the fixed frame wall (here the used gap is 30 µm). However care should be taken to not neglect the slide damping caused by the existence of etch-holes in the proof mass. Therefore the effect of these etch-holes at matching frequency should also be studied. If necessary, vacuum package is needed for the gyroscope to reduce the damping.

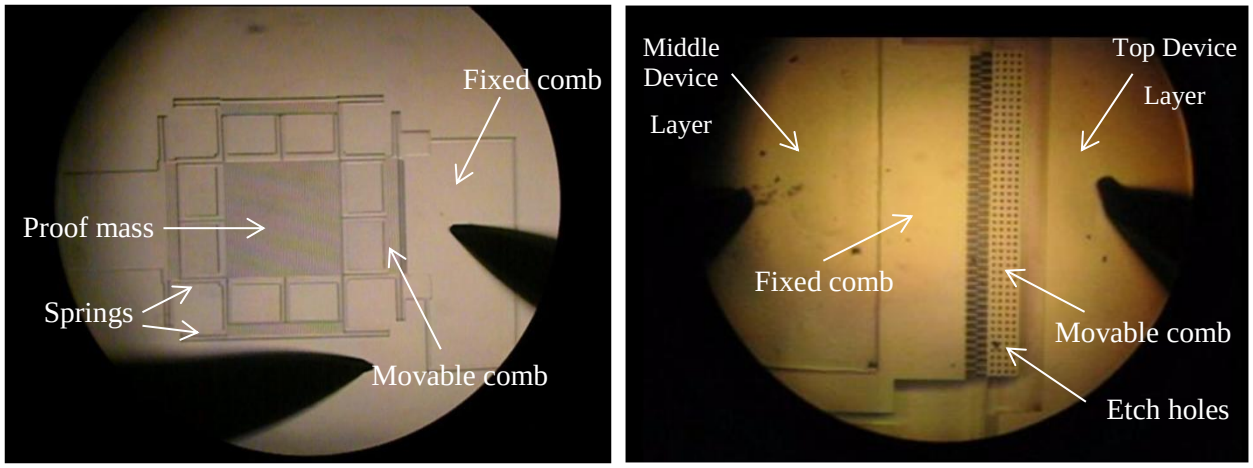

(a) (b)

Figure 5-13: Gyroscope drive mode testing by applying differential voltage between the movable and the fixed part of the comb drive, (a) 47 µm single SOI device, and (b) 47 µm double SOI test structure, the top device layer (waveguide layer) has been etched partially to reach the middle device layer (actuator layer).

5.2.3 Optical loss measurements

Cut-back method is used to measure the propagation loss of the optical waveguides. Light with input power P_0 is coupled to a waveguide of length L_1 and the output power P_1 is measured; the measurement is repeated for the same but shorter waveguide L_2 to determine the output power P_2, knowing that the intensity decays with propagation distance z, as

$$I = I_0 e^{-\alpha z}, \tag{5.1}$$

the propagation loss of the length of waveguide (L_1-L_2) is therefore related to the difference in the measured outputs:

$$\frac{P_1}{P_2} = \exp[-\alpha(L_1 - L_2)] \tag{5.2}$$

so that

$$\alpha = \left(\frac{1}{L_1 - L_2}\right) ln\left(\frac{P_2}{P_1}\right) \tag{5.3}$$

This equation is accurate if the condition of the waveguide endfaces, widths, and input power remain constant. Also the accuracy of this method is improved if multiple measurements are taken. Three waveguides with different lengths are measured. Figure 5-15 shows the optical loss versus the waveguide length. Single SOI devices and double SOI devices with thickness of 47 μm and different lengths (1250 μm, 2500 μm, 5000 μm, and 7500 μm) integrated with U-grooves were fabricated and optically measured (Figure 5-14).

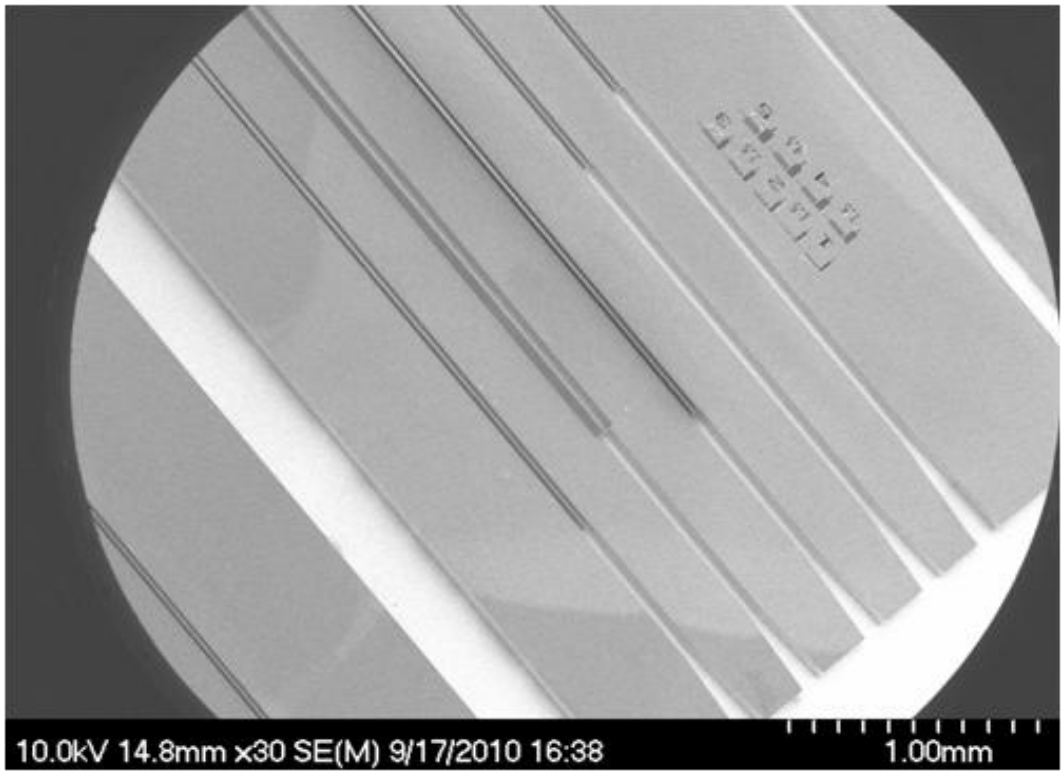

Figure 5-14: SOI fabricated waveguides with different length integrated with U-grooves.

Three waveguides with different lengths of 1250 μm, 2500 μm, and 5000 μm are measured with a 4 mW laser (Agilent 8164 B) emitting at 1550 nm. Figure 5-15 and Figure 5-16 show the measured optical loss against the waveguide length for single and double SOI waveguides respectively. In the case of single SOI, as the waveguide with 5000 μm length had damaged during the fabrication, the waveguide with 7500 μm length was measured instead.

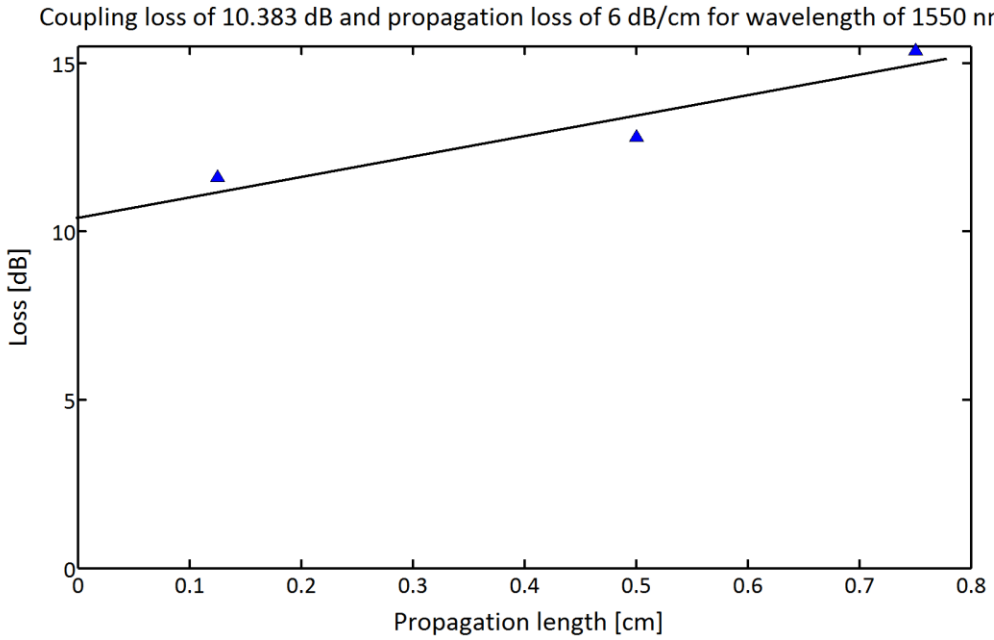

Figure 5-15: Waveguide transmission versus waveguide length for 47 μm thick single SOI device.

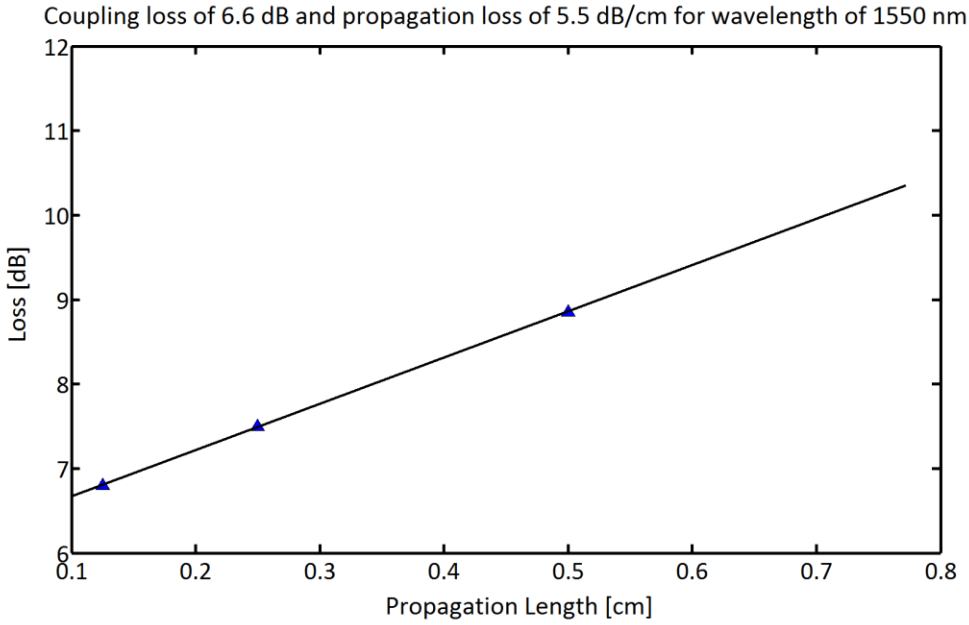

Figure 5-16: Waveguide transmission versus waveguide length for 47 μm thick double SOI device.

Note that the linear fit to the data cuts the *y*-axis above the origin. This suggests a loss for zero propagation length. This is because the data are expressed as insertion loss not propagation loss, and therefore the loss corresponding to zero propagation length is the total coupling loss to the waveguide. Coupling loss of 10.4 dB and 6.6 dB are extracted from these graphs for single and

double SOI devices respectively. The propagation loss of 6 dB/cm and 5.5 dB/cm are extracted from these graphs for the single and double SOI devices. Lower loss for the double SOI is expected since the thickness of the top layer where the optical waveguides are fabricated is 15 µm, whereas for single SOI device this thickness is 47 µm. Thinner SOI results in having less area of scalloping on the waveguides sidewalls that are generated during DRIE process, leading to less scattering loss coming from the interaction of light with the waveguide sidewalls.

5.2.4 75 µm thick SOI

Similar experimental setup as Figure 5-5 is used to characterize the VOA-based accelerometers fabricated on 75 µm-thick SOI wafers. Unlike the 47 µm double SOI devices, coupling was easier in this case since the device layer was thicker. Standard 125 µm telecom optical fibers (P1-SMF28e-FC2, Thorlabs) were used to inject and detect the optical signal to/from the sensor microchip. Optical fibers were bonded to the U-grooves using UV-curing optical adhesives (Thorlabs NOA63) through reservoirs. These reservoirs as shown in Figure 5-18 (a) are positioned beside the U-grooves and as far as possible from the input silicon waveguide to avoid the sudden flowing of the epoxy into the chip. They are fabricated at the same time (DRIE) as other sensor components (proof mass, springs,…). In order to prevent the epoxy flow into the MEMS structure, 2 µm-wide staggered dams are used at the input and output waveguides. Figure 5-17 (a) shows the optical setup with the sample bonded to the fibers.

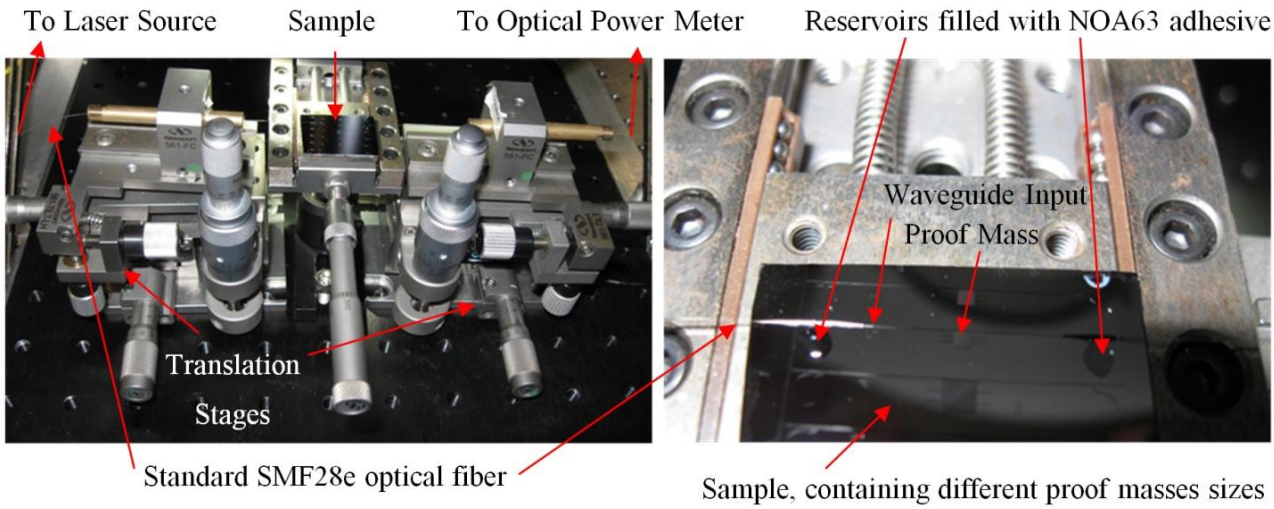

(a) (b)

Figure 5-17: (a) Sample glued to the optical fibers mounted on the optical setup, (b) Close up view of sample.

Figure 5-17 (b) is a close up view of the sample.

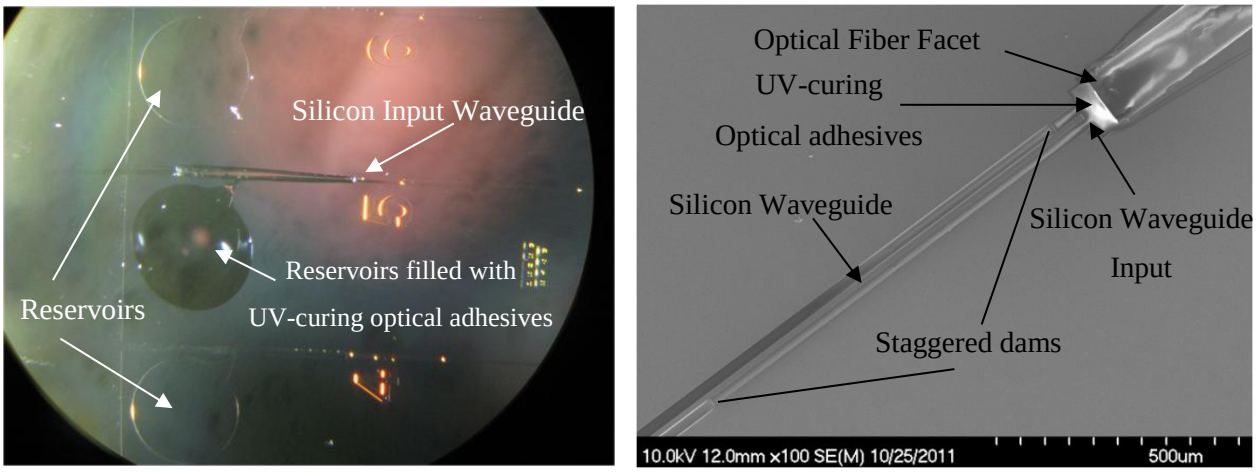

(a) (b)

Figure 5-18: (a) Epoxy reservoir integrated with U-groove and fiber filled by UV-curing optical adhesives, (b) SEM of the bonded optical fiber to the input waveguide after curing. Staggered dams are indicated in the picture.

Accelerometer has 1.75×10^{-7} kg proof mass and is suspended by four span beams with 1000 µm lengths and 2 µm widths having an overall stiffness of 0.8 N/m (Table 3-2) providing 2.14 kHz natural resonance frequency. Dimension of the device component can be find in appendix (I) Figure 5-19 shows the SEM photograph of the fabricated device.

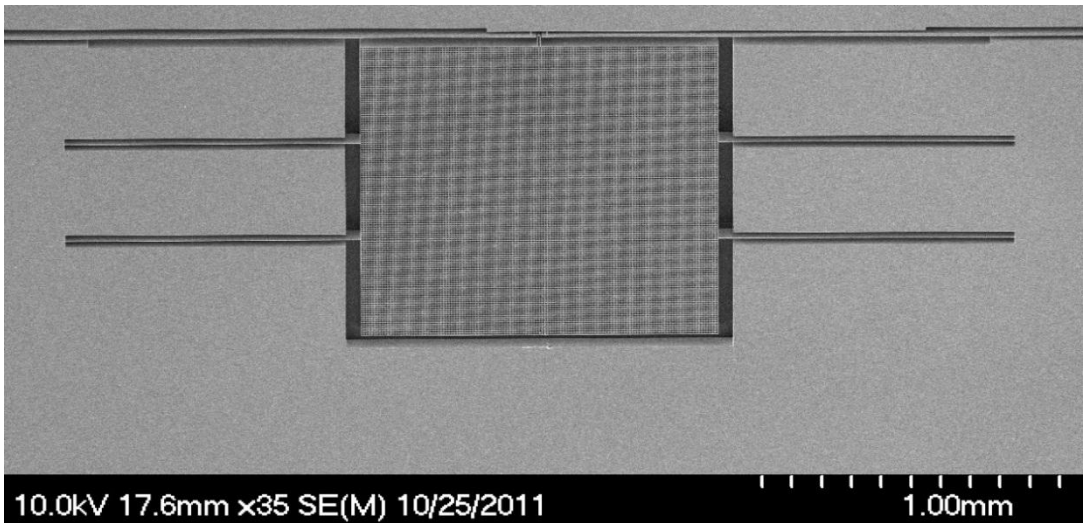

Figure 5-19: SEM photograph of the VOA-based optical accelerometer fabricated on 75 µm SOI. Strip waveguides widths at the VOA sensing junction interface are tapered to 12 µm.

Light (λ=1550 nm) from a 4 mW laser source (Agilent 8164 B) is coupled into the input waveguide. The transmitted light is then measured by an optical power meter (Newport 840-c). Figure 5-20 shows the detected output power versus the applied acceleration applied by gravity. Due to coupling loss from optical fibers to waveguides and from waveguides to waveguides (from Eqs: (2.55) and (2.56), 1.6 dB for each silicon/air interface and 0.2 dB for each fiber/air interface), the measured output power is low. The whole setup is attached to an inclinable board that can be tilted. Accelerations up to 0.7g (towards the fixed Bragg mirror) are applied to the device as a consequence of gravity by tilting the board ($g\ sin\theta$). Consequently, the movable Bragg mirror (Figure 3-6) moves towards the fixed Bragg mirror and blocks more light leading to less power coupling from the input waveguide to the output waveguide at the VOA junction. As a result, power decreases, as the angle of inclination increases. Measured output powers were slightly fluctuating for each measurement (each angle of inclination). For example when 0.1g acceleration is applied (indicated on the blue line in Figure 5-20), the measured power output was fluctuating within 0.2463 µW, 0.2437 µW, and 0.2411 µW leading to ±0.0026 µW or ± 0.046 dB fluctuation. These fluctuations are believed to be coming from the produced stress on the fiber generated from the glue (with UV-curing optical adhesive). The reading power uncertainties (the accuracy of reading of power by the photodetector) are very small compared to the power fluctuation arising from the fiber stress and therefore can be neglected.

Sensor response repeatability was checked over four days. As seen in the graph, the measured output powers degrade over time, showing 0.06 µW average drop power per day. This is due to the shrinkage of the optical adhesive over time, leading to misalignment between optical fibres and the chip. Errors arising from the board height measurement (reading error or uncertainty) are also indicated in the graph (width of the markers in horizontal direction). The slopes of the lines in Figure 5-20 have slightly changed from day to day. Table 5-2 shows the average power fluctuation, average line slope and line slope fluctuation of the sensor over four days of measurement. By averaging the values presented in Table 5-2 over time (days), the average power fluctuation is ±0.040 dB, and the average sensitivity of the device is 3.44±0.40 dB/g, where ±0.40 dB/g is the average line slope fluctuation. Compared to 47 µm double SOI device (sensitivity of 1.47±0.25 dB/g), sensitivity has increased by a factor of 2.5x by reducing both resonance frequency and the width of the waveguides at the VOA junction.

Table 5-2: Average power fluctuation, average line slope and line slope fluctuation of the VOA-based accelerometer sensor over four days of measurement.

Day	1	2	3	4
Average Power Fluctuation (±dB)	0.042	0.032	0.046	0.039
Average Line Slope (dB/g)	2.314	3.734	3.633	4.085
Line Slope Fluctuation (±dB/g)	0.058	0.739	0.697	0.093

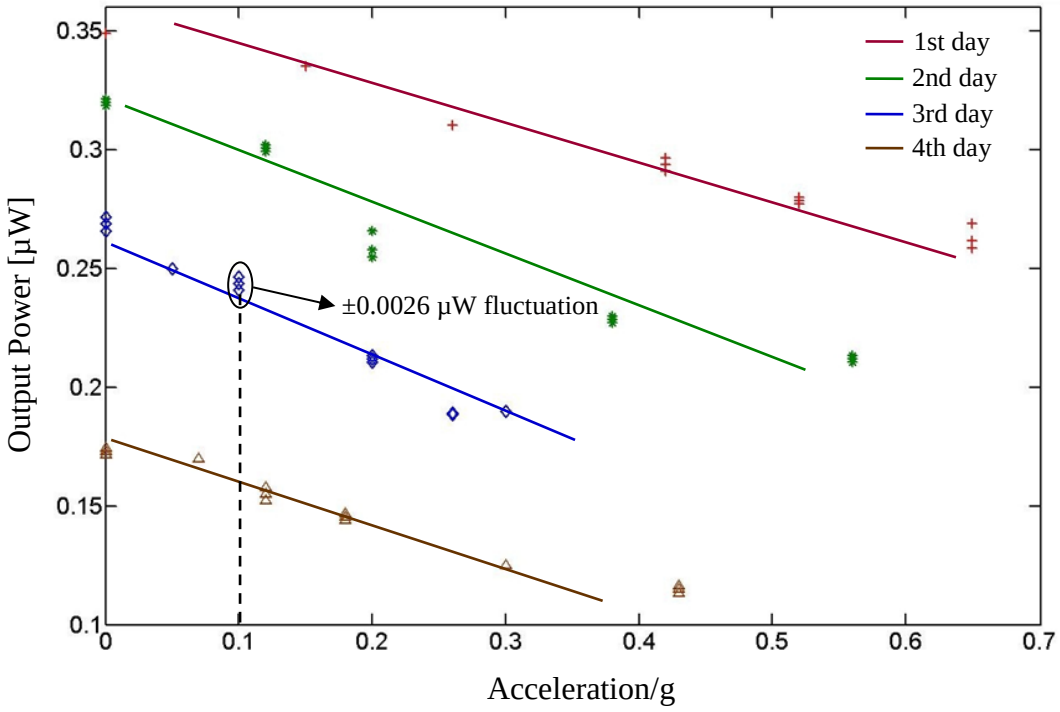

Figure 5-20: The static responses of the 75 µm thick VOA-based accelerometer (having a natural resonance frequency of ω_n= 2.14 kHz) to applied accelerations measured at four different days.

Let's now compare the experimental results with simulations. The widths of both input and output waveguides at the VOA junction are 12 µm. The corresponding initial beam radius extracted from Figure 2-13 for the input waveguide is 4 µm. The distance between the input waveguide and the middle of Bragg mirror is 8 µm. The new beam radius at the middle of mirror position extracted from Figure 2-15 is 4.12 µm. The maximum displacement of proof mass

caused by maximum applied acceleration in this experiment (0.7g) can be calculated from (3.7) as 1.5 μm. However, the maximum displacement to achieve a linear response depends on the lateral fundamental mode size in the waveguide at the VOA sensing junction. From Figure 2-17, the maximum allowed displacement to achieve a linear response with linearity better than 0.5% when the beam radius is 4.12 μm is approximated to be ±1.4 μm. On the other hand, corresponding applied acceleration to achieve 1.4 μm displacement calculated from (3.7) is 0.65g. Therefore from theory, device shows only linear responses from 0 to 0.65g.

Now if the mirror displaces 1 μm (x_0=+1) from its initial position (x_0=0) due to an applied acceleration, from Figure 2-18, ΔL_a=2.1 dB, leading to 2.1 dB/μm sensitivity. On the other hand from Table 3-2, for our device (having proof mass of 1000 μm×1000 μm fabricated on 75 μm SOI wafer and spring parameters listed on the last row of the table), the proof mass displacement sensitivity is 2.2 μm/g leading to total 4.62 dB/g sensitivity for the device. The difference between theory and experiment arises from the approximation made in the simulation (listed in section 2.6.2.2) and fabrication imperfections (such as deviation of lateral dimensions generated by photolithography and etching deviations (such as notching)).

5.3 Conclusions

Mechanical testing was performed after each device release and prior to optical characterization by using a probe station setup to ensure that the device is completely released. Vibration tests are also accomplished by actuating samples with a piezo actuator to verify the predicted sensor resonance frequency from theory. The piezo actuator frequency is tuned and the accelerometer displacement is measured. As the actuator frequency approaches the resonant frequency of the device, the proof mass displacement amplifies.

The static responses of all types of accelerometers were measured by exposing them to gravity by the way of attaching the whole setup to an inclinable board that can be tilted. Force is then applied to the devices as a consequence of gravity by tilting the board. The static responses of FP-based accelerometers fabricated on 30μm-thick SOI wafers integrated with strip and rib waveguides were successfully measured by using this method of measurement. Butt coupling method was used to couple light from optical fibers to the silicon strip/rib waveguides. The FP-based accelerometer fabricated on 30 μm-thick SOI wafer having natural resonance frequency of 10.5 kHz demonstrated 2.5 nm/g sensitivity and 4 mg resolution. Since the sensor sensitivity and

resolution are both inversely proportional to the system natural resonance frequency, the sensor performance was improved by lowering the sensor natural resonance frequency to 2.75 kHz (using bigger proof mass and softer springs) leading to 90 nm/g sensitivity and 111μg resolution for the sensor. Both sensors show linear responses over their tuning range and their performance have the potential to reach μg resolution if larger mass and softer spring is used. As the sensor sensitivity is proportional to the resonance frequency of the device and the resonance peak finesse (or cavity quality factor) and is independent of the modal distribution in the waveguide, using rib or strip waveguide did not affect the device performance.

Since the sensor sensitivity and resolution are both proportional to the system proof mass, using thicker SOI wafers increases the attainable sensor proof mass, consequently improving the sensors performance. This also allows integrating optical fibers to the chip and moreover minimizing the misalignment issues and signal instabilities. Furthermore, it reduces the cross-axis sensitivity of the sensor (due to the greater cross-axis stiffness).

The static response of VOA-based accelerometer fabricated on 47 μm-thick double SOI wafer was also tested. Using 47 μm- thick SOI wafers enabled us to passively integrate 80 μm optical fibers to the chip using U-grooves. The reason of utilizing double SOI wafer is to guide the light only inside the top device layer providing thinner waveguides and therefore lowering scattering optical loss from the side-walls roughness that have been generated during DRIE process. To verify this assumption, propagation loss of 47 μm- thick single SOI and double SOI strip waveguides were measured using cut-back method, showing 0.5 dB/cm less propagation loss for double SOI waveguides.

The VOA-based accelerometer fabricated on 47 μm double SOI wafer has a vertically extended proof mass by adding the mass of the underlying Si wafer to the sensor proof mass on the device layer. The widths of waveguides at the VOA junctions are 20 μm. This vertically extended mass (VEM) VOA-based accelerometer fabricated on 47 μm double SOI wafer, demonstrated 1.47±0.25 dB/g sensitivity.

VOA-based accelerometers fabricated on 75 μm-thick SOI wafers were also tested by exposing them to gravity. 75 μm-thick SOI wafers enabled us to interface the silicon waveguides to the standard 125 μm telecom optical fibers using U-grooves. The sensitivity (compared to vertically extended mass VOA-based accelerometer fabricated on 47 μm double SOI) was improved by a

factor of 2.5±0.3 by reducing both, the resonance frequency (to half) and the width of the waveguides at the VOA junction (from 20 μm to 12 μm), leading to 3.4±0.4 dB/g sensitivity. Sensor shows a linear response over 0.6 g applied acceleration. As fibers were bonded to the chip by UV-curing optical adhesive, some fluctuations at the output power were observed arising from the produced stress on the fiber generated from the glue, causing misalignments between fibers and silicon waveguides.

Gyroscopes actuation in the drive mode was verified by applying differential voltage between the movable part (attached to the system proof mass) and the fixed part of the comb drive. Driving displacement of gyroscopes fabricated on 47μm-thick single SOI excited at 10 Hz were measured to be 3 μm using optical profilometer when 100 V is applied to the electrical pads of the gyroscopes. Device shows to be in the weak damping status at low frequencies. Large driving displacement leads to higher sensitivity for the device. To achieve large driving displacement, device needs to be actuated with frequencies equal or close to its resonance frequency. However the nature of damping is different at higher frequencies due to the existence of etch-holes on the proof mass. The effect of etch-holes on slide damping needs to be therefore studied as it can show a significant impact on the damping at higher frequencies. For comparison, the VEM approach seems to have an advantage (easier controlling on damping) as no etch-holes are needed to release the structure.

CHAPTER 6 CONCLUSIONS AND FUTURE WORK

6.1 Conclusions

Fully integrated high performance optical MEMS inertial sensors were presented for the first time. Although optical inertial sensors with high performance have been previously reported, none of them is integrated with optical waveguide for in-plane detection purposes. In this work, in-plane optical accelerometers and gyroscopes with two different designs were successfully fabricated on SOI wafers with different device layer thicknesses. Optical accelerometers were also successfully characterized. These inertial sensors are designed for micro-satellites navigation purposes where a compact and low power microchip is required. As all of the sensors (accelerometers and gyroscopes) presented here are designed for in-plane detections, multiples of them with various dynamic ranges can be integrated on the same chip (such as 0 to 10 mg, 0 to 100 mg, and 0 to 1 g), providing a broad measurement range. The most important characteristic of these sensors is that they are immune to electromagnetic interferences making them suitable for space applications. Two different designs with different working principle integrated with optical waveguides were presented. First one is a micro electromechanical systems Fabry-Perot (MEMS FP) based sensor. It is actuated by an applied acceleration to provide a shift in the FP resonance wavelength. Device shows a linear response (linear shift in the FP resonance wavelength to the applied acceleration). The second one is a MEMS variable optical attenuator (VOA)-based sensor. A Bragg mirror that is attached to the sensor proof mass is positioned in the middle of the gap of two optical waveguides: input and output waveguides. When the device is actuated by the applied acceleration, the intensity of the transmitted light to the output waveguide is modulated by the displacement of the Bragg mirror. Sensor shows a relatively linear response (linear shift in the transmitted light intensity to the applied acceleration).

Two types of waveguides are used namely, strip and rib waveguides. Strip waveguides are multimode and are fabricated at the same DRIE step as the rest of the structure. Rib waveguides however are single mode and one additional photolithography and DRIE is required to fabricate them. The main advantage of rib waveguides is that, unlike the strip waveguide they do not lift up during the structure releasing process. On the other hand, fabricating them requires photolithography on a structure with high topography. This requires good resist coverage on the

topography region. For that purpose a new method called dynamic surface tension (DST) was used.

Although FP-based devices seem to be highly sensitive even with nanometer displacements, they require more complex optical source (high quality laser) and detector (optical spectrum analyzer) compared to VOA-based devices (photodetector). This is because, the FP-based sensor is based on wavelength detection (interferometry) while, the VOA-based sensor is based on intensity detection. On the other hand, to obtain a relatively high sensitive VOA-based sensor, displacements in the order of few micrometers are required. However obtaining displacements at this order using MEMS technology are restricted by the fabrications constraints.

SOI wafers with different device thicknesses (30 μm, 47 μm, and 75 μm) are used to fabricate the devices. All Devices sensitivity is inversely proportional to the system natural resonance frequency. This means, not only springs with low spring constant are required, but also large proof mass is needed to increase the sensor sensitivity. As mentioned earlier, only few nanometer displacements can effectively modulate the FP resonance peak. Measurement showed that even 30 μm SOI can provide large enough proof mass for the sensor to provide nanometers of displacements in the presence of small accelerations (smaller than gravity). In other words, the produced gravity force is large enough to displace the proof mass in the order of few nanometers. However, thicker SOI wafers will still provide larger mass, offering better sensitivity (and resolution) for the device. FP-based accelerometers integrated with strip and rib waveguides fabricated on 30 μm SOI were successfully tested. As the sensor sensitivity is proportional to the resonance frequency of the device and the finesse or quality factor of the FP cavity and is independent of the modal distribution in the waveguide, using rib or strip waveguides do not affect the device performance.

On the other hand, in order to attain sensitive VOA-based devices, few micrometers displacements are required to significantly modulate the optical output power (requiring soft springs and large proof mass for the device). In order to obtain such a device with large mass and soft springs, a vertically extended mass (VEM) approach was introduced for the VOA-based devices where the attainable proof mass is extended further vertically by adding the mass of the underlying Si wafer (handle) to the sensor proof mass while the springs are defined on the SOI device layer. In this approach, springs are introduced in the device layer while the proof mass is

composed of the device layer and handle layer providing thin (soft) springs and large proof mass for the device, resulting in the highest achievable acceleration sensitivity for the sensor. With this configuration the in-plane size of proof mass in the SOI wafer plane can be smaller than those fabricated on 30 μm SOI wafer, as the desired mass can be obtain in vertical direction, leading to smaller size (in plane) for the sensor . Double SOI wafers are also used. The reason was to reduce the propagation loss in the waveguides by defining the optical waveguides only on the top device layer. With this configuration, the top device layer can be chosen to be thin as much as possible to reduce the scattering loss generated by the waveguide side wall roughness. However, a too thin layer can decrease the coupling efficiency between the fibers and waveguides. 15 μm-thick top device layer is used to make a compromise between the scattering loss and coupling efficiency. U-grooves along epoxy reservoir were integrated with the sensors. U-grooves reduce the misalignments errors between fibers and the chip. Although the VEM approach maximizes the attainable proof mass and can provide higher acceleration sensitivity, the fabrication requires two separate DRIE steps and the resulting fabrication yield is low. Therefore for the next step of work, 75 μm-thick single SOI wafers were used allowing the integration of standard single mode optical fibers to the chip. Coupling to waveguides is not an issue in this case, as the waveguides are thicker than the optical fiber core diameter. The sensitivity of the device in the case of VOA-based not only is inversely proportional to the system resonant frequency, it is also inversely proportional to the lateral guided mode size in the waveguides (which is directly related to the waveguides width) at the VOA junction (more intensity modulation for unit displacement). The sensitivity of the device was improved by a factor of 2.5 through reducing both, the resonance frequency and the width of the waveguides at the VOA junction using 75 μm-thick single SOI devices.

The tuning range of VOA-based devices is determined by the lateral guided mode size of the input waveguide at the VOA junction which is related to the waveguide width at the VOA junction. On the other hand, the linear response range is determined by the regions where the power of the guided mode is uniform. These are the regions located nearby the optical axis of the waveguide. Although increasing the waveguide width at the VOA junction enlarges the mode size and as a result, provides a larger tuning range for the device, at the same time it reduces the sensitivity of the device; unless the proof mass displacement is increased accordingly (by lowering the resonance frequency). In summary in order to obtain a VOA-based sensor with high

sensitivity and large tuning range with linear response, the width of input waveguide at the VOA junction needs to be increased while the proof mass displacement per unit applied acceleration is increased at the same time by lowering the natural resonance frequency (using large proof mass and soft springs). This is however associated with the price of narrowing the operational frequency bandwidth.

For gyroscopes, a MEMS electrostatic comb-drive with interdigital fingers was used to oscillate the MEMS proof mass along the x-axis. An applied angular rotation perpendicular to the sensor plane (z-axis) induces a Coriolis force, causing the proof mass and the attached VOA/FP movable mirror to displace along the y-axis, modulating the VOA actuator/FP gap and the resultant transmitted optical signal/wavelength. A matching condition between resonance frequencies in driving (x) direction and sensing (y) directions is required to obtain high displacement sensitivity for the gyroscope. The gyroscope displacement sensitivity is also proportional to the driving displacement (caused by comb-drive) and the mechanical quality factor of the sensor in y direction (Q_y), and is inversely proportional to the device resonance frequency. In other words, in order to get a sensor with high displacement sensitivity, a matching condition between the resonance frequencies in driving and sensing directions, high driving displacement, high quality factor in y direction, and low resonance frequency are required. The quality factor is inversely proportional with damping. Consequently, in order to gain a high quality factor in y direction, the sensor needs to be weakly damped in y direction. The driving displacement not only depends on the comb-drive characteristics (such as number of fingers (n_f), and space between the fingers (d)) and the applied voltage (V), it also directly relates to the quality factor in the driving direction (Q_x). However despite the sensing direction, not very high quality factor in driving direction is required to obtain displacements in order of micrometers at voltages below 100 V. For example a comb drive with n_f =42 and d=3 μm, at V=20 V ac, can periodically displace +/- 1 μm the proof mass of a system with a quality factor of Q_x=33 and spring constant of 77 N/m. Although reducing the spring constant can increase the driving displacement, it will make the system unstable and can also generate some cross sensitivities leading to the motion coupling from the drive mode to the sense mode, resulting in errors (noise) to the system. On the other hand, from the optics point of view, the sensitivity of the gyroscope is inversely proportional to the lateral guided mode size in the waveguide at the VOA sensing junction (which is directly related to the

width of the waveguide); therefore the mechanical and optical designs have to be both taken into account.

If for any reason (such as fabrication imperfections) the matching condition is not satisfied, the sensing displacement will be very small. To overcome this problem, a compliant microleverage mechanism was introduced to amplify the sensing displacement. A two stage micro-lever mechanism was proposed, leading to 7 x displacement amplification. In the case of FP-based gyroscope, a compliant structure is not required as displacements in the order of nanometers can effectively modulate the transmission peak of the FP. Although, it is found that the compliant structures can significantly amplify the sensing displacement, they may also disturb the matching condition due to modifying the structure stiffness in y direction. Further studies should be carried out to investigate the possible arising issues.

6.2 Future Work

VOA-based accelerometers can be integrated in future with rib waveguides using Dynamic Surface Tension (DST) method on 75 µm-thick SOI wafer. This will eliminate the waveguide lifting issue as well as the uncertainty of guided mode profile inside the waveguide. Vertically extended mass (VEM) approach can also be used to improve the sensor performance.

As waveguides fabricated on double SOI substrate do not contribute to a major improvement on the propagation loss (only 0.5 dB/cm), and as the fabrication process of the fabricated devices on double SOI substrates is very challenging, using double SOI substrate in future is not recommended.

The characterization of both VOA-based and FP-based gyroscopes fabricated on 75µm-thick SOI substrate is definitely a part of future work. The effect of adding compliant mechanism on the displacement sensitivity of the VOA-based gyroscope can also be experimentally verified. Finally integration of an array of two-axis of accelerometers and gyroscopes on a single 75µm-thick SOI substrate using T-bar waveguide splitters can be done in the future in order to demonstrate a multifunction micro navigator chip.

REFERENCES

[1] W. R. Jamroz, R. Kruzelecky, E. I. Haddad, *Applied Microphotonics*, Boca Raton: CRC Press, 2006.

[2] C. Acar, A.M. Shkel, "Experimental evaluation and comparative analysis of commercial variable-capacitance MEMS accelerometers," *Journal of Micromechanics and Microengineering*, v.13, pp.634-645, 2003.

[3] Y. Zhang, G. Meng, and N. Yazdi. (2012, June). A single-chip CMOS-MEMS microgravity accelerometer. Presented at Solid-state Sensors, Actuators, and Microsystems Workshop. Hilton Head Island. South Carolina.

[4] B. Vigna. (2012, June). It makes sense: how extreme analog and sensing will change the world. Presented at Solid-state Sensors, Actuators, and Microsystems Workshop. Hilton Head Island. South Carolina.

[5] "Silicon Gyroscope," *Boeing Company*, 1995-2011. [Online]. Available: http://www.boeing.com/defense-space/space/bss/factsheets/gyro/gyro.html [Accessed: April 1, 2010].

[6] H. Yang, M. Bao, H. Yin, and S. Shen, "Two-dimensional excitation operation mode and phase detection scheme for vibratory gyroscopes*," J. Micromech. Microeng*., vol. 12, no. 3, pp. 193–197, Mar. 2002.

[7] V. Josselin, P. Touboul, R. Kielbasa, "Capacitive detection scheme for space accelerometers applications", *Sensors and Actuators A,* vol.78, pp. 92–98, 1999.

[8] C. Ovrén, and M. Adolfsson B. Hök, "Fiber-Optic systems for temperature and vibration measurements in industrial applications," *optics and lasers in Engineering*, vol. 5, pp. 155-172, 1984.

[9] L. Jonsson and B. Hök, "Multimode fiber-optic accelerometers," *SPIE*, vol. 514, pp. 191-194, 1984.

[10] K. E. Burchan, G. N. De Brabander, and J. Tboyd, "Micromachined silicon cantilever beam accelerometer incorporating an integrated optical waveguide," in Integr. Opt. Microstruct.: *SPIE*, vol. 1793, pp. 12–18, 1992.

[11] D. Uttamchandani, D. Liang and B. Culshaw, “A micromachined silicon accelerometer with fiber optic interrogation”, *SPIE*, vol. 1792, pp. 27-33,1992.

[12] J. Marty, A. Malki, C. Renouf, P. Lecoy, F. Baillieu, “Fiber-Optic accelerometer using silicon micromachined techniques”, *Sensors and Actuators A*, vol. 46-47, pp. 470-473, 1995.

[13] E. Ollier, P. Lebey and P. Mottier, "Integrated micro-opto-mechanical vibration sensor connected to optical fibres," *Electronics Letters*, vol.33, no.6, pp.525-526, Mar 1997.

[14] B. Guldimann, P. Dubois, P.-A. Clerc, N.F. de Rooij, "Fiber Optic–MEMS Accelerometer with high mass displacement Resolution", *The 11th International Conference on Solid-State Sensors and Actuators*, Munich, Germany, June10–14, 2001.

[15] D. Haronian, "Geometrical modulation-based interferometry for displacement sensing using optically coupled suspended waveguides," J. of *Microelectromechanical Systems*, vol.7, no.3, pp.309-314, 1998.

[16] U. Krishnamoorthy, R. H. Olsson III, G. R. Bogart, M. S. Baker, D. W.Carr, T. P. Swiler, and P. J. Clews, “In-plane MEMS-based nano-g accelerometer with sub-wavelength optical resonant sensor,” *Sens. Actuators A, Phys*., vol. 145–146, pp. 283–290, 2008.

[17] N. C. Loh, M. A. Schmidt, and S. R. Manalis, “Sub-10cm3 interferometric accelerometer with nano-g resolution”, *Journal of Microelectromechanical Systems*, vol. 11, no. 3, pp. 182-187, 2002.

[18] N. A. Hall et al., “Micromachined accelerometers with optical interferometric read-out and integrated electrostatic actuation,” *J. Microelectromech. Syst*., vol. 17, no. 1, p. 37, 2008.

[19] A. Llobera, J. A. Plaza, et al., “Technological aspects on the fabrication of silicon-based optical accelerometer with ARROW structures,” *Sensors and Actuators A*, vol. 110, no. 1–3, pp. 395–400, 2004.

[20] J. A. Plaza et al., “BESOI-based integrated optical silicon accelerometer,” *J. Microelectromech. Syst.*, vol. 13, no. 2, pp. 355–364, 2004.

[21] J. John et al., "Planar Silicon Accelerometer with Fiber-Optic Sensing- A system level study," *in Proc. SPIE*, vol. 5062, 2003, pp.445-449.

[22] J. E. Ford, J. A. Walker, D. S. Greywall, and K. W. Goossen, "Micromechanical fiber-optic attenuator with 3 μs response," *J. Lightwave Technol.*, vol. 16, pp. 1663–1670, Sept. 1998.

[23] N. A. Riza and S. Sumriddetchkajorn, "Digitally controlled fault-tolerant multiwavelength programmable fiber-optic attenuator using a two dimensional digital micromirror device," *Opt. Lett.*, vol. 24, pp. 282–284, Mar. 1999.

[24] C. Marxer, P. Griss, and N. F. de Rooij, "A variable optical attenuator based on silicon micromechanics," *IEEE Photon. Technol. Lett.*, vol. 11, no. 2, pp. 233–235, Feb. 1999.

[25] B. Barber, C. R. Giles, V. Askyuk, R. Ruel, L. Stulz, and D. Bishop, "A fiber connectorized MEMS variable optical attenuator," *IEEE Photon. Technol. Lett.*, vol. 10, no. 9, pp. 1262–1264, Sep. 1998.

[26] G. Schröpfer, W. Elflein, M. de Labachelerie, H. Porte, S. Ballandras,"Lateral optical accelerometer micromachined in (100) silicon with remote readout based on coherence modulation", *Sensors and Actuators A*, vol. 68, pp. 344-349, 1998.

[27] T. Storgaard-Larsen, S. Bouwstra, O. Leistiko, "Opto-mechanical accelerometer based on strain sensing by a Bragg grating in a planar waveguide", *Sensors and Actuators A*, vol. 52, pp. 25-32, 1996.

[28] J. P. Laine, C. H. Tapalian, B. Little, and H. Haus, "Acceleration sensor based on high-Q optical microsphere resonator and pedestal antiresonant reflecting waveguide coupler," *Sens. Actuators A*, vol. 93, pp. 1–7, Aug. 2001.

[29] K. Tanaka, Y. Mochida, M. Sugimoto, K. Moriya, T. Hasegawa, K. Atsuchi, and K. Ohwada, "A micromachined vibrating gyroscope," *Sensors Actuators A*, vol. 50, pp. 111–115, 1995.

[30] P. Y. Kwok, M. S.Weinberg, and K. S. Breuer, "Fluid effects in vibrating micro-machined structures," *J. Microelectromech. Syst.*, vol. 14, no. 4, Aug. 2005.

[31] C. Jeong, S. Seok, B. Lee, H. Kim, and K. Chun, “A study on resonant frequency and Q factor tunings for MEMS vibratory gyroscopes,” *J. Micromech. Microeng.*, vol. 14, no. 11, pp. 1530–1536, 2004.

[32] M. Lutz et al., “A precision yaw rate sensor in silicon micromachining,” in *Tech. Dig. 9th Int. Conf. Solid-State Sensors and Actuators (Transducers’97),* Chicago, IL, June 1997, pp. 847–850.

[33] N. Yazdi, F. Ayazi, and K. Najafi, “Micromachined inertial sensors,” in *Proc. IEEE 86*, 1998, pp. 1640-1659.

[34] H. Qu, D. Fang, and H. Xie, “A single-crystal silicon 3-axis CMOSMEMS accelerometer,” *Proc. IEEE Sensors*, vol. 2, pp. 661–664, Oct. 24–27, 2004.

[35] H. Y. Hung, D. R. Chang, and W. P. Shih, “Design and Simulation of a CMOS-MEMS Gyroscope with a Low-Noise Sensing Circuit,” *in 2010 IEEE Int. Conf. on Computer, Communication, Control and Automation*, vol. 2, pp. 253-256.

[36] H. Xie and G. K. Fedder, "Integrated micro electromechanical gyroscopes," *J. Aerosp. Engrg.*, vol. 16, pp. 65-75, 2003.

[37] A. Perez and A. M. Shkel, "Design and Demonstration of a Bulk Micromachined Fabry–Perot µg-Resolution Accelerometer," *IEEE Sensors Journal*, vol. 7, no. 12, pp. 1653-1662, 2007.

[38] W. K. Burns, "*Optical fiber Rotation Sensing*, New York: Academic Press, 1994.

[39] M. Bass, “Integrated optics,” in *Handbook of optics*, 3e ed., vol. 2, New York: McGraw-Hill, 1994, pp. 35-36.

[40] G. Tao, X. Zhang, X. Liu, S. Chen, and T. Liu, “A new type of fiber Bragg grating based seismic geophone,” *Appl. Geophys.*, vol. 6, pp. 84–92, Mar. 2009.

[41] Y. Zhang, Z. F. Yin, and B. Chen, “A novel fiber Bragg grating based seismic geophone for oil/gas prospecting,” in Smart Structures and Materials 2005*: Sensors and Smart Structures Technologies for Civil, Mechanical, and Aerospace, Pts 1 and 2*, 2005, vol. 5765, pp. 1112–1120.

[42] C. Shi, N. Zeng, H. Ho, C. Chan, M. Zhang, W. Jin, and Y. Liao, “Cantilever optical vibrometer using fiber Bragg grating,” *Opt. Eng.*, vol. 42, pp. 3179–3181, 2003.

[43] W. Noell, et al.,“Applications of SOI-based optical MEMS,” *Selected Topics in Quantum Electronics, IEEE Journal of* , vol.8, no.1, pp.148-154, Jan-Feb 2002.

[44] A . Lipson, E. M. Yeatman, "Free-space MEMS tunable optical filter on (110) silicon," IEEE/LEOS Optical MEMS, pp. 73-74, 2005.

[45] M. A. Perez, “Micromachined Accelerometers with Elastomeric Suspensions using Embedded Optical Detection for Serial Sensor Networks,” M.Sc.A., University of California, Irvine, USA, 2004.

[46] S-S. Yun, K.-W. Jo, J.-H. Lee, "Crystalline Si-based in-plane tunable Fabry-Perot filter with wide tunable range," *IEEE/LEOS Optical MEMS*, pp. 77-78, 2003.

[47] J. Masson, F. B. Koné and Y.-A. Peter, "MEMS Tunable Silicon Fabry-Perot Cavity," SPIE Optomechatronic Micro/Nano Devices and Components III, Lausanne, Switzerland, October 2007.

[48] M. Andrews, I. Harris and G. Turner, “A comparison of squeeze-film theory with measurements,” *Sensors Actuators* A, vol. 36**,** pp. 79–87, 1993.

[49] E. Hecht, “Optics,” 4nd ed., Boston: Addison-Wesley, 2002.

[50] M. Perez, A. M. Shkel, "Conceptual Design and preliminary characterization of serial array system of high-resolution MEMS accelerometers with embedded optical detection,” *Smart Structures and Systems*, vol. 1, no. 1. December 2004.

[51] D. Atherton, , N. K. Reay, J. Ring, and T. R. Hicks, “ Tunable fabry-perot filters,” *Optical Engineering*, vol. 20, no.6, pp. 806-814, 1981.

[52] G. T. Reed, and A. P. Knights, *Silicon Photonics*, UK: John Wiley & Sons Ltd., 2004.

[53] D. Marcuse, “Power distribution and radiation losses in multimode dielectric slab waveguides,” *Bell Syst. Tech. J.*, vol. 51, No. 2, pp. 429–454, 1972.

[54] D. Marcuse, *Light Transmission Optics*. London, UK: Van Nostrand Reinhold, 1972.

[55] D. Marcuse, *Theory of Dielectric Waveguides*. London, UK: Academic, 1991.

[56] D. Marcuse, “Radiation losses of dielectric waveguides in terms of the power spectrum of the wall distortion function,” *Bell Syst. Tech. J.*, vol. 48, pp. 3233–3243, Dec. 1969.

[57] D. Marcuse, “Mode conversion caused by surface imperfections of a dielectric slab waveguide,” *Bell Syst. Tech. J.*, vol. 48, pp. 3186–3214, Dec. 1969.

[58] D. Marcuse, “Derivation of coupled power equations,” *Bell Syst. Tech. J.*, vol. 51, pp. 229–237, Jan. 1972.

[59] D. Marcuse, “Power distribution and radiation losses in multimode dielectric slab waveguides,” *Bell Syst. Tech. J.*, vol. 51, pp. 429–454, Feb. 1972.

[60] D. Marcuse, “Higher-order scattering losses in dielectric waveguides,” *Bell Syst. Tech. J.*, vol. 51, pp. 1801–1817, Oct. 1972.

[61] D. Marcuse, “Higher-order loss processes and the loss penalty of multimode operation,” *Bell Syst. Tech. J.*, vol. 51, pp. 1819–1836, Oct. 1972.

[62] K. K. Lee, D. R. Lim, H.-C. Luan, A. Agarwal, J. Foresi, and L. C. Kimerling, “Effect of size and roughness on light-transmission in a Si/Sio_2 waveguide: Experiments and model,” *Appl. Phys. Lett.*, vol. 77, pp. 1617–1619, 2000.

[63] F. Grillot, L. Vivien, S. Laval, D. Pascal, and E. Cassan, “Size influence on the propagation loss induced by sidewall roughness in ultrasmall SOI waveguides,” *IEEE Photon. Technol. Lett.*, vol. 16, no. 7, pp. 1661–1663, Jul. 2004.

[64] D. Lenz, D. Erni, and W. Bächtold, “Modal power loss coefficients for highly overmoded rectangular dielectric waveguides based on free space modes,” *Opt. Express*, vol. 12, pp. 1150–1156, Mar. 2004.

[65] M. Reed, T. M. Benson, P. Sewell, P. C. Kendall, G. M. Berry, and S. V. Dewar, “Free space radiation mode analysis of rectangular dielectric waveguides,” *Opt. Quantum. Elctron.*, vol. 28, pp. 1175–1179, 1996.

[66] Z. H. Wang, “Free space mode approximation of radiation modes for weakly guiding planar optical waveguides,” *IEEE J. Quantum Electron.*,vol. 34, no. 4, pp. 680–685, Apr. 1998.

[67] S. G. Johnson, M. L. Povinelli, M. Soljacic, A. Karalis, S. Jacobs, and J. D. Joannopolous, “Roughness losses and volume-current methods in photonic-crystal waveguides,” *Appl. Phys. B*, vol. 81, pp. 283–293, 2005.

[68] M. Kuznetsov and H. A. Haus, “Radiation loss in dielectric waveguide structures by the volume current method,” *IEEE J. Quantum Electron.*, vol. QE-19, no. 10, pp. 1505–1514, Oct. 1983.

[69] T. Barwicz and H. A. Haus, “Three-dimensional analysis of scatteringlosses due to sidewall roughness in microphotonic waveguides,” *J. Lightwave Technol.*, vol. 23, no. 9, pp. 2719–2732, Sep. 2005.

[70] J. P. R. Lacey and F. P. Payne, “Radiation loss from planar waveguides with random wall imperfections,” *Proc. Inst. Electr. Eng.*, vol. 137, pp. 282–288, Aug. 1990.

[71] T. Bierhoff, A. Wallrabenstein, A. Himmler, E. Griese, and G. Mrozynski, “Ray tracing technique and its verification for the analysis of highly multimode optical waveguides with rough surfaces,” *IEEE Trans. Magnetics*, vol. 37, no. 5, pp. 3307–3310, Sep. 2001.

[72] C. G. Poulton, C. Koos, M. Fujii, A. Pfrang, T. Schimmel, J. Leuthold, and W. Freude, “Radiation modes and roughness loss in high indexcontrast waveguides,” *IEEE J. Sel. Top. Quantum Electron.*, vol. 12, no. 6, pp. 1306–1320, Nov./Dec. 2006.

[73] I. Papakonstantinou, R. James, and D. Selviah, "Radiation- and Bound-Mode Propagation in Rectangular, Multimode Dielectric, Channel Waveguides With Sidewall Roughness," *J. Lightwave Technol.* Vol. 27, No. 18, pp. 4151-4163, 2009.

[74] A. Di Donato et al., “Stationary mode distribution and sidewall roughness effects in overmoded optical waveguides,” *J. Lightw. Technol.*, vol. 28, no. 10, pp. 1510–1520, May 2010.

[75] Eng, T.T.H.; Ho, J.Y.L.; Chan, P.W.L.; Kan, S.C.; Wong, G.K.L.; , "Large core (~ 60 μm) SOI multimode waveguides for optical interconnect," *Photonics Technology Letters, IEEE* , vol.8, no.9, pp.1196-1198, Sept. 1996.

[76] C. C. Chang et al., " SOI-based trapezoidal waveguide with 45° microreflector for noncoplanar optical interconnect," *Optics Letters*, vol.37, no.5, pp.782-784, March 2012.

[77] D. Gloge and E. A. J. Marcatili, “Multi mode theory of graded-core fibers,” *Bell Syst. Tech. J.*, vol. 52, pp. 1563-1578, 1973.

[78] C. M. Miller,“Transmission versus transverse offset for parabolic – profile fiber splices with unequal core diameters”, *Bell System Tech. J.*, pp. 917-927,1976.

[79] C. Gao, and G. Farrell, “Power Coupling between two Step-index Multimode Fibers of Different Numerical Apertures with an Angular Misalignment”, *Microwave and Optical Technology Letters*, Vol. 43, No. 3, pp. 231-234, November 2004.

[80] M. J. Adams, D. N. Payne, and F. M. E. Sladen , "Splicing tolerances in graded-index fibers," *Applied Physics Letters* , vol.28, no.9, pp.524-526, May 1976.

[81] D. Gloge, “Offset and tilt loss in optical fiber splices”, *Bell System Tech. J.*, pp. 905-915, 1976.

[82] Y. Yamada, M. Kawachi. M. Yasu, and M. Kobayashi, "High-silica multimode channel waveguide structure for minimizing fiber-waveguide- fiber coupling loss," *J. Lightwave Technol*., vol. LT-4, 1986.

[83] P. DiVita and U. Rossi, “Theory of power coupling between multimode optical fibres”, *Optical and quantum electronics*, vol. 10, pp. 107-117, 1978.

[84] G. Aldabaldetreku, G. Durana, J. Zubia, and J. Arrue, “Investigation and comparison of analytical, numerical, and experimentally measured coupling losses for multi-step index optical fibers,” *Optics Express*, vol. 13, no. 11, pp. 4012-4036, 2005.

[85] C. M. Miller and *S.* C. Mettler, “A loss model for parabolic-profile fiber splices,” *Bell Syst. Tech. J.* , vol. 57, no. 9, pp. 3167-3180, Nov. 1978.

[86] S. C. Mettler, “A general characterization of splice loss for multimode optical fibers,” *Bell Syst. Tech. J.*, vol. 58, no. 10, pp. 2163–2182, 1979.

[87] D. Lenz, D. Erni, and W. Bächtold, “Modal power loss coefficients for highly overmoded rectangular dielectric waveguides based on free space modes,”*Opt. Express*, vol. 12, pp. 1150–1156, 2004.

[88] Zi Hua Wang, "Free space mode approximation of radiation modes for weakly guiding planar optical waveguides," *Quantum Electronics, IEEE Journal of*, vol.34, no.4, pp.680-685, Apr 1998.

[89] Barwicz, Tymon; Smith, Henry I.; "Evolution of line-edge roughness during fabrication of high-index-contrast microphotonic devices," *Journal of Vacuum Science & Technology B: Microelectronics and Nanometer Structures*, vol.21, no.6, pp.2892-2896, Nov 2003.

[90] A. Q. Liu, X. Zhang, J. Li, S. H. G. Teo, F. L. Lewis, B. Borovic, "MEMS Variable Optical Attenuators," in *Photonic MEMS Devices: Design, Fabrication and Control*, New York: CRC Press, 2009, pp. 190-199.

[91] M. Saruwatari and K. Nawata, "Semiconductor laser to single-mode fiber coupler," *Appl. Opt.*, vol. 18**,** pp. 1847-1856, June 1979.

[92] U. Fischer, T. Zinke, J.-R. Kropp, F. Arndt, and K. Peterman, "0.1 dB/cm waveguide losses in single-mode SOI rib waveguides," *J. IEEE Photon. Technol. Lett.*, vol. 8, no. 5, pp. 647–648, 1996.

[93] P. K. Tien, "Light waves in thin films and integrated optics," *Appl. Opt.*, vol. 10, pp. 2395-2413, Nov. 1971.

[94] K. Petermann, "Properties of optical rib-guides with large cross-section," *Archiv für Elektronik undÜberetragungstechnik*, vol. 30, pp. 139-140, 1976.

[95] R. A. Soref, J. Schmidtchen, K. Petermann, "Large single-mode rib waveguides in GeSi-Si and Si-on-SiO_2", *IEEE J. Quantum Electron.*, vol.27, pp. 1971-1974, 1991.

[96] Y. A. Vlasov and S. J. McNab, "Losses in single-mode silicon-on-insulator strip waveguides and bends," *J. Opt. Express*, vol. 12, pp. 1622-1631, 2004.

[97] T. Aalto, "Microphotonic silicon waveguide components," Dr. Sc., Helsinki University of Technology, Espoo, Finland, 2004.

[98] S. M. Grist et al., "Silicon photonic micro-disk resonators for label-free biosensing," *Opt. Express*, vol. 21, no. 7, pp. 7994–8006, 2013.

[99] K. De Vos, I. Bartolozzi, E. Schacht, P. Bienstman, and R. Baets, "Silicon-on-insulator microring resonator for sensitive and label-free biosensing," *Opt. Express*, vol. 15, no. 12, pp. 7610–7615, 2007.

[100] R. St-Gelais, T. Kerrien, H. Camirand, A. Poulin, and Y.-A. Peter, "Silicon-On-Insulator In-Plane Gires-Tournois Interferometers," *IEEE Photon. Technol. Lett.*, vol. 24, pp. 2272 - 2275, 2012.

[101] C. A. Barrios, V. R. Almeida, R. R. Panepucci, B. S. Schmidt, and M. Lipson, "Compact silicon tunable Fabry–Pérot resonator with low power consumption," *IEEE Photon. Technol. Lett.*, vol. 16, no. 2, pp. 506–508, Feb. 2004.

[102] M. W. Pruessner, T. H. Stievater, and W. S. Rabinovich, "Integrated waveguide Fabry–Pérot microcavities with silicon/air Bragg mirrors," *Opt. Lett.*, vol. 32, no. 5, pp. 533–535, 2007.

[103] M. W. Pruessner, T. H. Stievater, and W. S. Rabinovich, "In-plane microelectromechanical resonator with integrated Fabry-Pérot cavity," *Appl. Phys. Lett.*, vol. 92, no. 8, p. 081101, 2008.

[104] M. W. Pruessner, T. H. Stievater, M. S. Ferraro, and W. S. Rabinovich, "Thermo-optic tuning and switching in SOI waveguide Fabry-Perot microcavities," *Opt. Express*, vol. 15, pp.7557-7563, 2007.

[105] A. Leblanc-Hotte, R. St-Gelais, and Y.-A. Peter, "Optofluidic Device for High Resolution Volume Refractive Index Measurement of Single Cell," in *International Conference on Miniaturized Systems for Chemistry and Life Sciences*, Okinawa, Japan, pp. 1330-1332, 2012.

[106] K. Solehmainen, T. Aalto, J. Dekker, M. Kapulainen, M. Harjanne, K. Kukli, P. Heimala, K. Kolari, and M. Leskelä, "Dry-etched silicon-on-insulator waveguides with low propagation and fiber-coupling losses," *J. Lightw. Technol.*, vol. 23, no. 11, pp. 3875–3880, 2005.

[107] Allan W. Snyder and John D. Love, *Optical Waveguide Theory*, London: Chapman and Hall, 1983.

[108] B. E. A. Saleh, and M. C. Teich, *Fundamentals of Photonics*, NY: John Wiley, 1991, pp. 258-261.

[109] W. S. Mohammed, A. Mehta, and E. G. Johnson, "Wavelength Tunable Fiber Lens Based on Multimode Interference", *J. Lightwave Technology*, vol. 22, no. 2, pp. 469-477, 2004.

[110] A. A. Seshia, "Integrated Micromechanical Resonant Sensors for Inertial Measurement Systems," Ph. D. dissertation, University of California, Berkeley, U.S.A, 2002.

[111] H. Dong, "Design and Analysis of a MEMS Comb Vibratory Gyroscope,"M.Sc.A, University of Bridgeport, Bridgeport, U.S.A, 2009.

[112] K. Okamoto, *Fundamentals of optical waveguides*, MA: Academic Press, 2006, pp. 27-31.

[113] Y.-A. Peter, "Microsystem," École Polytechnique de Montréal, Course note, February 2008, Chapter 4, Micro Mechanical Systems.

[114] X.-P.S. Su, "Compliant leverage mechanism design for MEMS application," Ph. D. dissertation, University of California, Berkeley, U. S. A, 2001.

[115] X.-P.S. Su, H. S. Yang, and A. M. Agogino, "A resonant accelerometer with two-stage microleverage mechanisms fabricated by SOI-MEMS technology," *Sensors*, vol. 5, no. 6, pp. 1214–1223, Dec. 2005.

[116] M. J. Walker, Comparison of Bosch and Cryogenic Processes for Patterning High Aspect Ratio Features in Silicon. London, U.K.: OxfordInstrum. Plasma Technol., 2001.

[117] Wu, Banqiu; Kumar, Ajay; Pamarthy, Sharma; "High aspect ratio silicon etch: A review," *Journal of Applied Physics*, vol.108, no.5, pp.051101-051101-20, Sep 2010.

[118] H. K. Taylor, H. Sun, T. F. Hill, A. Farahanchi, and D. S. Boning, "Characterizing and predicting spatial non-uniformity in the deep reactive ion etching of silicon," *J. Electrochem. Soc.*, vol. 153, no. 8, pp.C575–C585, Jun. 2006.

[119] M. Lipson, "Guiding, modulating, and emitting light on silicon-challenges and opportunities," *J. Lightw. Technol.*, vol. 23, no. 12, pp. 4222–4238, Dec. 2005.

[120] "Thick resist processing," *Microchemical company*, Version 2009-11-11. [online]. Available:http://www.microchemicals.eu/technical_information/thick_resist_processing.pdf. [Accessed: October 18, 2012].

[121] S. Gupta and R. Gupta, "A parametric study of spin coating over topography," *Ind. Eng. Chem. Res.*, vol. 37, pp. 2223–2227, 1998.

[122] N. P. Pham et al., “IC-compatible process for pattern transfer in deep wells for integration of RF components”, Proc. SPIE conf. vol.4174, pp.390-397, 2000.

[123] V. G. Kutchoukov et al., “New photoresist coating method for 3-D structured wafers”, *Sensor & Actuator A*, vol. 85, pp. 377-383, 2000.

[124] N. P. Pham et al., “Spray coating of photoresist for pattern transfer on high topography surfaces”, *J. Micromech. Microeng.*, vol.15, pp. 691- 697, 2005.

[125] *Nanometrix Inc.* [Online]. Available: http://www.nanometrixinc.com. [Accessed: October 17, 2012].

[126] L. Yu, Y.Y. Lee, F.E.H. Tay, C. Iliescu, “Spray coating of photoresist for 3D microstructures with different geometries”, *J. Phys. Conf. Ser.*, vol. 34, pp. 937–942, 2006.

[127] K. Fisher and R. Suss, “Spray coating-a solution for resist film deposition across severe topography”, IEEE/SEMI Int. Elec. Manuf. Tech. Symp. pp 338-41, 2004.

[128] J. Schneider, “Method and apparatus for thin film/layer fabrication and deposition,” U.S. Patent No. 2009/0181162 A1, July 16, 2009.

[129] K. Zandi, Y. Zhao, J. Schneider, and Y.-A. Peter, "New Photoresist Coating Method for High Surface Topography," *23rd IEEE Intl. Conf. on Micro Electro Mechanical Systems*, Hong Kong, pp. 392-395, 2010.

[130] L. K. White, “Planarization properties of resist and polyimide Coatings”, *J. Electrochem. Soc.*, vol. 130, pp. 1543-1548, 1983.

PUBLICATIONS RELATED TO THIS WORK

1. K.Zandi and Y.-A. Peter, “An Integrated Silicon-On-Insulator Optical MEMS Accelerometer Based on Variable Optical Attenuator,” to be submitted to *IEEE J. of MEMS.*

2. K.Zandi, J. A. Bélanger, and Y.-A. Peter, “Design and Demonstration of an In-Plane Silicon On-Insulator Optical MEMS Fabry Pérot-Based Accelerometer Integrated With Channel Waveguides,” *IEEE J. of MEMS*, vol. 21, no. 6, pp. 1464-1470, 2012.

3. K. Zandi, J. Zou, B. Wong, R. V. Kruzelecky, and Y.-A. Peter, “VOA-Based Optical MEMS Accelerometer,” *IEEE/LEOS International Conference on Optical MEMS and Nanophotonics*, Istanbul, Turkey, 2011.

4. K. Zandi B. Wong, J. Zou, R. V. Kruzelecky, W. Jamroz, and Y.-A. Peter, "In-Plane Silicon-On-Insulator Optical MEMS Accelerometer Using Waveguide Fabry-Perot Microcavity With Silicon / Air Bragg Mirrors," *23rd IEEE Intl. Conf. on Micro Electro Mechanical Systems*, Hong Kong, pp. 839-842, 2010.

5. K. Zandi, Y. Zhao, J. Schneider, and Y.-A. Peter, "New Photoresist Coating Method for High Surface Topography," *23rd IEEE Intl. Conf. on Micro Electro Mechanical Systems*, Hong Kong, pp. 392-395, 2010.

APPENDIX 1 – Design parameters for VOA-based accelerometer fabricated on 75 µm-thick SOI substrate

Proof mass width: 1210 µm

Proof mass length: 1210 µm

Etch-holes dimension: 5 µm ×5 µm

Distance between etch-holes: 4 µm